Development of a low-cost, simple-to-use microfluidic device for analysis of glioblastoma multiforme movement

by

Abigail Fay Kreznor

B.S., Bucknell University, 2018

AN ABSTRACT OF A DISSERTATION

submitted in partial fulfillment of the requirements for the degree

DOCTOR OF PHILOSOPHY

Department of Chemistry
College of Arts and Sciences

KANSAS STATE UNIVERSITY
Manhattan, Kansas

2024

Abstract

Glioblastoma multiforme (GBM), a type of adult primary brain cancer, exhibits rapid tumor progression and extremely low survival rates. The cancerous cells utilize the signaling pathways within the central nervous system to encourage cancer-promoting behaviors that manipulate the immune response and degrade the extracellular matrix to aid tumor proliferation. Additionally, GBM applies cellular mechanisms to enable mobility through both perivascular spaces and constrictive tissues within the brain. These characteristics of GBM greatly diminish the effectiveness of traditional cancer treatment methods. The higher age of patients diagnosed with GBM contributes to other significant issues during treatment, such as comorbidities and higher risk of surgical complications. A better understanding of GBM, especially how the tumor microenvironment influences the mobility of this cancer, could be vital to developing improved therapeutics.

While many established methods have been used to study the cell environment and resulting migration, the majority of these techniques suffer from instability, imprecision, and providing only endpoint analysis. Microfluidic devices offer an alternative platform for cell studies with significant advancements by coupling enhanced fluidic control with real-time, live cell imaging. Gradient-producing devices can create complex and stable experimental conditions for more elaborate modeling of the tumor microenvironment. Although traditional microfluidics fabrication requires expensive equipment and advanced training, substantial progress in the field of 3D printing has greatly increased the capabilities of this fabrication technique while simultaneously reducing the startup costs and level of expertise needed. This work presents the development of a low-cost and simple-to-use microfluidic device to study GBM movement.

The initial exploration of LCD-based and digital light projection resin 3D printing included the optimization of printing and post-print processing for the fabrication of microfluidic devices. Critical material properties of the cured resin, such as temperature resistance, autofluorescence, and biocompatibility, were assessed. Out of the multiple sealing methods examined, 3M™ microfluidic tape was selected as the best reversible option, and a treatment procedure was developed to enable cell culture on its adhesive surface. A protocol for casting polydimethylsiloxane devices from resin 3D-printed molds was created, and an appropriate environment for cell culture was maintained using a microscope stage incubator and a miniature heating pad for external tubing. After testing a variety of methods for fluidic operation, a miniaturized and automated system was implemented. Confirmation of gradient formation, the key factors that influence the gradient profile and stability, and a basic analysis of shear stress within the device were completed. Finally, initial results from GBM migration studies were reported to provide proof-of-concept for the devices developed in this work.

Development of a low-cost, simple-to-use microfluidic device for analysis of glioblastoma multiforme movement

by

Abigail Fay Kreznor

B.S., Bucknell University, 2018

A DISSERTATION

submitted in partial fulfillment of the requirements for the degree

DOCTOR OF PHILOSOPHY

Department of Chemistry
College of Arts and Sciences

KANSAS STATE UNIVERSITY
Manhattan, Kansas

2024

Approved by:

Major Professor
Christopher T. Culbertson

Copyright

Abstract

Glioblastoma multiforme (GBM), a type of adult primary brain cancer, exhibits rapid tumor progression and extremely low survival rates. The cancerous cells utilize the signaling pathways within the central nervous system to encourage cancer-promoting behaviors that manipulate the immune response and degrade the extracellular matrix to aid tumor proliferation. Additionally, GBM applies cellular mechanisms to enable mobility through both perivascular spaces and constrictive tissues within the brain. These characteristics of GBM greatly diminish the effectiveness of traditional cancer treatment methods. The higher age of patients diagnosed with GBM contributes to other significant issues during treatment, such as comorbidities and higher risk of surgical complications. A better understanding of GBM, especially how the tumor microenvironment influences the mobility of this cancer, could be vital to developing improved therapeutics.

While many established methods have been used to study the cell environment and resulting migration, the majority of these techniques suffer from instability, imprecision, and providing only endpoint analysis. Microfluidic devices offer an alternative platform for cell studies with significant advancements by coupling enhanced fluidic control with real-time, live cell imaging. Gradient-producing devices can create complex and stable experimental conditions for more elaborate modeling of the tumor microenvironment. Although traditional microfluidics fabrication requires expensive equipment and advanced training, substantial progress in the field of 3D printing has greatly increased the capabilities of this fabrication technique while simultaneously reducing the startup costs and level of expertise needed. This work presents the development of a low-cost and simple-to-use microfluidic device to study GBM movement.

The initial exploration of LCD-based and digital light projection resin 3D printing included the optimization of printing and post-print processing for the fabrication of microfluidic devices. Critical material properties of the cured resin, such as temperature resistance, autofluorescence, and biocompatibility, were assessed. Out of the multiple sealing methods examined, 3M™ microfluidic tape was selected as the best reversible option, and a treatment procedure was developed to enable cell culture on its adhesive surface. A protocol for casting polydimethylsiloxane devices from resin 3D-printed molds was created, and an appropriate environment for cell culture was maintained using a microscope stage incubator and a miniature heating pad for external tubing. After testing a variety of methods for fluidic operation, a miniaturized and automated system was implemented. Confirmation of gradient formation, the key factors that influence the gradient profile and stability, and a basic analysis of shear stress within the device were completed. Finally, initial results from GBM migration studies were reported to provide proof-of-concept for the devices developed in this work.

Table of Contents

List of Figures

List of Tables

List of Equations

List of Abbreviations

5-chloromethylfluorescein diacetate (CMFDA)

Acrylonitrile butadiene styrene (ABS)

Blood brain barrier (BBB)

CC motif chemokine ligand 18 (CCL18)

CC motif chemokine ligand 5 (CCL5)

Central nervous system (CNS)

Comprehensive geriatric assessment (CGA)

Computer-aided design (CAD)

Deionized (DI)

Dimethylsulfoxide (DMSO)

Dulbecco's Modified Eagle Medium (DMEM)

Ethanol (EtOH)

Extracellular matrix (ECM)

Fetal bovine serum (FBS)

Fibroblast growth factor 1 (FGF-1)

Fluorinated ethylene propylene (FEP)

Glioblastoma multiforme (GBM)

Hepatocyte growth factor (HGF)

Hexamethyldisilazane (HMDS)

Hyaluronic acid (HA)

Lab-on-a-chip (LOC)

Micro total analysis systems (μTAS)

Microfluidic paper-based analytical device (μPAD)

Norland Optical Adhesive (NOA)

Phosphate-buffered saline (PBS)

Polydimethylsiloxane (PDMS)

Poly-D-lysine (PDL)

Polyether ether ketone (PEEK)

Polyethylene terephthalate glycol (PETG)

Perfluoroalkoxy alkane (PFA)

Poly-lactic acid (PLA)

Polyvinyl acrylate (PVA)

Propidium Iodide (PI)

Reynolds number (R_e)

Rhodamine B (RhB)

Transforming growth factor-α (TGF-α)

Acknowledgements

To my mom and dad, Nancy and Bill. You two always encouraged me to be an active participant in my education and to be the best I could possibly be. I am so grateful for the opportunities you provided for me. Whether it was during science-themed Girl Scout events or on geological hiking trips, you both taught me that girls are meant to be scientists as much as anything else. You both have been great examples of perseverance. I would not be who I am today without your guidance, support, and love. Thank you, I love you.

To my brother, Phil. It's incredible how much the relationship between a big brother and little sister can grow as they both get older. I know I can come to you for a nice phone call, a fun trip to DSM, and even financial advice. You have done so much to help me feel supported during my time in grad school, and I cannot thank you enough for it. I love you.

To my undergraduate academic and research advisor, Tim Strein. I will never forget the incredible department tour you took my family on when we visited Bucknell. From the basics of analytical chem to the frontiers of microscale separations, you opened my eyes. Thank you for being such a crucial player in my chemistry education.

To my advisor, Chris. Thanks for offering me a spot in your lab and believing in each crazy idea I ever came up with. It wasn't easy, but we finally finished this together.

To the best coworker, and friend, a grad student could have, Jay. I know it wouldn't have been possible for me to do all this without you. You taught me almost everything I know about traditional microfluidics fabrication, cell culture, and so much more. Not only did you go above and beyond as a research mentor, but you became my best friend. I can't thank you enough for all you've done for me professionally and personally.

To my lab mate and friend, Kushan. It was so exciting to get another grad student in our little group when you joined. You've been there to bounce ideas and vent to. It's been a pleasure to know you and your family. I wish you success as you finish your program.

I would like to shout out a few people from the KState Chemistry Department I don't think get enough recognition. Jim is so much more than a scientific glassblower. To Jim, you've been a fantastic hallway neighbor and vital source of positivity. Thank you for your friendship and your participation in a constant exchange of baked goods. Bart has one of the most important roles in this department. To Bart, I could not have done this without you happily ordering all the strange things I've asked for. Thank you so much for always being so helpful and friendly. Tobe is a miracle worker. To Tobe, thank you for fixing or building everything I've ever asked for.

To my incredible fiancé, Nathan. Coming home to you after every tough day in the lab made it easier. I can't explain how much your support and love has meant to me while I fought through it all. You are my biggest source of joy. If I tried to put all my feelings into words, I'd have to write a second dissertation. I love you so much, thank you for your unending patience, now let's finally get married!

Dedication

For those who have lost their battles with cancer. Too many of our family members and friends have been taken too soon. We think of you fondly, we miss you dearly, and we hope you are at peace.

Chapter 1 - Introduction

1.1 Glioblastoma multiforme

Glioblastoma multiforme (GBM) is an incredibly deadly form of adult brain cancer. The average age of incident for primary GBM is 62 years old, and less than 5% of patients survive 5 years post diagnosis occurring in roughly 3 per 100,000 in the age-adjusted population.[1, 2] Common symptoms can include headache, functional deficiencies, vision loss, intracranial pressure, numbness, and seizures.[3-6] The persistence of such symptoms will prompt imaging of the brain, initiating the diagnosis process, followed by tumor sample biopsy involving genotypic, phenotypic, and histopathological analysis.[7] Many factors have been investigated to determine potential causes or risk factors for GBM, including genetic factors. Primary GBM has a higher incident rate in males than females, 1.4-1.6:1, respectively, with little evidence providing significant associations between any form of drug use or dietary exposure to smoked meats.[1, 7] Exposure to various kinds of radiation has also been explored by researchers, including frequencies from cell phone use and extremely low frequency magnetic fields, resulting in more definitive results from elevated exposure to ionizing radiation and more inconclusive results from nonionizing radiation.[2] One of the most critical characteristics of GBM is its rapid growth. Within weeks, increased tumor mass and a significant necrotic center can develop, contributing to the tumor microenvironment and the impacts GBM has on the brain.[3]

1.1.1 Manipulation of brain environment

As the GBM tumor progresses, it begins to manipulate the surrounding environment. Noncancerous cells, often microglia, the primary immune cell of the central nervous system (CNS), were found to make up a significant proportion of the tumor mass, with tumor-associated microglia comprising up to 30% of the tumor.[8-10] This recruitment is facilitated through the

release of chemical signals which promote cell migration toward the source. Microglial cells survey their environment, migrate toward the site of injury, and react to chemical signals in either a proinflammatory or anti-inflammatory way, often defined as the M1 or M2 phenotype, respectively.[11] The responsibilities of these immune cells can include phagocytosis, recruitment of T-cells, and anti-inflammatory signaling.[12] Under healthy CNS function, the balance between M1 and M2 phenotypes is used to eliminate threats and contribute to repair mechanisms afterward. Although microglia should be recruited to destroy GBM, the cancer cells instead use chemical signals to encourage aspects of tumor growth, further recruit other healthy cells, and contribute to immunosuppression and a pro-tumor environment by forcibly inducing and sustaining the M2 phenotype (Figure 1.1).[8, 13]

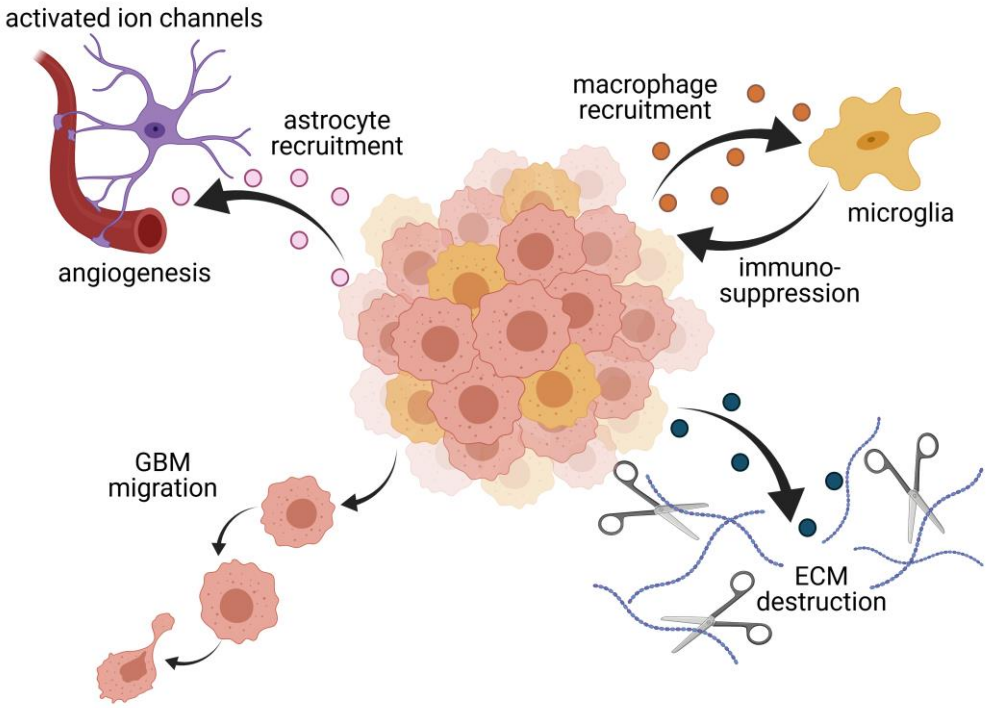

Figure 1.1. The manipulation of the brain by GBM. The signals released by cancer cells initiate pro-tumor conditions, the recruitment of other healthy cells, and overall cancer progression. Created with BioRender.com.

The manipulation of the CNS by GBM contributes to the recruitment of astrocytes as well. Healthy astrocytes play an influential role in the CNS by supporting neurons and blood vessels to contribute to the structure of the brain. These cells release signals, support the blood-brain barrier (BBB), aid in the production and use of neurotransmitters, and preserve nutrient levels.[14, 15] There is considerable communication between GBM, astrocytes, and microglia. The ion channels maintained by astrocytes are employed to increase communication within the tumor microenvironment.[4] Astrocytes are utilized by GBM to promote angiogenesis supporting the proliferation of GBM throughout the brain (Figure 1.1). These corruptive measures contribute to the extremely fast development of GBM and the incredibly destructive nature of this fatal brain cancer.

1.1.2 Enhanced mobility of GBM

One of the most significant characteristics exhibited by GBM is its enhanced mobility. This contributes to the highly invasive nature of this cancer.[16] As described above, healthy cells are used by GBM to assist in the degradation of the brain environment, allowing cancer cells to more easily move through the brain. The extracellular matrix (ECM) and its various cues, such as small cell-signaling proteins, topography, and stiffness, have influence over cancer progression and metastasis.[17-19] The mobility of GBM is dissimilar to other forms of cancer that typically metastasize utilizing the bloodstream. GBM cells can move through both the fluid-filled perivascular space surrounding blood vessels and the more restrictive functional tissue of the brain neuronal and glial cells.[20] To enable this migration within tight spaces, GBM releases free cytoplasmic water from the cell, which results in volume decreases up to 30-35%.[21] The speed of GBM migration fluctuates in response to the surrounding cell environmental, but velocities of 15-25 μm/hr and up 100 μm/hr have been reported.[22, 23]

Another important factor with influence over GBM mobility is hyaluronic acid (HA). HA is a major component of the ECM, especially within the brain, which is often overexpressed around tumors.[16, 24] The transmembrane glycoprotein CD44, expressed by many cancer cells including GBM, triggers mechanisms for cell proliferation, mobility, angiogenesis, and apoptosis, and has a critical role to play in tumor progression.[25] CD44 interacts with a significant number of key cell factors including ankyrin, impacting cytoskeletal structure, RhoA, influencing migration, NHE1, contributing to ECM destruction and tumor invasion, and ERK2, increasing transcription mechanisms (Figure 1.2).[16, 24, 26] All these signaling pathways are affected by HA-CD44 interactions and contribute to the invasiveness of GBM and its increased mobility through the brain.

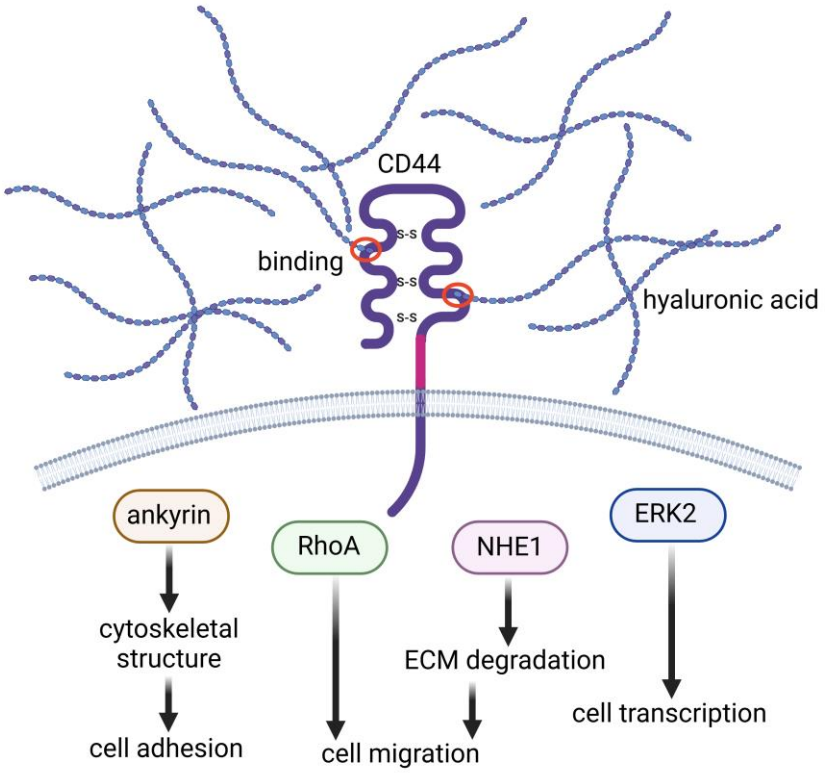

Figure 1.2. The binding of extracellular HA to CD44 triggers a range of cell responses that contribute to the mobility and invasiveness of GBM. The presence of HA in the brain ECM, and its elevated concentration in the tumor environment, influences the rapid progression of GBM. Created with BioRender.com.

To further highlight the influence HA and CD44 have on GBM progression, some researchers have investigated inhibiting CD44. Wang *et al*. used verbascoside, which exhibited higher binding potential to CD44, to lower the interactions between HA and CD44 and found GBM proliferation was suppressed.[27] Similarly, Xu *et al*. reported that CD44 knockdown, and the resulting reduced binding of HA, decreased tumor growth rates in vivo, prolonged the survival rate of experimental mice, and increased GBM sensitivity to common chemotherapy drugs.[28] As a result of findings such as these, more research has focused on better understanding this relationship and exploiting it for GBM treatment.

1.1.3 Ineffective treatments for GBM

Despite considerable research, minimal improvements have been made for GBM treatment.[3] Once this brain cancer is diagnosed, the standard treatment regimen starts with the maximum surgical removal followed by radiation and the use of chemotherapy to prevent further tumor development.[3, 29, 30] Effective surgical removal relies on extracting as much tumor mass as possible. The typical challenges that come with surgery are even greater for such a delicate and important location as the brain. Additionally, the highly mobile nature of GBM makes it a nearly impossible target for localized treatment methods like surgical resection. Radiation therapy also has its limitations. There is conflicting research on the effective radiation dosage for GBM.[3] Furthermore, multiple studies have shown increased resistance to radiation treatment exhibited by GBM cells.[4, 31] Finally, treatment utilizing chemotherapy, often temozolomide, is also subject to drawbacks. The BBB prevents the majority of anticancer drugs from reaching brain tumors.[30] While alternative drug delivery methods, such as nanoparticles, intranasal delivery, direct injection via probe or blood vessel in the proximity of the tumor, or temporary disruption of the BBB utilizing focused ultrasound, have been developed, this has not increased the success of

these methods.[32] All of these challenges result in ineffective treatment of this incredibly aggressive form of cancer.

Besides the customary battles that come with a cancer diagnosis, additional concerns factor into treatment strategies for older patients. As the population of elderly people increases, the number of cancer diagnoses also increases, and this creates new challenges for cancer researchers and medical staff.[33] There are many ways to assess the overall health and potential risks for elderly patients, including comprehensive geriatric assessment (CGA). This tool measures the impact of critical factors such as comorbidities, cognition, nutrition, emotional status, social support, and living environment.[34] The CGA can be used by a patient's medical team to determine the most effective and least harmful cancer treatment plan.

There are many unknowns when it comes cancer treatment in aging populations, and this can be linked to a lack of data since the elderly can be underrepresented in clinical trials.[33] While there are considerable uncertainties in therapeutic guidelines and the potential impacts of cancer treatments on elderly bodies, there are some undeniable risk factors. The increasing incidence of comorbidities in older patients, and the resulting higher medication usage, contributes to the elevated risk of adverse drug reactions with chemotherapy drugs.[34] Elderly patients are also at higher risk for surgical complications. Due to all these limitations for GBM treatment, it is clear that a better understanding of this brain cancer is essential so that more effective therapeutic strategies can be developed. This work seeks to expand on GBM research by focusing on a better understanding of the mobility of this cancer.

1.2 Cell migration

General cell migration is a critical process of life.[35-37] Cell migration begins during development of the embryo, where cells migrate and differentiate for specific roles. Different

types of cell migration continue throughout life during both healthy and disease conditions.[35, 37] While most of the instances of cell migration have health benefits, such as immune response, skin cell turnover, or wound repair, dysregulation of cell migration can contribute to severe negative health consequences or even aid in disease progression, as described above during the recruitment of healthy cells into the GBM tumor mass.[10, 13, 35, 36, 38, 39] It is clear that cell migration plays a key role in the development of GBM, but for this migration to begin, a signal must first be generated, released, and sensed by another cell.

1.2.1 Chemotaxis

There are many potential sources of information for cells provided by the ECM including topography, stiffness, mechanical stress, and chemical signals.[40] Due to the fluctuating nature of the ECM, there is an incredible amount of information for cells to constantly gather. The protein signals that regulate cell migration can include membrane receptors, kinases, and cytoskeletal and adhesion elements, and such signals can induce chemotaxis.[37]

Chemotaxis is the directional migration of a cell in response to an external chemical gradient released from other cells or extracellular vesicles.[38, 41] A chemoattractant, the chemical signal responsible for cell migration towards a region of higher signal concentration, is bound to receptors on the sensing cell membrane. An asymmetric distribution of bound receptors results in cell polarization, creating a cell front, the cell region facing towards the higher concentration of chemoattractant, and cell rear, facing the opposite direction.[35, 41, 42] Concentration differences as low as 2% between cell front and rear can induce migration in some cell types.[43] Binding between signal and receptor contribute to a cascade of internal actions. At the cell front, the polymerization of actin causses protrusions of the cell membrane.[37, 44] The cell's ability to adhere to the ECM allows these protrusions to grip onto the surrounding environment. In response,

contraction forces at the cell rear cause the release of the cell membrane from the ECM and thus contributes to overall forward motion (Figure 1.3).[41] This process can be utilized for brief or prolonged periods of cell migration depending on the source of the signal and its diffusion coefficient.[38]

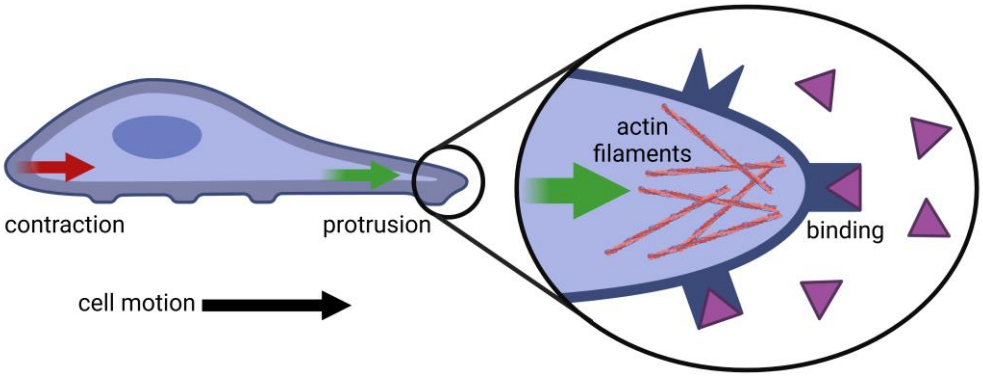

Figure 1.3. The binding of chemoattractants to receptors on the cell membrane triggers the polymerization of actin filaments. This asymmetric distribution of binding polarizes the cell. The filaments push on the membrane causing protrusions at the cell front. This forward motion, in combination with contraction at the back of the cell, work together to cause cell motion toward higher concentration of chemoattractant. Created with BioRender.com.

1.2.2 Traditional methods for studying chemotaxis

Due to the importance of understanding chemotaxis and the role it plays in overall health, many methods have been developed to analyze this form of cell motion. These methods rely on effective modeling to study chemotaxis since the formation and maintenance of chemoattractant gradients in vivo is unpredictable as a result of diffusion and changing biological conditions.[38] The Boyden chamber is often used for these studies. For experiments carried out in a Boyden chamber, the cells are seeded into an insert, often fitted for a well plate, with a porous membrane bottom. This setup is then placed in a solution with the selected chemoattractant. The strength of the chemotactic response is quantified by the number of cells which migrate through the membrane.[45] While this method is often used for its relative simplicity and the convenience of

easily purchasable products, it has many limitations such as a lack of time stability, an undefined and inconsistent gradient, the potential to misidentify chemokinesis, random cell movement, as chemotaxis, and the inability to be paired with live cell imaging which means that it can only provide endpoint results.[45-47]

The Dunn chamber is another option that can be used for chemotaxis experiments. For this work, two concentric circular wells are recessed into a glass slide with a bridge between them. A coverslip seeded with cells is inverted over the wells and sealed leaving a small gap, typically 20 μm, between the top of the bridge and the coverslip.[47] The chemoattractant solution is pipetted into the outer well and a linear gradient is formed based on diffusion across the bridge gap between the two wells. Although this method is paired with time-lapse microscopy for live cell morphology and migration tracking, there are still limitations to this method. Using the Dunn chamber requires very precise and practiced movements to avoid any bubbles which would interfere with gradient formation and cell behavior.[47] Additionally, the chemoattractant gradient formed using the Dunn chamber is temporary and results can suffer from poor reproducibility.[45]

Alternatively, a simple micropipette assay can be done. For this experiment, a micropipette is used to deliver a chemoattractant to a particular area within an established tissue culture, forming the gradient via diffusion. The experimental setup is less complex than the Dunn chamber and can also be coupled with time-lapse microscopy for live cell tracking. While this assay can be as simple as direct, manual pipetting, more control can be achieved by incorporating a programmable pressure pulsing system, such as a Picospritzer, to deliver specified bursts of chemoattractant.[48] This method still provides short temporal stability and limited gradient stability if manual pipetting is used.[45]

Although the methods described above are often utilized for chemotaxis studies, they share many limitations especially concerning the stability of the experimental conditions. An improved method for cell migration studies needs to be used to better understand the GBM tumor microenvironment and the migration that occurs there. Since the biological systems within and surrounding the GBM tumor are complex, an experimental method which provides more control over the environmental conditions, and the ability to incorporate more aspects of the tumor environment, should result in a better model for observing and interpreting key information related to GBM migration.

1.3 Microfluidics

Microfluidics can serve as an extremely useful platform to overcome the previously described limitations of common chemotaxis studies. As defined by George Whitesides, a pioneer within the field, microfluidics is "the science and technology of systems that process or manipulate small (10^{-9} to 10^{-18} liters) amounts of fluids, using channels with dimension of tens to hundreds of micrometers."[49] Microfluidics includes the design, fabrication, and implementation of these devices for a range of applications. Microfluidics devices are also known as microfluidic chips, micro total analysis systems (μTAS), and lab-on-a-chip (LOC) devices.[50] The first reported microfluidic device was a miniaturized gas chromatograph developed by S. C. Terry *et al*. in 1979.[51] During the past several decades, there has been significant progress in this field including the development of integrated valves, especially the Quake valve, that can be used to create mixers, actuators, pumps, and sensors.[52] Complete chemical analyses can be performed on these devices by integrating chemical reactions, separations, mixing, and particle manipulation and/ or capture. Many of these techniques are made possible due to the fluid dynamics properties

that occur in micron scale channels that are different from those generally experience in larger scale channels and pipes.

1.3.1 Enhanced fluidic control

Due to the small channel dimensions, different fluid flow dynamics occur within microfluidic devices. The significant surface-to-volume ratios in channels on these devices enhance the capillary effect, amplify the influence of surface properties, and result in increased surface tension.[53] The Reynolds number (R_e) is used to quantitatively define fluid flow within channels by providing a dimensionless value using

Equation 1.1. Reynolds number equation.

$$R_e = {\rho v L}/{\mu}$$

where ρ is the fluid density, v is the fluid velocity, L is the characteristic linear dimension (usually the hydraulic diameter of the channel for microfluidics), and μ is the fluid viscosity.[54] For Reynolds numbers below 2000, the flow is characterized as laminar. For Reynolds numbers greater than 2000, the flow is generally described as turbulent.[55] The small channel dimensions on microfluidic devices result in laminar flow, in which parallel streams of fluid mix only as a result of diffusion perpendicular to the direction of flow, as opposed to the eddies and convection present in turbulent flow (Figure 1.4).

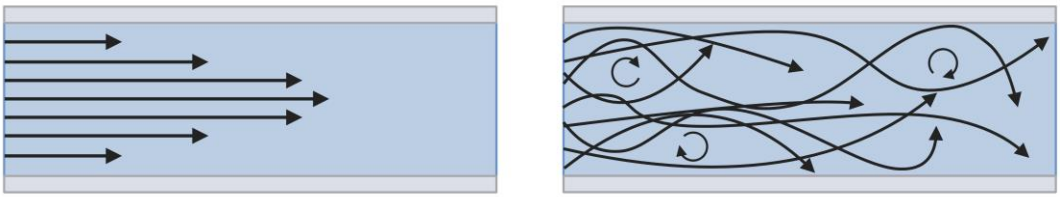

Figure 1.4. Under laminar flow, parallel streams of fluid move together in the same direction (left). Mixing only occurs via diffusion between the streamlines perpendicular to the direction of flow. In contrast, turbulent flow is far more chaotic with eddies and convection (right). Mixing and fluid flow is far less controlled under turbulent flow. Created with BioRender.com.

Laminar flow provides far greater control over the flow within microfluidic devices than can be achieved in traditional chemotaxis experimental apparatuses, such as well plates or Dunn chambers. Critically, discrete spatial control is possible within channels, enabling the formation of controllable gradients. As long as constant flow is maintained, a stable gradient can be preserved allowing for far more temporal control than more traditional chemotaxis analyses. Different gradient profiles are possible depending on the complexity of the device design, and multiple methods have been developed to form gradients within microfluidic devices.

1.3.2 Gradient formation within microfluidic devices

Microfluidics have been utilized for gradient generation, especially for applications of cellular analysis, in many different ways. Selection of an appropriate method depends on the needs of the experiment and the desired complexity of the apparatus. Gradient formation can be as simple as bringing two separate channels together at an angle, called the Y-shape or Y-junction method.[18] As the distance down the combined channel increases, more diffusion can take place between the streams. This very basic method is not prone to blockages, but there is not much refined control over the gradient profile. Flowrate and diffusion coefficient have significant influence over the resulting gradient, and it is difficult to model requiring more complex simulations.[56]

Droplet mixing and diluting can also be used for gradient generation. This method provides very fast gradient formation.[18] By utilizing microscale channel geometries, the concentration within a droplet can be tailored, and an array of droplets can be used to form a gradient.[57] This form of gradient generation can be particularly useful when studying tumor spheroids and provides significant control, but these microfluidic systems, and the required equipment, are typically more complex.[56]

One of the earliest examples of gradient generation was developed by the Whitesides Group, reported by Jeon *et al*. in 2000, and used a network of microchannels with repeated regions of splitting, mixing, and recombining.[43] This method of gradient generation is often called the tree-shape method. Different streams are combined at the start of each mixing serpentine, and the significant length of these channels allows for complete mixing via diffusion before splitting again. Finally, all the channels are recombined, and the resulting gradient can be calculated using an equivalent electric circuit approach due to the analogous relationship between electrical resistance and flow resistance. Each mixing serpentine section has significantly higher resistivity than the far shorter horizontal channels, and this, in combination with the symmetry of the design, results in even flow splitting at each branch of the system. As reported by Jeon *et al*., the flow splitting at each intersecting branch can be calculated using

Equation 1.2. Splitting ratio for flow proceeding to the left.

$$(B - V)\Big/(B + 1)$$

Equation 1.3. Splitting ratio for flow proceeding to the right.

$$(V + 1)\Big/(B + 1)$$

where B is the total number of vertical branches above that splitting point and V is the numerical position of that vertical channel within the row, starting with 0 from left to right (Figure 1.5).[43]

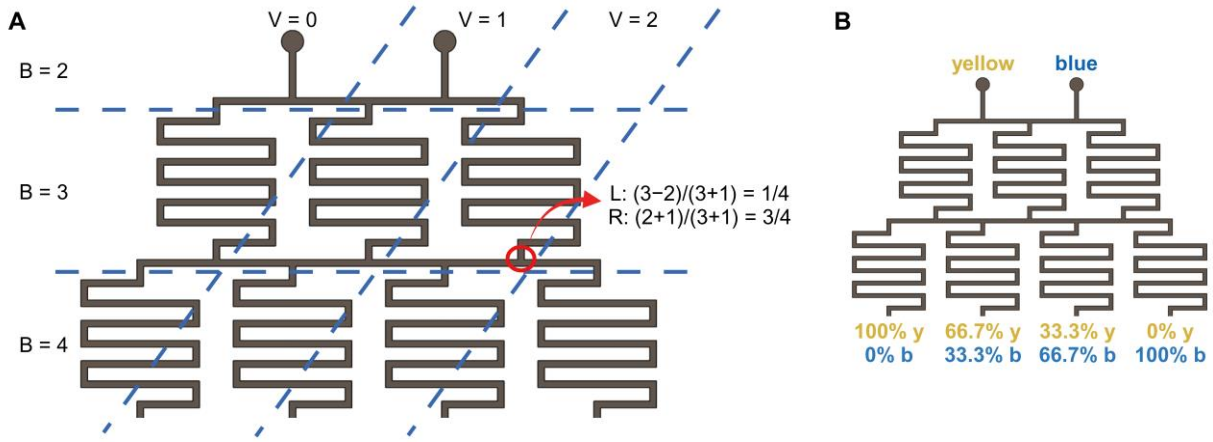

Figure 1.5. Schematic of a tree-shape gradient microfluidic device mixing channels highlighting sample calculations for determining flow splitting at branching intersections (A). The resulting concentration gradient can be modeled using these calculations, and an example is shown (B).

Some limitations of this method include increased potential of channel blockage in the serpentine regions, a larger device footprint, and the higher fluid shear stress, but this method maintains simplicity in its design and ability to be modeled.[56] Based on these reasons, the tree-shape method was selected as the gradient generation process for this work.

1.3.3 Other benefits of microfluidic devices

Besides the previously discussed reasons for using microfluidics, there are other benefits to using these kinds of devices. Microfluidics require significantly lower working volumes of reagents and samples.[55] This is critical for bioassays where sample size is often limited, enabling testing that would not be possible for bulk processes. Using microfluidic devices significantly lowers the cost of consumables used and the amount of waste produced during analyses, an increasingly important factor as more researchers aim for higher cost-effectiveness and lower environmental impact. The size of these devices means features can be created which are comparable in size to what a cell actually experiences in vivo in blood vessels or interstitial channels, improving the fidelity of the modeled cell environment.[58] This results in the ability to

assess both intra- and intercellular interactions and mechanisms. Many cellular studies commonly rely on imaging, and microfluidics can often easily incorporate image analysis into the experimental setup by using transparent materials.[57] Overall analysis time is often reduced for microfluidic devices compared to bulk analysis, and high-throughput experiments with increased sensitivity and improved resolution are possible, especially for standard biological assays.[49, 59] The amount of laboratory space required for a functioning microfluidics setup can be considerably lower than traditional equipment and instrumentation. As described previously, advancements in this field have greatly increased the possible applications for these devices, and research is continuously being done to grow the number of tasks and analyses microfluidics can do. Unfortunately, a common barrier to utilizing microfluidics is the often complex fabrication process to make these devices.

1.3.4 Traditional microfluidic fabrication methods

The methods used for the fabrication of microfluidic devices can traditionally be characterized as photolithography, molding, subtractive manufacturing, and additive manufacturing. A brief summary of the most common methods will be outlined within this section.

1.3.4.1 Photo- and soft lithography

Photolithography is one of the most commonly used techniques for fabricating designs on the micro scale. This process was developed for applications within the electronics industry, especially the production of integrated circuits.[60] For this fabrication method, a photomask of the desired pattern, comprised of opaque and transparent regions, is first designed using computer software. The appropriate photoresist, a light-sensitive liquid, is coated onto a smooth surface, typically a silicon wafer. The photomask is used to control which regions of the photoresist are

exposed to light. Irradiation causes a chemical change in the exposed photoresist, allowing for certain regions to be strengthened via polymerization or weakened via decomposition reactions.[60] Regions of photoresist are selectively removed by solvent exposure depending on whether a negative or positive tone photoresist was used, producing the desired pattern. This is then used as a master mold for forming microfluidic devices.

Soft lithography, developed by the Whitesides Group, is the process of making microfluidic devices from a master mold using polymeric materials, often polydimethylsiloxane (PDMS).[61] To make a device, a selected ratio of polymer base and curing agent are mixed together. This ratio influences the resulting flexibility of the PDMS device and can be tailored for the desired application. The mixed liquid polymer is typically degassed under vacuum to remove bubbles and then poured onto the master mold and baked until cured, although PDMS can cure at room temperature in roughly 48 hr.[62] The selected baking temperature and time are influenced by the mixture ratio, thickness of poured PDMS, and desired stiffness. The PDMS slab is peeled from the mold once cooled to room temperature. The molded device can then be reversibly sealed using contact adhesion by placing the PDMS on a glass slide or other smooth surface. The devices can also be irreversibly sealed using plasma or UV-assisted bonding to activate the PDMS surface prior to placing it on a glass surface.[61]

Photolithography and soft lithography are often used together for microfluidics fabrication, especially within academia. One of the greatest benefits to using photolithography is the impressive resolution, which is achievable due to the highly advanced optical exposure systems and photoresists that are used.[60, 63] PDMS has been highly utilized in academic research due to its elasticity, transparency, gas permeability, biocompatibility, electric insulation, hydrophobic surface tunability, and the low material costs.[49, 53-55, 63] However, there are

limitations to these fabrication methods. While the PDMS molding process is relatively simple, establishing a working photolithography setup in a laboratory is far more complicated. The photomask printing process is often outsourced to a third-party company, increasing the time between device design and being able to use new photomasks, thus reducing the pace of device prototyping. The cost of silicon wafers, photoresists, developer solvents, a spin coater, an optical exposure system, and clean hoods or cleanroom equipment can be prohibitive. The training to use this equipment correctly and the time to fabricate a working master mold and ultimately a PDMS device is extensive. The laboratory space required is also demanding. Overall, a working photo- and soft lithography operation can be difficult to establish, especially for a lab less familiar with the field of microfluidics.

1.3.4.2 Thermoplastic molding

There are a subset of fabrication methods that involve different types of thermoplastic molding. These methods use standard thermoplastic materials, such as polystyrene, polyurethane, polyvinylchloride, polyethylenetetraphthalate glycol, or polymethyl methacrylate. Injection molding utilizes a hollow mold that is filled with molten thermoplastic to shape devices.[64] For the process of microthermoforming, a thin sheet of thermoplastic is heated and stretched over a mold tool, and a pressure difference is applied to form the thermoplastic into the desired shape.[65] Hot embossing is a similar imprinting technique where elevated temperature and a hydraulic press are used to transfer the desired pattern from a mold, or stamp, into a thermoplastic.[64] In a similar way to PDMS device fabrication, the shaped thermoplastic is removed from the mold or stamp following cooling.

One critical advantage of thermoplastic molding is the long-lasting nature of the molds. The molds are typically made of rigid materials, such as brass, steel, or silicon, so hundreds of

devices can be fabricated from the same mold without risk of damage or degradation. Additionally, thermoplastic molding techniques are more easily scaled up for commercial production compared to photo- and soft lithography. There are, however, also limitations to these fabrication methods. The thermal expansion coefficient of the selected material must be appropriate, as these materials deform with temperature, which can impact the ability to fabricate and, critically, seal these devices.[64] Since thermoplastics are stiffer materials than PDMS, moving elements such as valves would require more force applied to larger features to achieve the same result.[66] Additionally, these fabrication methods greatly reduce the ability to perform rapid prototyping since a new mold must be produced for each altered design, and the production of these molds is often outsourced. For molds produced in-house, chemical etching or micromachining capabilities are needed, requiring extensive training and more specialized equipment.[64] The machinery used in thermoplastic molding techniques can be expensive and take up significant laboratory space as well.

1.3.4.3 Etching and micromachining

Two common subtractive fabrication methods are etching and micromachining. Etching was utilized by Terry *et al*. for the first microfluidic device.[51] Chemical etching was also employed by the electronics industry. The etching process can be done in silicon or glass, and typically uses hydrofluoric acid, potassium hydroxide, tetramethylammonium hydroxide, nitric acid, and/ or ethylenediaminepyrocatechol.[51, 64] The selected etching solution can impact the shape of etched channels. These devices are robust but also fragile. One of the most significant limitations of etching is the inherent safety risks associated with using these chemicals, requiring significant training and strict operating protocols during the etching process.

While machining has been historically used for metals, micromachining of thermoplastics has grown significantly, especially for polystyrene, which is an industry standard material for tissue culture, is autoclavable, and compatible for surface modification.[67, 68] For this fabrication method, a computer-controlled rotating cutting tool, or endmill, is used to remove excess material from the starting piece until the desired pattern is formed.[69] The selection of the endmill size allows for complex, 3D features to be created. More recent developments in this field have reduced the barriers associated with the required laboratory space and technical expertise to use this equipment. Micromachining can be relatively quick, depending on the complexity of the design, allowing for faster prototyping if outsourcing is eliminated. Two potential limitations of micromachining are the resulting surface roughness following milling, which could impact imaging capabilities, and the fragility of the smaller milling tools required for microfabrication.[69]

1.3.4.4 Paper, printing, and wax

Another option for microfluidic device fabrication is the patterning of paper. The inherent wicking capability of paper via capillary action is a result of cohesion between liquid molecules at the liquid-air interface and adhesion between the paper fibers and liquid molecules.[70] This results in passive fluid flow through the fibers of the paper. Lateral flow assays have been utilized since the 1940s to move samples through pre-dried reagents toward a result readout region.[71] The first microfluidic paper-based analytical device (μPAD) was created by the Whitesides Group in 2007 for the analysis of glucose and protein in artificial urine.[72] Microchannels are formed in paper by defining hydrophilic regions for fluid flow surrounded by hydrophobic barriers. There are many methods to produce channel patterns from as simple as cutting paper either manually or using a programmable knife or laser, to more complex techniques such as photolithography, wax, inkjet, and laser printing, chemical vapor deposition,

and stamping.[72-75] Depending on the channel patterning method, these μPADs can be very affordable and accessible. μPADs do not rely on external equipment for fluid pumping, reducing the cost and complexity of device implementation.[76] Paper itself is a very inexpensive and readily available material that is biocompatible, flexible, easily stored, and simple to dispose of. Some researchers are developing new strategies for using paper as a tool for 3D tissue modeling.[77]

There are some key limitations of these devices. Variations and inconsistencies in the paper structure can impact fluid flow and the results of μPADs.[74] Reagents that are pre-dried onto the paper can degrade over time.[73] Additionally, the open-air nature of many μPADs means they are subject to temperature and humidity changes as well as evaporation, which can influence accuracy and precision of these devices. Many μPADs utilize color changes for detection or analysis, sometimes requiring additional optics for image analysis. Although paper microfluidics have incredible potential, these limitations contribute to the fact that μPADs are not a practical option for the complexities of gradient generation and cell migration studies.

1.4 Accessible microfluidics fabrication

Although there are a multitude of potential applications for microfluidic devices, and many methods of device fabrication, a majority of the commonly used techniques remain inaccessible. Most of these methods require the use of expensive equipment, rigorous processes, and steep learning curves for successful fabrication and operation. The startup cost for microfluidics fabrication can be incredibly high, especially when considering cleanroom facilities. Additionally, the amount of laboratory space which must be dedicated to fabrication equipment can be significant, often limiting the number of research groups that attempt to incorporate microfluidics work into an established workspace. The required knowledge for

effective microfluidic design and operation, in addition to the necessary laboratory infrastructure to run complex microfluidic devices, have been significant barriers for adopting this technique, especially within the field of biology.[55] By increasing the accessibility of microfluidics research, more scientists could contribute to the potentially cutting-edge research that this field enables. This kind of collaboration, especially between diverse scientific disciplines, is essential when approaching challenging topics such as cancer research. In this section, the accessibility of 3D printing as a microfluidics fabrication technique, and other aspects for simplifying device fabrication, will be discussed.

1.4.1 3D printing

3D printing, a form of additive manufacturing, has been a rapidly expanding technology utilized in the field of microfluidics within the past decade.[78] There are several advantages to selecting 3D printing as a fabrication method. Over the years, many improvements have been made in achievable resolution, printing speed, user interface, and the ability to integrate external components.[79, 80] The overall start-up cost of 3D printing has also decreased substantially, depending on the kind of 3D printer and material selected.[66] Additionally, as more types of printers have become commercially available, a wider range of materials can be used. The use of 3D printing also enables simple sharing of digital design files between facilities with comparable printers, broadening the number of labs where device fabrication can occur and eliminating precarious shipping of microfluidics. These characteristics have enabled 3D printing to be at the forefront of rapid, in-house microfluidic device prototyping.

1.4.1.1 Some previous applications of 3D printing for microfluidic cell studies

Recently, applications of 3D printing have expanded into bioscientific and bioanalytical studies. These kinds of device applications are especially appropriate for printing methods which

utilize biocompatible materials like acrylonitrile butadiene styrene (ABS) and poly-lactic acid (PLA).[66] 3D printing microfluidic devices in-house allows for far more tailoring of the design. For example, the ability to customize prints for the specific needs of different biological systems allows for culturing more challenging tissue samples.[81] There have been many applications of 3D-printed materials for cell culture.[78, 82-84] 3D printing methods can be utilized to develop more sophisticated apparatuses enabling greater control over experimental conditions. For instance, Au *et al.* were able to print fluidic valves and pumps for a microfluidic perfusion system for CHO-K1 cells.[83] Many steps of the bioanalysis can be incorporated into the device design, simplifying the process compared to traditional cell studies. Electrical lysis within 3D-printed microfluidic devices was reported by Gross *et al*.[85] Devices have also been developed to test drug transport and the resulting impacts on cells.[86] Imbedded biomaterials or hydrogels deposited via bioprinting have been utilized to better mimic 3D tissue culture and the complex mechanisms that occur between cells and their environment.[79] 3D-printed devices have also been used for cancer studies.[80, 87] 3D printing provides tremendous potential for bioanalytical cell studies.

1.4.2 Resin 3D printing

As the first commercially-available kind of 3D printing, a broad variety of configurations have been developed for stereolithography.[79] For the majority of this work, two types of commercially available printers are used 1) LCD-based, and 2) light projection-based resin 3D printing. This fabrication method relies on an appropriate slicing computer software, here Chitubox Basic, to divide the design into cross-sectional layers of a user-set height. During the 3D printing, as shown in Figure 1.6, a vat containing the precursor liquid resin is positioned above either an LCD screen which itself sits above an LED array (Figure 1.6 A) or a piece of tempered glass (Figure 1.6 B). When layers of the design are illuminated, 405 nm light is

transmitted in the corresponding pattern based on the LCD screen or the projector. This light passes through the transparent plastic window at the bottom of the vat and into the liquid resin causing polymerization. A motorized build plate is positioned within the vat one layer height above the transparent window allowing the photocurable resin to adhere to the build plate. Following polymerization, the build plate is lifted, peeling the cured resin layer up from the bottom of the resin vat and allowing liquid resin to refill the space previously occupied by the cured layer. The build plate is then repositioned in the vat one additional layer height from the bottom, and the entire process is repeated for the full height of the design. This printer configuration, often called the bat configuration, results in the design printed layer-by-layer attached to the build plate hanging in an inverted orientation.[79]

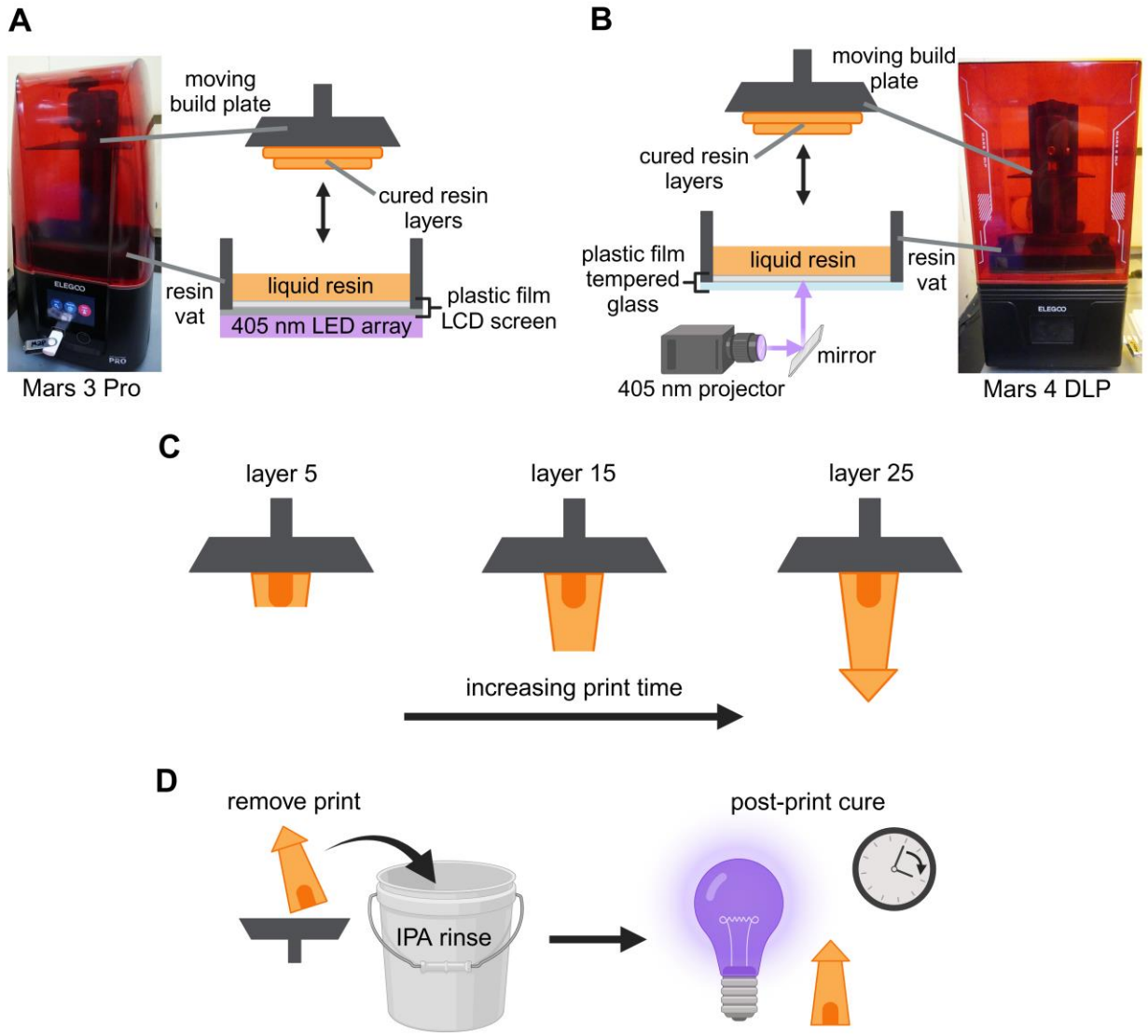

Figure 1.6. During resin 3D printing, a moving build plate is lowered into the resin vat. 405 nm light is transmitted through the transparent film at the bottom of the vat to cure cross-sectional layers of a 3D object from either an LCD screen (A) or a projector (B). After the polymerization of that layer, the build plate is repositioned, and the process is repeated as the design is printed layer-by-layer, inverted on the build plate (C). When the printing process is completed, an isopropyl alcohol rinse is used to remove excess uncured resin before a final post-print cure (D). Created with BioRender.com.

Since the entire cross-sectional area of each layer is polymerized at once, the height of the design determines the length of the printing process. Printing parameters such as the length of light exposure, print orientation, resting time before and after build plate positioning, and the

speed of the build plate can be tuned to achieve the desired resolution and successful fabrication. Once the print is completed, post-print processing occurs. This typically begins with a rinse in a suitable solvent, often isopropyl alcohol, to wash away excess uncured resin. After the print is dried, additional curing is completed to ensure the strength and integrity of the print. The length of post-print curing is influenced by the design, namely its complexity and the presence of internal void regions, and the power of the light source. While this can be completed over multiple hours in direct sunlight, separate cure stations can be purchased or made to shorten this process to a few minutes. Extended exposure to intense light will lead to resin degradation.

1.4.2.1 Formulation and characterization of photosensitive resin

The material used in commercial resin 3D printers is a photosensitive liquid resin comprised of a proprietary combination of UV absorbers, photoinitiators, primarily acrylate and methacrylate mono-/oligomers and crosslinkers, and additives.[88-90] Photoinitiators exposed to radiation of an appropriate wavelength break down into radical species leading to radical chain polymerization of the mono-/oligomers and crosslinkers.[91] Other additives, such as plasticizers, are incorporated into the structure and provide increased rigidity or strength to the cured polymer material. UV absorbers are used to limit the penetration of light within the resin solution, and are often kept in low concentration.[88] Dyes can also be added to the resin to provide color. It is important to note that temperature and humidity can impact the photopolymerization reaction and the resulting print capabilities.[92] Using commercial resins decreases the startup cost and provides as straightforward option for researchers new to resin 3D printing. Many printer manufacturers also sell their own resins designed to be compatible with their printers. The proprietary nature of commercial resins does limit the amount of detailed knowledge available to

users, and relying on these resins leaves users subject to potential impacts resulting from formulation changes.

When considering resin 3D printing for bioanalytical research, two factors must be assessed: 1) the biocompatibility of the material, and 2) the suitability of the material for the method of analysis. Many of the resin components are considered toxic for tissue culture.[93] Some biocompatibility assessments have included using zebrafish embryo toxicity assays, GC-MS and LC-MS/MS of leachates, and direct tissue culture on 3D printed materials.[93-95] One common preparation step is print sterilization via ethanol, isopropyl alcohol, or UV exposure prior to cell seeding.[81] More researchers have worked to develop treatment procedures to increase biocompatibility of resins. Piironen *et al.* investigated both cell adhesion and proliferation on a range of commercially available resins and found autoclaving to be a critical process for improved cell culture, although the thermal stability of the resins limited the applicability of this sterilization method.[82] The Pompano Group investigated overnight room-temperature and heated saline leaching, as well as autoclaving, as potential treatment methods for resin prints, which decreased cytotoxicity for sensitive primary murine splenocytes for up to 4 hours of exposure.[92] Poly-D-lysine has also been explored as a potential surface treatment for printed devices.[95] There have been some developments in the resin printing industry to design resins that meet biocompatibility standards as well.[66]

Other characteristics of resin, such as surface roughness, optical clarity, and autofluorescence are also important for bioanalytical applications involving tissue culture. The resulting surface roughness of a print is influenced by the printing orientation as a result of the layer-by-layer fabrication technique and the surface topographies of the bottom of the resin vat and build plate.[88, 95] This roughness can impact cell adhesion, which can be significant depending

of the selected cell type and the application of the printed design. Besides its importance for cell culture, surface roughness also effects clarity of a print.[84] For cell studies, where imaging analysis is often critical, optical clarity is key. There are a variety of transparent resins that can be purchased commercially, but some can be subject to more prevalent yellowing over time from light exposure. Since many bioassays rely on fluorescent imaging, both the autofluorescence of the cured resin material and its susceptibility to staining by fluorescent dyes are important. Longer wavelengths of excitation cause lower observed autofluorescence, as is expected from plastic materials.[96] The roughness of the resin surface could provide recesses for fluorescent staining, or the chemical composition of the material itself could be conducive to retention of fluorescent dyes. It is clear that there are many factors to consider when selecting which resin to use.

To better tailor resin characteristics to research needs, some labs have created their own resin. For example, Gong *et al.* used mathematical modeling to determine resin formulation to achieve smaller channel dimensions.[90] Steyrer *et al.* were able to tune the material properties of their resin to increase the strength and glass transition temperature of the cured polymer.[89] Other groups have worked towards designing resins that cure using visible light, like Park *et al.* who utilized a single photoinitiator to develop a UV- and visible light-sensitive resin that maintained transparency and strength.[97] While creating a custom resin can provide far more control over the resulting print characteristics, this work often necessitates building a 3D printer that is compatible with the unique resin formulation. Additionally, focusing on the optimization of a particular resin quality may result in compromising a separate characteristic. As is evident, there are many strategies that can be utilized for developing a photosensitive resin, and more research has focused on assessing and improving commercially available resins for bioanalytical work.

1.4.3 Ease of use

To design accessible microfluidics, the overall ease of use for both fabrication and implementation must be considered. Since commercially available resin 3D printers are designed for the hobbyist community, a very moderate level of expertise is required to use this technology. Only an adequate understanding of computer-aided design (CAD), if creating your own designs, slicing software, and the selected type of 3D printing is necessary. Additionally, there is a considerable online community which can provide guides, troubleshooting suggestions, and other support for both new and experienced users. As mentioned before, digital design files can be shared among labs with comparable 3D printers, increasing overall access to these devices. This reasonable level of expertise enables more scientists to create without the vast range of knowledge required for more complex manufacturing or access to in-house workshops. Furthermore, the health risks associated with using commercial resin 3D printers are intended to be minimized, and the necessary safety measures are designed to be achievable for the average consumer. As a result, this kind of 3D printing should be relatively easy to incorporate into a laboratory setting which already has elevated access to safety and personal protective equipment. The physical space required for this fabrication technique is also quite small compared to more traditional microfluidics fabrication methods, as it is designed to be easily performed within hobbyists' homes.

There are additional factors that should be evaluated when trying to design an accessible microfluidic device. Incorporating equipment or mechanisms other researchers are familiar with, such as luer locks and threaded connections, help to make 3D-printed microfluidic devices more approachable to new users and more compatible for interface with existing equipment.[66] The use of syringe pumps to provide flow, instead of more complex pumping manifolds reliant on

compressed air and/ or microcontrollers and coding, is also far more feasible for the average research lab without previous microfluidics experience. The selected mode of analysis or detection method should also be considered when trying to develop a microfluidic device that is practical for use by non-experts. It is clear that there are several considerations that must be addressed when focusing on accessibility of microfluidic device design and use.

1.4.3.1 Channel sealing

One unique consideration when working with microfluidic devices is the process of sealing off microfluidic channels. When 3D printing microfluidic devices, channels can be fully enclosed or partially open, although enclosed channels can present more complications during fabrication. The achievable resolution when printing fully enclosed channels can suffer due light spreading and/ or scattering contributing to unintended curing of liquid resin within the channel. Proper drainage of excess resin from enclosed channels can also be difficult to achieve and could require changes in print orientation. To avoid these pitfalls, microfluidics can be designed with direct printing of only 3 out of 4 sides of a rectangular channel. An appropriate method for sealing these channels is the last fabrication step before these devices can be used.

More traditional PDMS microfluidic devices are often sealed by placing the open channels on a glass slide. This kind of reversible seal is more suitable for device applications utilizing negative pressure but may not withstand positive pressure within the channels. The seal can be strengthened using oxygen plasma treatment or extended exposure to high temperature, creating an irreversible seal between the PDMS and glass surfaces.[98] Plasma treatment has also been used to irreversibly seal 3D-printed microfluidics to PDMS using a commercial silicone spray or (3-Aminopropyl)triethoxysilane.[99] Unfortunately, irreversible sealing can increase the obstacles associated with using the device, often lengthening fabrication time and complexity.

Irreversibly sealed devices are often far less reusable, suffering from the pitfalls of clogging and the inability to clean, which can be highly undesirable for biological applications of microfluidic devices. Some researchers are working on novel ways to reversibly seal devices, including utilizing adhesives, magnets, and even "…special contact geometries adapted from the field of bio-inspired dry adhesives" that are comparably strong to the established irreversible methods.[100] The development of approachable sealing methods is critical to increasing the range of researchers employing microfluidics in their work.

1.5 Conclusion

In the following chapters, the discussion of a novel microfluidic fabrication method will be presented. The development of this procedure, and the adjustments that were made in response to various challenges, are included in detail. This fabrication process will prioritize simplicity and affordability to highlight the accessibility of this method for cellular research, especially for labs that are less familiar with microfluidics. The goal of this research is to better understand GBM chemotaxis in response to chemoattractant gradients. This knowledge could then be used to improve treatment methods for GBM and contribute to saving lives of those suffering with this diagnosis.

Chapter 2 - Development of a 3D-printed microfluidic device

2.1 Introduction

The development of a microfluidic device can require a significant amount of prototyping before a useful design is finalized. Resin 3D printing provides a low-cost, accessible, and rapid method of microfluidics fabrication especially when printers and products designed for the hobbyist community are utilized. A deeper exploration of the consequences of using products at this price point is needed to assess how suitable this fabrication strategy is, especially for cell research. In this chapter, many critical factors of the resin printing process, material properties, and microfluidic device fabrication are investigated. Numerous modifications in device design were prompted by the findings of this work. Reported below is the significant progress towards an accessible option for microfluidic cell studies and an improved understanding of low-cost resin 3D printing.

2.1.1 Device design

The device has two inlets where two separate solutions can be pumped into the channels. The serpentine mixing region is comprised of branched rows of mixing channels with one additional serpentine in each subsequent row. The fluidic principles behind the mixing and gradient formation can be found in Chapter 1. Each device is designated as an n-part gradient device where n is the number of mixing serpentines within the last row of the mixing region. The separate streams are recombined at the observation channel. Cells could be seeded within this wide channel and experience the resulting gradient formed from the serpentine mixing region. External distance markers are positioned at constant intervals down the observation channel to allow for more consistent imaging alignment. The observation channel tapers into a single outlet at the base of the design.

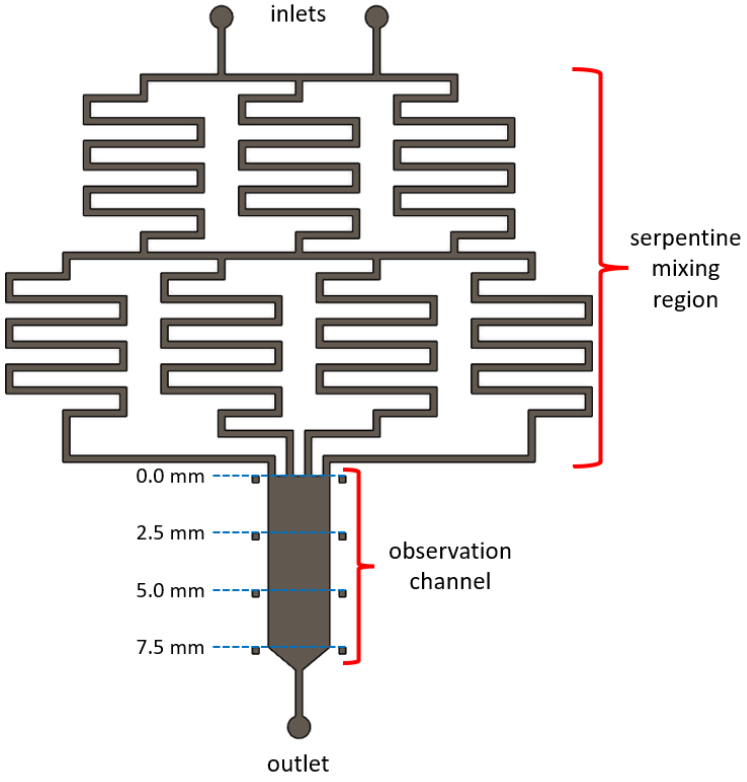

Figure 2.1. An example of a 4-part gradient device design. Two inlets are positioned at the top of the device which lead into the serpentine mixing region. The mixing channels recombine at the observation channel. External distance markers are positioned at constant intervals down the observation channel. A single outlet leads out from the observation channel.

2.2 Materials and methods

2.2.1 Reagents, materials, equipment, and software

A wide variety of products were used for this research, the details of which are provided below.

2.2.1.1 Resin 3D printing, processing, and assessment

Autodesk AutoCAD, Autodesk Fusion 360, the Photon Workshop, and the Chitubox slicer were used to create all design drawing, 3D object, and sliced files. Several resin 3D printers were used during this research. The Anycubic Photon S printer was purchased from Anycubic (Guangdong, China). The Elegoo Mars 2 Pro Mono, Elegoo Mars 3 Pro 4K, and

Elegoo Mars 4 DLP printers were purchased from Elegoo (Guangdong, China). Multiple resins were used as well. Anycubic 3D Printing UV Sensitive Resins in Basic Green, Basic Red, Grey, and Black and Elegoo ABS-Like Photopolymer Resin Translucent and Standard Photopolymer Resin in Red and Black were all purchased through Amazon (Seattle, WA, USA). Elegoo perfluoroalkoxy alkane (PFA) Release Liner Film fluorinated ethylene propylene (FEP) Release Liner Film, 99% isopropyl alcohol from Florida Laboratories, 2-gallon gamma seal bucket, net slit pots, Behrens 10-quart galvanized steel pail, 24-Watt LED 395-405 nm light strip from YGS-Tech, 3M™ 400, 1000, and 2000 grit sandpaper, soft toothbrushes Minwax Polycrylic Protective Finish in clear gloss, Sylvania Headlight Restoration Kit, Amazon Basics PBT Paint Brushes, and Scotch Magic tape were all purchased through Amazon (Seattle, WA, USA). Kimtech Science Kimwipes, Fluorescein, and Rhodamine B were purchased from Thermo Fisher Scientific (Waltham, MA, USA). Photomasks were printed by Fine Line Imaging (Colorado Springs, CO, USA).

2.2.1.2 Sealing devices, testing, and improving seals

3-(trimethoxysilyl)propyl methacrylate, toluene, and Fisherbrand Plain Glass microscope slides were purchased from Thermo Fisher Scientific (Waltham, MA, USA). Fugitive glue was purchased from Hotmelt.com (Eden Prairie, MN, USA). Norland Optical Adhesive (NOA) 86H was purchased from Norland Products (Jamesburg, NJ, USA). Dow Sylgard 184 PDMS elastomer base and curing agent were purchased from Ellsworth Adhesives (Germantown, WI, USA). The MakerGear M2 FDM printer, purchased from MakerGear LLC (Beachwood, OH, USA), and 1.75 mm polyethylene terephthalate glycol (PETG) filament, purchased from eSUN (Nanshan District, Shenzhen, China), were used to print device frames. Elmer's Glue-All® multi-purpose glue, Loctite Brush-on Super Glue, and transparency film were purchased through

Amazon (Seattle, WA, USA). 3M™ Microfluidic Diagnostic Tapes 9793R, 9795R, and 9964 were provided by 3M™ (St. Paul, MN, USA). Heptane 99.0+%, ethyl acetate, Alconox Powdered Precision Cleaner, and sodium hydroxide, purchased from Thermo Fisher Scientific (Waltham, MA, USA), were used in an attempt to remove tape adhesive. Poly-D-lysine (PDL) hydrobromide (MW 70,000-150,000), purchased from Sigma Aldrich (St. Louis, MO, USA), and sodium hyaluronan (HA40K-1), purchased from Lifecore Biomedical (Chaska, MN, USA), were used to coat the tape adhesive. Multi-Phaser Programmable Syringe Pumps, purchased from New Era Pump Systems Inc. (Farmingdale, NY, USA), were used to provide fluidic control. The pressure transmitter (0-10 DC Output-DIN C Wire Connection 0-50 PSI), Plastic Barbed Tube Fittings for 1/16" Tube ID x 10-32 Male Pipe, 0.508 mm thick PDMS sheet, Nylon plastic wing nuts 8-32, and Nylon plastic socket head screws 8-32 were purchased from McMaster-Carr (Robbinsville, NJ, USA). Nitrogen gas, 99.99% purity, was purchased from Matheson Tri-Gas Inc. (Manhattan, KS, USA).

2.2.1.3 Tissue culture

C6 glioma cells (rat, ATCC, CCL-107) and U-87 MG glioblastoma cells (human, ATCC, HTB-14) were purchased from American Type Culture Collection (Manassas, VA, USA). 24- and 96-well plates (BioLite 96 Well Multidish), petri dishes, polystyrene BioLite Cell Culture Treated Flasks 75 cm2 (T75), 15 mL centrifuge tubes, Ham’s F-12K (Kaighn’s) Medium, Dulbecco’s Modified Eagle Medium (DMEM) high glucose, trypsin-EDTA (0.25%) phenol red, 1X phosphate-buffered saline (PBS), US sourced fetal bovine serum (FBS), heat inactivated horse serum, penicillin streptomycin 100X, 10 mg propidium iodide (PI), Trypan Blue Solution 0.4%, and Hausser Scientific Bright-Line Phase hemocytometer were purchased

from Thermo Fisher Scientific (Waltham, MA, USA). Clorox concentrated bleach was purchased though Amazon (Seattle, WA, USA).

2.2.1.4 Imaging equipment

The X-Cite 120 Fluorescence Illumination System was purchased from EXFO America Inc. (Richardson, TX, USA). The Nikon Eclipse TE2000-U inverted microscope, Nikon SMZ1500 stereoscopic zoom microscope, Nikon B-2A filter cube, and Nikon G-2A filter cube were purchased from Nikon Instruments Inc. (Melville, NY, USA). The Koolertron 5MP 20-300X USB Digital Microscope Magnifier Video Camera, 8 LED illumination with intensity control, base stand, and imaging software was purchased from Hong Kong Karstone Technology Co., Limited (Hong Kong). The Sony Alpha a6400 camera was purchased from Sony Corporation of America (New York, NY, USA). To connect the Sony Alpha a6400 camera to the microscopes the Coupling T-Ring for Sony E Mount (NEX/A7/QX/VG Series) from Telescope Adapters (Cape Coral, FL, USA) and the 1.3X Large Format Adapter System for a Nikon 38 mm ISO Port (BS13NN) were purchased from Best Scientific (Swindon, Wiltshire, United Kingdom).

2.2.1.5 Other laboratory equipment

All ultrapure water was generated from a Barnstead E-pure system (Dubuque, IA, USA). The Branson 3510 Ultrasonic cleaner was purchased from Branson Ultrasonics Corp. (Danbury, CT, USA) The Laurell WS-400-6NPP-LITE Spin Processor was purchased from Laurell Technologies Corporation (Lansdale, PA, USA). The XP-2 Stylus Profiler was purchased from AMBiOS Technology (Santa Cruz, CA, USA). Single Channel Manual Pipettes with Universal-Fit Shafts were purchased from Mettler-Toledo Rainin (Oakland, CA, USA). Fisher Scientific

Isotemp Vacuum Oven Model 280A purchased from Thermo Fisher Scientific (Waltham, MA, USA).

2.2.2 Resin 3D printing and assessment procedures

When resin 3D printing, there are a variety of print settings to be optimized. These settings include the duration of light exposure, layer height, positioning of the print on the build plate, and rest time. A detailed protocol for resin 3D printing, including specific settings for the various 3D printers, resins, and designs, is included in Appendix A. The selected print settings were assessed by collecting images of prints for comparison while varying settings to determine which conditions led to the most successful results.

2.2.2.1 Resin post-print processing

Three increasing intensities of post-print rinsing were explored. First, a gamma seal bucket filled with IPA and a net slit pot were used to manually rinse prints. Second, a soft-bristled toothbrush was used to gently clean excess resin off prints, especially within microchannels. Third, a Branson 3510 ultrasonic cleaner was used to sonicate prints for approximately 5 min in fresh IPA.

A key part of the print processing to be examined was the post-print cure. The potential impacts of the post-print cure were explored by exposing identical test prints, made from Elegoo ABS-like translucent resin, to increasing lengths of exposure (Table 2.1). After the intended length of exposure, images were collected using the Sony Alpha a6400 camera for comparison.

Table 2.1. Resin print labels and corresponding length of post-print cure.

Round 1 Print	Post-print cure exposure length (s)	Round 2 Print	Post-print cure exposure length (s)
A	30	A	270
B	60	B	300
C	90	C	330
D	120	D	360
E	150	E	390
F	180	F	420
G	210	G	450
H	240	H	480

Two methods for improved print transparency were examined. Three identical test prints were fabricated in the Elegoo ABS-like translucent resin to compare results. A single coat of the Minwax Polycrylic Protective Finish in clear gloss was applied to the back of a test print using a paintbrush and left to dry for at least 12 hr. The Sylvania Headlight Restoration Kit was also used on a separate test print following the provided directions. An adapted process was developed that combined the two tested methods to improve print transparency. A progression of wet sanding using 400, 1000, and 2000 grit sandpaper on a level granite surface was used to smooth the back of a print and remove the build plate texture. Following a rinse with ultrapure water, the print was dried using compressed air. A single coat of Minwax Polycrylic Protective Finish was applied to the print with a paintbrush. This coating was set to dry in a laminar flow hood for at least 12 hr before the print could be used further.

2.2.2.2 Testing resin properties

Multiple physical properties of the Elegoo ABS-like translucent resin were investigated. This work began with thermal resistance testing. Identical prints were fabricated to test a range of temperatures for varying lengths of time, as detailed in Table 2.2. A set of images were collected for each test print on the Nikon SMZ1500 stereoscopic zoom microscope using the Sony Alpha a6400 camera to capture the initial state of the microfluidic channels. A 20 g weight was used to test the strength of the resin print and resistance to deformation as well.

Table 2.2. Procedure for resin temperature resistance testing involving 4 separate test prints. After each specified length of exposure at the experimental temperature, images were collected to compare.

Print	Temperature (°C)	Length of exposure (min)
1	60	5
1		15
1		45
1		90
2	80	10
2		40
2		160
3	100	10
3		40
3		160
4	100	420

Each print was placed into an oven, set to the assigned temperature, and exposed for increasing lengths of time. After each timepoint was reached, the print was removed from the oven to take

comparison images. The print and camera were aligned, the weight was positioned in the middle of the print, and images assessing print rigidity were collected. The images of the microchannels were taken afterward.

The surface roughness of the printed devices was examined using the XP-2 Stylus Profiler. A detailed protocol for the profilometer is included in Appendix C. Polished devices were sanded with damp 2000 grit sandpaper on the channel face until an even frosted appearance was achieved (Figure 2.2). After polishing, prints were rinsed with ultrapure water and dried with compressed air.

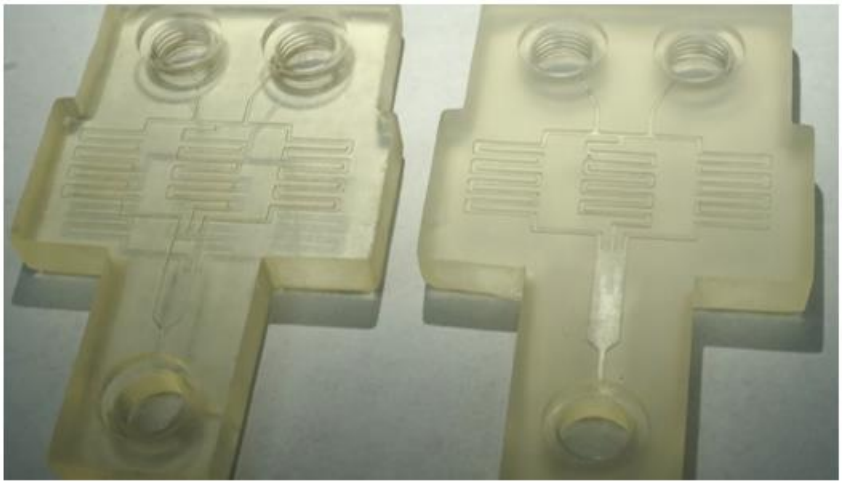

Figure 2.2. Unpolished (left) compared to polished (right) 3D-printed devices.

Three separate regions were measured on both unpolished and polished devices, the surface of the device outside of the channels, the depth and surface of an inlet reservoir, and the depth and surface of the observation channel.

Autofluorescence of the cured resin was tested using the X-Cite 120 Fluorescence Illumination System at 470 and 535 nm excitation. Fluorescein and Rhodamine B (RhB) were used to make 10 μM fluorescent solutions in ultrapure water. The fluorescent intensity of the cured resin and the appropriate fluorescent solution were captured at both excitation wavelengths on the Nikon Eclipse TE2000-U inverted microscope using the Sony Alpha a6400 camera. Each

fluorescent solution was pipetted onto a glass slide, topped with a coverslip, exposed to the corresponding excitation wavelength, and the resulting fluorescent intensity was collected. The cured resin was positioned on the microscope, exposed to both excitation wavelengths, and the resulting fluorescent intensity was collected A clean glass slide was used as a blank measurement, and the resulting fluorescent intensity was subtracted from the resin and fluorescent solution measurements. Image analysis was completed using ImageJ and Igor Pro with detailed protocols provided in Appendix C.

The resin's susceptibility to fluorescent staining was also explored. Test prints containing microchannels were exposed to a 10 μM RhB solution for two lengths of time, 4 or 30 min. Three methods for RhB removal were tested: 1) a rinse with ultrapure water, 2) sonication in ultrapure water for 15 min, and 3) a rinse in ultrapure water with gentle brushing from a soft-bristled toothbrush. All test prints were dried using compressed air before staining was assessed. The print was placed on the Nikon Eclipse TE2000-U inverted microscope and exposed to 535 nm excitation from the X-Cite 120 Fluorescence Illumination System. Fluorescent images were collected using the Sony Alpha a6400 camera.

2.2.2.3 Examining further factors influencing print quality

Multiple resins with a range of opacity were tested by printing the same design to compare the resulting print quality. Detailed printing protocols are provided in Appendix A. When switching between resins, the excess resin was filtered and collected for future use. The resin vat was cleaned with IPA and fully dried before the next resin was added. Images were collected using the Nikon Eclipse TE2000-U inverted microscope and Sony Alpha a6400 camera for the transparent and translucent resins and the Koolertron 5MP USB digital microscope for the opaque resin.

Photomasks were incorporated into the resin 3D printing process to assess the resulting improvement in achievable printed feature resolution. Prints were designed as a solid base with a known number of channel layers. Once all base layers were completed, the printer was manually paused, the build plate was raised to the top and was carefully removed from the printer. The resin vat was removed from the printer for photomask positioning over the LCD screen. To place the photomask, an in-house tool was used to ensure the following printed features would align with previously printed base and features, such as inlet and outlet reservoirs. Scotch Magic tape was used to secure the photomask before the resin vat and build plate were returned to the printer and the print was continued for the channel layers. The standard post-print processing steps were followed. Images were collected using the Nikon Eclipse TE2000-U inverted microscope and Sony Alpha a6400 camera for the transparent resin and the Koolertron 5MP USB digital microscope for the opaque resin.

2.2.3 Sealing methods

Descriptions of all sealing methods investigated in this work are detailed below.

2.2.3.1 Rigid seals

The first method examined to seal 3D-printed devices was direct printing onto glass slides. A solution of 2% 3-(trimethoxysilyl)propyl methacrylate in toluene was prepared to improve adhesion between the resin and glass during 3D printing and transferred into an appropriately-sized container for glass slide treatment. Fresh glass slides were cleaned using an Alconox soap solution followed by a rinse with ultrapure water. Slides were then dried using compressed air, rinsed in IPA, and dried again before being submerged in the treatment solution for 2 hr. Treated slides were stored in toluene until ready for use. Before printing, the build plate was removed from the printer and strips of fugitive glue were positioned and adhered by heating

using a heat gun. A treated glass slide was dried and gently pressed into the activated fugitive glue on the build plate. Once cooled to room temperature and secure attachment of the slide was confirmed, the resin printer was releveled and programmed to the new z-axis zero location to account for the adhesive and glass slide following the manufacturer's instructions, included in Appendix A. Resin 3D printing proceeded as described previously. Following printing, the glass slide was gently cleaned with an IPA-soaked Kimwipe before careful removal from the build plate by gently twisting the glass slide. The print was then carefully processed following the standard post-print procedure. Resin attachment to the glass slide was tested after a minimum 12-hr resting period.

NOA 86H clear optical cement was also tested as a means to seal a 3D-printed device against a glass slide. A fresh glass slide was placed on the Laurell spin coater. 1000 μL of NOA 86H was pipetted into the middle of the slide. After establishing vacuum and nitrogen gas flow, one of the following 2-step spin programs was followed:

1. 10 s, 500 rpm, acceleration 100 rpm/s
2. 30 s, 1000 rpm, acceleration 300 rpm/s

or

1. 10 s, 500 rpm, acceleration 100 rpm/s
2. 30 s, 3000 rpm, acceleration 300 rpm/s

The coated glass slide was removed from the spin coater, and a printed microfluidic device was placed onto the slide channel side down. Three binder clips were used to secure the device in place during the adhesive bake in a vacuum oven under approximately 20 inHg at 100 °C for 1 hr. Other explored NOA 86H procedures included the changes listed below:

1. Reduction in volume of NOA 86H used, 900 and 800 μL tested

2. Reduction in length of bake, 10-min intervals tested
3. Removal of binder clip clamping
4. 12+ hr between post-print processing and attempted sealing
5. Elimination or substantial reduction of post-print curing
6. Elimination of bake under vacuum
7. Lowered bake temperature, 80 °C tested
8. Slow oven temperature ramping, start 35 °C to 80 °C over 100 min tested

After at least 12 hr, the seal was tested by attempting to fill the device channels with water. Additionally, a range of oven temperatures, 35-80 °C, were tested with 3D-printed devices without the presence of NOA 86H to determine the impact of elevated temperatures on thicker resin prints.

Finally, PDMS was tested to seal 3D-printed devices to glass slides. A 10:1 ratio of elastomer base to curing agent was used. 5 g of base and 0.5 g of curing agent were measured on a toploading balance into a plastic cup. After thorough mixing and degassing under vacuum, the PDMS was poured onto a fresh glass slide in the spin coater. Vacuum and nitrogen gas flow was established before spinning for 45 s at 2000 rpm. Three separate baking and sealing procedures were tested,

1. 5 min bake at 80 °C before manually pressing 3D-printed device into PDMS layer
2. 3 min bake at 80 °C before manually pressing 3D-printed device into PDMS layer
3. 3 min bake at 80 °C before clamping 3D-printed device into PDMS layer using C-clamps

After at least 12 hr, the seal was tested by attempting to fill the device channels with water.

As an alternative to sealing 3D-printed devices onto a glass slide, a device holder was designed to apply constant pressure to the device and into a slab of PDMS on a glass slide. FDM

3D printing was used to fabricate upper and lower frames from PETG filament. A 3 mm thick glass plate was custom cut to fit into the lower frame. Initially, in-house PDMS slabs were tested. A 10:1 ratio elastomer base to curing agent PDMS was mixed and degassed before it was directly poured onto the glass surface in lower frame for baking at 80 °C for 45 min. This resulted in a slab thickness between approximately 1 and 2 mm. Sheets of PDMS were also purchased, cut to size, and tested in the device holder. 3D-printed devices were either unchanged or polished with damp, 2000 grit sandpaper on a level granite surface until a consistent frosted appearance covered the channel side of the device, as shown before in Figure 2.2. Polished devices were rinsed with ultrapure water and dried using compressed air before use. The selected device was then placed onto the room-temperature PDMS slab in the lower frame and clamped into place with the upper frame using a set of 8-32 hex screws and wing nuts. The seal was tested by attempting to fill the device channels with water.

2.2.3.2 Flexible seals

A combination of polyvinyl acrylate (PVA) adhesive, Elmer's Glue-All® multi-purpose glue, and cyanoacrylate adhesive, Loctite Brush-on Super Glue, were used to seal 3D-printed devices to transparency film. First, a clean transparency sheet was cut to the appropriate size for the device. Using a paintbrush, a thin layer of PVA glue was applied over the surface of the transparency leaving a border of 0.5 cm around the perimeter. The super glue was then applied along only the edges of the selected device, being careful to avoid placing any glue near or in the channels. The prepared device was placed onto the transparency and gently pressed into place. Two thin, metal or plexiglass plates were placed on either side of the sealed device and secured using C-clamps (Figure 2.3).

Figure 2.3. A 3D-printed microfluidic device sealed to transparency film using a combination of PVA and cyanoacrylate adhesives. Once clamped into place, as shown, water was flushed through the channels to dissolve the water-soluble PVA adhesive.

A disposable pipet filled with ultrapure water was used to fill the open inlet reservoirs while a suction cup applied at the outlet rapidly pulled water through the channels via vacuum aspiration to clean out the water-soluble PVA adhesive. At least 10 mL of ultrapure water was used in the cleaning process before the clamped device was set aside to fully cure for 24 hr. Once unclamped, the seal was tested by attempting to fill the device channels with water.

A line of Microfluidic Tapes produced by 3M™ were tested to seal microfluidic devices made from PDMS, cured resin, and glass. The tape, 9793R and 9795R were first cut to fit the selected device allowing a reasonably-sized perimeter around the edges. The release liner was peeled from the tape and the adhesive side was slowly applied to the device, placed channel-side up, from one edge to the other avoiding bubbles. A blunt tweezer or edge of a plastic card was used to remove bubbles being careful to avoid pressing the tape into any channels. Tape-sealed devices were then flipped over, manual pressure was applied for 2 min to the rigid devices, and placed in a laminar flow hood for at least 4 hr before use. The seal was tested by attempting to

fill the device channels with water. An in-line pressure transmitter was used to track the pressure buildup within the microfluidic channels during seal strength testing. A programmable syringe pump was used to provide constant flow while a clamp was secured on the outlet tubing. Higher flowrates were tested, resulting in higher pressure buildup, until the tape seal burst, or a time threshold was surpassed. A 1 M NaOH solution in water and a 50/50 mixture of ethyl acetate and n-heptane were tested separately as adhesive removal solutions by first submerging pieces of 3M™ tape in these test solutions. Tape-sealed devices were also filled with the adhesive removal solutions and sonicated as an option for adhesive removal.

2.2.4 Tissue culture

All cell types were cultured in a humidified environment at 37 °C and 5% CO_2 in T75 polystyrene culture flasks. C6 cells were grown in F-12K medium supplemented with heat inactivated horse serum (15% v/v), FBS (2.5% v/v) and penicillin streptomycin (5% v/v). U-87 cells were grown in DMEM (high glucose) medium supplemented with FBS (10% v/v) and penicillin streptomycin (5% v/v). All cells were passaged when 80% confluency was reached, approximately every 3-5 days. Detailed tissue culture protocols are provided in Appendix B.

2.2.5 Biocompatibility testing

Multiple methods were used to assess the biocompatibility of key materials utilized in this microfluidic device fabrication and implementation. The details of those experiments are provided in the following sections.

2.2.5.1 Cured resin tests

Initial biocompatibility tests focused on potential extractables, or leachates, released from the cured resin material under cell incubation conditions. Resin pieces 7.5 mm wide, 7.5 mm long, and 2.5 mm tall were printed and subject to standard post-print processing before soaking

in a bleach solution (10% v/v), rinsed with ultrapure water, dried, and sterilized with UV light for 5 min on each side in the biosafety cabinet. To assess the impacts that resin extractable species may have on cell health, the prepared pieces of cured resin were floated in 24-well plates seeded with C6 rat glioma cells, and the viability was monitored over time using trypan blue (Figure 2.4).

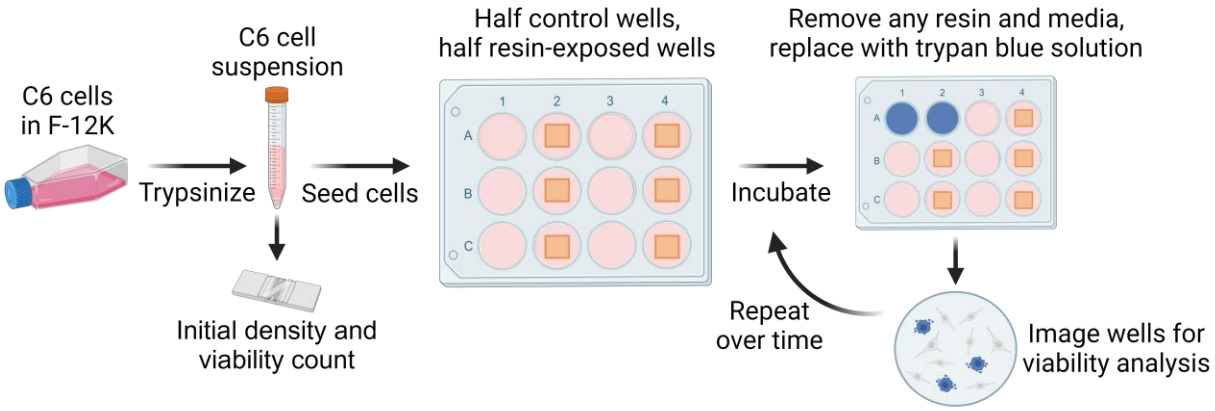

Figure 2.4. Procedure for resin extractables biocompatibility testing on C6 cells. Created with BioRender.com.

950 µL of complete F-12K was pipetted into each well prior to cell seeding and stored in the incubator to maintain temperature and pH. Following trypsinization, a hemocytometer was used to confirm the C6 cells had a starting density of 4.6-6.2 × 10^5 cells/mL and at least 96% viability. Resin pieces were carefully placed to float in half of the experimental wells using sterile tweezers. 50 µL of cell suspension was added to each well. The prepared well plate was stored inside the incubator until imaging was completed at 0.5, 1, 2, 4, 6, 8, 10, and 12 hr after cell seeding. At each timepoint, the resin floats were carefully removed from the wells. Supernatant from the control and resin-exposed wells was collected to assess the number of detached cells as another method for evaluating cell health. A mixture of 150 µL PBS and 50 µL trypan blue was added to the selected wells for imaging. Images were collected on the Nikon

SMZ1500 stereoscopic zoom microscope using the Sony Alpha a6400 camera at magnification between 4X and 10X. Imaging analysis was completed using ImageJ. Further protocol details are provided in Appendix C.

2.2.5.2 3M™ tape tests

Both native and treated 9795R tape adhesive was examined as a tissue culture surface. 7.6 mm tall cylinders of 5.5 mm ID glass tubing were cleaned with a bleach solution (10% v/v), rinsed with ultrapure water, dried using compressed air, and sterilized with UV light for 10 min on each side in the biosafety cabinet. The glass was adhered to the 9795R tape, forming a pseudo well plate, and stored inside a petri dish. For treatment solutions, PDL and HA were both dissolved in PBS, separately and together. A range of 50-100 μg/mL PDL and 0.5-2.0 mg/mL HA were tested. For the final treatment solutions, 50.0 μg/mL and 1.0 mg/mL were used for PDL and HA, respectively. 50 μL of each treatment solution were pipetted into the tape wells and stored at 4 °C overnight. The treatment solution was rinsed from the tape wells with complete DMEM growth medium before experiments began.

To assess the impact these various surfaces had on U-87 human GBM cell health, morphology and viability were compared between cells grown on untreated tape, treated tape, and control cells grown in 96-well plates, using brightfield imaging and PI staining (Figure 2.5). 55 μL of complete DMEM medium were added to all wells prior to cell seeding and stored under incubation to maintain temperature and pH. Following trypsinization, a starting cell density of 4.0-6.7 $\times$ 10^5 cells/mL and at least 97% viability were confirmed via hemocytometer. For both the tape-grown and control cells, 15 μL of cell suspension were added to each well. Cells were stored inside the incubator until imaging was completed at 0.5, 1, 2, 4, 6, 8, 10, and 24 hr after cell seeding. 30 μL of 100 μg/mL PI in DMEM were added to each well prior to imaging.

Brightfield images were collected using the Nikon Eclipse TE2000-U inverted microscope and Sony Alpha a6400 camera, and PI images were collected via the Nikon G-2A filter cube. All images were collected at 10X (NA = 0.30) and 20X (NA = 0.45) magnification. Imaging analysis was completed using ImageJ. Further protocol details are provided in Appendix C.

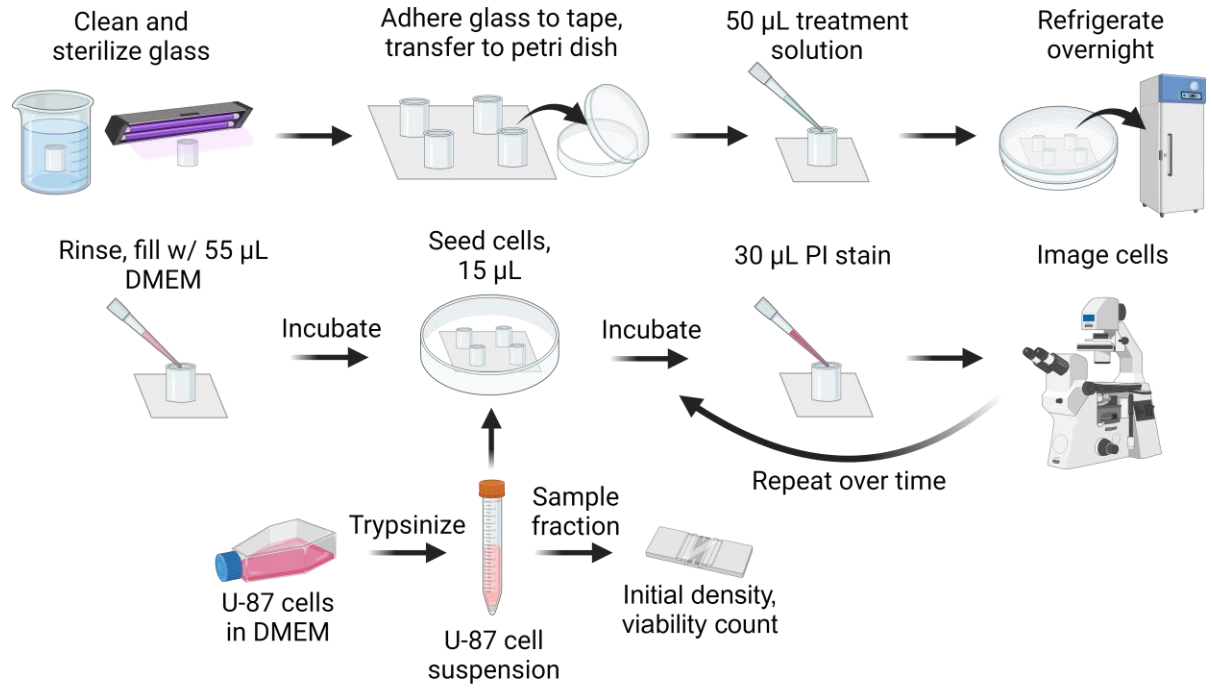

Figure 2.5. Procedure for tape biocompatibility and treatment studies on U-87 cells. Created with BioRender.com.

2.3 Results and discussion

2.3.1 Printer settings and print processing

Multiple print settings and post-print processing procedures must be optimized to successfully print microfluidic designs on a commercial resin 3D printer. The details of this optimization are provided below.

2.3.1.1 Settings during printing

The most critical print setting is the duration of light exposure for each layer. This setting determines the extent of crosslinking and the strength of the printed features. The initial layers

are subject to longer exposure to ensure proper adhesion to the build plate. Light exposure for the remaining layers is tailored based on the selected resin, print layer height, complexity of the design, and orientation of the print. Thin resin test prints can be used to expedite the light exposure optimization process. It is important to have test features of the desired dimensions incorporated into the test print design to ensure appropriate light exposure for the desired resolution. Underexposure resulted in uncured resin, while light overexposure caused excess curing (Figure 2.6). This print setting was continuously optimized throughout the device development process as smaller channel dimensions were attempted using different resin printers and a range of resins.

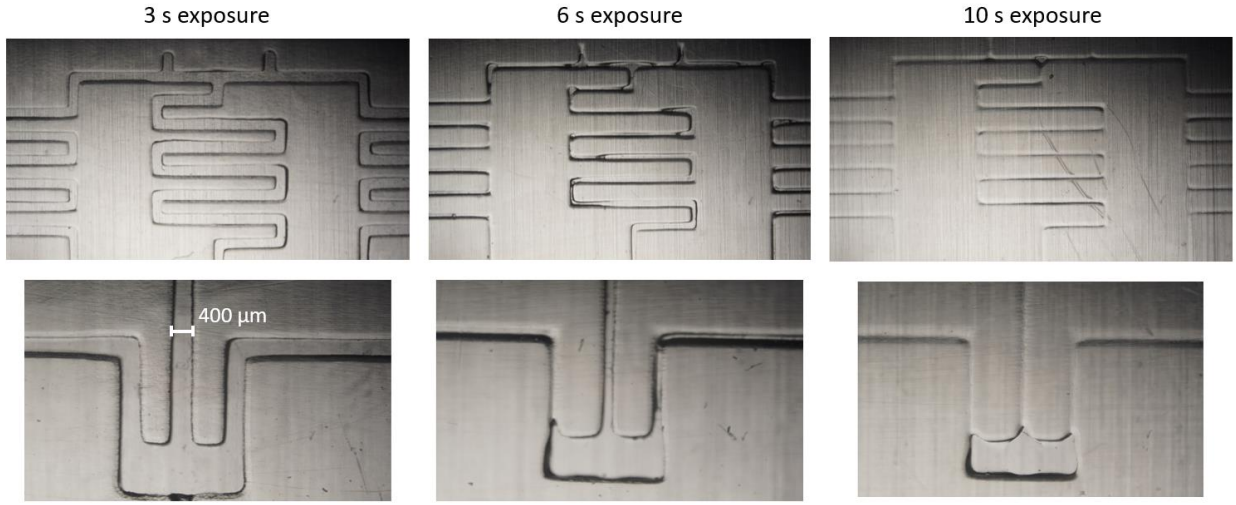

Figure 2.6. The resulting print quality from a range of light exposure lengths. Surplus light during layer curing contributed to excessive resin curing within channels, reducing the desired dimensions, even completely clogging channels. The test gradient mixing channels were designed to be 400 µm wide and 500 µm deep.

Another factor in resin 3D printing is layer height. All design files must be digitally sliced into layers for the printing process. This layer height impacts both print quality and the time required to complete the print. The layer height resolution, or z-axis resolution, is defined by the stepper motor of the printer. Typically, shorter layer height results in better resolution for details tens to hundreds of microns in dimension. It is beneficial to have feature dimensions

evenly divisible by the layer height to improve upon dimensional accuracy in the final print. Other insights into layer height are reported further in this chapter.

Positioning of the print on the build plate is another important factor to consider when resin 3D printing. During the slicing process, the designed object file must be positioned, and there are many considerations that can influence this. For traditional resin 3D printing in the hobbyist community, build plate positioning is influenced by the placement of printing support structures. This typically involves optimizing the printing angle to reduce the number of support structures required to successfully print the design. The optimal orientation of the print can also be changed to reduce the total cross-sectional area of each layer to lower the force required to peel the cured layer up from the bottom of the resin vat. If the force is too much, the build plate can be dislodged from its level position and cause subsequent layers to be misaligned and/ or damage the printer. Alternatively, compared to most objects printed by hobbyists, microfluidic devices can be printed flat to the build plate to eliminate the need for any supports as long as the cross-sectional area of the layers is not too large (Figure 2.7).

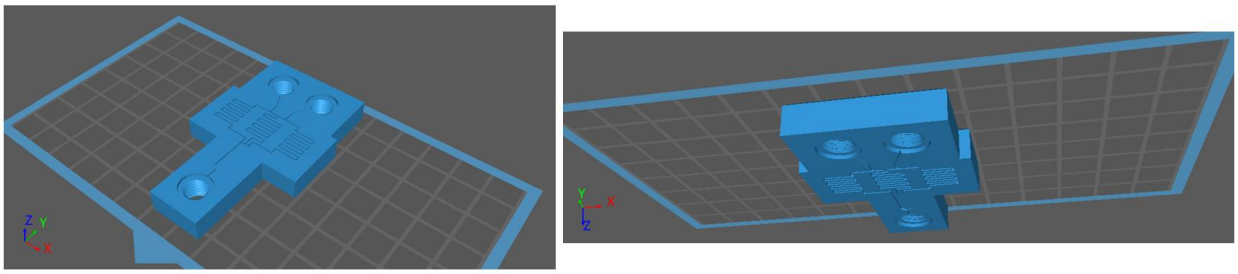

Figure 2.7. Positioning of microfluidic device design on the virtual build plate within the slicing software. Devices are printed flush to the build plate (left). During the printing process, the orientation is reversed, and the back of the device is printed first with the channel layers printed last (right).

Repeated printing in the exact same location on the build plate causes excessive stress on the same region of the plastic film at the bottom of the resin vat. Over time, the damage reduces the transparency of the film, resulting in less effective light transmission and print inaccuracies

or defects. Overuse will eventually cause a tear in the film and a resin leak onto the LCD screen and potentially into the electronics within the printer. Most hobbyist resources advise varying the build plate positioning to reduce wear on the plastic film and increase its lifespan. Unfortunately, variation in LCD pixel or LED performance can result in regions with different printing capabilities unless the screen or light array is replaced. This can make build plate position incredibly important when attempting to consistently fabricate features with microfluidic dimensions. Print alignment with specific illuminated LCD pixels has also been a strategy implemented to fabricate microchannels by employing, typically undesirable, light broadening from pixels further away to narrow void regions in prints.[101] Considering all these factors, the positioning of a print on the build plate is a critical step in resin 3D printing.

As newer resin printers were purchased and used, additional print settings became adjustable within their slicing software packages. A surprisingly important factor for printing microfluidic devices was the introduction of rest times between steps in the resin 3D printing process. Most slicers have three separate rest times included: 1) before lift, introducing a delay following the layer cure but before the build plate lifts to peel the cured layer from the vat, 2) after lift, introducing a delay after the build plate completes its lift from the vat, and 3) after retract, introducing a delay after the build plate lowers back into the vat before the subsequent layer is cured. Previous inconsistencies in print quality were remedied following the addition of a 5 s rest time before lift and 1 s rest times after lift and after retract.

It has been theorized that the pause before lift allows for a more thorough completion of the polymerization process before the forceful removal of the most recent layer from the resin vat. The other delays, after lift and after retract, permit both the resin and build plate to settle after displacement or assigned movement, respectively. Different resin viscosities would cause

varying levels of force to be exerted on and by the build plate when moving through the resin. It is speculated that these resting periods provide time for the resin printer to come to a complete stop before and after potentially straining processes. Although an exact understanding of the nature of this improvement is unknown, and the rests add time to each layer of the printing process, the rests are justified by the significant improvement in print quality.

2.3.1.2 Post-print processing

The first step following the resin 3D printing process is a rinse in an appropriate solvent, typically IPA. The rinse is used to remove the excess uncured resin on the print, which was repeatedly lowered into the resin vat as subsequent layers were printed. This process is key since the post-print cure would polymerize the excess resin and alter the print dimensions, a consequence that would be significantly detrimental for microfluidic devices. Due to the scale of the printed dimensions, clearing excess resin from negative, or recessed, features required more thorough consideration. Initially, a soft-bristled toothbrush was used to carefully clean prints, but this strategy had two potential issues. A toothbrush could not reach all areas that needed to be cleaned, such as the threaded inlet and outlet holes, and brushing before the post-print cure could result in print scratching or damage to the surface. As an alternative, an ultrasonic bath sonicator was used to aid in cleaning microfluidic prints. After the initial IPA rinse with manual agitation, prints were transferred to a small container filled with fresh IPA. This container was placed in the bath for approximately 5 min to effectively rinse microfluidic prints.

Although 405 nm light is required to cure the resin, including for the final post-print cure, excessive exposure to light contributes to eventual resin yellowing and degradation. This yellowing also reduces the transparency of the resin. To assess the impact of excessive light exposure, an experiment was designed where replicate prints were subjected to increasing

lengths post-print curing time (Table 2.1). Direct light exposure for less than 8 min did not result in any excessive yellowing or material degradation, and only minor visual differences were observed between the print with the shortest exposure, 1A, and longest exposure, 2H (Figure 2.8). The primary source of yellowing was the printing process itself. Increasing the print layer height may reduce the overall yellowing by lowering the instances of repeat light exposure, but this could impact print quality, and yellowing is not a significant issue at this time.

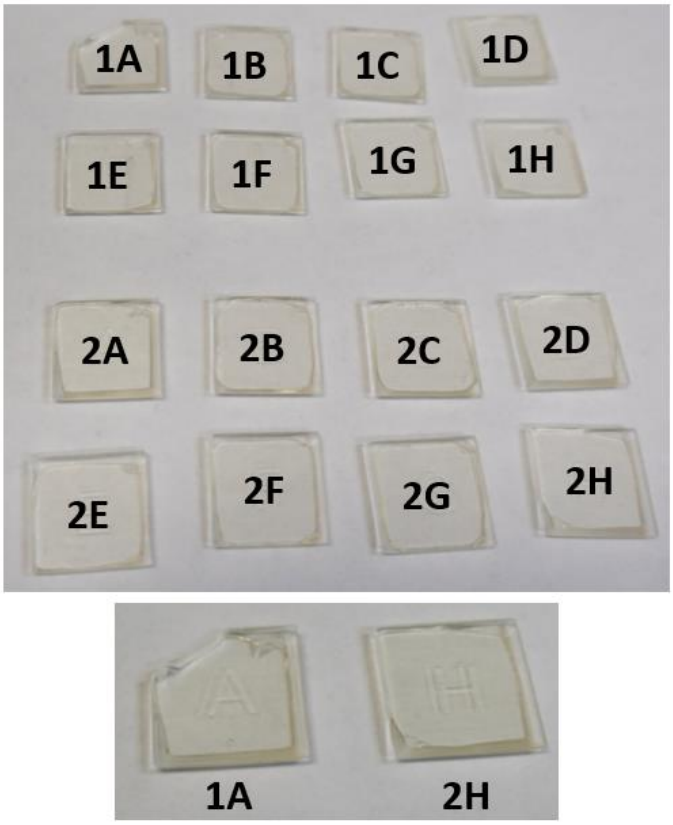

Figure 2.8. Results of yellowing experiment from round 1 and 2 (upper image). Direct comparison between 1A and 2H (lower image). Excessive yellowing or degradation was not evident for post-print curing under 8 min. Note: Damage to print 1A was caused during removal from the build plate and not as a result of curing.

The build plates of most resin 3D printers have a texturized surface to improve attachment during printing. As a result of this, the side of the resin print in contact with the build plate is left with the corresponding texture. Any scratches in the build plate, often a result of

print removal, also transfer to future prints. This results in a significant decrease in clarity for prints made from transparent resins. During the printing of microfluidics as described above, the first layer of the print is to the top of the device, and the last layers printed contain the channels. The clarity of the top of the devices does not have significance when using an inverted microscope for widefield fluorescence microscopy, but it would provide a way to monitor device filling and function more easily from above and enable imaging with an upright microscope.

Two methods were tested to improve print clarity: 1) the application of Minwax Polycrylic Protective Finish in clear gloss and 2) the use of a Sylvania Headlight Restoration Kit. The Minwax coating was selected based on recommendations from resin 3D printing online forums. The plastic covers over headlights are subject to scratching and yellowing over time. Headlight restoration kits are designed to improve the clarity of these plastic covers to allow more illumination for drivers. Due to the similarities between photosensitive resins and automotive headlight covers, a headlight restoration kit was selected as a possible print treatment.

After treatment, it was evident that both methods tested improved the print clarity as can be seen in Figure 2.9.

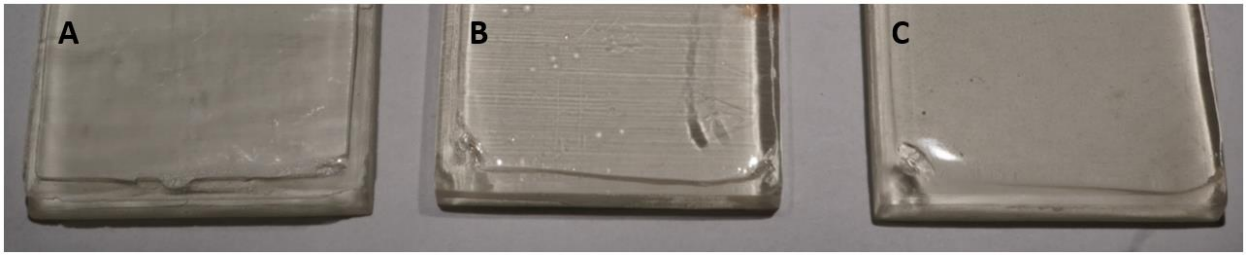

Figure 2.9. Comparison between untreated (A), Minwax-coated (B), and headlight kit-treated (C) resin prints.

Although the clarity was improved for the Minwax-coated print, the texture of the build plate was still visible (Figure 2.9 B). The print treated with the headlight restoration kit showed the

greatest improvement in clarity (Figure 2.9 C), but the number of steps and cost of the proprietary kit were critical drawbacks. The wet sanding process, inspired by the headlight kit, and the Minwax finish were combined to provide the most effective and simplified method for improving the clarity of transparent resin prints (Figure 2.10).

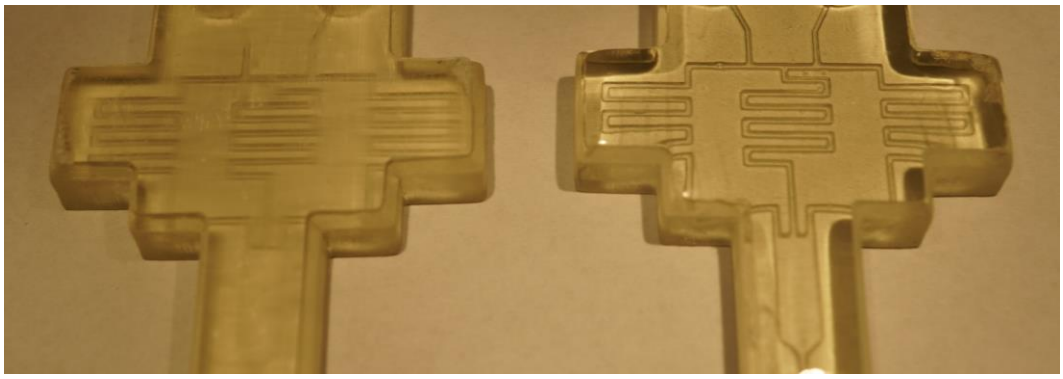

Figure 2.10. Comparison between untreated (left) and treated (right) microfluidic devices. This improvement in print clarity was due to the finalized post-print polishing and coating procedure utilizing wet sanding and the Minwax Polycrylic Protective Finish in clear gloss.

2.3.2 Resin material properties

One of the major motivations behind this work is developing accessible and affordable fabrication. Although customized resin formulation has its benefits, utilizing commercially-available resin was key to maintaining an approachable method for microfluidic cell research. As a result, there were many key material properties of the cured resin that required examination to ensure the 3D-printed devices can be used for chemotaxis studies. The details of these assessments are explained below.

In order to maintain cell viability, a temperature of 37 °C must be maintained throughout experiments. Additionally, the possibility of device sterilization at elevated temperatures would aid in establishing the reusability of the 3D-printed devices. The temperature resistance of the cured resin was explored to determine what environmental conditions it could withstand. The Elegoo ABS-like translucent resin, designed to be transparent and colorless, was not marketed

with specified high temperature resistance but was readily available for commercial purchase and, therefore, selected for this work.

The test print design incorporated a range of channel dimensions including a 2800 μm wide observation channel and 400 μm wide serpentine mixing channel. All channels were 500 μm deep. The comparison images collected at each time interval allowed for deformation in channel dimensions and print rigidity to be monitored upon exposure to 60, 80, and 100 °C. After no observable change in printed features or material rigidity was detected at 60 °C, the length of temperature exposure was increased for 80 and 100 °C experiments. Finally, an extended exposure at 100 °C was tested following continued print stability. In general, no significant differences were identified during these tests (Figure 2.11).

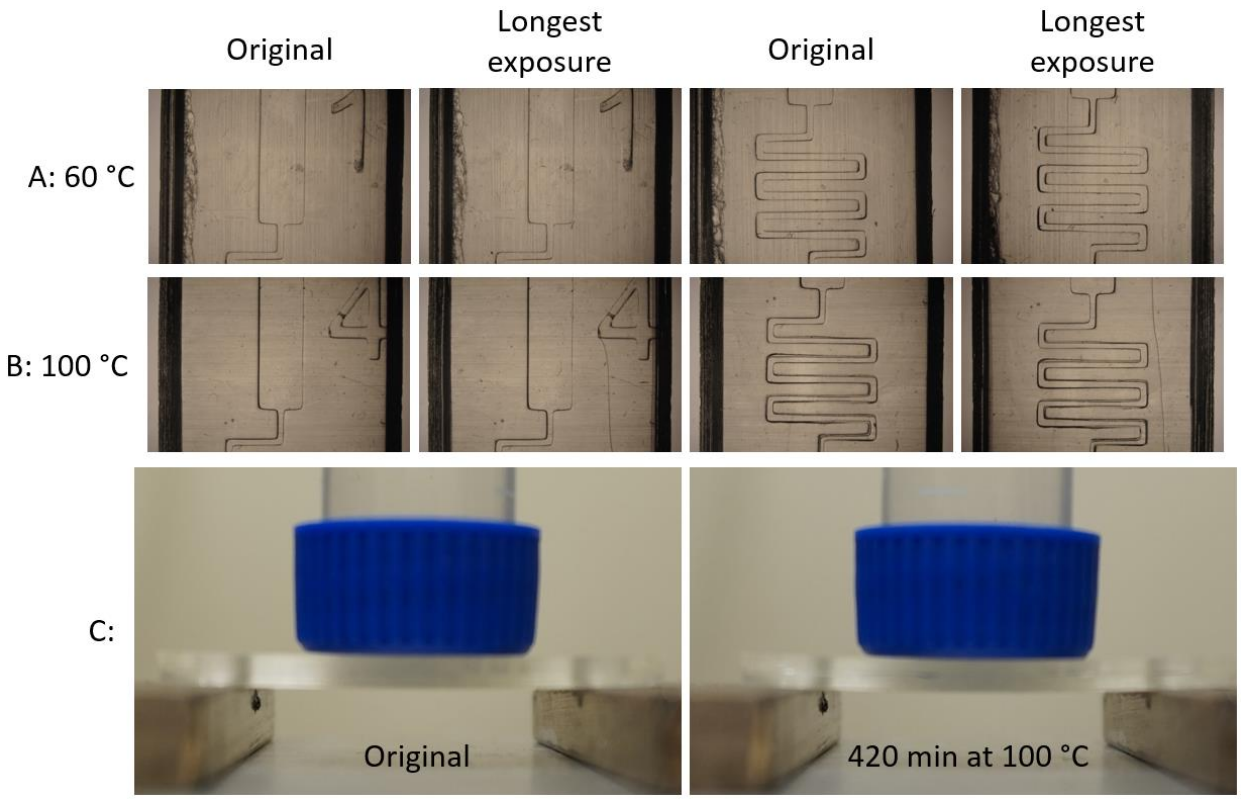

Figure 2.11. Results from temperature testing. After 90 min at 60 °C, no deformation was observed in the channels (A). Following 420 min at 100 °C, a potential scratch was identified, but the origin of this new feature was unknown (B). The 20 g weight caused no noticeable deflection in the test print after the longest exposure at the highest temperature (C).

A possible scratch was observed in the print exposed to 100 °C for 420 min, but it was unknown as to whether this occurred during temperature exposure or transfer to imaging locations (Figure 2.11 B). The overall temperature resistance of this resin covered a wider temperature range than expected and provided more insight for future work on 3D-printed device development.

The surface roughness of 3D-printed microfluidic devices was an important factor to consider due to the potential impacts on critical aspects, such as fluid flow and cell attachment and viability. A profilometer was used to assess surface features of unchanged and polished devices both in and out of printed channels. These studies provided surface topography for the face of the device that would be sealed to another material and for what would be the ceiling of the microchannels. Polishing the channel face of devices with 2000 grit sandpaper reduced the largest surface variations, typically greater than 1000 nm tall, while the smaller variations in surface texture remained (Figure 2.12 right).

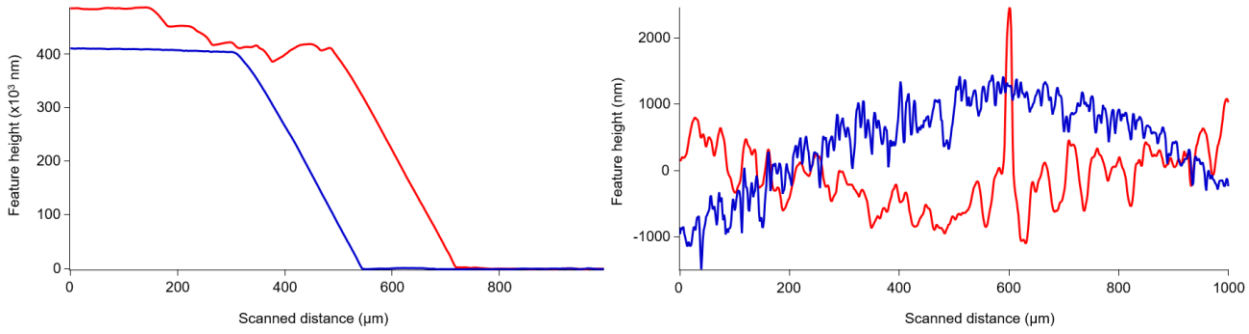

Figure 2.12. Profilometer results from unpolished (red) and polished (blue) device surfaces. Polishing reduced variations in the surface near channel walls (left) and reduced the overall range of surface feature heights (right).

Although the serpentine mixing channels were too narrow to measure with the installed profilometer stylus, the wider observation channels and inlet reservoirs were far more accessible. This permitted the actual channel depth to be evaluated and compared to the original design. These profilometer scans began outside on the face of the device and descended into the channel (Figure 2.12 left). The measurements confirmed that the printed channels were within 100 µm of

the desired dimension in the z direction. As reported in literature, the cell diameter of U-87 GBM is often stated to be between 10 and 30 μm.[102] Microchannel depths ranging from 200 to 500 μm with variations within 50-100 μm would have little impact on the cells themselves besides the resulting increase in shear force due to small channel dimensions. Flowrate considerations and the subsequent shear force estimations will be discussed further in Chapter 4. Variations in the 3D-printed surfaces less than 1000 nm in height are considerably smaller than the desired channel dimensions and would have little impact on the functionality of the device.

Fluorescent stains have been selected as the method to track cell position and health during future experiments. Excessive autofluorescence of the cured resin microfluidic device would interfere with the fluorescence imaging. To assess the autofluorescence of the cured resin material, two commonly-used wavelengths of excitation were selected, 470 and 535 nm. Fluorescent intensity was measured for both the fluorescent solutions and cured resin.

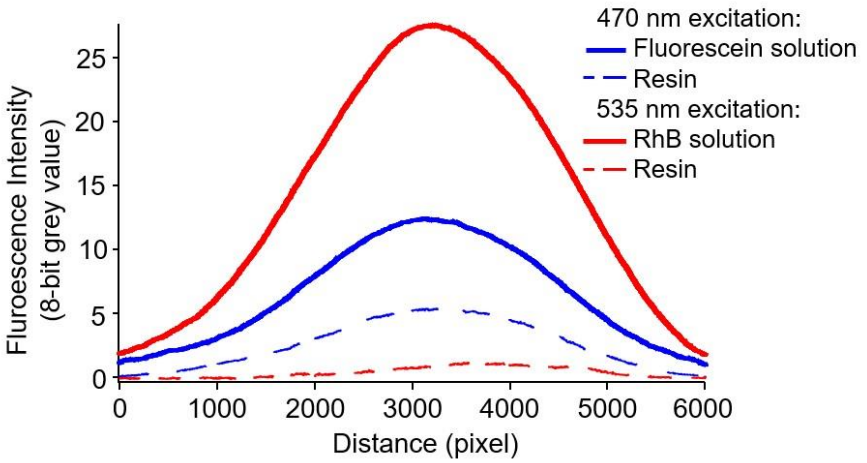

Figure 2.13. Autofluorescence of the cured resin material was measured at two wavelengths of excitation, 470 nm (blue) and 535 nm (red). The intensity of the fluorescence given off by the resin (dashed lines) was compared to 10 μM fluorescein and RhB solutions (solid lines). Low autofluorescence of the resin material was confirmed at these commonly-used wavelengths.

As was expected, based on previous studies, shorter excitation wavelength contributed to higher autofluorescence in plastics.[96] Critically, the measured autofluorescence from the cured resin

material was substantially lower than the dilute fluorescent solutions (Figure 2.13). These results confirmed that these wavelengths of excitation could be implemented in future cell studies within resin 3D-printed devices without substantial background interference from the resin itself.

In addition to confounding autofluorescence, fluorescent staining would be detrimental to future cell studies. The native surface roughness of the cured resin could provide small recesses to harbor fluorescent stains, conflicting with fluorescent imaging. RhB, notorious for retention within porous and hydrophobic surfaces, was used to assess the cured resin's susceptibility to staining. Short exposure, 4 min, to the 10 μM RhB solution caused a mild amount of staining within microchannels, while long exposure, 30 min, contributed to moderate staining (Figure 2.14).

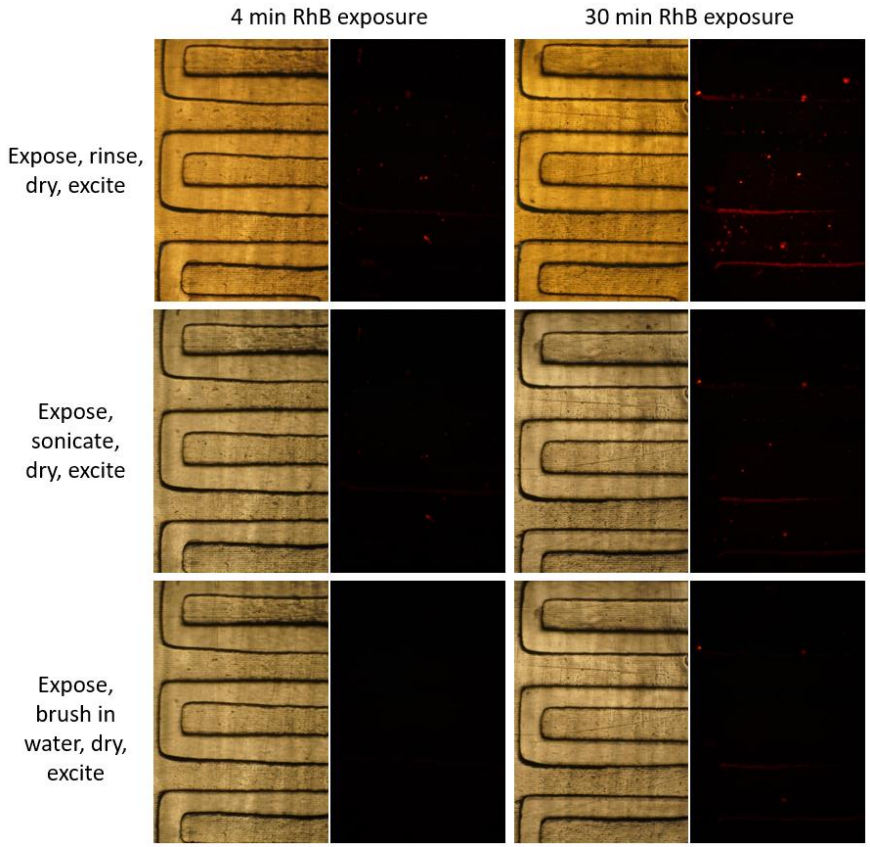

Figure 2.14. 10 μM RhB was exposed to printed resin microchannels for both 4 and 30 min (left and right, respectively) to compare the resulting fluorescent staining. Initial tests examined the level of staining after rinsing with water and drying (upper). Other RhB-exposed prints were sonicated in water for 15 min and dried before assessing staining (middle). Finally, RhB staining was measured after exposed prints were cleaned with a toothbrush in water before drying and imaging (lower). Most of the prominent RhB staining was effectively removed with moderate rinsing and agitation. This testing confirmed printed devices could be stained, but, more importantly, they could be rinsed and reused for future tests after exposure to fluorescent solutions.

Multiple methods were assessed to remove retained RhB from the microchannels. A combination of a water rinse and agitation was most effective for clearing away RhB. The intrinsic roughness of the cured resin did contribute to fluorescent staining, but this could be remedied to allow for repeat use after exposure to fluorescent solutions.

Since cells will not be cultured directly on the resin surface, based on the current microfluidic design, biocompatibility was assessed by growing C6 cells in culture media exposed to cured resin. This test investigated the presence of any extractable chemical species from the

resin that could impact cell health. Pieces of resin were placed floating above the seeded cells in 24-well plates. To perform trypan blue viability staining at the specified timepoints, both the resin float and supernatant were carefully removed from the control and resin-exposed wells. GBM cells are adherent, and therefore dead or dying cells could potentially detach and be lost to the supernatant impacting the accuracy of the viability measurements. To account for this, the supernatant was collected and subject to another hemocytometer assessment in addition to the trypan blue staining completed on the cells remaining in the wells. The results of three replicate experiments are shown below in Figure 2.15.

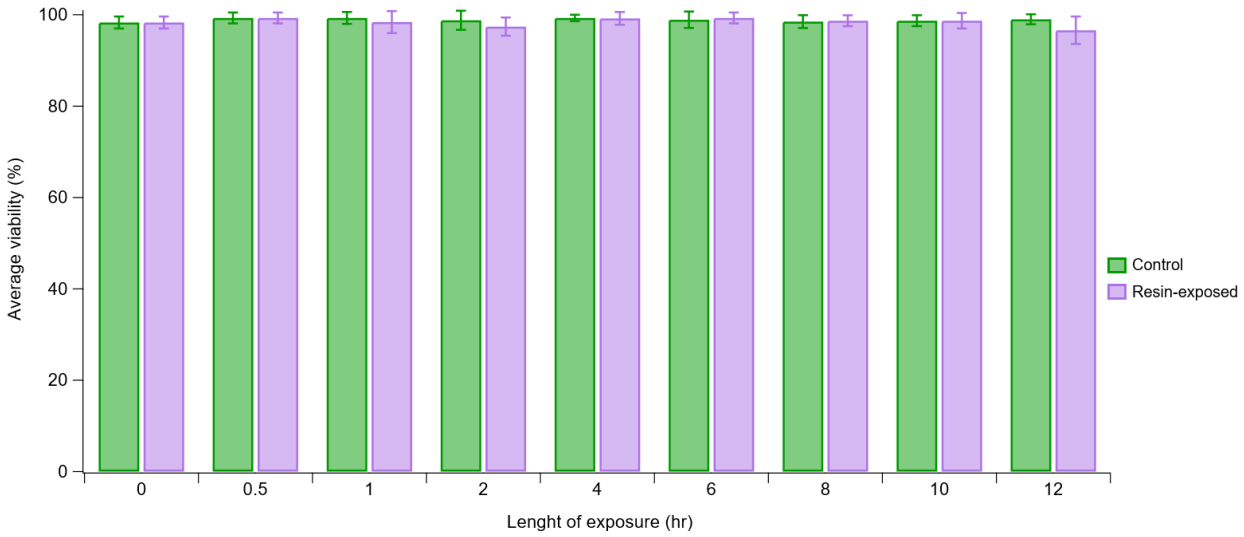

Figure 2.15. Results from resin extractable biocompatibility analysis. Exposure to cured resin material did not have a significant impact on C6 cell viability over a 12-hr experiment under standard incubation conditions. Error bars represent standard deviation, n = 3.

Over the 12-hr experiments, there was no substantial decrease in cell viability for the resin-exposed wells compared to the control. Both the F and *t* tests, at a 95% confidence level, revealed the standard deviations and means were not significantly different for the control and resin-exposed conditions. Furthermore, the assessment of the supernatant revealed an insignificant number, between zero and four, of live or dead cells detached from their culture surface. These results were promising for continued use of this resin as the main material of the

microfluidic device and confirmed a low or negligible presence of extractables from the resin, even at 37 °C. Moreover, during future chemotaxis experiments, a constant flow of fresh media and chemoattractant would be required to maintain a stable gradient. Cells seeded in a 3D-printed device would not remain in stagnant media for longer than the amount of time needed to secure cell attachment before continuous flow was established. This supply of fresh media would reduce the potential accumulation of leaching chemical species within the device.

There were three significant caveats to consider when assessing these results. The cells used for this work were rat glioma cells and, thus, could provide less relevant insight toward a better understanding of GBM for human patients. Additionally, the more clumped growth observed during the experiments was atypical compared to the stretched monolayer normally observed (Figure 2.16). Although trypan blue is a standard used for cell viability assessment via hemocytometer, its use in well plates was less straightforward. The intensity of this stain meant an overconcentrated solution could interfere with imaging when used in excess.

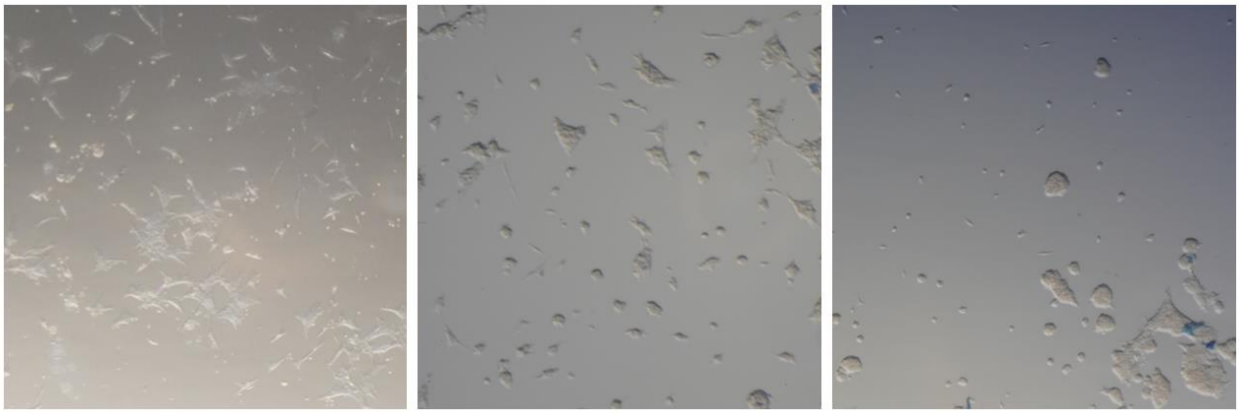

Figure 2.16. Comparison of C6 growth 12 hr after seeding in 24-well plate during cell density testing (left), biocompatibility testing control conditions (middle), and biocompatibility testing resin-exposed conditions (right). Atypical, clumped growth was observed during all biocompatibility testing.

To alleviate these concerns, three approaches are proposed for future work. Human-derived U-87 GBM cells will be used for remaining testing and device development. This

transition was only delayed due to application and approval of biosafety level 2 designation. Future cell studies with U-87 cells will begin with an exploration of cell seeding densities to ensure more representative cell growth and morphology is maintained during experiments. To improve upon the method of image-based viability testing, fluorescent stains will be used to monitor cell death. Propidium iodide will be used as an alternative to trypan blue to signify dead cells. Additionally, an Annexin V stain would allow for dying cells to be distinguished from live and dead cells to provide further information on overall cell health.

2.3.3 Strategies to improve printer capabilities

Although the commercially available LCD-based resin 3D printers have impressive capabilities for their cost, they are not intended for microfluidics fabrication. Many limitations remain, especially related to actual achievable resolution. Print settings optimization and control over environmental factors are critical for enhancing the resulting print quality, but there are inherent limits as to how much improvement can be achieved. In the section below, two strategies to improve upon the capabilities of these printers are explored.

As described previously, resin 3D printing relies on the transmission of light into the resin vat. This process results in some amount of light scattering or broadening, especially when the light must pass through multiple materials such as glass, plastic, and the resin itself. The angles of incidence and refraction are different when light moves between two media of different refractive indices, as understood through Snell's Law. These factors all contribute to light exceeding the intended region of resin curing. Resin additives, like absorbers or dyes, limit the amount of light penetration within the liquid resin (Figure 2.17).[88]

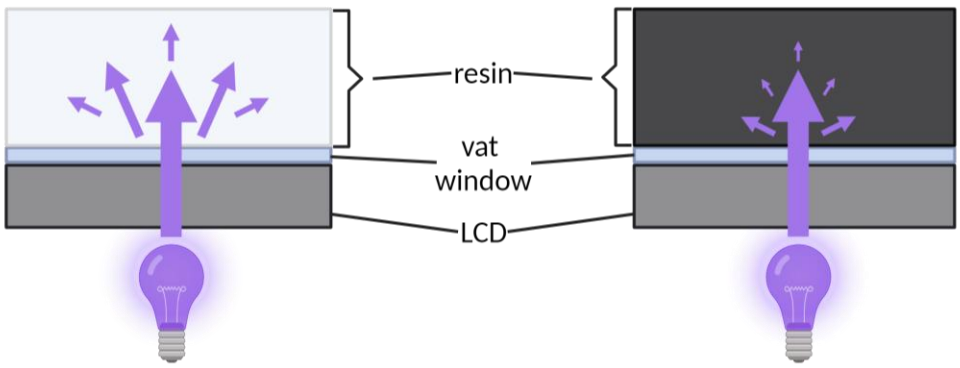

Figure 2.17. More opaque resin reduces the amount of light spreading that occurs during curing. Created with BioRender.com.

Based on this knowledge, the impact of resin opacity on the achievable resolution was explored. Three separate resins were compared: 1) a colorless and transparent resin, 2) a red translucent resin, and 3) an opaque black resin. Both identical and very minimally adjusted print settings were explored to print 200 μm wide by 200 μm deep microfluidic channels. As hypothesized, the increasing opacity of the selected resins provided substantial improvements by resulting in significantly less clogging of the printed microchannels as shown in Figure 2.18 below. This provided better understanding towards further miniaturization of the channel dimensions, although printing devices in opaque resin would eliminate the ability to monitor device filling and function from above.

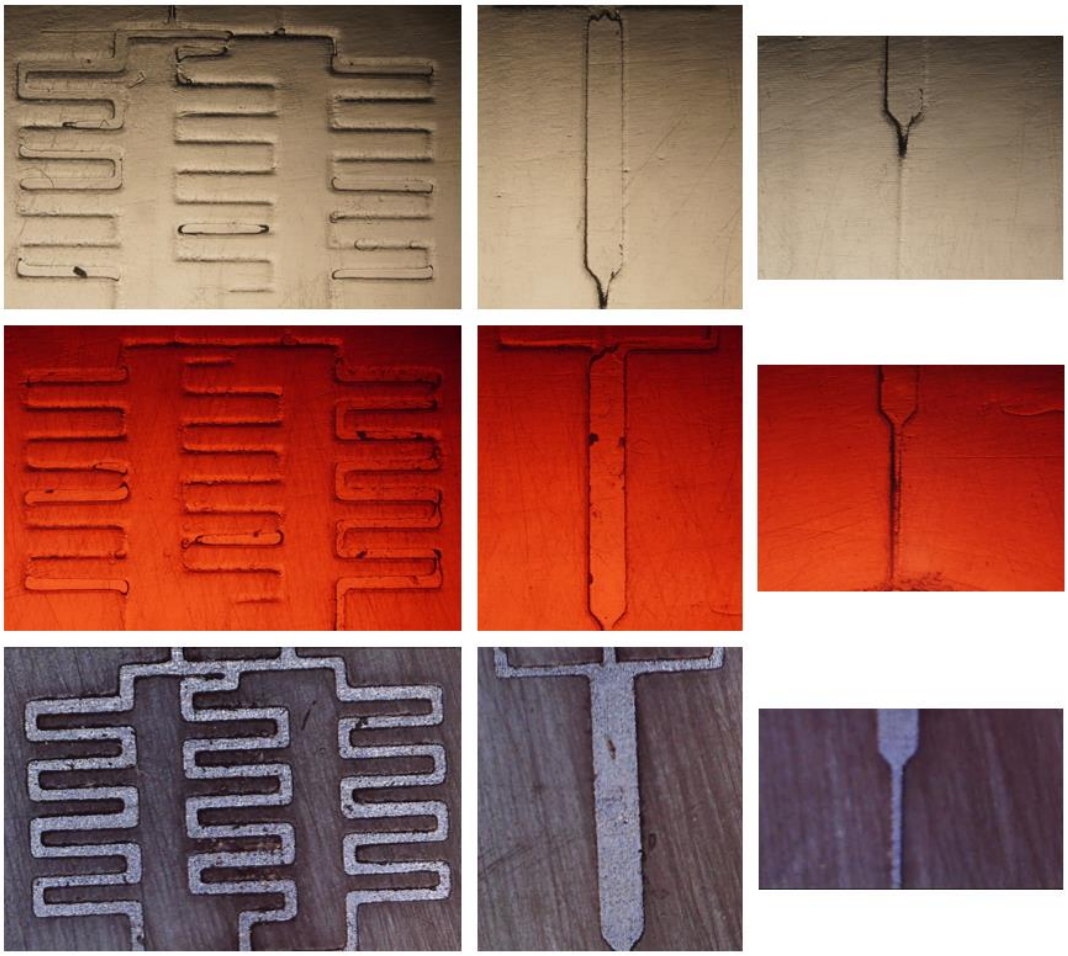

Figure 2.18. The impact of increasing resin opacity on print quality for 200 μm wide by 200 μm deep serpentine mixing channels. The colorless and transparent (upper) and red translucent (middle) designs were printed with the same settings, but the more opaque red resin contributed to the more successful result. The opacity of the black resin (bottom) improved the print quality even further.

Another idea for improving print resolution was to incorporate the use of photomasks into the LCD-based resin 3D printing process. The XY resolution of an LCD-based resin printer is determined by the pixel size of the screen. By placing a photomask over the LCD screen, sections of pixels would be blocked, and smaller features could be printed. This strategy meant pausing the printing process after the correct number of layers, removing the resin vat from its position above the LCD screen, securing a photomask in place on the screen, replacing the vat,

and continuing the print for the channel layers. The photomask method was tested with both opaque black and transparent colorless resins.

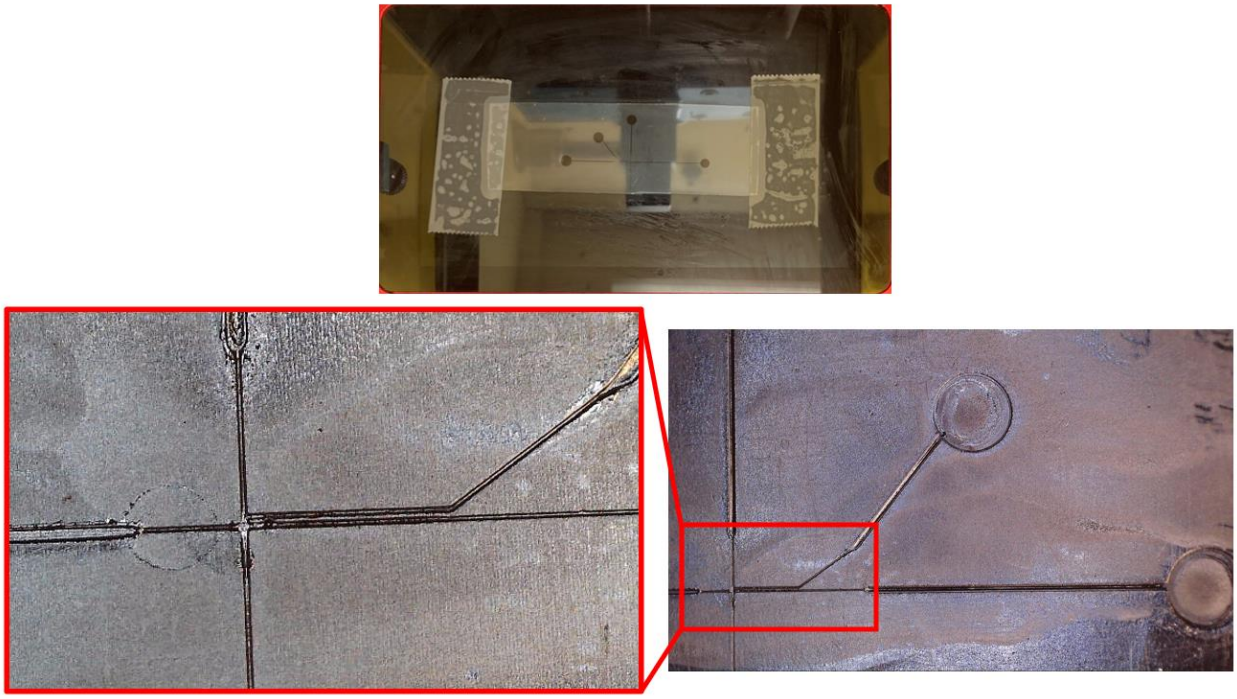

Figure 2.19. Resin printing results from initial photomask test using opaque black resin.

Initial tests with the opaque black resin used a photomask that had 50, 100, and 200 μm wide channels. During the first attempt, an IPA-soaked kimwipe was used to clean excess uncured resin from the build plate and partially finished print during the pause to align the photomask, but this prevented the channel layers from attaching to the printed base. A successful print utilizing the photomask was achieved after further optimization of the method (Figure 2.19). Following this success, a colorless and transparent resin was used with a gradient device photomask that had 100 μm wide serpentine mixing channels. This required a more precise photomask alignment procedure to ensure the reservoirs matched well with the 3D-printed threaded holes. A range of settings for length of light exposure, layer height, and channel depth were explored with a summary of results shown in Table 2.3 and Figure 2.20 below.

Table 2.3. Print settings and measured profilometer results for photomask method resin printing of gradient design in colorless, transparent resin. Corresponding visual results shown in Figure 2.20.

Print	Light exposure (s)	Layer height (µm)	Designed channel depth (µm)	Measured observation channel depth (µm)	Measured inlet reservoir depth (µm)
A	3.5	20	300	192	195
B	3.5	20	100	116	115
C	2.5	20	200	194	196
D	2.5	25	50	72.7	78.6

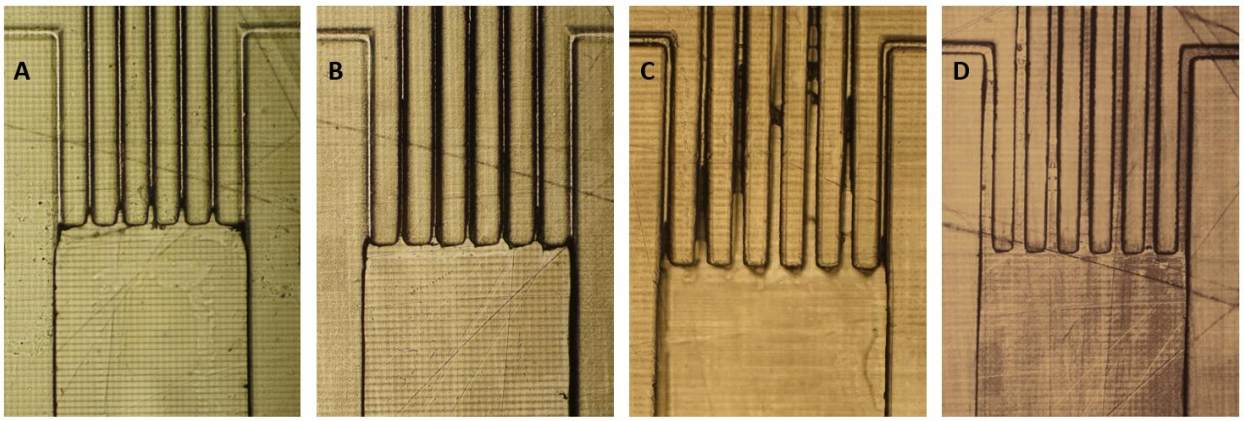

Figure 2.20. Results from printing 7-part gradient design in colorless, transparent resin using the photomask method. Various print settings and channel depths were explored during the optimization process, and the corresponding printing details and results are reported in Table 2.3. All micrographs were collected at 4X magnification.

The 7-part gradient photomask printing investigation provided insight into the effectiveness of this fabrication method for more complex designs and smaller channel dimensions. As experienced before, longer light exposure caused more unintended channel clogging (Figure 2.20 A-B). None of the settings used in this testing resulted in a functional

device due to channel blockages. One key factor explored in this work was the resulting channel depth. The 100 μm wide serpentine mixing channels were too narrow to assess with the profilometer stylus, but the observation channel and inlet reservoir provided alternative locations to measure. The results in Table 2.3 revealed that the physically measured channel depths were typically within 30 μm of the designed channel depth, except for the deepest dimension tested, 300 μm.

It has been theorized that there is a significance to the proportion the layer height is of the desired channel depth. The 20 μm layer height resulted in the most accurate results for the 200 μm channels and the furthest for the 300 μm with the 100 μm channels falling in between. The 25 μm layer height for the 50 μm channel depth was off by a larger amount. These print settings would have resulted in only two layers printed for the channels, as opposed to 10 for the 20 μm layers of the 200 μm channels. These findings contributed to a few potential conclusions: 1) the thickness of the photomask positioned below the resin vat contributed to errors in the printed channel depths, 2) the stepper motor of the resin 3D printer should be recalibrated regularly, and 3) a relationship exists between the set layer height and the desired channel depth to produce more accurate print dimensions, and further exploration is required if strict accuracy is a concern for future microfluidic designs.

Although this photomask method provided some promising results, there were a few key drawbacks to keep in mind. The researcher printing their microfluidic device would need to be present to pause the print at the correct layer to manually align the photomask. Additionally, the alignment of the photomask over the LCD screen would need to be more precise or refined from the current method to ensure print success. Further optimization of this photomask resin printing process would be needed to find compatible settings for the desired channel dimensions. Finally,

this method would require access to a high-resolution photoplotter or printer able to produce photolithography-quality photomasks, which would either increase the equipment costs or the time required to test designs due to outsourced photomask production.

A more straightforward option to improve printing capabilities would be to purchase a more advanced resin 3D printer. Within the past six years of working on this research project, multiple companies have consistently produced newer printers for purchase at the hobbyist price point. Improvements in LCD screens have resulted in lower achievable XY resolution than ever before. As newer printer models are brought to market, the cost of older models is continuously decreasing. One of the most significant improvements in the last few years was the release of DLP-based resin 3D printers for less than $500 USD. As described in section 1.4.2, the use of a projector, as an alternative to the LED array and LCD screen, offers sharper printed features, less variation in light intensity across the entire build area, and a longer lifespan for the light source. After employing the Elegoo Mars 4 DLP resin printer in this work, both print quality and consistency improved. This trend in commercial resin 3D printing will continue to provide more advanced printers to non-expert consumers for an affordable price.

2.3.4 Attempted device sealing methods

Multiple methods were tested for sealing the 3D-printed microfluidic devices. The results of these tests are discussed in the following sections.

2.3.4.1 Attachment to glass slides

Glass slides were selected as the first material to seal 3D-printed devices due to 1) the ability to perform fluorescence imaging through the glass, 2) the biocompatibility of glass, and 3) its common use with microfluidic devices. Based on the work of Gong *et al.*, a treatment solution of 2% 3-(trimethoxysilyl)propyl methacrylate in toluene was used to improve the adhesion of the

cured resin to glass.[103] Glass slides were soaked in the treatment solution for 2 hr and then stored in toluene before printing.

The treatment did improve attachment of the resin (Figure 2.21 A), however, the potential impacts on the biocompatibility of the treated glass were concerning. Fugitive glue, an adhesive that forms a non-permanent bond between two surfaces and often used to reversibly attach plastic cards to paper, was employed to attach treated glass slides to the build plate of the resin printer. This adhesive is also residue-free upon removal. A new z-axis zero location, or z = 0 setting, was programmed to accommodate the increased depth of the build plate as a result of the attached glass slide to avoid crashing the glass slide into the bottom of the resin vat. The fugitive glue was useful as a simple method to secure the glass slide to the build plate, but the flexible nature of the bond resulted in sporadic twisting of the glass slide during the printing process, misaligning the resin layers (Figure 2.21 B).

Initial tests to print enclosed channels directly onto glass caused a reduction in channel dimensions due to excess resin (Figure 2.21 C-D). This was concerning considering the test channels, 2 mm wide by 2 mm tall, were significantly larger than the desired microchannel dimensions of future devices, below 500 μm. All these results revealed that direct 3D printing onto glass slides would be unsuccessful for microfluidic device fabrication.

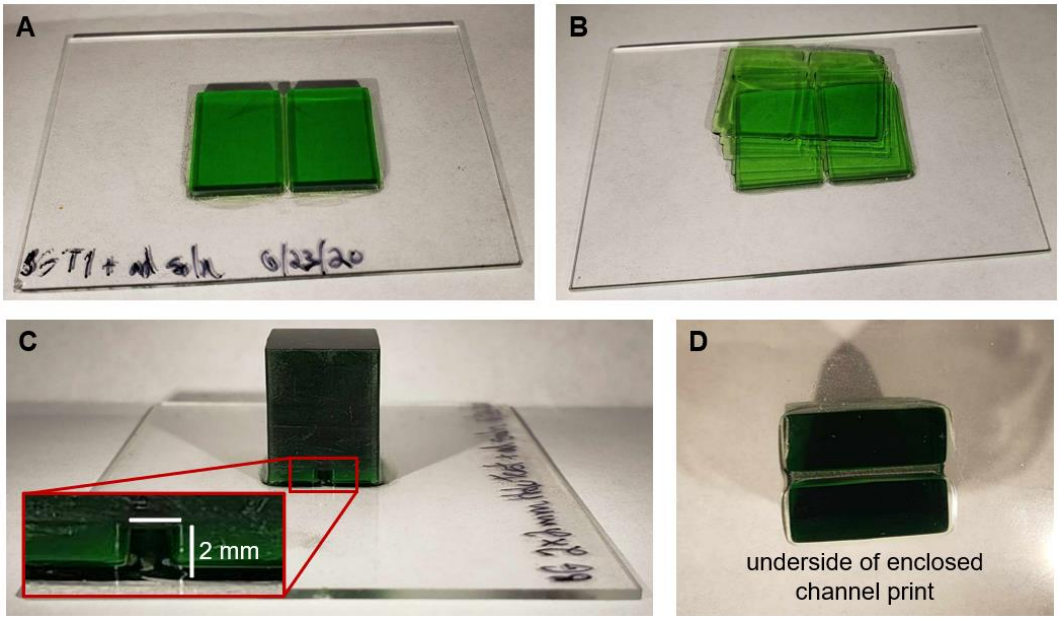

Figure 2.21. Results from direct resin 3D printing onto glass slides. The 2% 3-(trimethoxysilyl)propyl methacrylate in toluene treatment solution improved adhesion between the cured resin and glass. Although the attachment of the glass slide to the build plate using fugitive glue was successful, occasional twisting of the glass slide caused misaligned resin layers (B). Tests printing enclosed channels directly onto glass slides resulted in excess resin reducing the desired channel dimensions (C-D).

The next strategy for sealing printed devices onto glass was to utilize an optical adhesive from Norland Products. When selecting an adhesive, multiple factors were considered: 1) adhesion between glass and plastic, 2) method for curing, 3) biocompatibility, and 4) solvent compatibility, and NOA 86H was selected. It has excellent adhesion to glass and plastic, which is useful for this application. This adhesive can be cured using heat, in addition to UV light, which eliminated further degradation of the UV-sensitive resin. NOA 86H is reported as USP Class VI biocompatible and has a good range of solvent resistance once cured.[104]

After a thin layer of NOA 86H was coated onto the glass, a 3D-printed device was placed channel-side-down and clamped into place before cured in an oven between 80 and 100 °C. Although previous temperature exposure tests demonstrated fairly significant temperature resistance for the cured resin up to 100 °C, the procedure resulted in extensive cracking through

the resin devices (Figure 2.22 A). It was theorized that the increased thickness of the printed devices, 6.5 mm compared to the 2.5 mm thick temperature test prints, amplified the impact of thermal expansion. This expansion of the resin material and/ or the release of volatile species within the cured resin, as a result of heating, caused the cracking between layers of the print. Further bake temperature tests on printed devices, without the presence of NOA 86H or glass slides, were completed. When printed devices were placed in an oven preheated to 80 °C, damage to the devices occurred within 6 min (Figure 2.22 B). Additionally, slowly ramping the oven temperature from 35 to 80 °C over 100 min also resulted in device damage (Figure 2.22 C). Other tests utilized hot plates to determine if a more open-air baking environment would reduce damage. Further temperature experiments were completed on devices that were not subject to the standard post-print cure to test if a more pliable polymer would respond better to baking. All examined conditions resulted in cracked or chipped devices.

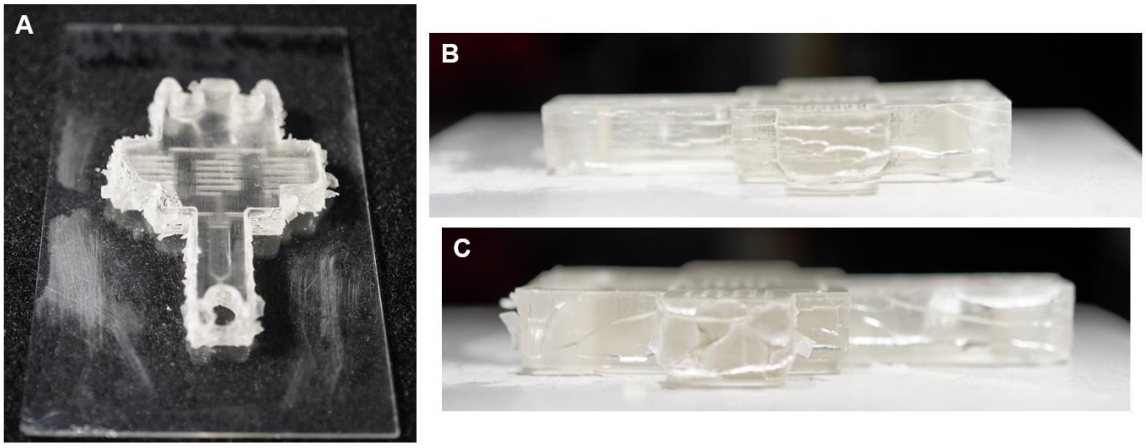

Figure 2.22. Exposure to elevated temperatures while curing NOA 86H resulted in severe damage to the resin material. Within 6 min, exposure to 80 °C resulted in cracking between cured resin layers (B). Slowly ramping the oven temperature from 35 to 80 °C over 100 min also contributed to cracking as well (C).

Since the minimum temperature required to cure NOA 86H is 80 °C, and using additional UV light to cure the adhesive would contribute to resin degradation, the strategy of using optical adhesive to bond 3D-printed devices to glass slides was determined to be an unviable option.

A thin layer of PDMS was also tested to seal devices onto a glass slide. PDMS was selected to act as a more flexible adhesive between the rigid glass and resin. The optical transparency and clarity of PDMS would also allow for imaging. Various baking and sealing procedures were tested but resulted in unsuccessful attachment. To avoid uncured PDMS clogging device channels, the layer had to be almost completely crosslinked from the bake. This resulted in a less malleable PDMS consistency which did not bond well to the devices. Additionally, if the PDMS was not cooled before coming into contact with the 3D-printed device, the range of temperatures would cause the resin to expand and contract and often release from the PDMS. Clamping the device into place also failed to create a lasting seal for the devices. At this point, it was evident that attempting to seal two rigid materials together, even with a more flexible layer in between, was an ineffective strategy for this work, and a more creative alternative would need to be explored.

2.3.4.2 Pressure-based device holder

To overcome the previous sealing limitations, a device holder, which would provide physical pressure to seal a 3D-printed device to a thin sheet of PDMS over a glass slide, was developed (Figure 2.23). The motivation was that constant pressure would improve the seal and keep the resin from releasing from the PDMS, as was observed in previous tests. In general, maintaining sufficient pressure, especially at the middle of devices, was often difficult due to the flexibility of the PETG frames (Figure 2.23 E). This caused consistent leaking when filling devices. Brass support bars with drilled through holes were implemented into the holder design. These were positioned across the upper frame, aligned with the hex screws, and tightened into place using the wing nuts to reinforce the structure, reduce warping, and increase the applied pressure in the middle of devices, however leaking still persisted.

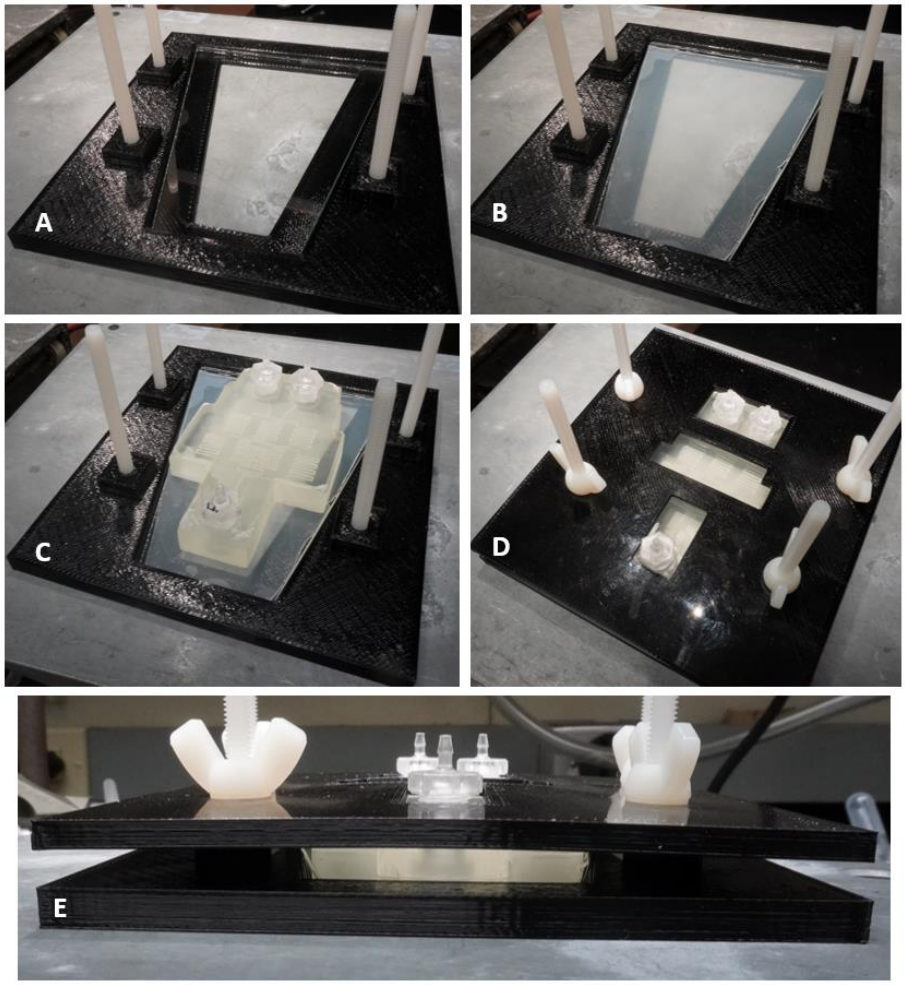

Figure 2.23. Design of a device holder to apply constant pressure to seal 3D-printed devices to a PDMS slab. A plate of glass was custom cut to fit in the lower frame (A). A slab of PDMS was placed over the glass (B). Printed devices were placed onto the PDMS (C), and the upper frame was clamped into place using wing nuts (D, E). Unfortunately, many limitations of this device holder prevented it from being a viable option for device sealing.

As described previously, unchanged devices and polished devices were examined using a profilometer. Polishing the channel side of the devices removed larger defects in the overall surface smoothness. This result was considered as a way to improve device sealing. Although polished devices initially formed and retained a better seal within the device holder, leaking was still observed over time. Besides the listed limitations, reliance on a device holder would require a separate design for each new iteration of the device, greatly reducing the practicality and efficiency of this sealing method.

2.3.4.3 Adhesive on transparency film

The next iteration of sealing 3D-printed devices involved a combination of adhesives and a more flexible material, transparency film. Transparency film is typically made of polyester or cellulose acetate, and this material was selected due to its low cost, optical transparency, and flexibility. To seal the 3D-printed device to the transparency film, a PVA adhesive was used. PVA-based adhesives are water-soluble, meaning uncured adhesive could be rinsed from the microchannels using a gentle solvent resulting in little impact on biocompatibility. Elmer's Glue-All® multi-purpose glue was selected due to its availability for low-cost purchase, clear finish when dry, non-toxic formula, and the variety of surfaces it can bind together. To utilize both a water-soluble adhesive and improve the seal strength, a cyanoacrylate glue was applied to the edges of the 3D-printed device before placement on the transparency. Cyanoacrylate adhesives, marketed as super glues, are often water-resistant and set faster than PVA adhesives. This perimeter would reinforce the seal and help keep the device in place during the clamping and water flush. Loctite Brush-on Super Glue was selected for this application due to its easy and controllable application process.

Although this sealing method was simple and provided a strong enough seal to successfully fill the devices (Figure 2.24 A-C), there were some flaws. The most critical issue was the accumulation of glue residue on the ceiling of the microfluidic channels. Instead of fully removing the water-soluble adhesive, the water flush adhered glue to the top of the channels (Figure 2.24 C-D). The adhesive buildup did not cause observable disruption to gradient formation, but the possible impacts on cells cultured within the devices was a potential concern.

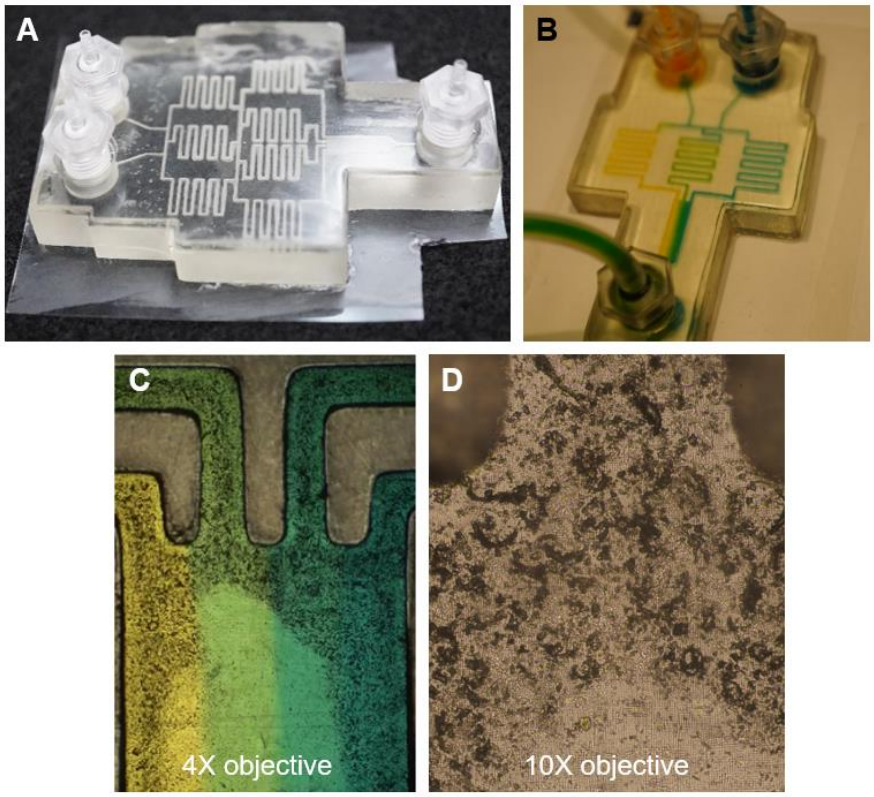

Figure 2.24. PVA and cyanoacrylate adhesives were used in combination to seal 3D-printed devices onto transparency film (A). This seal was strong enough to fill the devices and form gradients using syringe pump (B-C). The unsuccessful removal of the PVA adhesive resulted in an accumulation of glue debris on the ceiling of the microchannels (C-D).

Additionally, although liquid could flow through the channels, a full 24 hr were required to fully cure the adhesives, significantly lengthening fabrication time. Sealed devices also necessitated delicate handling to avoid bending the transparency film and breaking the adhesive bond. Finally, this method resulted in an irreversible seal reducing how reusable these devices were. Based on these results, it was apparent that incorporating a flexible material into the device sealing process was valuable, and the search for an alternative, flexible sealing method continued.

2.3.5 3M™ microfluidic tapes

In order to maintain overall simplicity in device fabrication, and flexibility of the selected sealing materials, a line of tapes developed by 3M™ were explored as a new method of device

sealing. Tape is a very user-friendly option for channel sealing due to the simplicity of using it. Once cut to an appropriate size and the release liner is removed, the tape can be easily applied to the device surface. The flexibility of the tape enables slow and deliberate application from one edge to the other. The potential to collapse the tape into wider microfluidic channels is one of the few concerns during the tape sealing process. When considering microfluidics for research, the ability to clean and reuse devices can be a significant benefit, decreasing the amount of waste and the time devoted to device fabrication. This often necessitates a reversible sealing method, which can be uncommon for many traditional fabrication techniques. Utilizing tape, depending on the product selected, can enable a strong but reversible seal. Most importantly, these 3M™ tapes have been designed with desirable characteristics such as high optical clarity, minimal autofluorescence, low extractables, and low cytotoxicity.[105-107] Besides these qualities, and overall ease of use during the fabrication process, there is precedent for utilizing tape for bioanalytical applications. Tape has been employed before with microfluidic devices, some of which were 3D-printed, including this specific product line from 3M™.[108-112] Based on these factors, the 3M™ tapes were selected as a simple approach for reversible channel sealing.

2.3.5.1 Strength of tape seal

The two tapes selected for initial experiments were 9793R and 9795R. While both tapes used a polyolefin backing material, 9793R utilized a pressure-sensitive acrylate adhesive, and 9795R utilized a delayed-tack silicone acrylic adhesive.[105, 107] Tests with multiple types of microfluidic devices were used to determine the strength of the tape seal on different materials including PDMS, 3D-printed resin, and etched glass. For each experiment, a programmable syringe pump was used to provide constant flow into the straight-channel tape-sealed devices. A clamp was placed on the outlet tubing to allow for pressure to build up as the device filled with

water. An in-line pressure transmitter was used to monitor pressure within the channels in real-time during experiments.

Both microfluidic tapes were able to maintain a seal at higher internal pressures than the PDMS device reversibly sealed on a glass slide. Considerably high flowrates were required to cause seal failure for the tape experiments, maximum 50 mL/hr, compared to the PDMS and glass slide experiments, maximum 5.5 mL/hr. The fittings connecting the tubing to the 3D-printed and etched glass devices required a water-resistant adhesive, Clear Gorilla Glue, to prevent leaking and test the strength of the tape seal alone. Additionally, the flexibility of the tapes allowed the fluid to swell around the channels before rupturing the seal (Figure 2.25).

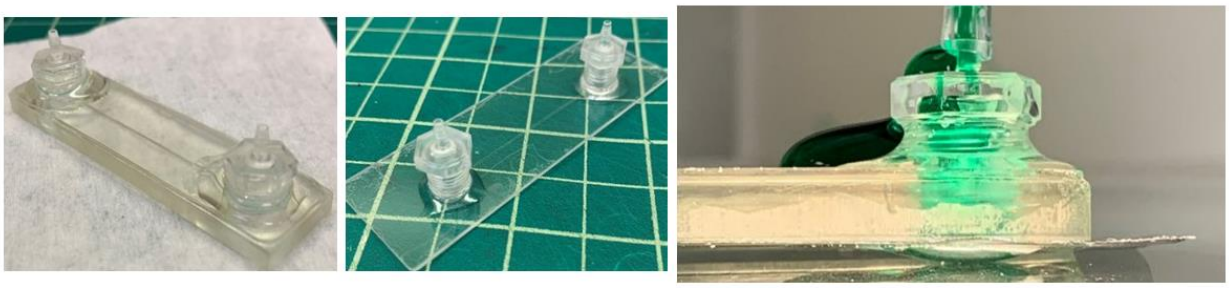

Figure 2.25. Water-resistant adhesive was used to seal fittings for 3D-printed (left) and etched-glass devices (middle) to strengthen that interface for testing of the two kinds of microfluidic tapes. During some testing, the strength of the tape seal and the flexibility of the material resulted in expanded pools of liquid before the seal was finally compromised (right).

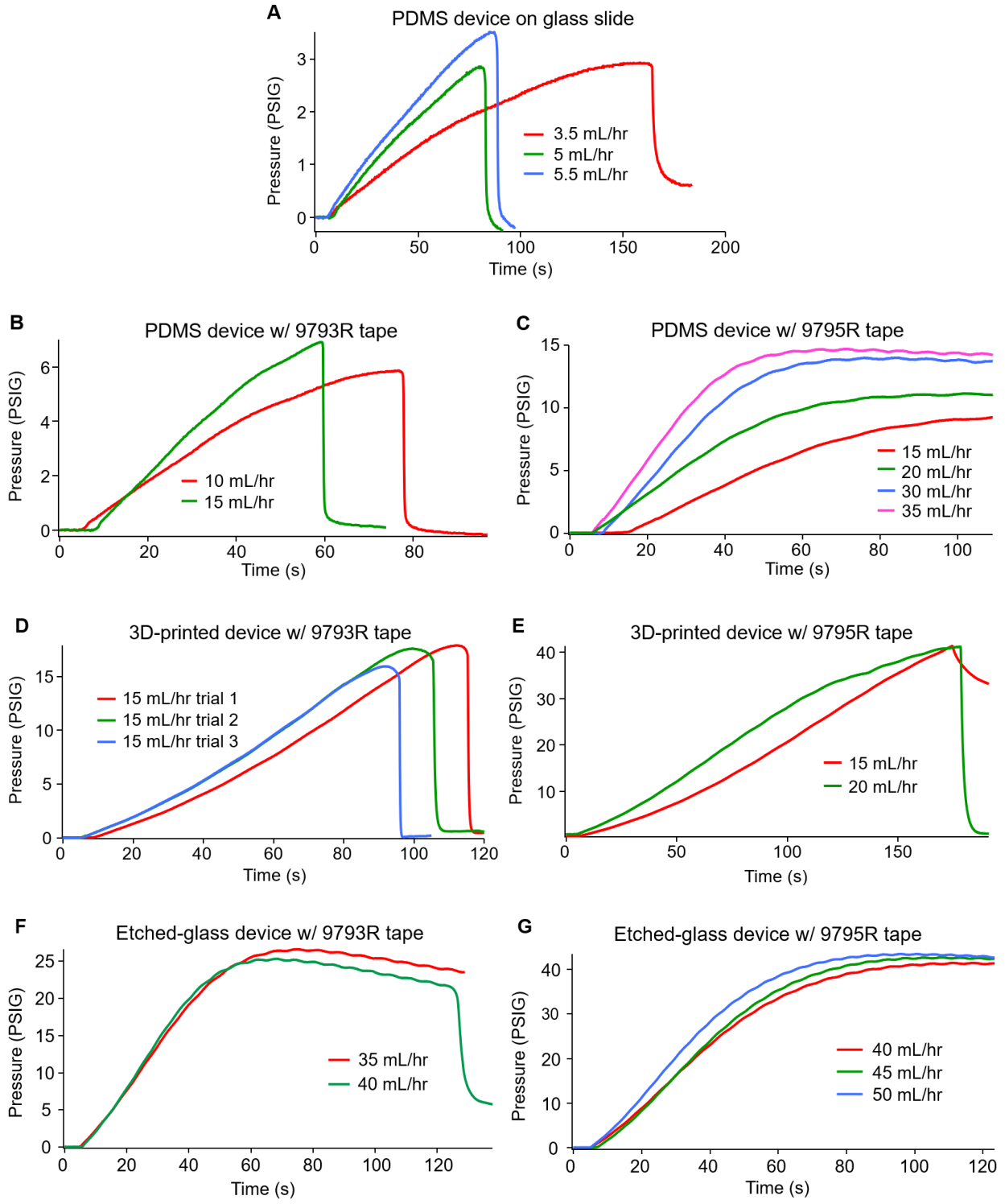

Figure 2.26. The microfluidic tapes could withstand far higher internal pressure than the PDMS devices reversibly sealed on glass slides (A). For all three types of devices, PDMS, resin 3D-printed, and etched-glass, the 9795R tape (C, E, G) could withstand higher pressures than the 9793R tape (B, D, F). During some experiments, the 9795R tape failed to rupture under the investigated flowrates (C, G).

The 9795R tape maintained its seal under far higher channel pressures for all three types of microfluidic devices investigated and even failed to rupture during multiple tests (Figure 2.26). Based on these results, the 9795R tape was selected for all future experiments.

2.3.5.2 Attempted adhesive removal

By utilizing microfluidic tape to seal devices, the adhesive layer remains exposed within the channels. This could potentially contribute to issues in stable gradient formation or cell attachment. To minimize these issues, attempts were made to remove the exposed adhesive layer within the channels by dissolving it in an appropriate solvent. Initially, a 1 M solution of sodium hydroxide in water was tested as a removal solution. The sodium hydroxide was unsuccessful at removing the exposed adhesive over a 1-hr test soak, even when sonication was included during the soaking procedure. There were additional concerns that a sufficiently strong solution of sodium hydroxide would not only remove the adhesive but degrade the cured resin material.

After further communication with representatives from 3M™, a 50/50 blend of heptane and ethyl acetate was recommended for adhesive removal. During preliminary testing, individual pieces of tape submerged in the removal mixture did result in adhesive removal. Tests showed the adhesive layer would fully detach from the backing material leaving the two parts isolated but intact. Simple 3D-printed devices sealed with 9795R tape were filled with the adhesive removal mixture, and the recorded results showed the adhesive layer beginning to peel up from the backing. To improve the chance of adhesive dissolution, sonication was included in the soak procedure, but this still resulted in only separation between the backing and adhesive (Figure 2.27).

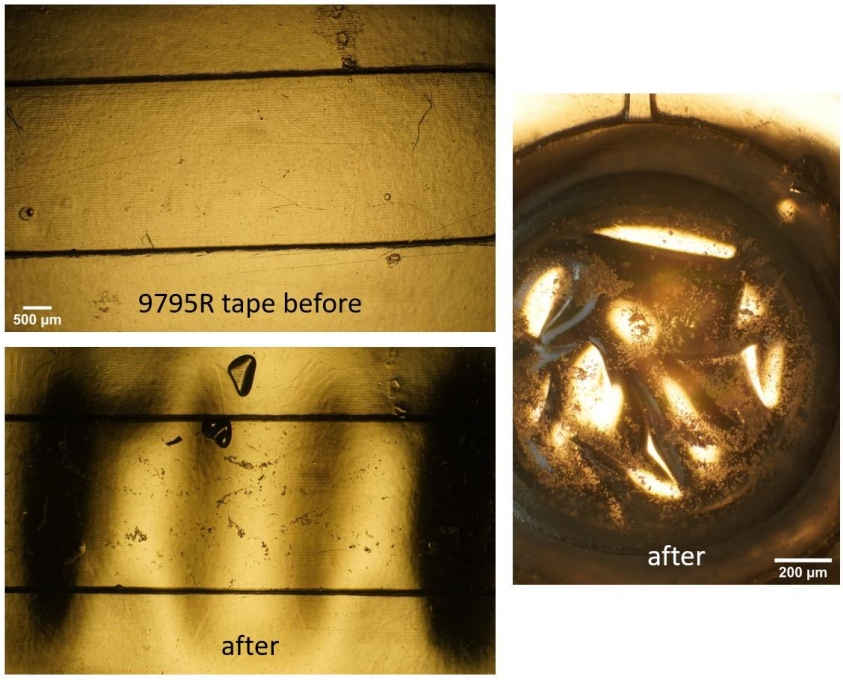

Figure 2.27. A 50/50 mixture of ethyl acetate and n-heptane was used to remove the exposed adhesive within the microfluidic channels. Tape-sealed devices were filled with the removal mixture and sonicated for 30 min. Instead of dissolving the adhesive into the solution, the entire adhesive layer sloughed off the tape backing causing puckering of the tape surface (left bottom) and accumulation of adhesive clogging within the channels (right).

This ineffective removal of the exposed adhesive within the microchannels meant the potential impacts of the native adhesive surface on cell growth in addition to alternative treatment options needed to be explored.

2.3.5.3 Adhesive surface treatment procedure

By utilizing tape to seal 3D-printed microfluidic devices, adhesive is exposed at the bottom of the channels where adherent cells would attach. Initial tests compared U-87 growth on the untreated adhesive surface to growth in a polystyrene well plate. Following cell seeding, images collected at various time intervals were used to assess cell morphology, attachment, and viability over time. U-87 cells cultured in the well plate exhibited standard stretched morphology and strong attachment while those on the untreated adhesive remained spherical, clumped in dense groupings, and detached from the surface (Figure 2.28).

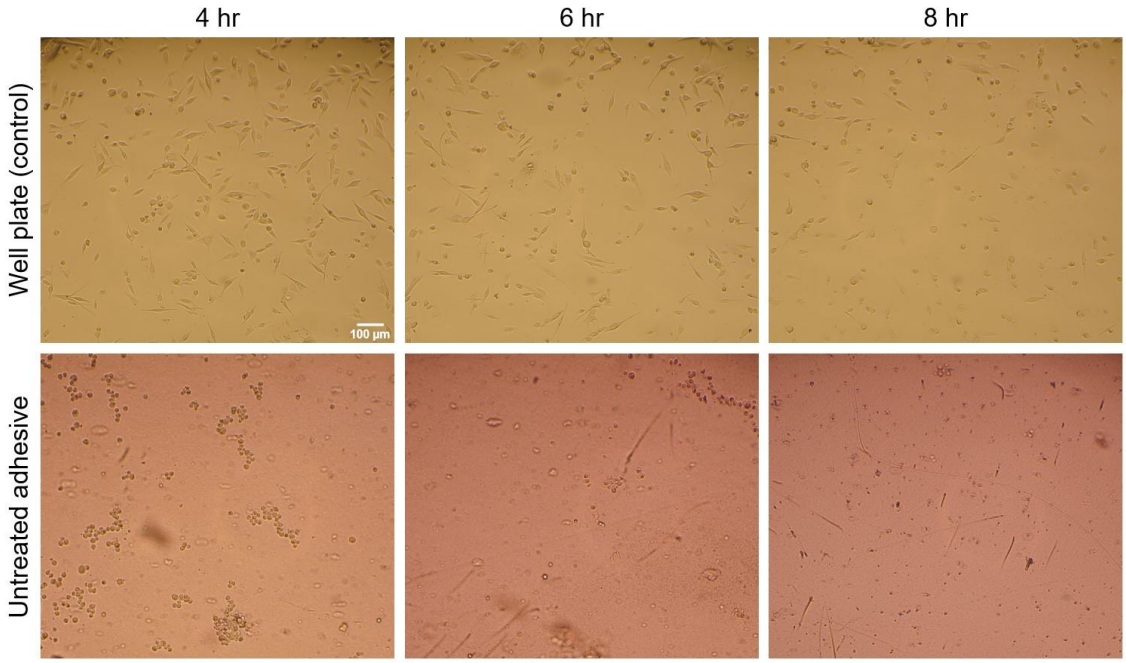

Figure 2.28. Comparison of U-87 growth between a polystyrene 96-well plate (upper) and the untreated adhesive surface of the 9795R tape (lower). Over time, a distinct difference in cell morphology was evident. U-87 cells on the adhesive surface were more spherical, clumped together, and detached from the surface throughout the experiment compared to the stretched morphology and consistent attachment in the well plate.

These results highlighted the need for a surface treatment to improve the exposed adhesive surface for adherent tissue culture.

PDL and HA were initially investigated for coating the tape adhesive due to the frequent usage of PDL in tissue culture, the importance of HA in the ECM, and the usage of HA in biocompatible coatings.[113-116] Working concentrations of 50 µg/mL for PDL and 1 mg/mL for HA were determined based on experimental optimization with the U-87 cell line to provide the most comparably standard cell morphology and least amount of cell clumping. The stability of HA solutions has been maintained up to 60 days when stored under refrigeration, and solutions of PDL are stable up to 2 years under refrigeration.[117, 118] Individually, both the HA-PBS and PDL-PBS solutions improved cell attachment and morphology compared to the untreated

adhesive surface, and, by 4 hr after cell seeding, more comparable growth to the polystyrene well plate was observed (Figure 2.29).

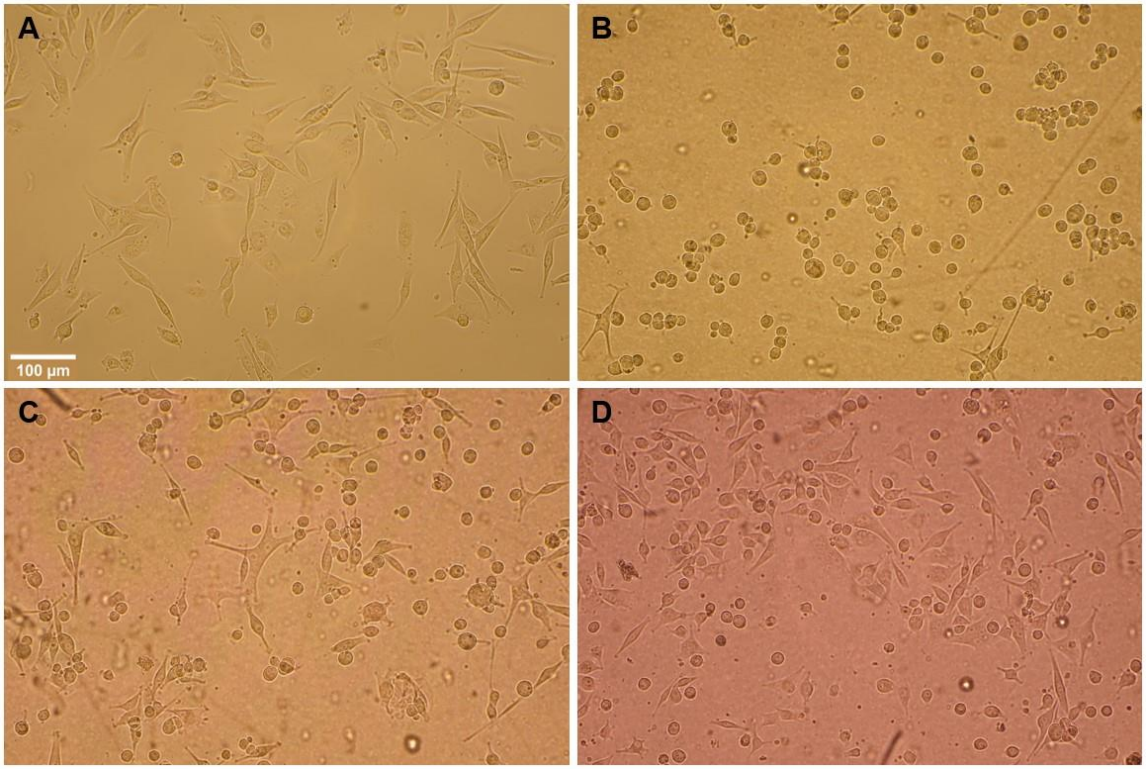

Figure 2.29. U-87 cells grown on polystyrene (A), untreated 9795R tape (B), HA-PBS treated 9795R tape (C), and PDL-PBS treated 9795R tape (D) 4 hr after cell seeding.

By combining HA and PDL into one treatment solution, a more stretched morphology and less clumped distribution of cells was achieved. Long-term tests between U-87 cells in a well plate and on the HA+PDL in PBS-treated adhesive surface demonstrated more similar growth and viability achieved by 3-6 hr after cell seeding as well as maintained morphology and viability up to 24 hr (Figure 2.30).

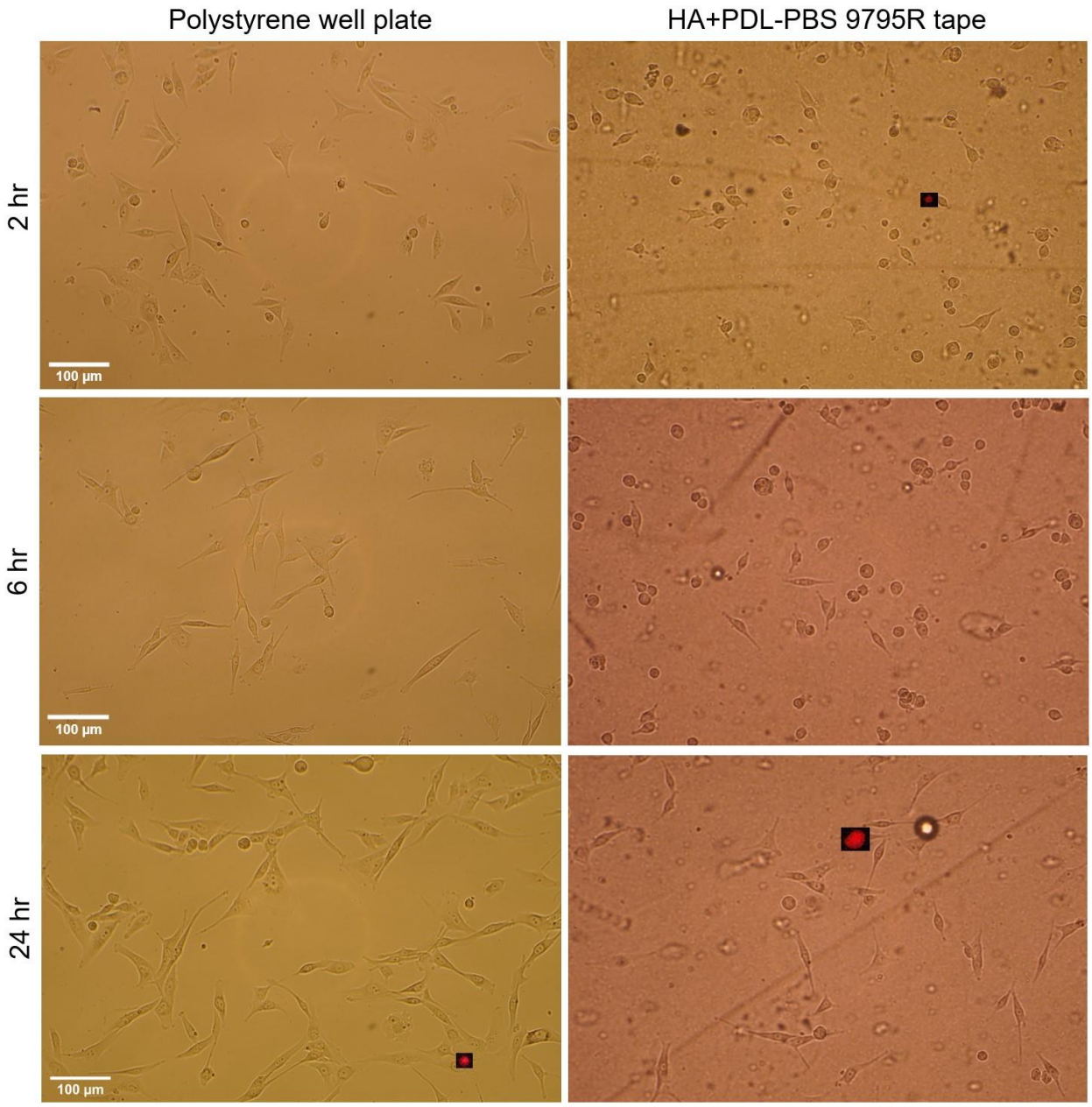

Figure 2.30. U-87 cells grown on polystyrene well plates compared to the HA+PDL-PBS treated adhesive surface. At 2 hr after cell seeding, a significant difference in morphology is observed (A and B). By 6 hr, more cells on the treated tape have stretched (D). At 24 hr, overall morphology is significantly more comparable between the two conditions (E and F). Similar cell viability was observed throughout the experiment using PI staining, and each dead cell was overlayed on the corresponding brightfield images (red).

This combination of HA and PDL in PBS was selected as the treatment solution for all future experiments involving cells cultured on the 9795R adhesive surface. An overnight soak achieved substantial improvement in the development of adherent cell culture on the exposed adhesive.

2.4 Conclusions

The resin 3D printing process was intensely investigated as a fabrication method for gradient-producing microfluidics and cell studies. Although similar work has been previously published, such a thorough exploration of print settings and processing, material properties, and microfluidic fabrication has not been reported for products at such an accessible level and price point.[79, 80, 93, 95, 101, 119] Considerable progress was made towards a 3D-printed microfluidic device for the study of GBM migration, while some key obstacles remain.

The resin 3D printers used in this work provided acceptable print quality and resolution upon extensive optimization. Many of the resin properties were more favorable for the future work than expected, such as the limited surface roughness and low autofluorescence and susceptibility to staining by fluorescent dyes. The lack of elevated temperature resistance was a more significant issue and contributed to limitations in device sealing methods. Initial biocompatibility testing of the cured resin material revealed negligible levels of leachable chemical species, but the importance of this topic should not be overlooked for future cell experiments and could be further analyzed using a method like LCMS. A significant variety of sealing methods were investigated incorporating a range of materials. The 3M™ tape provided both a strong and reversible seal, and a treatment method for the adhesive surface was developed to encourage healthy cell attachment and growth. Although tape sealing resulted in many positive outcomes, implementing this device sealing method for more complex gradient designs was challenging. The same leak issues experienced when testing other sealing methods returned for the gradient serpentine channels of 3D-printed devices. Due to these persistent complications in the device development process, an alternative strategy for device fabrication needed to be explored.

Chapter 3 - Development of a PDMS microfluidic device formed using resin 3D-printed molds

3.1 Introduction

The implementation issues explained previously inspired the change to using 3D-printed molds to fabricate PDMS devices. Soft lithography itself is a relatively low-cost microfluidic fabrication method, but the most costly part is the photolithography equipment used to produce molds. Utilizing resin 3D printing to make molds instead removes many of the limitations related to PDMS device fabrication, especially related to cost. The time and expertise required for making molds with resin printing is also significantly less than photolithography using silicon wafers and photoresists. As presented in Chapter 2, accessible resin 3D printers and resins must be assessed to ensure this is an appropriate fabrication method for microfluidic cell studies. In this chapter, the process of printing positive features, as opposed to previously explored negative features, molding PDMS devices from cured resin, and the development of an environment favorable to tissue culture outside of an incubator are investigated. This work highlights an alternative fabrication approach for soft lithography and an initial example of how this fabrication technique could be applied for microfluidic cell studies.

3.2 Materials and methods

3.2.1 Reagents, materials, equipment, and software

A wide variety of products were used for this research, the details of which are provided below, in Chapter 2, or in the Appendices.

3.2.1.1 Resin 3D printing and testing

Many of the product descriptions for resin 3D printing and processing from Chapter 2 are still applicable for this work. An additional 8K standard photopolymer resin in Space Grey was also purchased from Elegoo through Amazon (Seattle, WA, USA).

3.2.1.2 PDMS baking and assessment

The products previously used in PDMS soft lithography described in Chapter 2 were used in these studies. Scotch double-sided tape was purchased through Amazon (Seattle, WA, USA). A single-axis translation stage was purchased from Thorlabs (Newton, NJ, USA). A fiber optic dual gooseneck illuminator, xylenes, and a stainless-steel lab lift were purchased from Thermo Fisher Scientific (Waltham, MA, USA). Hexamethyldisilazane (HMDS) was purchased from Sigma Aldrich (St. Louis, MO, USA).

3.2.1.3 Tissue culture

The tissue culture products and protocols for U-87 cells provided in Chapter 2 and Appendix B were used in this work. Annexin V CF350, the corresponding 5X binding buffer solution, and NucSpot 568/580 were purchased from Biotium Inc. (Fremont, CA, USA). Dimethylsulfoxide (DMSO) was purchased from American Type Culture Collection (Manassas, VA, USA). 200 proof ethanol was purchased from Decon Labs Inc. (King of Prussia, PA, USA). 3 mL syringes were purchased from BD (Franklin Lakes, NJ, USA). Masterflex polycarbonate 4-way stopcocks were purchased from Cole-Parmer (Vernon Hills, IL, USA). A CO_2 controller for miniature incubators (CO2-MI), CO_2 sensor upgrade for miniature incubators (CO2-UP), miniature incubator with heated base (TC-MIW), heated lid for miniature incubator (TC-MWPL), 9.5 mm spacer to elevate incubator cover (TC-I-E), and 2-channel temperature controller (TC-1-100-I) were purchased from Bioscience Tools (Highland, CA, USA) to provide

a controllable tissue environment for time-lapse imaging experiments. An additional CO_2 sensor, the S8 5% CO2 Sensor Development Kit, was purchased from CO2Meter.com (Ormond Beach, FL, USA). Carbon dioxide, bone dry 99.8%, was purchased from Matheson Tri-Gas Inc. (Manhattan, KS, USA). A 10 x 5 cm electric heating pad (product 1481) was purchased from Adafruit Industries (New York, NY, USA) and powered by a B&K Precision 1761 DC power supply (Yorba Linda, CA, USA). An Extech EA15 Type K thermocouple and thermometer were purchased through Amazon (Seattle, WA, USA),

3.2.1.4 Imaging equipment

In addition to the imaging equipment described in Chapter 2, the Nikon UV-2E/C filter from Nikon Instruments Inc. (Melville, NY, USA) and the SEL30M35 30 mm f/3.5 e-mount Macro Fixed Lens from Sony, purchased through Amazon (Seattle, WA, USA), were used.

3.2.1.5 Other laboratory equipment

Reference Chapter 2 for further details about the additional laboratory equipment utilized during this work.

3.2.2 Device fabrication procedures

Both the Mars 3 Pro 4K and Mars 4 DLP resin 3D printers were used to make the molds for PDMS soft lithography. Details of the printing parameters are provided in Appendix A. The standard processing was followed including the IPA rinse and sonication, drying with compressed air, and post-print cure. To confirm the actual printed feature heights, an XP-2 profiler was used, and protocol details are included in Appendix C. Some mold prints were subject to sterilization and extraction procedures. The selected prints were sterilized with 70% ethanol (EtOH), transferred into the biosafety cabinet for 20 min of UV sterilization, flipping halfway through, and placed in sterile petri dishes. Enough sterile 1X PBS was pipetted into each

petri dish to fully submerge the print. Each treatment vessel was then stored in an incubator at 37 °C for 24 hr. Following the PBS soak, all petri dishes were transferred to the biosafety cabinet, the PBS was removed via aspiration, and resin molds were left to dry in the biosafety cabinet before stored until use.

The PDMS bake procedure was optimized. Simple and 4-part gradient design molds were used for these experiments (Figure 3.1). Molds were prepared for baking by first using Scotch tape to remove any debris. Plexiglass frames were secured to aluminum baking plates with double-sided tape at each corner and weighed down for at least 15 min before the cleaned mold was positioned in the middle. The selected PDMS mixtures were thoroughly mixed and degassed in a vacuum desiccator, poured over the chosen resin mold, and placed in an oven at the designated temperature for varying lengths of time. After the specified bake length, the device was cooled to room temperature before the frame was removed and the PDMS was peeled from the resin mold. A more detailed protocol is provided in Appendix C.

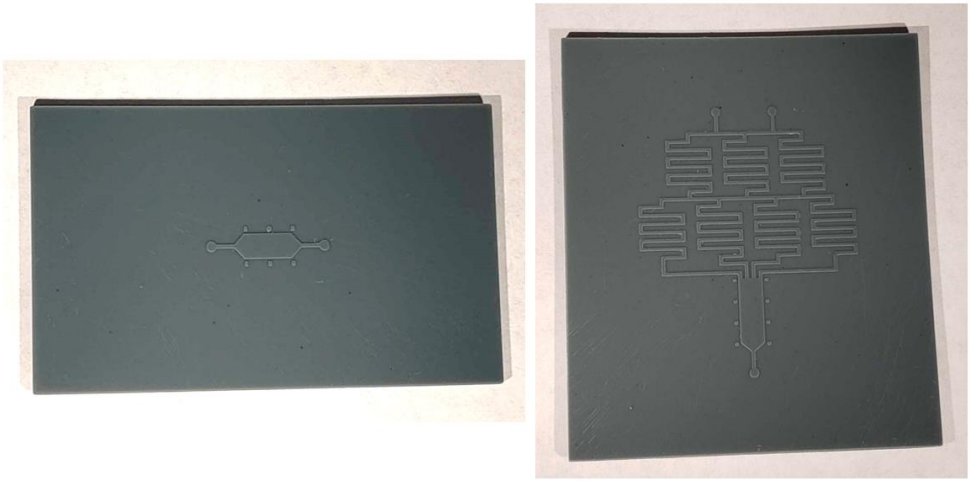

Figure 3.1. Sample simple (left) and 4-part gradient (right) molds 3D-printed in resin.

Initial tests, using simple molds and PDMS mixtures of 10:1 elastomer base and curing agent, were completed at 40 °C for 15 and 17 hr. 5:1 PDMS was also tested using simple molds at 40 °C for 2, 3, 4, 6, 8, 15, and 17 hr. When testing with the 4-part gradient molds, a mixture of

HMDS and xylenes (1:1 v/v) was investigated as a releasing agent for the PDMS peeling process by pipetting 150 μL of the mixture onto the molds and using the spin coater at 1000 rpm for 32 s to form a smooth layer coating the mold before pouring PDMS. The room temperature and humidity were monitored during these experiments.

To assess the potential impacts of repeat exposure to 50 °C for PDMS baking, both the resin mold and PDMS surface were monitored using contact angle measurements. Images were collected using the Sony Alpha a6400 camera with a macro lens. The in-house contact angle imaging setup used a single-axis translation stage to align the camera with a lab lift, both secured to an optical table. One end of a cardboard box was cut away and a sheet of white printer paper was secured over the opening. The opposite end was trimmed to fit around the camera setup. A fiber optic dual gooseneck illuminator was used to light the imaging area from behind with the paper acting as a light diffuser. Each sample was placed on the lab lift and adjusted to the appropriate height, depending on sample thickness. 5 μL of ultrapure water were pipetted on the sample surface, keeping the tip elevated above to allow the droplet to fall a short distance to the sample. A photo of the in-focus droplet was taken after approximately 30 s. The procedure was repeated three times for each surface tested. Initial images of the unused resin mold surface and resin-free PDMS surface were used to establish native results. After each repeat baking, five in total, the PDMS was peeled from the mold. The resin and PDMS surfaces, which were in contact during the bake, were assessed with this method. All images were cropped, rotated 180 degrees to orient the droplet upside down, and analyzed using the Contact Angle plugin in ImageJ. The Manual Points Procedure was used to determine the contact angle for each image based on the reported Theta C value.

Inlet and outlet reservoirs were punched into the PDMS using a blunted 23-gauge needle. As described in Chapter 2, 9795R tape was used to seal the PDMS devices. Since the PDMS devices are a flexible elastomer, 2 min of manual pressure was not used to help seal the tape to the PDMS. Extra caution was used to avoid collapsing the tape into the channels. Sealed devices were set to rest for at least 4 hr before use.

3.2.3 Establishing tissue culture environment for future cell studies

Four separate stains were used to track cell position, morphology, and viability. Detailed protocols for each fluorescent staining experiment can be found in Appendix B. Initial tests to establish a working concentration of PI were completed with U-87 cells in 96-well plates. Approximately 25, 50, 75, and 100 μg/mL PI staining solutions were tested by diluting a stock solution of 1000 μg/mL PI stain. Images were collected on the Nikon Eclipse TE2000-U inverted microscope using the Sony Alpha a6400 camera, Nikon G-2A filter cube, and the X-Cite 120 Fluorescence Illumination System. A description of the working volumes is summarized below in Table 3.1. To ensure cell death, media was removed from some wells and replaced with the equivalent volume of 70% EtOH before imaging. Image processing was completed on ImageJ.

Table 3.1. Volumes used in 96-well plate PI concentration testing.

Vol DMEM and U-87 cell suspension (μL)	Vol DMEM (μL)	Vol U-87 cell suspension (μL)	Vol 1000 μg/mL PI stock (μL)	Resulting [PI] (μg/mL)
157	149	8	18	102.9
162	154	8	13	74.3
166	158	8	9	51.4
171	163	8	4	22.9

5-chloromethylfluorescein diacetate (CMFDA) was tested as a fluorescent stain to track cell position and morphology. Based on provided product information, a procedure was developed to stain the U-87 cells. 1 mg CMFDA was dissolved in 215.1 μL of DMSO to create a 10 mM stock solution. Aliquots were diluted further in serum-free DMEM to create a range of working concentrations to test (Table 3.2). These CMFDA solutions were stored in 15 mL conical tubes and frozen until use.

Table 3.2. Volumes used to create a range of concentrations for working CMFDA staining solutions.

[CMFDA] working solution (μM)	Vol 10 mM CMFDA stock solution (μL)	Vol serum-free DMEM (μL)
0.5	0.15	2999.85
1.0	0.3	2999.7
5.0	1.5	2998.5
10.0	3.0	2997.0
15.0	4.5	2995.5
20.0	6.0	2994.0
25.0	7.5	2992.5

The selected CMFDA working solution was placed in a water bath set to 37 °C. Once fully thawed, the DMEM was removed from the chosen T75 flask of U-87 cells. The warmed CMFDA working solution was added to the flask, and the cells were incubated in the stain for 30 min. The staining solution was then removed from the flask and the standard trypsinization procedure was followed to provide a cell suspension to be used for experiments. 100 μL of CMFDA-stained cell suspension was transferred into 96 well-plates. Images were collected on the Nikon Eclipse TE2000-U inverted microscope using the Sony Alpha a6400 camera, Nikon

B-2A filter cube, and the X-Cite 120 Fluorescence Illumination System. Image processing was completed using ImageJ.

The Annexin V CF350 conjugate was selected as the third fluorescent stain to simultaneously monitor cell health. As described in the product documentation, the 5X binding buffer solution was diluted to 1X using ultrapure water. Varying volumes of the Annexin V CF350 were tested to determine an appropriate working concentration for the U-87 cells, as shown in Table 3.3 below. Following CMFDA staining and standard trypsinization, 30 μL of U-87 cell suspension was added to 170 μL of DMEM in a 96-well plate. Two rows of 6 wells were prepared.

Table 3.3. Volumes used in 96-well plate for Annexin V CF350 concentration testing.

[Annexin V] working solution (μg/mL)	Vol Annexin V stock solution (μL)	Vol 1X binding buffer (μL)
0.25	1.0	199.0
0.5	2.0	198.0
1.0	4.0	196.0
1.5	6.0	194.0
2.0	8.0	192.0
2.5	10.0	190.0

After cells attached to the growth surface within the wells, the media was carefully removed before 50 μL of 70% EtOH were added, exposed to the cells for at least 3 min, and then removed. The first set of wells were subjected to two 100 μL rinses of 1X binding buffer solution before adding the desired volumes of both binding buffer and Annexin V stock solution. The range of binding buffer volumes were added to the second set of wells before the corresponding

volumes of Annexin V stock solution without the rinsing steps. The cells were incubated at room temperature in the dark for 15 min. The first set of wells were rinsed again with binding buffer before both sets of wells were imaged using the Sony Alpha a6400 camera on the Nikon Eclipse TE2000-U inverted microscope with the UV-2E/C filter cube and the X-Cite 120 Fluorescence Illumination System. Image processing was completed using ImageJ.

To test these three fluorescent stains together, further 96-well plate experiments were completed. U-87 cells were stained with CMFDA following previously described protocol. Two sets of 5 wells were seeded with 15 μL cell suspension into 85 μL DMEM and stored in the incubator for 2 hr. Two conditions were tested: 1) the addition of 22 μL of 1000 μg/mL PI stain solution, and 2) replacement of the Annexin V staining solution with 78 μL DMEM before the addition of 22 μL of PI stain. Once all three stains were added, images were collected at 2, 4, and 5.5 hr after cell seeding. 50 μL of 70% EtOH were added to the 5.5 hr wells before Annexin staining. Imaging was completed on the Nikon Eclipse TE2000-U inverted microscope using the Sony Alpha a6400 camera, B-2A, G-2A, and UV-2E/C filter cubes, and the X-Cite 120 Fluorescence Illumination System. Image processing was completed using ImageJ.

Direct, manual injection via syringe was tested as a method for introducing cells into tape-sealed devices. The established CMFDA staining protocol and trypsinization protocol were followed to create a U-87 cell suspension. A series of 4-way stopcock valves were used to connect cell suspension, DMEM, and PI solution, in 3 mL syringes, to a tape-sealed device (Figure 3.2 upper). After overnight treatment with HA and PDL in PBS, fresh DMEM was used to flush the treatment solution out of the device using syringe pump. The cell suspension syringe was inverted several times before the valves were turned to open flow to the device. Cell introduction was monitored using the inverted microscope until a reasonable number of cells

were distributed in the microfluidic channel, then the outlet tubing was capped, and the valves were switched back to media. The cell suspension syringe was then detached from the valve, the loaded device was carefully transferred and secured into an open petri dish, and the entire apparatus was sprayed with 70% EtOH before stored in an incubator (Figure 3.2 lower). At specified timepoints, the device was removed for imaging using the Nikon Eclipse TE2000-U inverted microscope using the Sony Alpha a6400 camera, B-2A, G-2A, and the X-Cite 120 Fluorescence Illumination System. PI staining solution was introduced using the syringe pump to assess viability over time. Some experiments included an hourly flush with fresh DMEM, using a syringe pump at 0.4 mL/hr, in addition to fluorescent imaging. Image processing was completed using ImageJ.

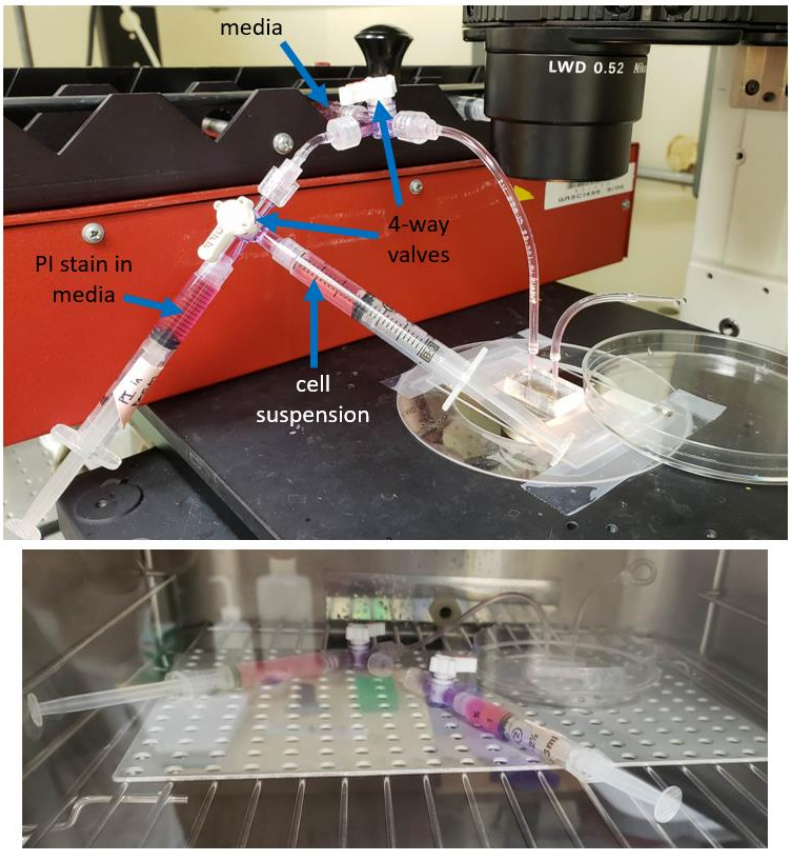

Figure 3.2. Set up for manual injection of cells into simple, tape-sealed PDMS devices. Multiple 4-way valves were used to allow interchange between media, PI stain solution, and U-87 cell suspension (upper). Cell seeding was monitored using the microscope, and the entire apparatus was transferred into the incubator after sterilization with 70% EtOH (lower).

A heating block, set at 37 °C, was investigated as a method of temperature control outside of the incubator. For these tests, tape-sealed, simple PDMS devices were secured onto a glass slide. U-87 cells, stained with CMFDA, were seeded into the devices. Following cell seeding, the devices were stored in the incubator for 1 hr to allow cells to successfully attach in a controlled environment. Two syringe pump flow conditions were tested: 1) constant flow of DMEM at 0.2 mL/hr, and 2) a 5-min flush of DMEM at 0.25 mL/hr each hour. The device outlets were connected to a waste container, filled with a bleach solution, to collect any waste during experiments. Devices were placed on the heating block and weighed down to ensure contact with the heated surface (Figure 3.3).

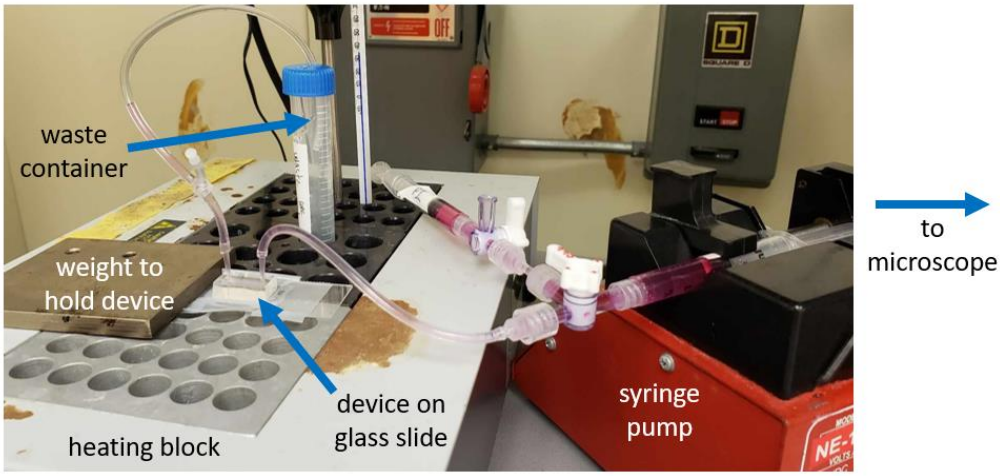

Figure 3.3. Apparatus for heating block testing.

The devices had to be carefully transferred from the heating block to the microscope. Images of the cells were collected at several timepoints on the Nikon Eclipse TE2000-U inverted microscope using the Sony Alpha a6400 camera and the X-Cite 120 Fluorescence Illumination System. Image processing was completed using ImageJ. A more detailed protocol is provided in Appendix C.

A miniature incubator setup with CO_2 and temperature control was used from Bioscience Tools for a controlled cell environment on the microscope stage. A device was secured to the base of the incubator and prepared for experiment by replacing all air within the channels with water. The device was then filled with the HA+PDL in PBS solution and treated at room temperature for 1 hr. Complete DMEM fresh from the incubator was used to flush the treatment solution from the channels. The atmosphere was then set to 5% CO_2, verified by the secondary CO_2 sensor, and the heated base and lid of the miniature incubator were set to 37 °C. The device would then sit in the controlled environment until cell seeding. The prepared U-87 cell suspension was injected manually via syringe from the outlet reservoir into the observation channel (Figure 3.4). Details of the cell suspension preparation can be found in Appendix B.

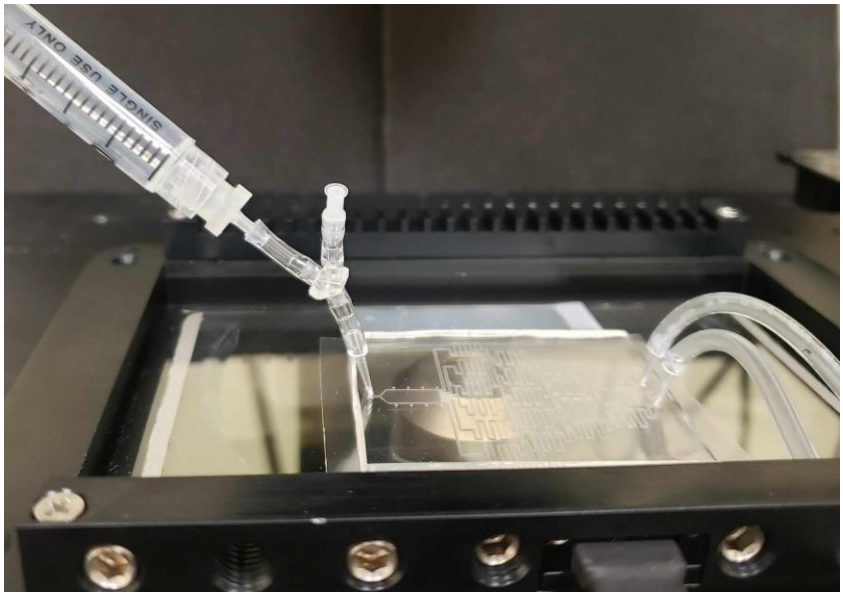

Figure 3.4. Fluidic setup for manual cell injection into the observation channel.

Manual injection was monitored using the microscope until desirable cell distribution and density was reached within the observation channel, primarily between 5.0 and 7.5 mm. The syringe was quickly removed, and the open tubing was capped. Finally, the miniature incubator was closed to reestablish the cell culture environment. After various lengths of time, PI was to be used to assess viability using previously described fluorescence imaging procedures.

As an alternative to PI, NucSpot 568/580 was tested to establish an appropriate working concentration for U-87 cell experiments in combination with CMFDA. Final concentrations of 1X, 0.5X, and 0.25X were investigated as advised by the product information sheet.[120] Initial testing followed the developed CMFDA staining protocols and used 96 well plates to seed 50 μL of CMFDA- and NucSpot-stained cells into 50 μL of DMEM with NucSpot. Well plates were then cultured within the miniature incubator, and images were collected hourly for 5 hr using the Nikon Eclipse TE2000-U inverted microscope using the Sony Alpha a6400 camera, B-2A and G-2A filter cubes, and the X-Cite 120 Fluorescence Illumination System. Image processing was completed using ImageJ.

Once an effective working concentration of NucSpot was determined, long-term cell viability experiments were performed within the miniature incubator. Following cell seeding, the setup was kept in the dark for the entirety of the experiment. Images for CMFDA and NucSpot staining were collected 15 min after cell seeding (0 hr timepoint) and at each additional hour for 8 hr. Additional experiments monitored cell health during exposure to constant 1.0 µL/min flow for 4 hr. A fabric with conductive fibers was used as a heating pad. The tubing and a thermocouple were secured to the fabric using tape as shown below (Figure 3.5). Previously described fluorescence imaging procedures and processing were used to assess cell viability.

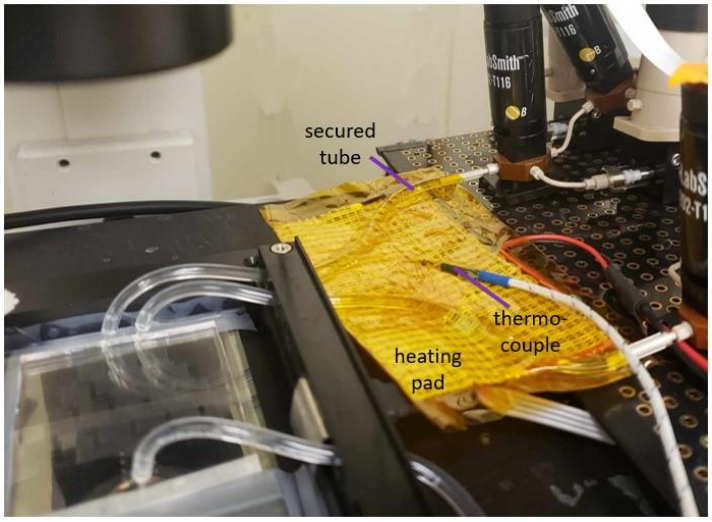

Figure 3.5. The external tubing and a thermocouple attached to the heating pad fabric using tape.

3.3 Results and discussion

3.3.1 Optimization of the device fabrication process

As described in more detail in Chapter 2, two critical changes greatly improved the print quality: 1) using the Mars 4 DLP resin 3D printer, and 2) using opaque resin. The cracking and gaping in printed microchannels from using the previous resin 3D printer were no longer persistent (Figure 3.6). Additionally, more consistent printing was observed regardless of print location on the build plate. This confirmed that light projection overcame the limitation of

varying pixel performance observed with the previous LCD-based resin printers. The print settings were optimized to fabricate 300 µm wide serpentine mixing channels for these resin molds with 700 µm spacing between the turns. It was theorized that these dimensions would contribute to easier removal of the cured PDMS slab when baking was completed.

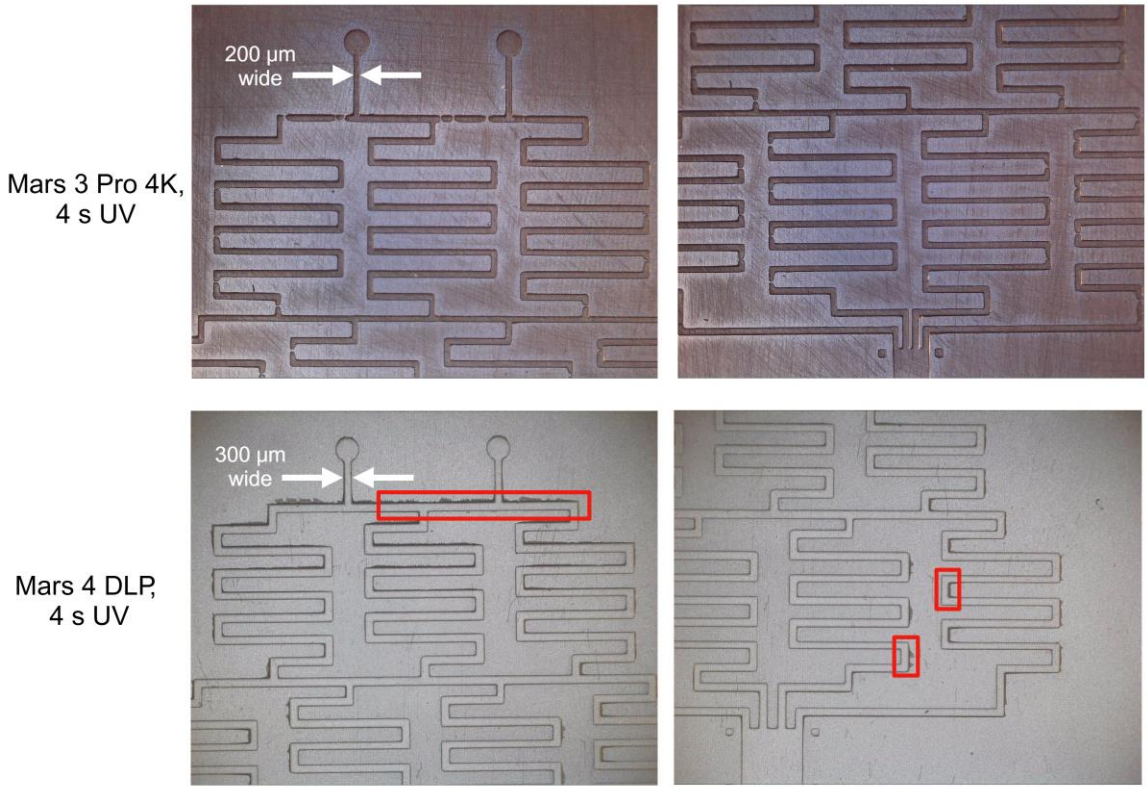

Figure 3.6. Improvements in print quality from Mars 3 Pro 4K (upper) to Mars 4 DLP (lower) when printing positive features for resin molds. Excess cured resin marked in red.

As detailed in Chapter 2, the profiler was used to assess printed features of the molds. These scans involved positioning the stylus atop the microchannels and scanning off the edge to the base, as opposed to scanning from the base into recessed channels. This difference allowed for the previously unmeasurable serpentine mixing channels to be measured using the profiler and contributed to a more thorough investigation of the printed channel height from a wider range of print locations. The actual feature height was typically within 25 µm of the desired height, depending on the selected layer height and normal layer light exposure settings. Again, a

relationship existed between layer height and the total height which influenced the final result. After some optimization, 200 μm tall channels were printed using 50 μm layers with a 4 to 5 s normal layer exposure. Some sample results are summarized in Table 3.4.

Table 3.4. Measured positive feature height from Mars 4 DLP-printed microfluidic channels designed to be 200 μm tall with 50 μm layer height printed with increasing duration of normal layer light exposure.

Print ID	1st scan height (μm)	2nd scan height (μm)	Average measured height ± standard deviation (μm)
2.5 s cure	199.689	192.377	196 ± 5
3.0 s cure	198.599	190.024	194 ± 6
3.5 s cure	200.655	196.943	199 ± 3
4.0 s cure	208.717	199.762	204 ± 6

Another important feature to consider was the presence of additional cured resin outside of the desired microchannel pattern. The lower images of Figure 3.6 highlight this common feature on the uppermost horizontal channel, designated the hump feature. The profiler was used to measure the hump on various prints by scanning from the full channel height down to the base of the mold over the hump. This was repeated three times, once to the left of both inlets, once between, and once to the right, to monitor differences across the printed design. The impact of varying normal layer light exposure was investigated, and the results are presented in Table 3.5.

Table 3.5. Measured heights of microchannels and hump features from 3D-printed molds designed to have 200 μm tall channels with varying normal layer light exposure.

Print ID		1st scan height (μm)	2nd scan height (μm)	3rd scan height (μm)	Average height ± standard deviation (μm)
3.0 s cure	Channel	182.402	180.254	181.938	182 ± 1
	Hump	0.000	0.000	0.000	0 ± 0
4.0 s cure	Channel	175.529	173.273	174.858	175 ± 1
	Hump	10.659	13.061	3.521	9 ± 5
5.0 s cure	Channel	174.051	170.917	170.639	172 ± 2
	Hump	8.867	20.272	0.000	10 ± 10
6.0 s cure	Channel	160.709	171.009	172.347	168 ± 6
	Hump	7.705	15.467	0.000	8 ± 8
7.0 s cure	Channel	177.452	176.877	177.190	177.2 ± 0.3
	Hump	8.586	14.010	2.410	8 ± 6
8.0 s cure	Channel	184.260	180.956	180.907	182 ± 2
	Hump	12.914	14.864	0.000	9 ± 8

The maximum measured hump feature height was 20.272 μm tall, and the average for all hump feature measurements was 7 ± 7 μm. This wide range in standard deviation represented how the hump feature was either present or nonexistent across all sampled prints. Additionally, compared to the average for all channels, 176 ± 6 μm, these hump features were notably smaller and should have little impact on device sealing, filling, or function. Although all prints measured lower than the desired 200 μm channel height, this difference should not create issues for the cells considering their reported diameter, only 10-30 μm.[102]

To be able to cast PDMS devices from the resin-printed molds, a fabrication procedure had to be established. There were several key parameters to consider: 1) the ratio of PDMS base to curing agent, 2) the oven temperature, and 3) the bake time. It is understood that these factors have considerable influence over the resulting PDMS flexibility.[121] The flexibility of the PDMS is a critical characteristic when peeling up cured PDMS from a mold. Both 10:1 and 5:1 (v/v) PDMS base to curing agent ratios were tested to examine a more flexible and stiffer option.

Based on the previous resin temperature exposure tests, all PDMS baking would occur below 60 °C. This meant longer baking would be required to fully crosslink the material. The 10:1 PDMS mixture necessitated a bake upwards of 15 hr to fully cure, which was determined to be too high of a tradeoff in fabrication time for any potential benefits of the more flexible PDMS. All future testing focused on 5:1 PDMS, which generally needed between 4 and 6 hr to cure. It should be noted that the ambient room temperature and relative humidity impacted the PDMS baking and were monitored and recorded throughout testing. Elevated humidity, $\geq 35\%$, coincided with a substantial number of failed moldings. A 1:1 (v/v) mixture of HMDS and xylenes was investigated as a releasing agent to improve PDMS removal from the mold. There was not a noticeable improvement in PDMS peeling between molds with and without the releasing agent, so this step was not included. The finalized PDMS baking procedure used 5:1 PDMS base to curing agent baked at 50 °C for 5.5 hr before cooling to room temperature, peeling, punching reservoirs, and sealing with tape (Figure 3.7).

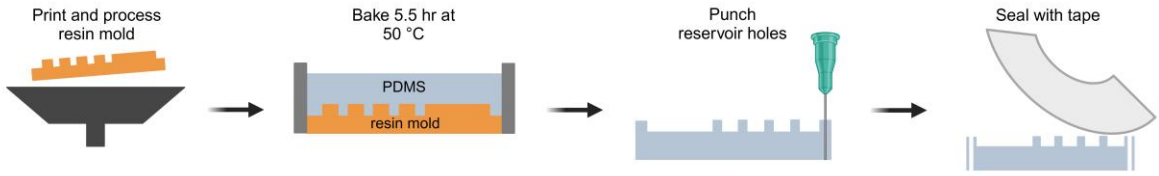

Figure 3.7. Fabrication procedure for resin-molded PDMS devices sealed with tape.

Potential leachable chemicals from the resin during the PDMS baking process were still a concern for this fabrication procedure. Based on the work by Musgrove *et al.*, a 24-hr soak in sterile PBS at 37 °C was investigated as a treatment procedure for the resin molds.[92] This treatment caused warping of the resin molds, likely due to 2-mm thickness of the base (Figure 3.8 A). Additionally, the PBS-soaked molds resulted in extensive issues during the PDMS baking procedure. Bubbling, or an air gap, was often formed between the treated resin mold and the PDMS, which contributed to incomplete curing of the elastomeric material compared to the untreated molds and an unusable microfluidic device (Figure 3.8 B, C).

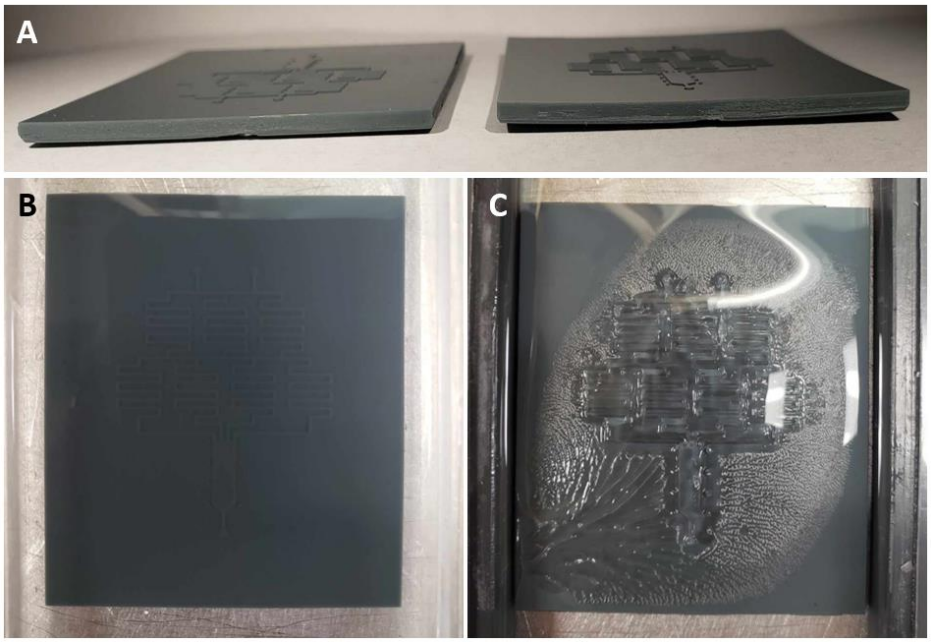

Figure 3.8. Results from the PBS treatment of resin 3D-printed molds. The 24 hr soak in PBS at 37 °C caused the molds to warp (A right). The untreated resin molds resulted in more consistent PDMS baking (B) than the PBS-treated molds, which often caused bubbling and incomplete curing at the interface between the resin and PDMS (C).

Due to these results, untreated resin molds would be used for PDMS soft lithography. Contact angle analysis was used to monitor both the resin mold and PDMS surfaces over replicate baking procedures. Untreated resin molds, before use, had a more hydrophilic surface (Figure 3.9 B) than native PDMS cured without the presence of resin (Figure 3.9 E). The water

contact angle was then assessed after each of 5 consecutive PDMS bakes. The most notable changes occurred in the resin surface which became more similar to the PDMS surface over time (Figure 3.9 A). Comparably, the PDMS contact angle was relatively consistent throughout the study (Figure 3.9 D).

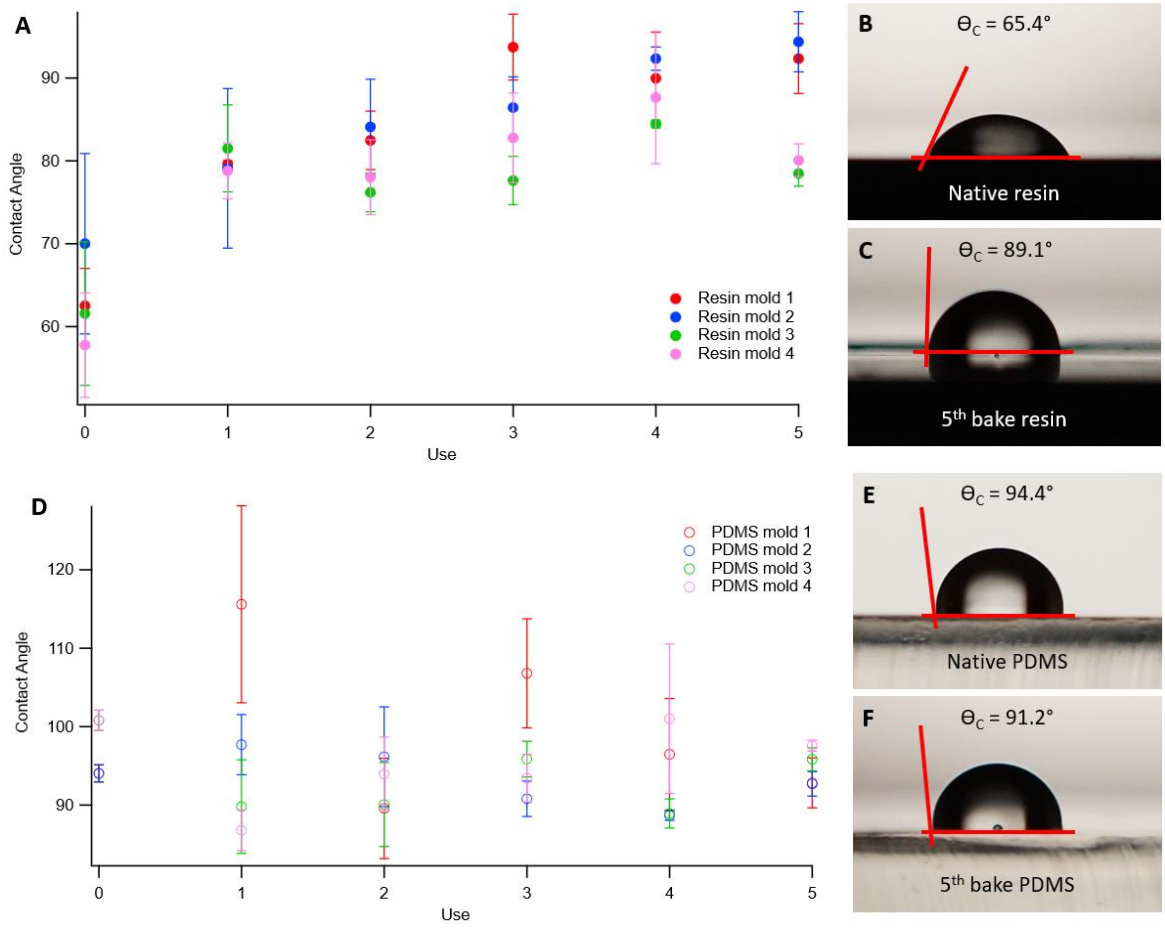

Figure 3.9. Summary of result from contact angle analysis of resin mold (A) and PDMS (D) surfaces. Error bars represent standard deviation (n = 3). Sample contact angle images for the resin (B, C) and PDMS (E, F).

These results provided one method to determine if volatile species from the resin were released into the PDMS during baking, which had been a serious concern. Alternatively, the PDMS has greater influence over the resin. It was theorized that during replicate baking procedures, a microlayer of PDMS is retained on the resin mold surface after peeling. This would cause a slight increase in microchannel dimensions as a resin mold is reused and should be considered if

strict adherence to design dimensions is necessary for the device application. The conclusions from the contact angle analysis were encouraging for this work.

3.3.2 Progress towards maintenance of tissue culture environment

To confirm these PDMS devices molded from resin prints are an appropriate environment for cell studies, methods needed to be developed to monitor cell health within the devices. This work began by determining a set of fluorescent stains to track cell position, morphology, and viability. As mentioned in Chapter 2, PI was selected as a preferable method for tracking cell death compared to trypan blue. It was already known that the G-2A Nikon filter cube could be used for excitation and emission of this dye (Figure 3.10 B). Two other filter sets were aligned within the inverted microscope that would allow for simultaneous detection. The B-2A set provided the apparatus for the use of CMFDA, which would be used as a general stain to monitor position and morphology of all cells (Figure 3.10 A). Finally, Annexin V could be implemented to distinguish apoptotic cells, and the CF350 conjugate was selected to be paired with the Nikon UV-2E/C filter cube (Figure 3.10 C). The working concentrations of each of these fluorescent stains were optimized with the U-87 cells as 5 μM CMFDA, between 20-30 μg/mL PI, and 1.5 μg/mL Annexin V CF350.

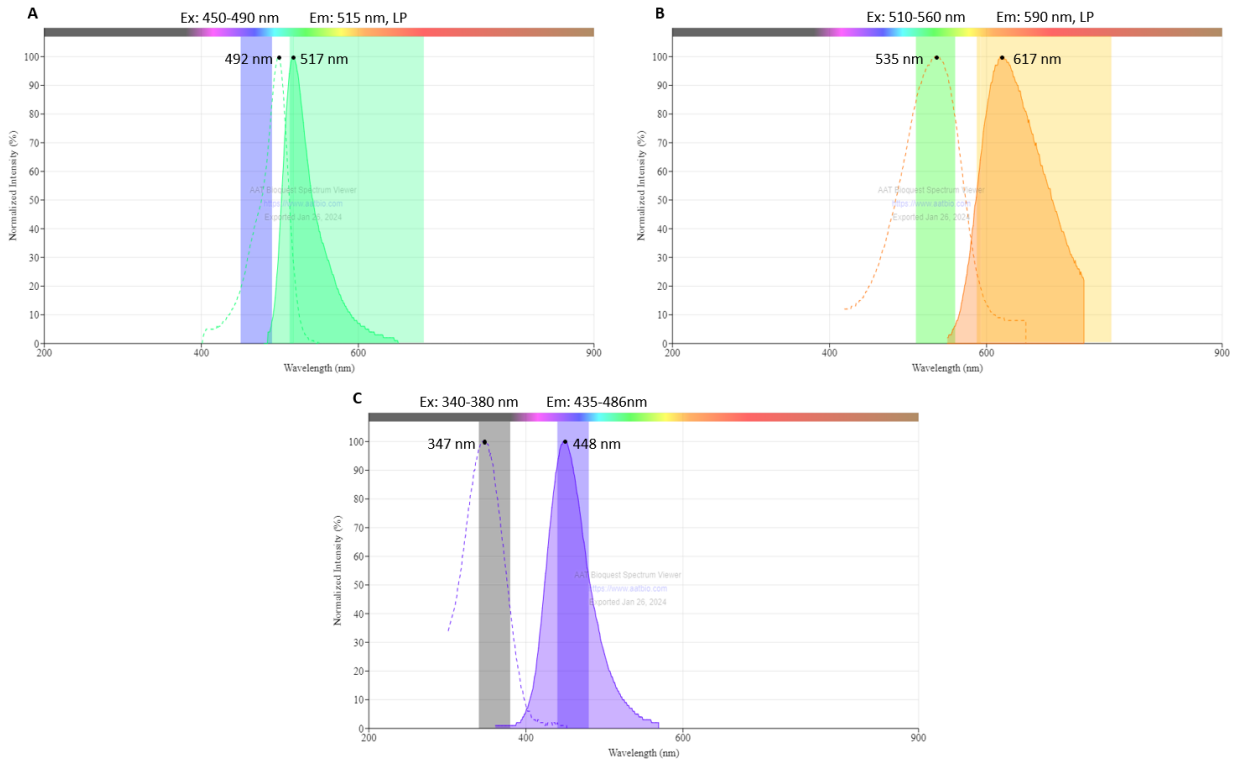

Figure 3.10. Excitation and emission spectra for CMFDA, PI, and Annexin V CF350 and the corresponding Nikon filter cubes B-2A (A), G-2A (B), and UV-2E/C (C). Due to the long pass emission filter used in B-2A, the PI emission would be visible during CMFDA imaging. Spectrum Viewer provided by AAT Bioquest.

Although all stains could be used together, use of the B-2A longpass emission filter meant both the 517 nm CMFDA emission and 617 nm PI emission would show during imaging. A sample of this fluorescent emission overlap is shown in Figure 3.11 B below. Live cells, stained green with only CMFDA, were still distinguishable from dead cells, which appeared yellow/ orange or red with the B-2A filter set as a result of PI.

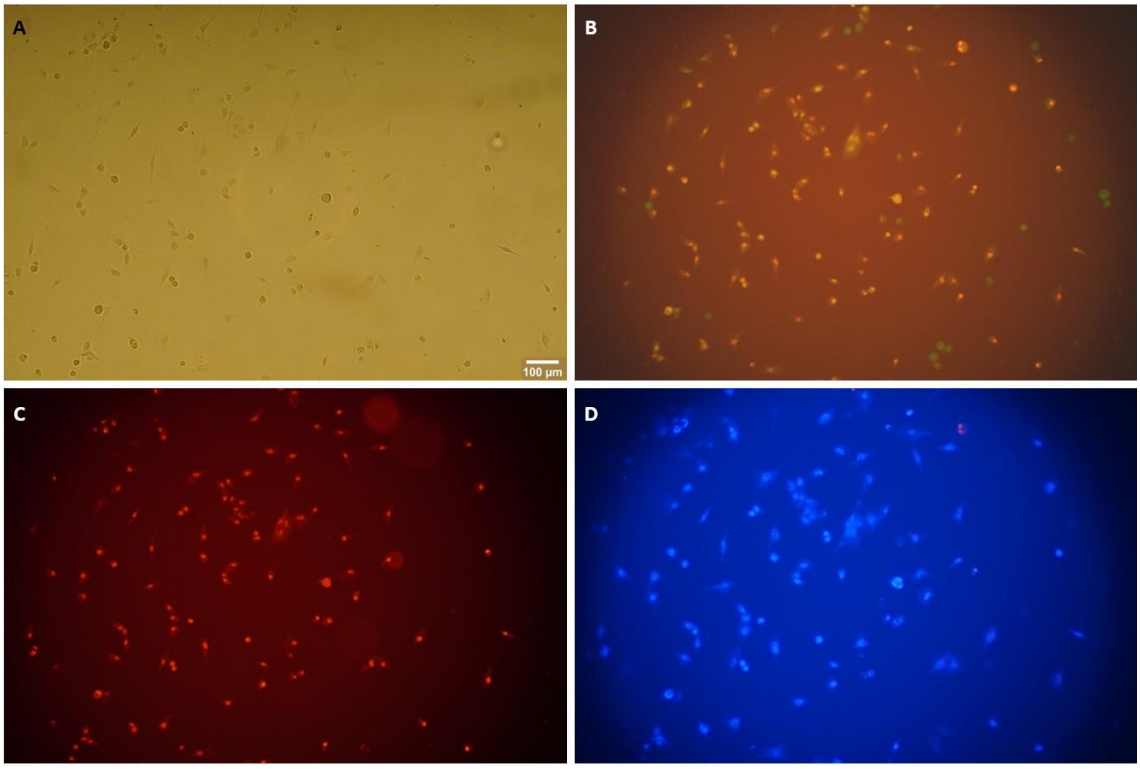

Figure 3.11. Fluorescence imaging results from staining U-87 cells with 5 µM CMFDA, 22 µg/mL PI, and 1.5 µg/mL Annexin V CF350. To induce cell death 5.5 hr after cell seeding, 70% EtOH was added to the well. This excessive level of cell death created an extreme situation where all stains would be at their highest intensity to determine if each could still be distinguished. Although the PI was visible during CMFDA imaging (B), some live cells could still be distinguished from dead cells when compared to the PI (C) and Annexin V CF350 (D) imaging.

Another factor that had to be adjusted from the standard staining protocol was the presence of Annexin V binding buffer and the amount of rinsing required. An experiment tested whether the multiple binding buffer rinses could be eliminated from the Annexin V staining protocol by comparing fluorescent intensity between rinsed and unrinsed wells, and it was determined that the rinse steps could be excluded. This would make Annexin V staining within sealed devices far easier since only one solution of Annexin V CF350 in binding buffer would be required instead of separate binding buffer and staining solutions.

When PI stain was added to wells containing Annexin V binding buffer, this enhanced the emission overlap during CMFDA imaging (Figure 3.12 left). Further tests were completed to

determine if this effect could be reduced. The two sets of experimental conditions compared wells where the PI solution was added to the Annexin V staining solution, containing binding buffer, to wells where the binding buffer was removed following Annexin V incubation and replaced with fresh media before the addition of PI stain. As theorized, the removal of binding buffer reduced the PI overlap for CMFDA imaging (Figure 3.12 right). This adapted protocol could be implemented in sealed devices by flushing Annexin V staining solution out of the device with media before switching the flow to the PI solution.

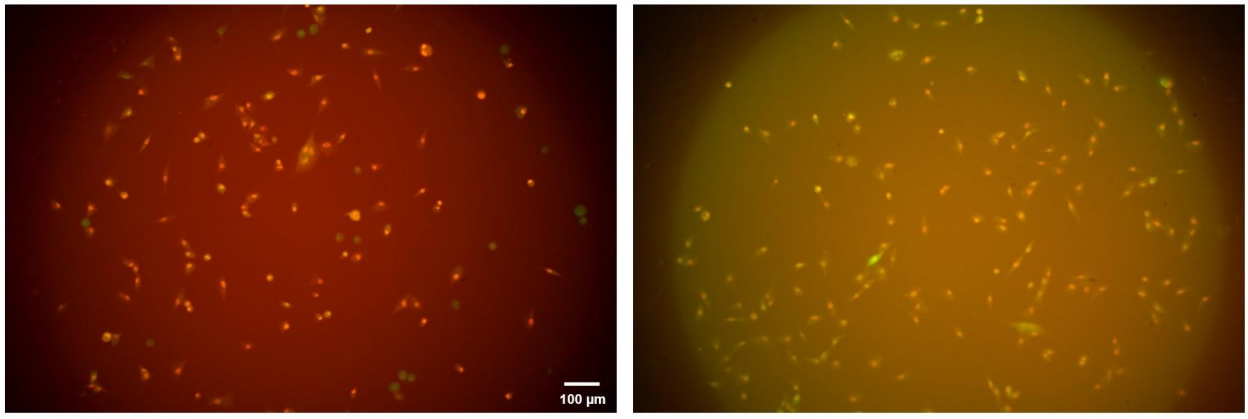

Figure 3.12. The presence of the Annexin V binding buffer solution enhanced the emission overlap between PI and CMFDA when using the B-2A filter set (left). Removal of the binding buffer before the addition of PI reduced the overlap during CMFDA imaging (right).

Initial work testing the viability of cells seeded in tape-sealed PDMS devices utilized CMFDA to track morphology and monitor cell attachment within devices. The most successful method to seed cells into devices was using direct, manual injection via syringe. It was critical to invert multiple times to ensure the cells had not settled, and that the syringe was held vertically with the plunger at the top and opening at the bottom. This positioning guaranteed that if cells settled during the slow seeding process, it would occur in the direction of flow towards the device. Visual inspection, using the inverted microscope, allowed the process of cell seeding to be monitored until enough cells were dispersed within the channel. Cell-loaded devices could then be stored within the incubator, after sterilization, until various timepoints were reached.

Observations from these experiments confirmed U-87 cells successfully attached to the treated tape within devices and began to achieve the standard stretched morphology, usually within 3-4 hr after cell seeding (Figure 3.13). Over time, PI staining revealed a larger population of cells dying within the stagnant media in the device. The addition of an hourly flush with fresh media maintained cell health and reduced the number of dead cells visible as a result of PI staining.

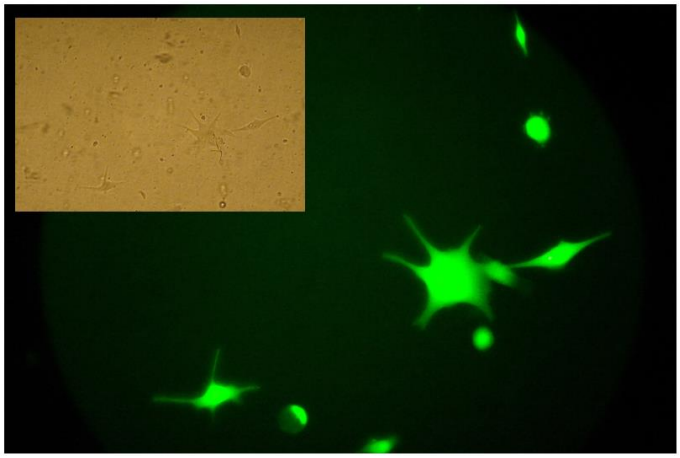

Figure 3.13. CMFDA-stained U-87 cells in a tape-sealed PDMS device. Cells were seeded by manual injection, stored in an incubator, and brightfield (inset) and fluorescent images were collected 3 hr after.

Even though the previous tests confirmed U-87 cells would attach within tape-sealed PDMS devices, the conditions under which these experiments were completed would not be possible for future cell chemotaxis studies. Devices would not be stored within the incubator since both continuous flow, to maintain gradient formation, and time-lapse imaging, to track cell movement, would be required. Appropriate environmental conditions had to be maintained outside of an incubator due to these restrictions. Initial work examined if only temperature regulation would be enough to maintain U-87 cell viability in sealed devices. A heating block, set to 37 °C, was used to provide temperature control.

The first heating block experiment followed the same procedure for preparing a tape-sealed device and seeding U-87 cells. The device was stored in the incubator for 1 hr to allow the

cells to attach in a controlled environment. Once transferred to the heating block and connected to the syringe pump, the device was subject to constant flow of DMEM at 0.2 mL/hr. The CMFDA imaging revealed mostly round cell morphology, unlike the typical stretched U-87 growth. Furthermore, there was an accumulation of debris within the device, especially within the inlet channel and where it connected to the wider channel (Figure 3.14 upper). The accumulation appeared to be both a mixture of cell debris, based on observed fluorescence, and possibly tape adhesive.

Since the exact cause of the debris was unknown, a second heating block experiment was conducted without continuous flow. All previous experimental steps were repeated, but a 5-min flush of DMEM at a flowrate of 0.25 mL/hr was performed each hour. CMFDA imaging showed more stretched cells than observed during the continuous flow test (Figure 3.14 lower). There was no accumulation of debris within the device, and less cell death was observed from PI staining as well.

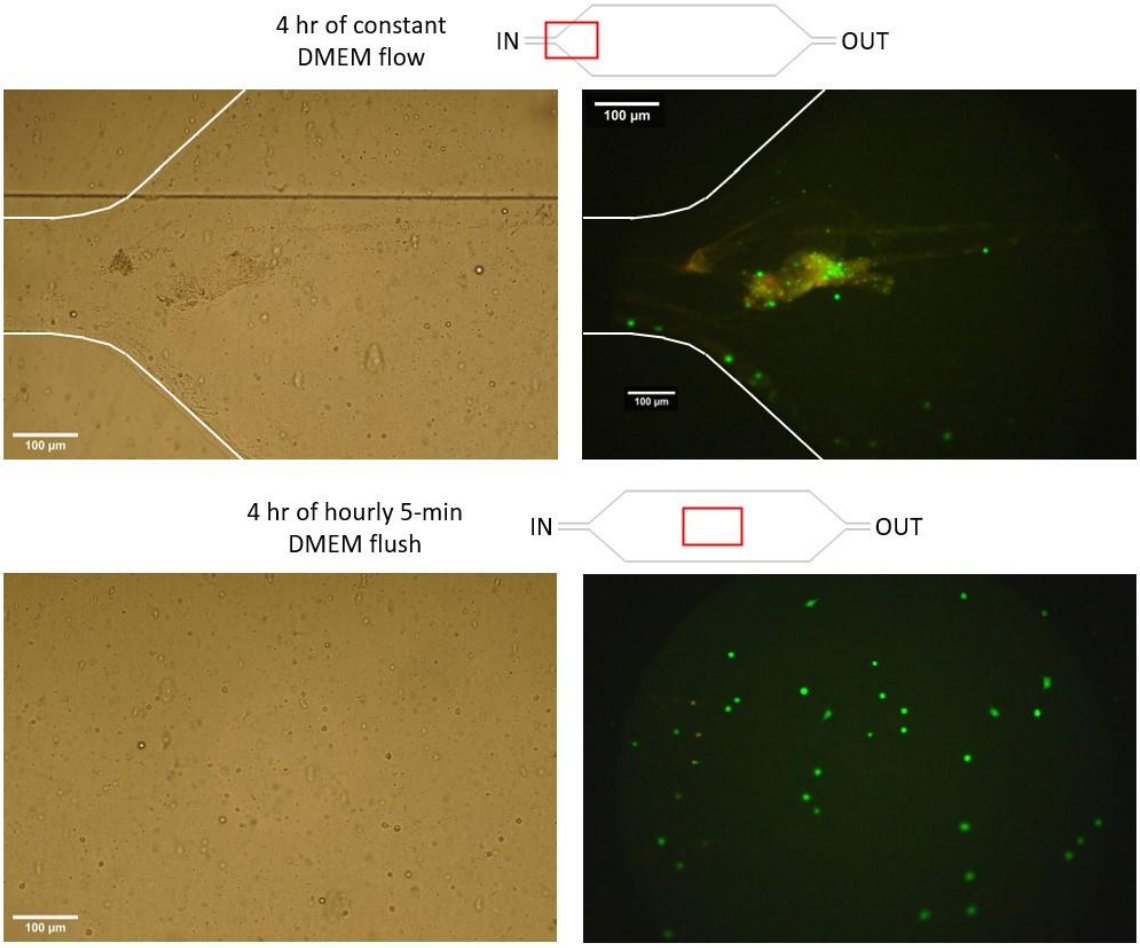

Figure 3.14. Sample results from heating block testing. Constant flow of DMEM at 0.2 mL/hr led to an accumulation of debris in the device (upper). A 5-min long flush of DMEM at 0.25 mL/hr each hour prevented the debris accumulation, and more cells were able to reach a stretched morphology (lower).

Though the hourly DMEM flushes resulted in improved conditions for cells seeded within the PDMS device compared to constant flow, there was still a loss as some cells detached from the surface over time. This cell loss was most likely caused by a lack of sufficient environmental control, and/ or a flowrate that was too high. It will be important to consider these factors when moving on with future cell work.

3.3.2.1 Miniature scope-top incubator

To achieve a stable environment on the microscope stage for longer cell imaging experiments, a miniature incubator setup providing both controllable CO_2 and temperature was

utilized from Bioscience Tools. The HA+PDL treatment step was altered from overnight under refrigeration to 1 hr at room temp. This provided effective coating of the exposed adhesive while decreasing the total time required for experimental preparation and avoiding disconnecting the device from fluidic control. HA+PDL-treated 6-part gradient devices were successfully seeded with U-87 cells using manual injection via syringe through the outlet, and stretched cell morphology was confirmed (Figure 3.15).

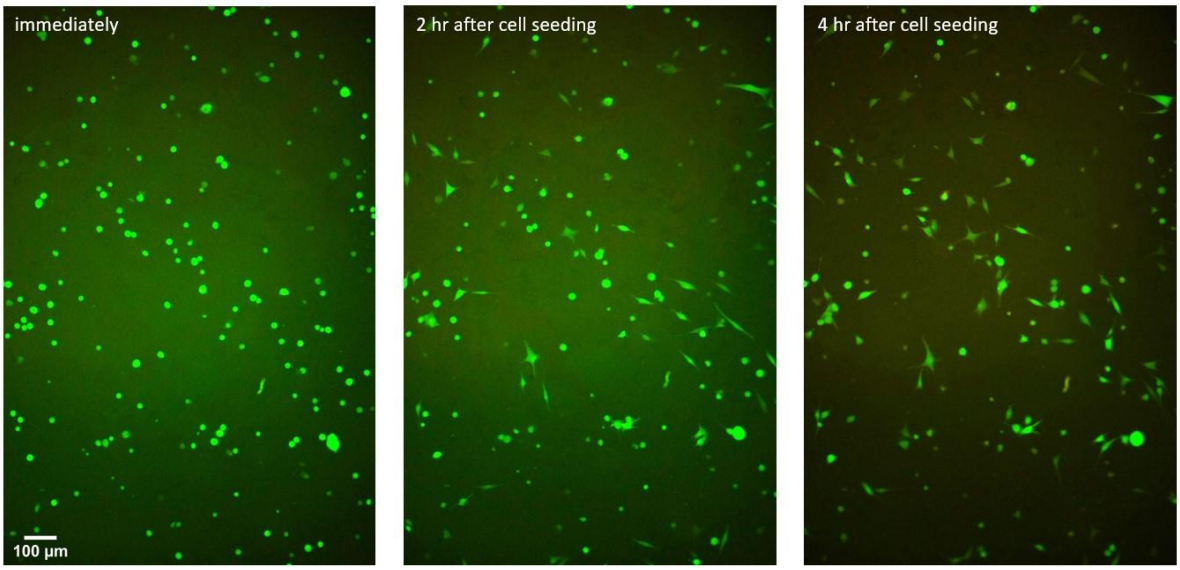

Figure 3.15. CMFDA-stained U-87 cells seeded within observation channel. Cells were maintained within the miniature incubator environment, successfully attached to the treated tape surface, and developed stretched morphology. Images were collected at 10X magnification positioned at 7.5 mm down the observation channel.

Initial viability experiments were attempted utilizing PI, but the inherent cytotoxicity of this stain meant it could only be utilized as an endpoint indicator of cell health. Additionally, the lower flowrates required when introducing PI into the device meant an hours-long delay between initiating flow and stain expression during imaging. Annexin V was considered as an alternative to PI that could be included within the cell media long-term without negative impacts on viability, but this would only show apoptotic cells and could underrepresent the actual number of dead cells. NucSpot 568/580 was selected as a more appropriate stain to monitor overall cell

death that could be utilized for up to 72 hr, as reported by Biotium, and could still use the Nikon G-2A filter cube (Figure 3.16).[120]

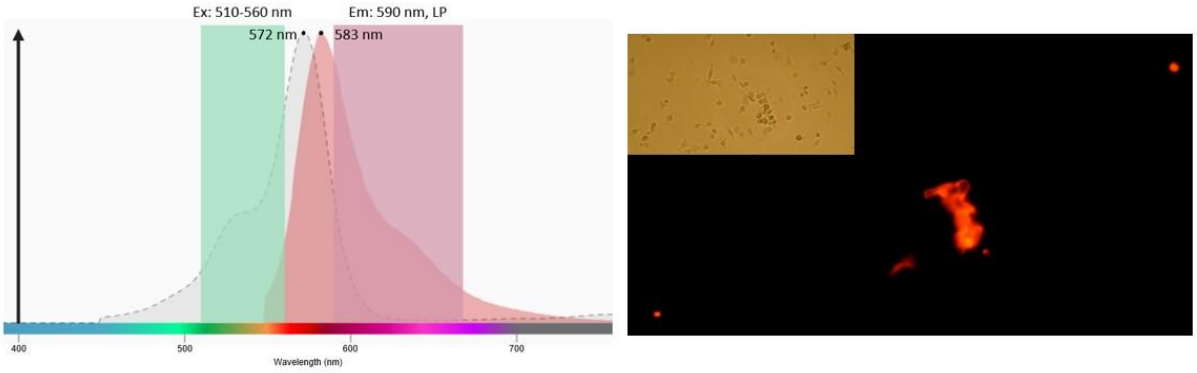

Figure 3.16. The excitation and emission spectra of NucSpot 568/580 and the corresponding Nickon G-2A filter set, made using the Biotium Fluorescence Spectra Viewer (left), and the resulting NucSpot imaging collected during a sample experiment at 10X magnification (right).

After optimization with U-87 cells completed in well plates, a working concentration of 0.25X NucSpot was implemented in all future experiments by including it as a component of the complete DMEM media. This allowed for a passive and continuous method of viability staining, overcoming the previous limitations. U-87 viability within 6-part gradient devices inside the miniature incubator was monitored during 8 hr experiments. CMFDA imaging confirmed typical, stretched cell morphology and NucSpot imaging established that limited cell death was observed within devices over the entire experiment length (Figure 3.17).

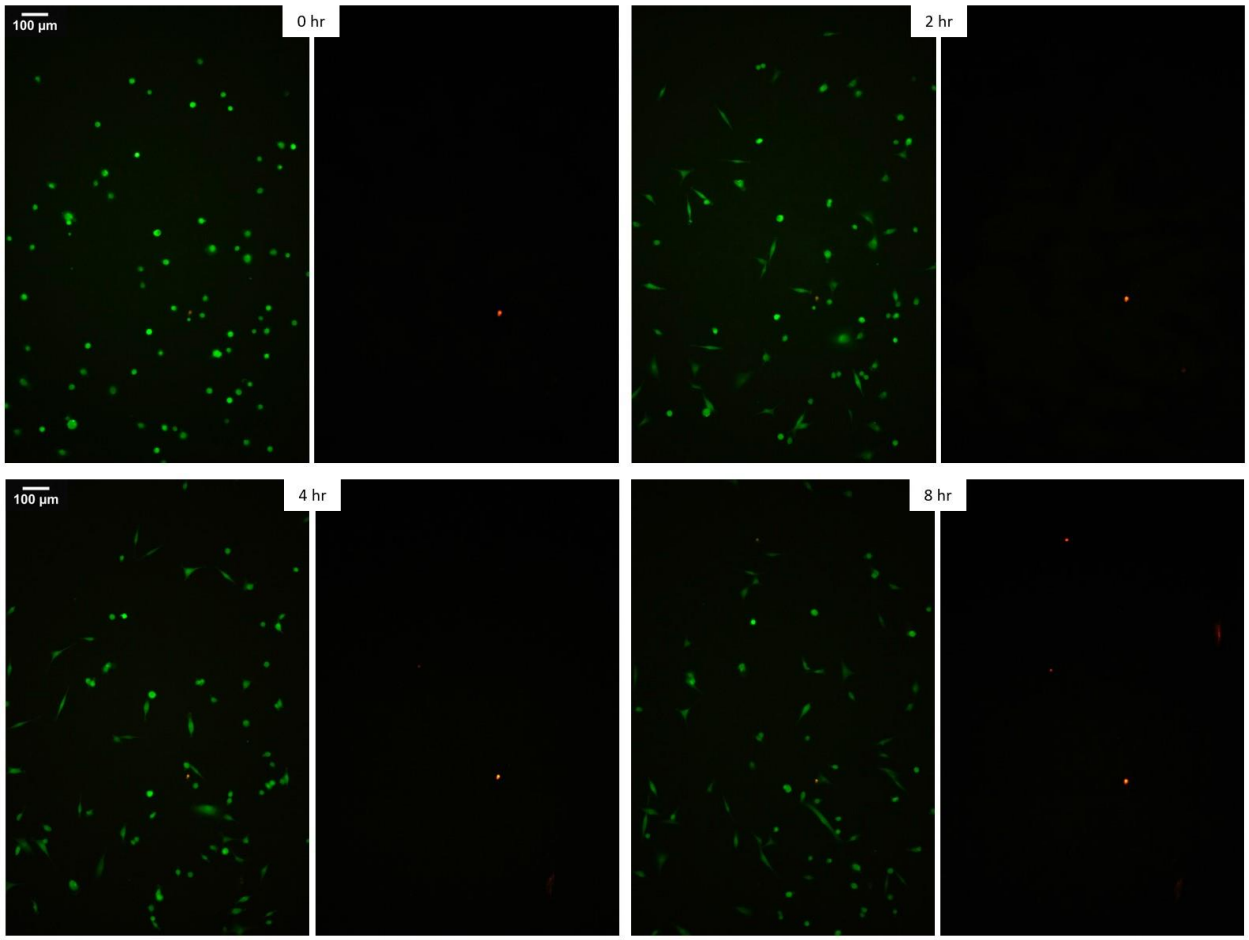

Figure 3.17. CMFDA (green) and NucSpot (red) fluorescent images collected over the 8 hr experiment at 10X magnification. These results confirmed both healthy cell stretching and only minimal increase in cell death.

The next factor examined was the impact of continuous flow on the cells. Although an expanded discussion of continuous flow, and the impact of shear stress on cells in the observation channel based on the selected flowrates for device operation, is presented in Chapter 4, initial experimental results are explored here. Since this device design relies on flow to maintain the gradient, the cells would need to withstand this. Ideally, the flowrate would be considerably low to avoid negative outcomes for the cells. To examine this, cells seeded within 6-part gradient devices were allowed to attach and grow for 4 hr before continuous 1.0 µL/min flow of fresh media for an additional 4 hr. The first round of testing found both a decrease in cell

stretching and a dramatic increase in cell death within the devices, specifically after flow was started (Figure 3.18).

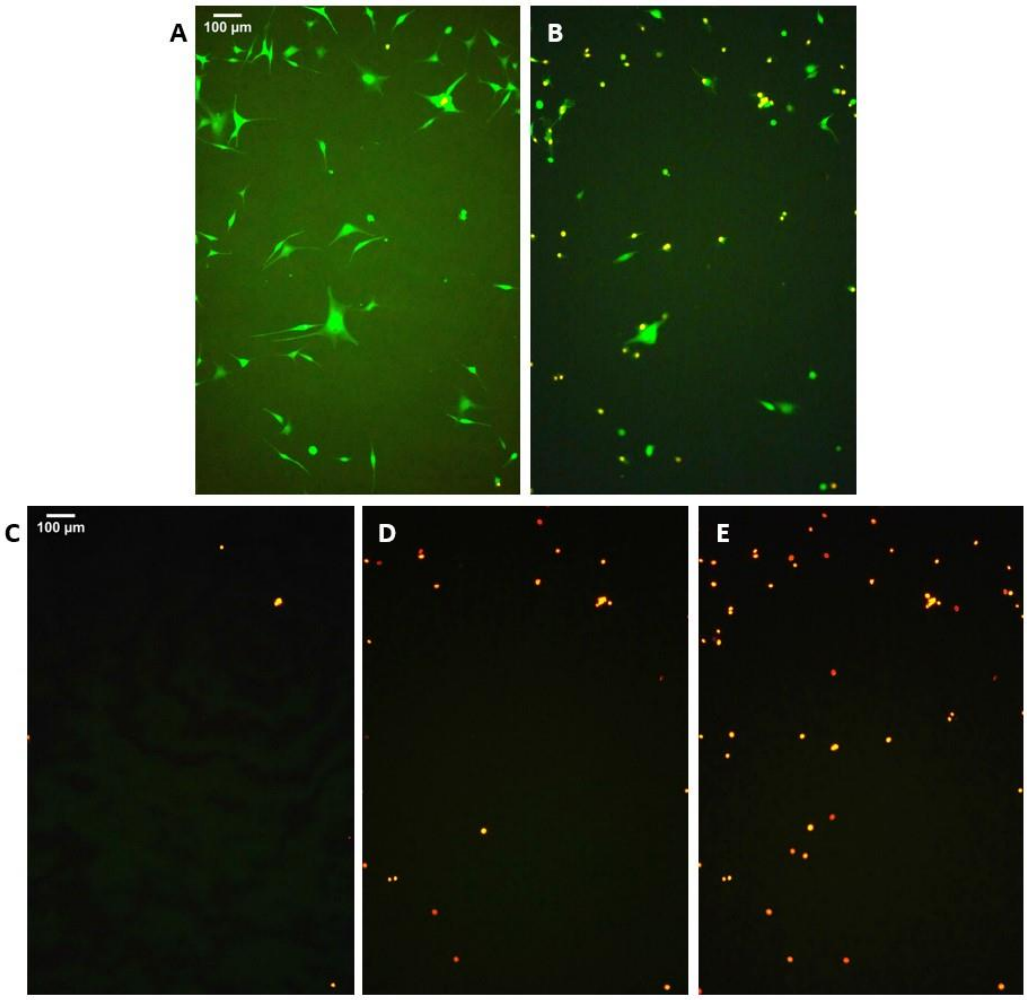

Figure 3.18. Fluorescent imaging of U-87 cells before flow resumed (A), and after 4 hr of continuous flow (B) revealed reduced cell stretching. While the starting number of dead cells was low (C), cell death dramatically increased after 2 (D) and 4 hr (E) of exposure to constant flow. All images collected at 10X magnification.

These initial results revealed an oversight in device and experiment design. The fluidic system and a significant length of tubing was kept outside the miniature, scope-top incubator. Although fresh media, from a secondary incubator, was added to the reservoirs when flow resumed, the media within the tubing, which reached the cells first, was not maintained at 37 °C during the 4 hr of no flow. It was theorized that this exposure to room temperature caused

thermal shock to the cells once flow was resumed and the unheated media reached the observation channel. To reduce this issue, a fabric containing conductive fibers was utilized as an improvised heating pad for the tubing. By applying 3 V of power, the fabric maintained a temperature between 38 and 40 °C. Once implemented into the experimental protocol, the rate of cell death in response to restarted flow was significantly reduced (Figure 3.19).

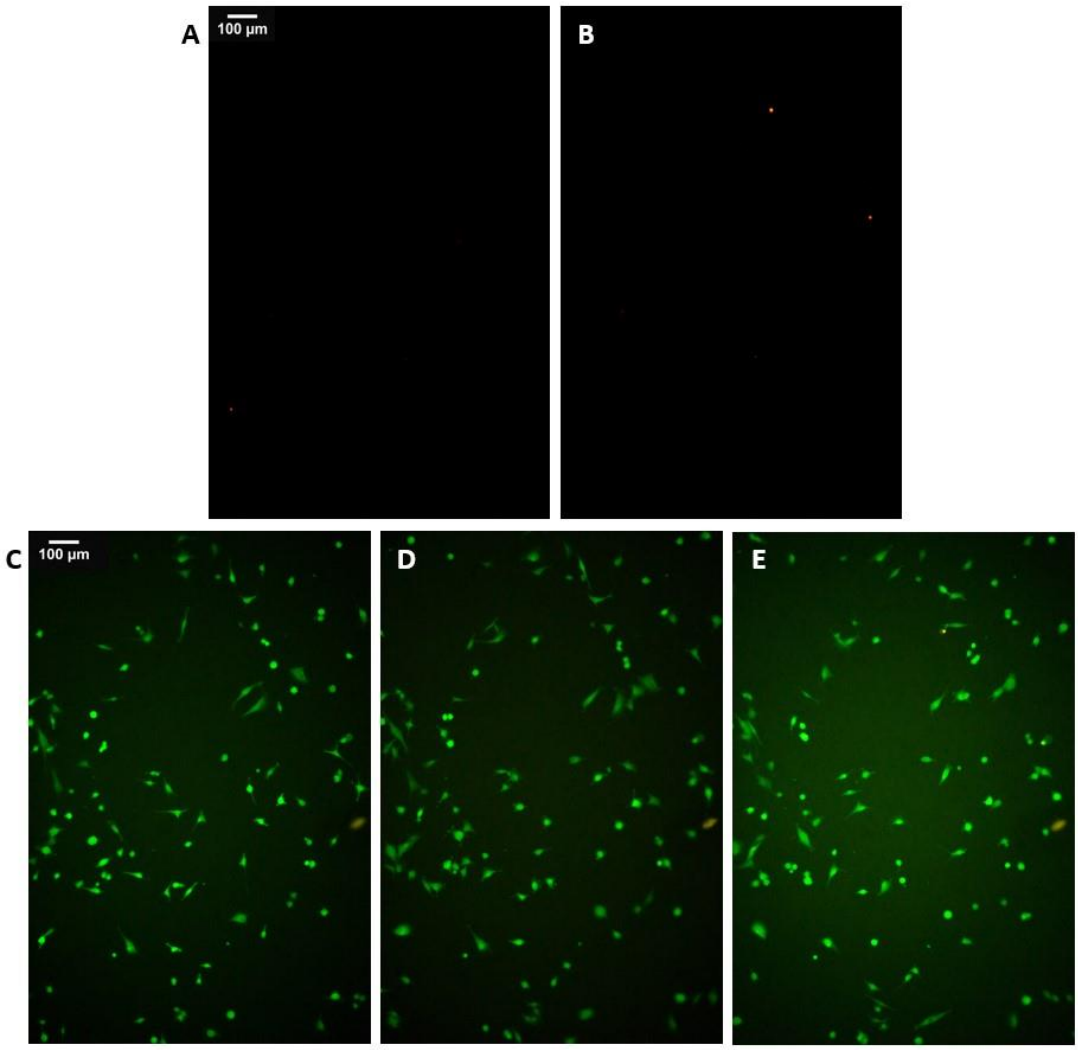

Figure 3.19. When the heating pad was implemented, the amount of cell death before flow (A) and after 4 hr of continuous flow (B) was fairly consistent. Although flow still reduced the extent of cell stretching overall (C vs D), it was possible to regain some of the stretched morphology within a few hours (E). The addition of the heating pad resulted in a significant improvement in the cell culture environment within the device when flow was resumed after cell attachment.

3.4 Conclusions

The transition from fully 3D-printed devices to resin-printed molds for PDMS soft lithography provided an appropriate alternative fabrication method for microfluidic cell studies. The overall low cost and simplicity were maintained while the sealing and filling limitations experienced with 3D-printed devices were overcome. Additionally, the utilization of PDMS, a standard material with a lengthy history in both microfluidics and bioanalytical research, has lessened some previous material property concerns. The Mars 4 DLP resin printer improved print quality and contributed to more consistent printing results following optimization. A protocol for forming PDMS devices from resin-printed molds was developed and contact angle analysis confirmed the molded PDMS surface was not influenced by the resin during baking.

A set of fluorescent dyes were selected and optimized to track U-87 cell position, morphology, and viability using protocols that could be adapted to simultaneous staining and microfluidic studies. Preliminary cell studies, in tape-sealed PDMS devices, confirmed cells would attach to the treated adhesive surface, but further testing, with only temperature regulation, revealed more environmental control would be required for extended chemotaxis experiments out of the incubator. The miniature, scope-top incubator, with both temperature and gas control and a heating pad for the external tubing, enabled longer experiments for the U-87 cells cultured and exposed to flow within the devices. This work established an initial proof-of-concept for bioanalytical applications using PDMS microfluidics made from resin 3D-printed molds. Continued development of an efficient method of fluidic control, and a closer examination of gradient formation within these devices, will provide a sufficient basis for future GBM chemotaxis studies.

Chapter 4 - Exploration of fluidic control and gradient formation during design development

4.1 Introduction

One of the key motivations behind the selection of microfluidic devices for cell studies is the enhanced fluidic control that is achievable. Chemotaxis experiments which utilize stable and well-understood gradients would allow for more controllable conditions and detailed assessment than other commonly used methods. There are a variety of options for fluidic control within the field of microfluidics. For this work, the user simplicity, cost, and amount of equipment required for these methods were critical factors considered when developing the fluid handling for these devices. In this chapter, the development of fluidic control is detailed as different versions of the microfluidic device were created, starting with fully 3D-printed devices through the transition into resin-molded PDMS devices. A reliable method for filling devices and removing bubbles from within the channels is reported here. Finally, the factors influencing gradient formation were explored as the work progressed closer to cell migration studies.

4.2 Materials and methods

4.2.1 Reagents, materials, equipment, and software

The various products and procedures used for this research are provided below, in previous chapters, or in the Appendices.

4.2.1.1 Device fabrication procedures

Both fully resin 3D-printed and resin-molded PDMS devices were fabricated for this work, and the materials used in those fabrication processes are described in Chapters 2 and 3. PDMS devices traditionally fabricated using photolithography required 100 mm silicon wafers

from University Wafer (South Boston, MA, USA), SU-8 2050 photoresist from Kayaku Advanced Materials (Westborough, MA, USA), 40K DPI photomasks printed from Fineline Imagine (Colorado Springs, CO, USA), a digital programmable hot plate from Torrey Pines Scientific (Carlsbad, CA, USA), and 2-(1-methoxy)propyl acetate from Thermo Fisher Scientific (Waltham, MA, USA). The Driel UV flood exposure system, Driel arc lamp power supply, and Thermo Oriel digital exposure control were purchased from the Newport Corporation (Irvine, CA, USA). A NIST traceable radiometer photometer model IL1400A was purchased from International Light (Peabody, MA, USA).

4.2.1.2 Fluidic connections and control

Earlier chapters should be referenced for previously used fluidic equipment. Barbed polycarbonate adapter for 1/16” tube x 1/16 NPT male (5117K85), barbed polypropylene adapter for 1/16” tube ID x 10-32 male pipe (5117K81), quick-Turn tube coupling sockets 1/16” barbed tube ID (51525K281), precision flow-adjustment valve handle-operated for 1/16” tube ID (48965K22), plastic barbed fitting wye connector for 1/16” tube ID (5117K65), and plugs for 1/16” tube ID (5463K73) were purchased from McMaster-Carr (Robbinsville, NJ, USA). Masterflex Transfer Tubing 1/16” ID x 1/8” OD and Masterflex luer adapter male to 1/16” tube ID barbs (30800-16) were purchased from Cole-Parmer (Vernon Hills, IL, USA). Alconox powder detergent was purchased from Grainger (Lake Forest, IL, USA). 0.1-10 µL micropipette tips were purchased from Thermo Fisher Scientific (Waltham, MA, USA). A variety of uProcess products were purchased from LabSmith (Livermore, CA, USA) including the uPB-08 breadboard with 8 device connections, EIB200 electronic interface controller, 4VM02 control manifold for automatic valves, SPS01 100 µL syringe pumps, AV202 automated 4-port selector valves, AV201 automated 3-port selector valves, BBRES 5 mL breadboard reservoirs, 1/16” OD

PEEK tubing, T116-101 CapTite plugs, and CT116-100 CapTite capillary connection fittings. Automated sequences were programmed using the uProcess software.

4.2.1.3 Imaging equipment and fluorescence work

See previous chapters for detailed descriptions of the equipment used for imaging.

4.2.1.4 Other laboratory equipment

Reference Chapter 2 for further details about the other laboratory equipment utilized during this work. Additionally, the MultiPro Model 395 from Dremel (Mount Prospect, IL, USA) and the PDC-32G Basic Plasma Cleaner from Harrick Plasma (Ithaca, NY, USA) were used.

4.2.2 Fabrication of gradient devices

Previous descriptions of the fabrication processes for fully 3D-printed and resin-molded PDMS devices can be found in Chapters 2 and 3. Photolithography was utilized for the fabrication of some PDMS devices before resin 3D printing was optimized. The photomask design was drawn using AutoCAD and printed at a resolution of 40K DPI. Approximately 10 mL of SU-8 2050 were poured from the original bottle into a smaller, amber vial at least two days before use due to the significant viscosity of the photoresist. A vacuum desiccator was used to aid in bubble removal. To make the mold for a gradient device, a clean silicon wafer was placed on the Laurell spin coater. 2-3 mL of SU-8 2050 were poured onto the center of the wafer, covering an area about 1.5” in diameter. After establishing vacuum and nitrogen gas flow, the following 2-step spin program was used:

1. 20 s, 500 rpm, 100 rpm/s
2. 30 s, 1700 rpm, 300 rpm/s

to yield a photoresist thickness of 100 µm. The coated wafer was removed from the spin coater and placed on a hotplate, preheated to 65 °C, for 5 min followed by a second hotplate, preheated to 95 °C, for 15 min. The wafer was stored in a laminar flow hood for 10 min to cool. The photomask was carefully aligned over the coated wafer, covered with a quartz block, and positioned within a UV flood exposure system. The duration of light exposure was calculated based on the photoresist thickness and the measured output power of the lamp (225 mJ/cm^2 desired). The exposed wafer was then baked at 65 °C for 3 min and then 95 °C for 9 min. Again, the wafer was set to cool for 10 min in the laminar flow hood. The wafer was transferred to a crystallization dish filled with 2-(1-methoxy)propyl acetate and developed using gentle swirling motions to remove the uncured photoresist. Development was complete when exposure to small volumes of IPA no longer resulted in cloudy, white streaking on the wafer surface. Nitrogen gas, delivered at less than 50 kPa from a blowgun, was used to dry the wafer.

A 10:1 PDMS elastomer base to curing agent ratio was used to form the gradient devices from SU-8 molds. 20 g of base and 2 g of curing agent were measured on an analytical balance and thoroughly mixed before degassed within a vacuum desiccator. A plexiglass frame was aligned on the wafer before pouring the PDMS over the SU-8 mold. The PDMS was baked at 80 °C for 90 min. After cooling to room temperature, the frame was removed and the PDMS slab was carefully peeled up from the SU-8 mold. The process of punching out inlet and outlet holes and sealing devices using 9795R tape was the same as described in Chapter 3.

4.2.3 Systems of fluidic control

Multiple versions of the inlet and outlet connections were used during this work (Figure 4.1). For fully 3D-printed devices, pipet tips and other fittings were press-fit into the device inlet and outlet holes as a first attempt to connect to tubing or provide reservoirs for fluids. Clear

super glue was used to reinforce these interfaces (Figure 4.1 A). Following increased resin printing optimization, threaded fittings were used, both NPT and 10-32 straight threads. These fittings were screwed into the inlets and outlets (Figure 4.1 B). The seal was further reinforced using Loctite Brush-on Super Glue. All fittings were secured in the 3D-printed devices before the channels were sealed.

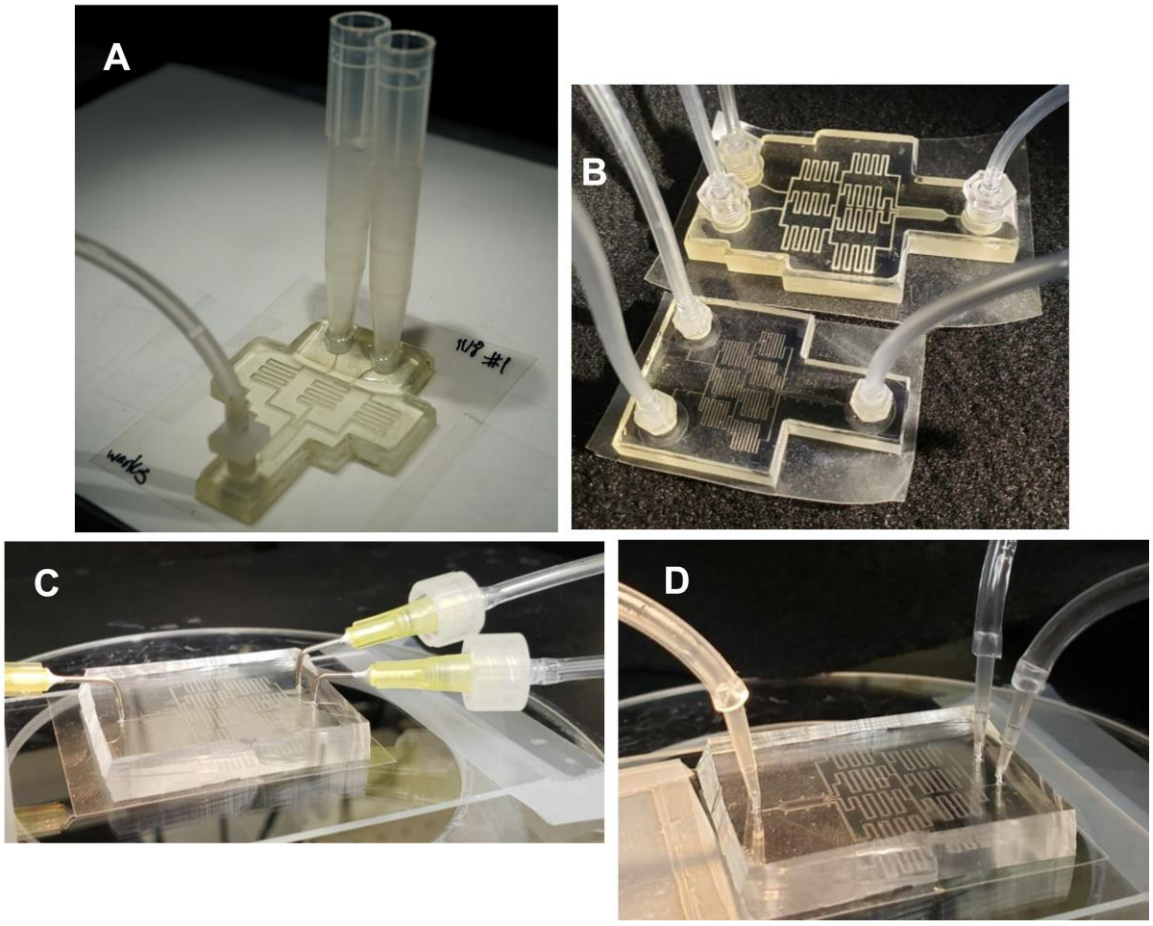

Figure 4.1. The progression of device inlets and outlets during design development. For initial resin 3D-printed devices, the inlets and outlets were press-fit using pipet tips or unthreaded fittings often reinforced using cyanoacrylate adhesive (A). Threaded fittings were incorporated once the features could be reliably printed beginning with 1/16 NPT threads and reduced down to 10-32 straight threads (B). 20-gauge needles bent 90°, without bevel, were paired with Luer lock fittings for early resin-molded PDMS devices (C). Micropipette tips, 0.1-10 µL with the upper section trimmed off, were narrow enough to fit inside 1/16” ID tubing and the PDMS device reservoirs (D).

For PDMS devices, 20-gauge needles were used for the inlet and outlet holes (Figure 4.1 C). The needles were blunted using a MultiPro Dremel tool and bent 90 degrees using pliers. A Luer lock to barb adaptor was used to connect the needle to the tubing. The prepared needles were pressed into the inlet and outlet holes ensuring enough depth to be held in place securely but not flush with the bottom. As an alternative option, 0.1-10 µL pipet tips were trimmed and stuck in the flexible 1/16" ID tubing. The tips were pressed into the device holes in the same way as the needles (Figure 4.1 D).

The first method tested to establish fluidic control utilized a single syringe pump in withdrawal mode. Open reservoirs, often syringes without plungers, were positioned above the device using a laboratory stand (Figure 4.2). A combination of gravity and vacuum, applied gently at the device outlet, was used to pre-fill devices with ultrapure water before gradient experiments began. Food dye was employed for qualitative gradient assessment based on the extent of color mixing. After the flowrate was set and the syringe pump started, gradient formation was monitored over time, and images were collected at various locations along the device using the Sony Alpha a6400 camera. Handle-operated valves could be integrated just below the reservoirs to enable manual flow adjustment if one inlet dominated the other based on experimental observations. The reservoirs could be refilled during the experiment, but once the plunger of the syringe in the pump was fully withdrawn, flow would be manually stopped. To allow for longer experiments, a 10 mL syringe was used in the pump.

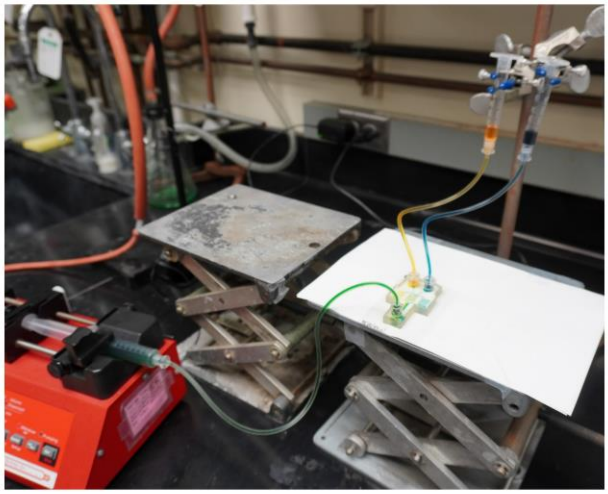

Figure 4.2. A single syringe pump, in withdrawal mode, used to provide controllable flow through a gradient-producing microfluidic device. 3 mL syringes, without plungers, were used as reservoirs for each inlet, while a 10 mL syringe was used in the pump.

A multi-syringe pump was also investigated as a method of fluidic control by introducing solutions through both inlets at once. Two syringes were filled with degassed solutions, secured within the multi-syringe pump, and all tubing was primed with fluid. An open syringe, typically a 10 mL syringe without the plunger, was connected to the outlet to act as a waste reservoir. The pressure-driven flow from the pump was used to fill the device by displacing the air in the channels. Gradient formation was monitored in the same way as before using dyed solutions. The total volume of the starting syringes, often 3 mL, and the selected flowrate set the total length of the experiment.

To aid in device filling, a new apparatus was created (Figure 4.3). Two syringes of different sizes were connected using a 4-way stopcock valve. The filling syringe, with 3 mL capacity, was used to apply manual pressure to fill the channels. Since complete filling could require higher volume, another syringe containing 10 mL was used to replenish the filling syringe as needed by switching the valve connections. A y-splitter was used to connect a

pressure transmitter to the path of fluid flow allowing applied pressure to be monitored while filling the device.

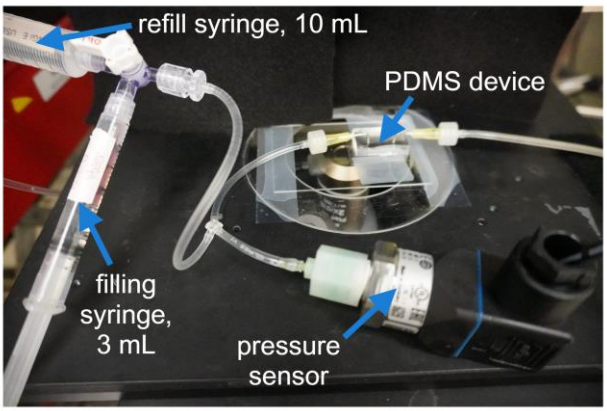

Figure 4.3. The filling apparatus utilized a 4-way valve to connect both the 3 mL filling syringe, which would be used to manually deliver the desired solution, and the 10 mL refill syringe, which would be used to replenish the volume within the filling syringe. A pressure transmitter was connected to enable real-time monitoring during the filling process.

Multiple solutions were tested during device filling including ultrapure water, a 50/50 (v/v) mixture of EtOH and ultrapure water, and dilute solution of Alconox soap in ultrapure water. Each solution was sonicated for at least 30 min beforehand in an ultrasonic bath to degas the fluids. All tubing was fully primed with the selected filling solution before connecting to the device and filling. Once all bubbles were removed from the device channels, the filling apparatus inlet was quickly exchanged for a prepared syringe pump to flush out the filling solution with another fluid. When preparing some simple devices, a length of tubing was connected at the outlet, filled with the desired solution, and connected back to the inlet to fully close the device.

Finally, LabSmith uProcess microfluidic automation products were used to provide a new method of fluidic control. Two identical fluidic setups were used, one for each device inlet (Figure 4.4). The automation interface allowed for communication between the uProcess software and the equipment, and a single valve control manifold was used to control four

separate valves. A pair of 5 mL reservoirs were connected to a 3-port valve. The 3-port valve was connected directly to a 4-port valve that could switch between two syringe pumps and the device inlet. To enable continuous flow, two syringe pumps were used, one syringe pump to dispense into the device while the other was refilled. The entire fluidic system was positioned on a breadboard.

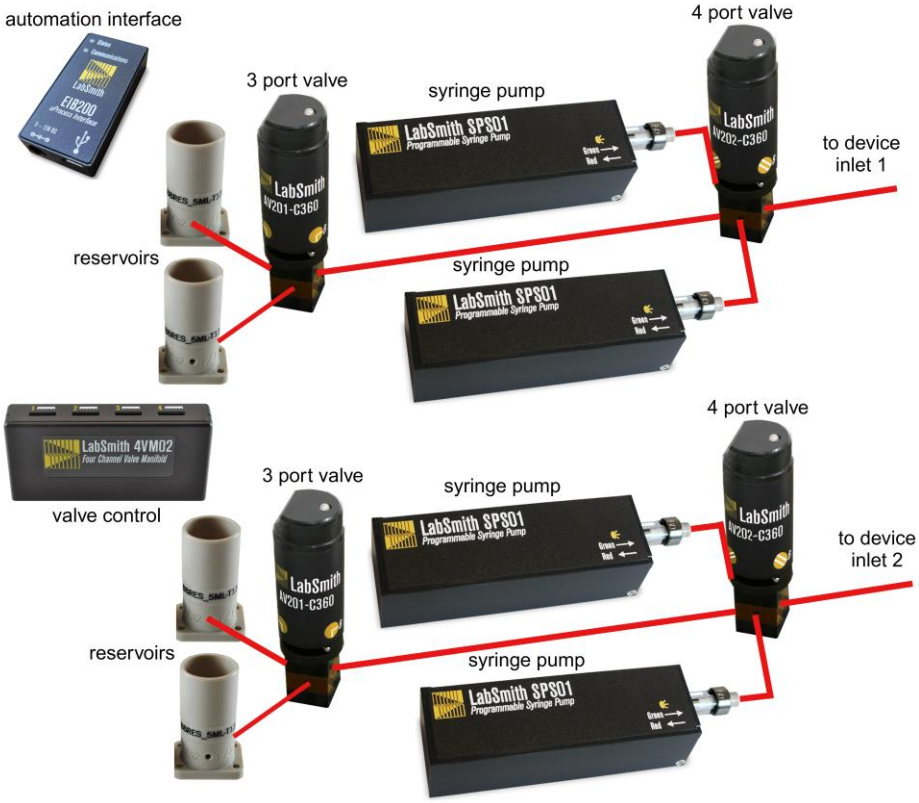

Figure 4.4. Approximate schematic of LabSmith equipment layout for gradient experiments. PEEK tubing is represented by red lines. The automation interface, valve control manifold, and syringe pumps were directly connected to the breadboard. Flat ribbon cables connecting the valve control manifold to all valves are excluded from the schematic for clarity. Component images taken from LabSmith.com product listings.

Polyether ether ketone (PEEK) tubing was used for all fluidic connections. The PEEK tubing was fed into flexible tubing, due to matching outer and inner diameters, and linked to the device inlets using trimmed pipet tips. The LabSmith equipment supported automation through the uProcess software programmable sequences. A sample sequence can be found in Appendix C.

As done before, all solutions were degassed using sonication, and all tubing was primed with liquid before connecting to the device.

4.2.4 PDMS surface modification procedures

The first method tested to modify PDMS surface was boiling in deionized (DI) water based on the work of Park *et al*.[122] A clean beaker was filled with DI water and positioned on a hotplate set to 225 °C until a rolling boil was maintained. Fresh PDMS slabs were transferred into the boiling water using tweezers and exposed for 30 min or 2 hr. The boiled PDMS was dried with a kimwipe before further analysis.

The other method explored for PDMS surface modification was plasma exposure under vacuum. A Harrick PDC-32G Basic Plasma Cleaner was used for this work. After the PDMS device was positioned within the treatment chamber channel-side up. The door was closed, and vacuum was established. Once power was supplied, the RF level was set to high, and the device was exposed to plasma for the desired amount of time: 1, 4, 6, or 8 min. The PDC-32G was powered down, vacuum was broken, and the device was removed from the treatment chamber and stored in a petri dish. The impact of both boiling in DI water and vacuum plasma treatment were monitored using water contact angle analysis, and details of this procedure are the same as those provided in Chapter 3. Contact angle images were collected before and after treatment procedures at various timepoints.

4.2.5 Protocol for assessment of gradient formation

Fluorescence was used to quantitatively examine gradient formation within the microfluidic devices as inspired by previously published work.[43, 123-126] 10 μM fluorescein solutions were made with ultrapure water and sonicated to degas before use. Devices were prefilled to remove all air from the channels before gradient experiments began following the

previously described filling protocols. One device inlet was filled with ultrapure water while the other was filled with the prepared fluorescein solution. After waiting the appropriate amount of time to establish stable flow at the observation channel, based on device length and flowrate, fluorescent imaging was completed. The external distance markers along the observation channel were used to appropriately align images using the digital crosshairs in the camera remote operation software. Brightfield images were collected first before the B-2A filter was used for fluorescent imaging. Camera shutter speed and ISO settings were appropriately adjusted between these sets of images. Once the full set of images were collected at each location within the device, the flowrate was adjusted, and the procedure was repeated. Further experimental details can be found in Appendix C.

4.3 Results and discussion

4.3.1 Progression of fluidic control

One of the areas of fluidic control that changed the most during the development of the device design was the inlet and outlet connections. For fully 3D-printed devices, the most straightforward options were explored first, pipet tips that were press-fit into reservoirs and glued into place. Although this method was crude, it enabled a quick strategy for starting to test other fluidic equipment. Threaded fittings were utilized once the achievable print quality was optimized, and two sizes were used. The seal was easily reinforced with super glue while screwing in the fittings. These small fittings still required a higher volume of liquid to fill, contributing to significant internal dead volume within the device.

The resin-molded PDMS devices offered more flexibility when selecting inlet and outlet connections. The use of 20-gauge needles reduced the internal dead volume at these interfaces, but there were still limitations. Preparing the needles for use was a laborious process involving a

moderate risk when using a power tool to shear off the bevel. The weight of the needle connections, when the Luer lock to barb adaptor was included, could deform the PDMS and dislodge the needle from the reservoirs as well. To regain simplicity in the inlet and outlet connections, 0.1-10 µL pipet tips were used. When the upper section of the pipet tip was trimmed off, it could easily be fitted directly into the 1/16" ID tubing. Although this method was unsophisticated, there were many benefits in its simplicity and the vast availability of pipet tips within a laboratory.

The initial experimental setup using a single syringe pump in withdrawal mode relied on negative pressure to pull liquid through device channels. The overall simplicity of this method was the fundamental motivation behind its implementation. This early work used ultrapure water dyed with food coloring to qualitatively monitor gradient formation. Unfortunately, negative pressure was not an effective method for creating a stable gradient. The flow from one inlet often dominated over the other, which resulted in incomplete gradient formation or complete absence of a gradient. Even the addition of manual valves, for small adjustments to the flowrate from individual inlets, could not overcome the limitations of this setup.

In response to these difficulties, a multi-syringe pump in infusion mode was used. This system relied on positive pressure to push fluid through the channels from both device inlets simultaneously. The resulting gradient was more reliable and fewer fluctuations in performance were experienced. The user simplicity of a multi-syringe pump is comparable to a single pump. The only changes to consider would be the expense of a multi-syringe pump and the increased tubing, fittings, and other fluidic accessories that would be required for an additional syringe. Another negative aspect of this method was the difficulty in removing trapped air from within the channels. For both fully 3D-printed and resin-molded PDMS gradient devices, the

elimination of bubbles within the branching channels was a considerable challenge often requiring many hours. Without any automation, this was a tedious process involving significant user interaction.

The LabSmith uProcess products aided in the creation of a more automated system of fluidic control. The uProcess sequences allowed for programmable fluid handling, and 5 mL reservoirs provided options for exchange between different fluid flows. Sequences can be created in two ways, through the user-friendly interface window or direct coding. Extensive manuals and robust technical support make these products very approachable to new users. One of the most substantial improvements was the greatly reduced footprint of the LabSmith setup (Figure 4.5). This allowed the equipment to be positioned close to the devices, reducing tubing length.

Figure 4.5. Comparison between the multi-channel syringe pump and LabSmith fluidic equipment for gradient experiments. Flat ribbon cables excluded from LabSmith equipment for clearer visual.

Additionally, the PEEK tubing and the low volumes within the valves resulted in a significant reduction in internal volume. Using the LabSmith equipment shown in the Figure 4.4 schematic, excluding the 1/16” ID Masterflex tubing, the total internal volume of the system was only 542.45 µL. Though the cost of this LabSmith equipment is higher than traditional syringe pumps,

the many benefits of this system and the automation it enables are highly desirable for microfluidic cell studies, especially for chemotaxis experiments lasting multiple hours.

4.3.2 Device filling

The formation and persistence of bubbles within microfluidic devices has been a significant issue reported in the literature.[127, 128] This often complicates the process of filling a device, and simply connecting the complex gradient devices to a syringe pump did not result in successful filling. The branched structure and many channel corners of this design make bubble removal even more challenging. Initial attempts to improve device filling started with the development of a filling apparatus shown previously in Figure 4.3. Since the limitation of the tape seal on PMDS devices was known from previous testing, detailed in Chapter 2, the manually applied pressure could be kept below an appropriate threshold for the filling process using the pressure transmitter.

In addition to the filling apparatus, alternative solutions were investigated to improve the filling process and reduce bubbles. A solution with lower surface tension than water would be used for filling the device and could be flushed from the channels once filling was completed. This is often achieved by using an organic solvent, such as ethanol, or through the addition of a surfactant in water.[129] Tests using different percentages of ethanol in water contributed to some degradation of the adhesive seal. The potential persistence of an organic modifier was also a concern for future cell culture within the devices. Alconox, the glassware soap, was selected as another option for this work. The general availability of Alconox in a laboratory setting, the nonhazardous composition, and the reported ability to be fully rinsed without residue all contributed to the selection of this surfactant.[130] A dilute solution of Alconox in ultrapure water

had a considerably lower contact angle on the 9795R adhesive surface than ultrapure water alone (Figure 4.6).

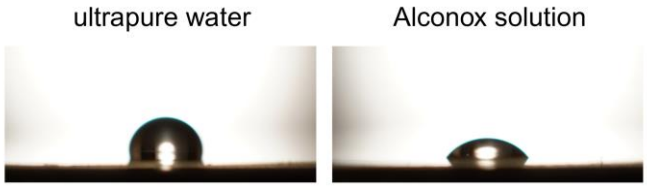

Figure 4.6. Contact angle comparison between ultrapure water (left) and the Alconox filling solution (right) on the 9795R tape adhesive surface.

The combination of the filling apparatus and Alconox solution were employed to fill PDMS devices with a simple channel design. All solutions were subject to sonication in an ultrasonic bath before filling to help remove dissolved gas. The real-time readout from the pressure transmitter was used as intervals of relatively constant pressure followed by intervals of increasing pressure were manually applied to aid in bubble removal (Figure 4.7 left). This resulted in the most success with shrinking the bubbles trapped within the devices. It was critical to observe the pressure readout, bubble size, and channel walls simultaneously to avoid rupturing the seal. During the bubble removal process, the pressure could expand flow beyond the molded channel walls producing bulging, but this was not indicative of device failure as long as the seal deformation was minimal (Figure 4.7 right). Flow could then be exchanged from the filling apparatus to the prepared syringe pump to remove any small bubbles with dark, pronounced outlines that remained.

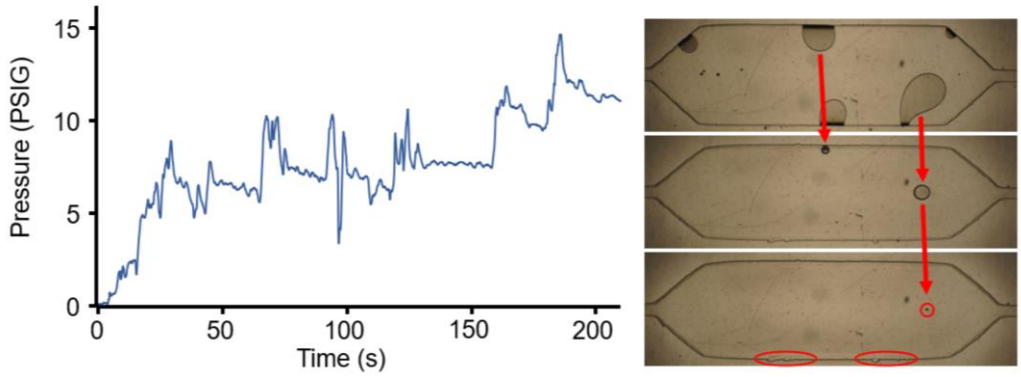

Figure 4.7. Sample readout from pressure sensor during bubble removal (left). Periods of increasing pressure application and relatively constant pressure were used to shrink bubbles over time (right). The pressure buildup could cause bloating and surpass the molded channel walls while still maintaining a seal (right bottom).

4.3.2.1 Examination of PDMS surface modification

To further simplify the filling process, two surface treatment procedures were investigated to decrease the hydrophobic nature of PDMS. It has been reported that boiling PDMS in DI water can be a simple, cost-effective, and mild method for the generation of surface-based hydroxyl groups.[122] For this research, 30 min and 2 hr boiling lengths was tested on PDMS slabs. Water contact angle measurements were used to analyze the impact of this treatment method, and the results are summarized in Tables 4.1 and 4.2 below.

Table 4.1. Contact angle analysis for PDMS samples boiled in DI water for 30 min (n = 9).

Average contact angle ± standard deviation			
Native PDMS	**Immediately post-boil**	**1 hr after boil**	**4 hr after boil**
99 ± 1.3°	92 ± 3.3°	92 ± 4.6°	91 ± 5.0°

Table 4.2. Contact angle analysis for PDMS samples boiled in DI water for 2 hr (n = 9).

Average contact angle ± standard deviation			
Native PDMS	**Immediately post-boil**	**1 hr after boil**	**4 hr after boil**
98 ± 1.9°	94 ± 2.6°	93 ± 2.1°	94 ± 1.8°

The boiled PDMS samples did gain a frosted appearance after boiling and drying. The frosted appearance began to fade over time, starting from the edges of the PDMS slab towards the middle around 1hr after boiling. By 4 hr after, this look faded completely, and the PDMS was completely transparent again. Based on the contact angle results, boiling in DI water had little impact on the PDMS surface, and this method of surface modification was determined to be ineffective for this application.

Plasma treatment has been more consistently utilized and reported on as a method for PDMS surface modification to improve wettability.[53, 121, 131, 132] The PDC-32G plasma cleaner from Harrick used in this work could not apply as high of voltage to the RF coil as many of the systems used by other researchers. Based on this, it was expected that the treatment impact would not be as long-lasting as has been reported. Again, contact angle analysis was performed to track the changes over time, and the results are shown below in Table 4.3.

Table 4.3. Contact angle analysis for plasma-treated PDMS (n = 3).

Length of plasma exposure (min)	Average contact angle ± standard deviation				
	Before treatment	0.5 hr after treatment	4 hr after treatment	8 hr after treatment	24 hr after treatment
1	88 ± 5.1°	59 ± 12°	74 ± 5.8°	82 ± 6.4°	92 ± 4.5°
4	83 ± 6.4°	55 ± 6.1°	69 ± 3.8°	72 ± 3.3°	81 ± 5.8°
8	94 ± 8.2°	58 ± 8.0°	79 ± 0.8°	86 ± 5.1°	87 ± 3.9°

There was a far more substantial decrease in water contact angle of the plasma-treated PDMS surfaces. Even the PDMS treated for only 1 min resulted in a significant change in contact angle. As time following the treatment progressed, the hydrophobic nature of the PDMS began to return, as was expected, and the impact of plasma treatment was lost by 24 hr.

Pairs of 6-part gradient devices were used to assess the impact of plasma treatment of device filling. One gradient device was subject to 6 min of plasma treatment while the other was left untreated. The plasma-exposed device was sealed with 9795R tape within 10 min after treatment concluded. After both devices were sealed with tape, a 4 hr waiting period elapsed before the devices were filled. The high flowrate filling uProcess sequence and LabSmith equipment were used. The plasma-treated and untreated devices performed equally with fluid flow reaching the outlet within 7 s. A comparable extent of initial air bubbles were observed, and continuous flow with periods of gentle agitation successfully filled all devices over similar lengths of time. Further optimization of the filling uProcess sequence greatly reduced the amount of time required to fill and remove bubbles from untreated devices, even as quickly as 25 min. Therefore, the implementation of plasma treatment into device fabrication and experimental preparation was not considered worthwhile given the additional machinery required.

4.3.3 Evaluation of factors influencing gradient formation

Experiments involving gradient formation began before resin 3D printing capabilities were fully optimized. As a result, these studies were completed using PDMS devices made from photolithographic molds and sealed with 9795R tape. Although the fabrication method and some of the device dimensions are different than the resin-molded devices, the same principles governing fluid flow and gradients should still apply. Fluorescein was used to assess gradient formation by filling the device with ultrapure water and a 10 μM aqueous solution of fluorescein at each inlet. As these streams proceeded through the serpentine mixing region of the device, a gradient in fluorescein concentration was formed. The resulting differences in fluorescent intensity could be measured across the observation channel, perpendicular to the direction of flow, to provide a visual profile corresponding to the gradient profile. These fluorescent profiles were used to determine how various factors influenced gradient formation within devices.

The first factor explored was flowrate. There were two important considerations when selecting and examining an appropriate flowrate for this microfluidic device. Primarily, the flowrate must be strong enough to maintain a stable gradient formation. A range of potential flowrates, set by syringe pump, were tested to observe the impact on gradient formation. Fluorescent imaging centered at the start of the observation channel, the 0.0 mm distance, demonstrated how well mixing occurred within the serpentines as those separate streams initially recombine. If the flowrate was too low or too high, the flow from one inlet can dominate over the other. This resulted in an uneven fluorescent intensity profile compared to a more consistent progression of fluorescent intensity across the observation channel when an appropriate flowrate was used (Figure 4.8).

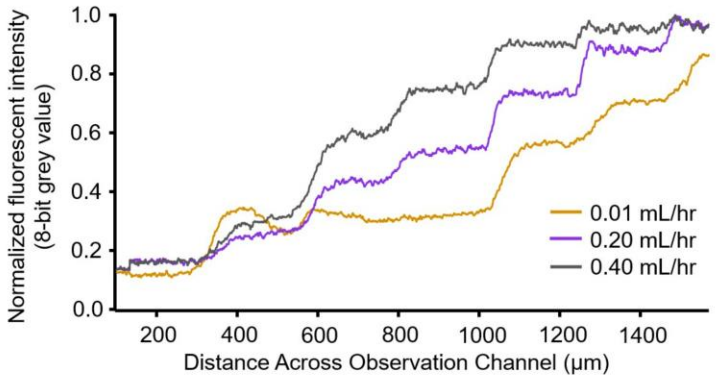

Figure 4.8. Changes in the selected flowrate impact the resulting gradient formation within the observation channel.

The second critical aspect of flowrate is the impact on cell health. A balance must be found between maintaining the gradient and ensuring suitable conditions for cells within the devices when determining experimental flowrates. Shear stress is the force applied across a specified cross-sectional area. This is created within microfluidic devices when fluid is passed through channels with boundary walls. Fluid shear stress (τ) can be calculated, under the assumption that cells experience wall shear stress between two parallel plates, using

Equation 4.1. Fluid shear stress between two parallel plates.

$$\tau = {}^{6\mu Q}/_{h^2 w}$$

where μ is the dynamic viscosity, Q is the flowrate, h is the channel height, and w is the channel width.[133] All cells experience different amounts of shear stress in the body, influenced by both normal or disease conditions, and the impact of this stress can have critical influence over cell function, gene expression, migration, and differentiation.[134-136] Attempts to accurately calculate shear stress within microfluidic devices can be challenging for a variety of reasons. The presence of cells within channels impacts fluid flow, some channel geometries like narrowed regions or corners create areas of higher stress, and pressure-driven flow can deform PDMS channels.[135, 137]

Although these limitations persist, an approximation of the range of shear stress generated within the resin-molded PDMS devices used in this work would provide more context about the experimental conditions the cells are subjected to.

A spreadsheet was used to calculate the resulting Reynolds number and shear stress based on the observation channel dimensions and the highest and lowest flowrates achievable using the LabSmith SPS01-080 syringe pumps. An annotated version of this spreadsheet is available in Appendix C. The values used for the density and dynamic viscosity of DMEM (high glucose) supplemented with 10% FBS (v/v) were 1.009 ± 0.003 g/cm^3 and 0.930 ± 0.034 mPa·s, respectively, as provided by Christine Poon.[138] Based on the dimensions of the observation channel for the 6-part gradient device design, and the maximum flowrate, 2800 µL/min, and minimum flowrate, 1.0 µL/min, the resulting high Reynolds number value was approximately 44.989, and the low value was approximately 0.016. These values remain below the threshold at 2000 signifying the transition from laminar to turbulent flow.[139]

Additionally, the calculated high and low shear stress values were approximately 0.303 and 1.080 x 10^{-4} dyne/cm^2. The physiological range for shear stress in the brain, used in studying the BBB with human fetal astrocytes, is between 1-2 dyne/cm^2.[140] Other researchers have reported shear stress within the brain tumor environment to be between 0.09-0.68 dyne/cm^2.[141] Li *et al*. used experimental flowrates to test fluid shear stresses of 0.12, 1.2, and 1.8 dyne/cm^2 on U-87 cells to monitor the resulting cell morphology and adhesion strength.[142] Although the lower end of the potential experimental flowrates would provide considerably lower shear stress than previously reported or used with healthy or cancerous brain cells, the highest flowrate does not exceed these reported shear stress levels. Working with this equipment should not create uninhabitable conditions for the U-87 cells due to flowrate and the resulting fluid shear stress.

Another factor investigated was the shape of the channels as they intersected with the observation channel. In the blunt entry design (Figure 4.9 left), constant spacing between the channels left void regions between the separate streams. The flared entry design (Figure 4.9 right) eliminated the spacing between the channels, and the potential impact of these design changes were examined. As shown in Figure 4.9, the entry shape altered the flow pathway. The flared entry channels caused significant deflection or bending in the fluid streams toward the side with higher fluorescein concentration, while the blunt design resulted in more direct flow into the observation channel.

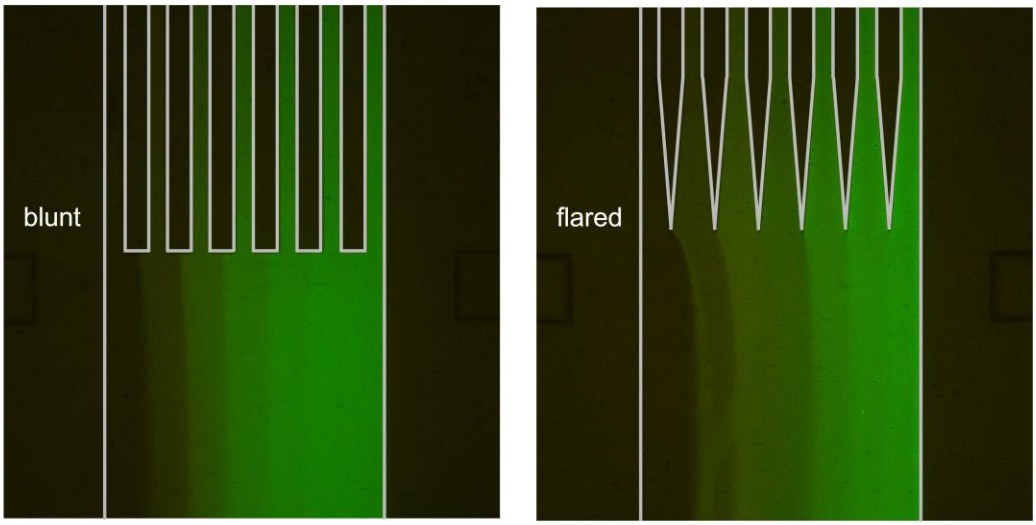

Figure 4.9. Comparison between blunt (left) and flared (right) channel shape into the observation channel. The flared channels resulted in a deflection or bend of the different streams into the observation channel that was not observed with the blunt channel shape.

The final element examined was the impact of distance on the gradient profile. For this work, the external distance markers were utilized to align fluorescent imaging at increasing distance down the observation channel (Figure 4.10 A and B). The increased distance produced a smoothing of the gradient intervals. As explained in Chapter 1, mixing under the conditions of laminar flow is based on diffusion, and this principle is used to form the streams of varying concentration in the serpentine mixing channels due to their significant length. The length of the

observation channel also allows for diffusion between the parallel streams of increasingly concentrated fluorescein, resulting in a more gradual increase in fluorescent intensity across the observation channel (Figure 4.10 C).

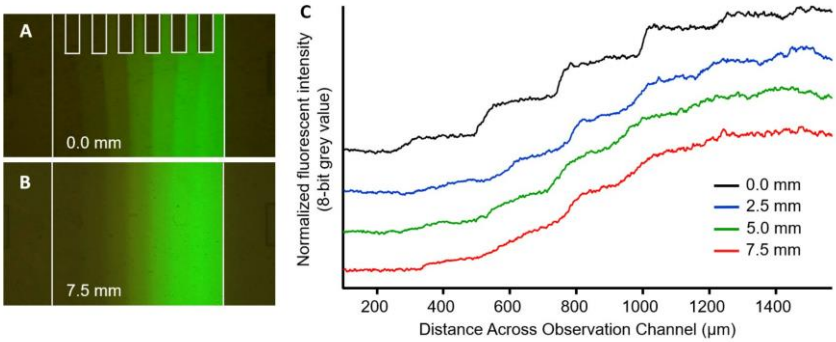

Figure 4.10. Fluorescent images were collected at specified distances from the start of the observation channel (A, B). The corresponding fluorescent intensity was compared to examine the impact on the gradient profile, and a smoothing of the gradient profile was observed as distance increased (C). Profiles were offset for clarity.

This gradient smoothing is critical when considering what conditions will be necessary to induce chemotaxis. An imbalance in chemoattractant binding across a single cell body must be present for directed cell migration. Therefore, distinct regions of relatively constant concentration far wider than a cell would not successfully cause chemotaxis unless a cell happens to be positioned at the interface of two of these regions. The more gradual gradient profile further down the observation channel would provide conditions more likely to induce chemotaxis. This work has highlighted a potential region-of-interest within the device for future cell experiments.

Finally, the LabSmith equipment was used to fill resin-molded, 6-part gradient PDMS devices. The same fluorescent analysis was repeated with this experimental setup, as described previously and in Appendix C. The analysis revealed the same gradient smoothing as previously observed when the larger multi-syringe pump was used (Figure 4.11). The slower flowrates achievable using the LabSmith equipment resulted in a more linear gradient profile (Figure 4.11

C). The steeper slope of this profile signified a larger change in fluorescent intensity over shorter distance.

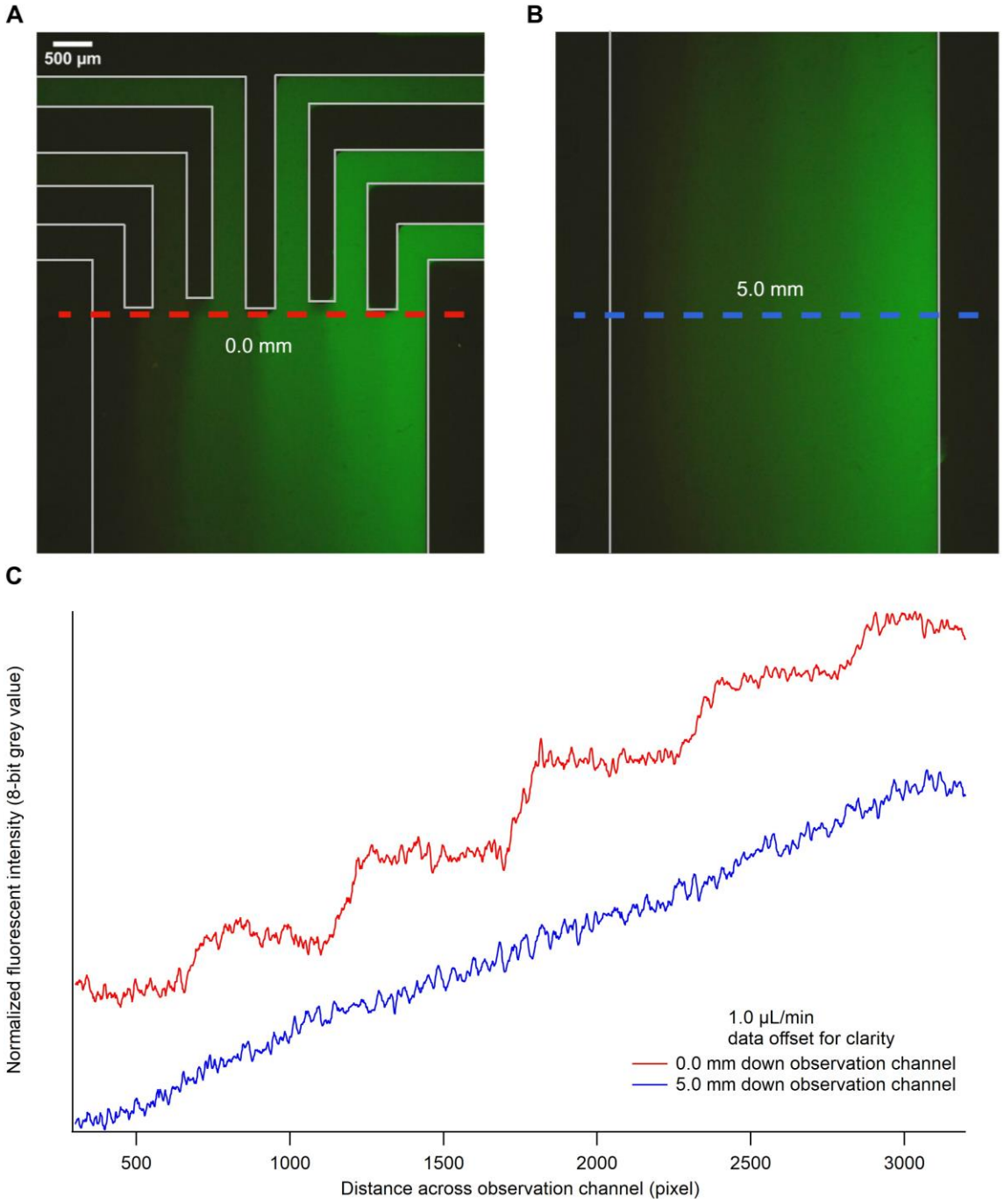

Figure 4.11. Fluorescent gradient formation at the start (A) and middle of the observation channel, 5 mm from the start (B) using the LabSmith equipment and a resin-molded PDMS device. Analysis of the fluorescent intensity profiles showed gradient smoothing as distance increased down the observation channel, even resulting in a near-linear gradient profile (C).

When utilized for future cell studies, these experimental conditions should provide a more dynamic chemoattractant gradient, with nearly continuous change in concentration across the observation channel, which will be essential for inducing chemotaxis.

To better identify how long this near-linear gradient could be sustained, more fluorescent gradient profiles were collected along the observation channel by aligning between the distance markers during a separate experiment.

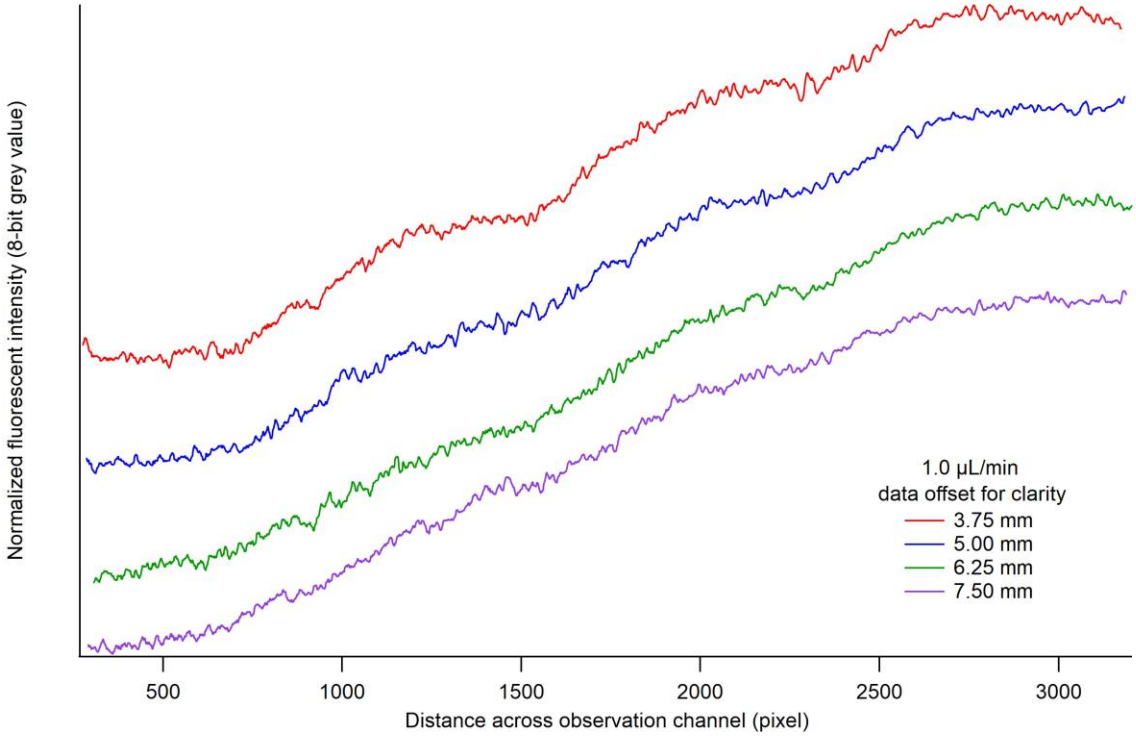

Figure 4.12. The fluorescent intensities were examined at more distances down the observation channel at a flowrate of 1.0 µL/min. The selected profiles represent the transition from wider regions of stable fluorescence to a more linear gradient profile.

The discrete and wide regions of the relatively stable fluorescence began to smooth by approximately 3.75 mm, and the more linear profile was established and maintained between 5.0 and 7.5 mm (Figure 4.12). This leaves a region of interest about 2.5 mm long and 4.3 mm wide for cell placement within the best gradient condition of the device. These results are very

promising for the upcoming migration experiments and will guide future experimental procedures.

4.4 Conclusions

Many iterations of fluidic control were tested as the device design changed during the development process. The transition to resin-molded PDMS devices eliminated the difficulty of ensuring a water-tight interface between the rigid resin and threaded fittings. Surfactant was incorporated into the filling process to reduce the liquid surface tension and the time required to fill a device. An initial filling procedure incorporated real-time pressure monitoring to aid in the lengthy bubble removal. Two methods of PDMS surface modification were investigated but resulted in minimal improvements in the filling process.

A finalized method of fluidic control was established utilizing the LabSmith uProcess equipment. This provided a simple-to-use method of experimental automation requiring small space and low internal volume. Different liquids could be easily interchanged using the incorporated reservoirs, which would be essential for more complex cell studies. The continuous filling setup allowed for reliable and faster filling of gradient devices using higher flowrates and stable gradient formation at lower flowrates. The calculated estimations of shear stress for the range of potential flowrates were all below or within reported physiological levels appropriate for future cell experiments. Examination of the gradient profiles within the microfluidic devices highlighted an area of interest in the observation channel where a more linear change in chemoattractant concentration could result in cell migration. This progress has overcome the remaining barriers to employing this device as a tool to investigate GBM chemotaxis.

Chapter 5 - Initial migration studies of GBM

5.1 Introduction

Microfluidic devices offer a unique platform for monitoring cell movement by enabling real-time, live cell imaging within a controlled environment. In these preliminary studies, multiple chemoattractants were tested to induce U-87 chemotaxis, and fluorescent imaging was used to track cell position within the observation channel in response to the generated gradients. Initial results showed some minor differences in GBM migration in response to various chemoattractant solutions and provided proof-of-concept for the use of this low-cost and simple microfluidic device for the study of cell movement.

5.2 Materials and methods

5.2.1 Reagents, materials, equipment, and software

The various products and procedures used for this research are provided below, in previous chapters, or in the Appendices. 6-part gradient PDMS devices, made from resin 3D-printed molds and sealed with 3M™ 97995R tape, were fabricated and prepared for experiments as detailed in Chapter 3. The LabSmith equipment and uProcess automation software were utilized as described in Chapter 4 for fluidic handling.

5.2.1.1 Chemoattractant solutions

Recombinant human hepatocyte growth factor (HGF) and recombinant human transforming growth factor-α (TGF-α) were purchased from PeproTech (Cranbury, NJ, USA).

5.2.1.2 Tissue culture

The tissue culture protocols used for U-87 cells provided in Chapters 2 and 3 were used for this work. Further protocol details can be found in Appendix B.

5.2.1.3 Imaging equipment and fluorescence work

See previous chapters for detailed descriptions of the equipment used for imaging procedures. Additional image assessment was completed using Microsoft Paint, ImageJ, and Igor Pro.

5.2.1.4 Other laboratory equipment

See the previous chapters for further details about any additional laboratory equipment that was used.

5.2.2 Migration study procedures

6-part gradient devices were prepared for cell experiments as detailed in Chapter 3. Following HA+PDL treatment, but before manual cell injection, the reservoir on one side of the fluidic system was filled with the chemoattractant solution. The tubing was primed with approximately 271 μL of fluid to enable chemoattractant gradient formation as soon as possible once flow was restarted by bringing the chemoattractant solution near to one device inlet. U-87 cells were maintained within the miniature scope-top incubator, without any flow, for 3 to 4 hr to allow for cell attachment. The external tubing heating pad was used to keep the solutions at an elevated temperature while cells attached. Images were collected at regular intervals, to track cell position and morphology at the specified imaging location (Figure 5.1), on the Nikon Eclipse TE2000-U inverted microscope using the Sony Alpha a6400 camera, Nikon B-2A filter cube, and the X-Cite 120 Fluorescence Illumination System.

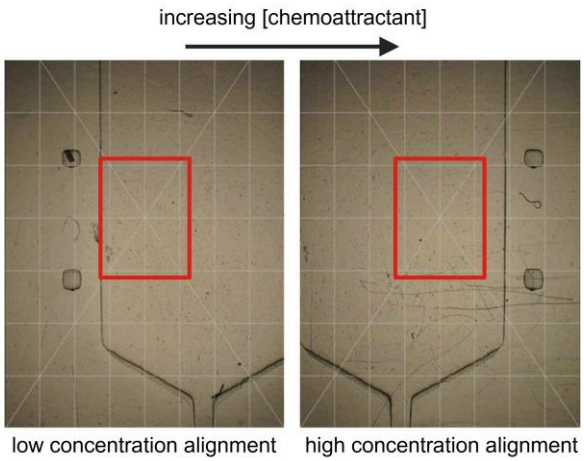

Figure 5.1. Digital crosshairs showing imaging alignment for cell migration experiments at both the lower and higher end of the chemoattractant concentration gradient.

Before restarting flow at 1.0 µL/min, the media and chemoattractant solutions within the reservoirs were refreshed with 100 µL of stock from the incubator. This reservoir replenishment was repeated as necessary throughout the length of the experiments. Images continued to be collected at regular intervals, and image processing and analysis was completed using Microsoft Paint, ImageJ, and Igor Pro. A more detailed protocol can be found in Appendix C.

5.3 Results and discussion

5.3.1 Initial analysis of cell motion

All cell migration analysis was completed using the same process. CMFDA images collected at each timepoint were converted to 8-bit grey scale, and 8 cells were manually selected for tracking based on morphology before restarting flow. The x and y coordinates of each marked cell were then used to define the cell positions at each timepoint (Figure 5.2).

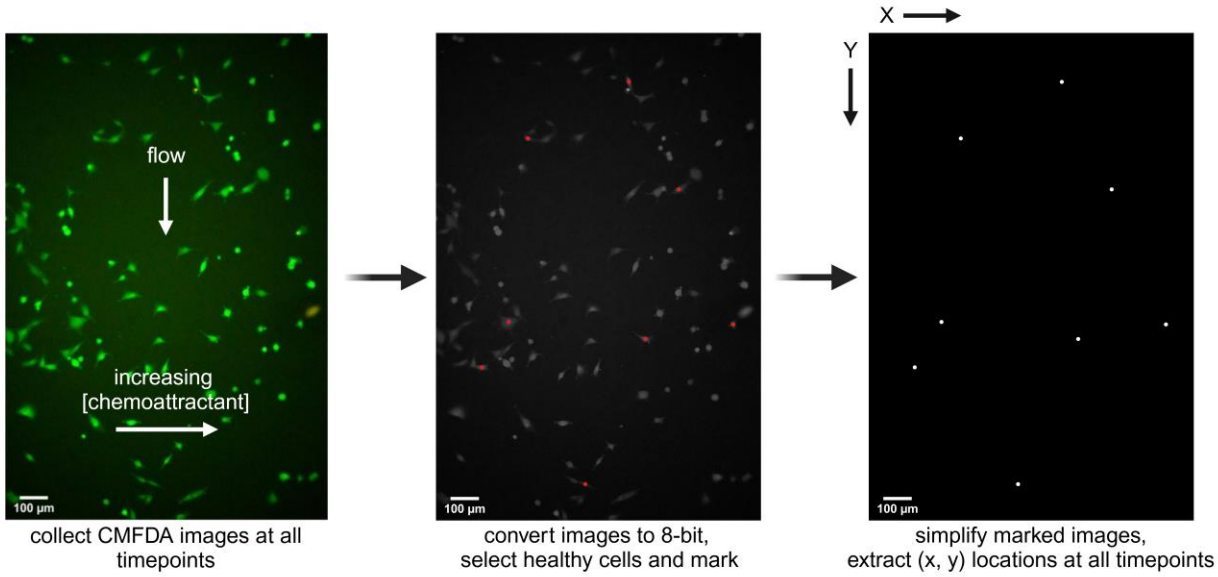

Figure 5.2. The process for monitoring cell positions during flow experiments. During all experiments, flow proceeded from the top to the bottom of the collected images and the gradient increased from left to right when chemoattractants were used (left). All CMFDA images were then converted into 8-bit, and 8 healthy cells were selected for tracking and manually marked (middle). Simplified, marked images were used to extract the (x, y) central coordinates of each mark at all timepoints (right). These coordinates were then used for tracking cell movement in response to experimental conditions.

Five timepoints, representing 3.5 or 4 hr of flow in total, were used for the initial evaluation. At a flowrate of 1.0 µL/min, it would take approximately 30 min for the entire volume of the 6-part gradient device to be replaced. Since the tubing was primed with the selected solutions prior to cell seeding, the desired chemoattractant gradient would be formed within that 30 min window. The cell movement was assessed by subtracting the x and y values of the first timepoint from the x and y values of the fifth timepoint for each of the 8 cells. Additionally, the x and y displacements were averaged to determine the overall direction and magnitude of GBM movement during the experiments.

To better understand the impact of various chemoattractants on cell migration, the movement of GBM cells under constant 1.0 µL/min flow without any chemoattract gradient was examined. Image collection was aligned at 6.25 mm down the observation channel in the y

direction and in the center of the observation channel in the x direction. The results from the migration analysis are reported below (Figure 5.3).

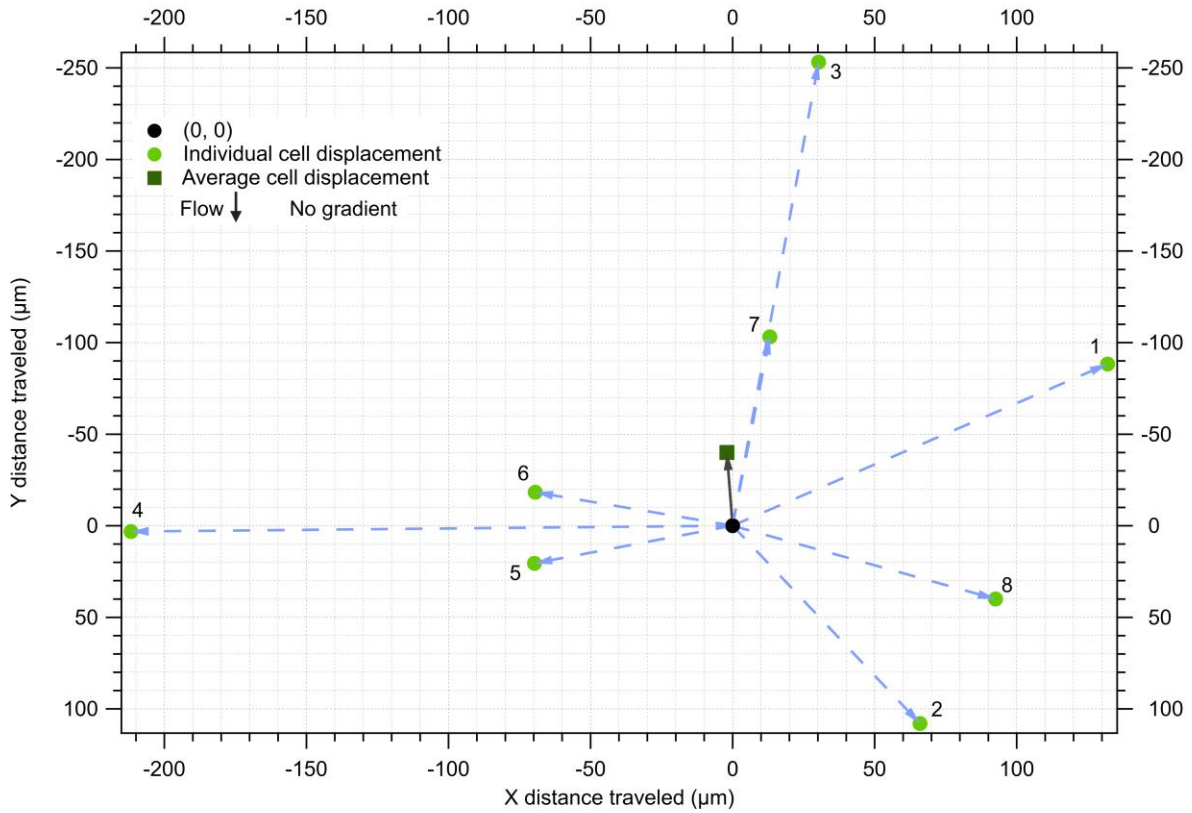

Figure 5.3. Analysis of U-87 cell movement when no chemoattractant gradient was present. The average direction of cell displacement in a negative y direction indicated that without a chemoattractant gradient, more substantial cell movement was observed against the direction of flow. Note: The y axis orientation to maintain consistencies between the direction of flow during image collection and displacement results.

A wide range of movement in the positive and negative x directions was observed for the selected cells, resulting in a very small x component for the average displacement. This can be explained by the more random and undirected movement exhibited by the cells as they investigated their environment. Furthermore, the average y component of the cell displacement was in a negative direction, against the direction of flow.

Following these results, a chemoattractant solution containing 1.0 nmol/L HGF was tested. HGF was selected for initial experiments due to its reported significant stimulation of chemotaxis for U-87 cells.[143] The camera was aligned at 6.25 mm down the observation channel, the region with the most linear gradient profile as determined in Chapter 4, and shifted in the x direction towards the end of higher concentration (Figure 5.1 right). Results from these experimental conditions are presented below (Figure 5.4).

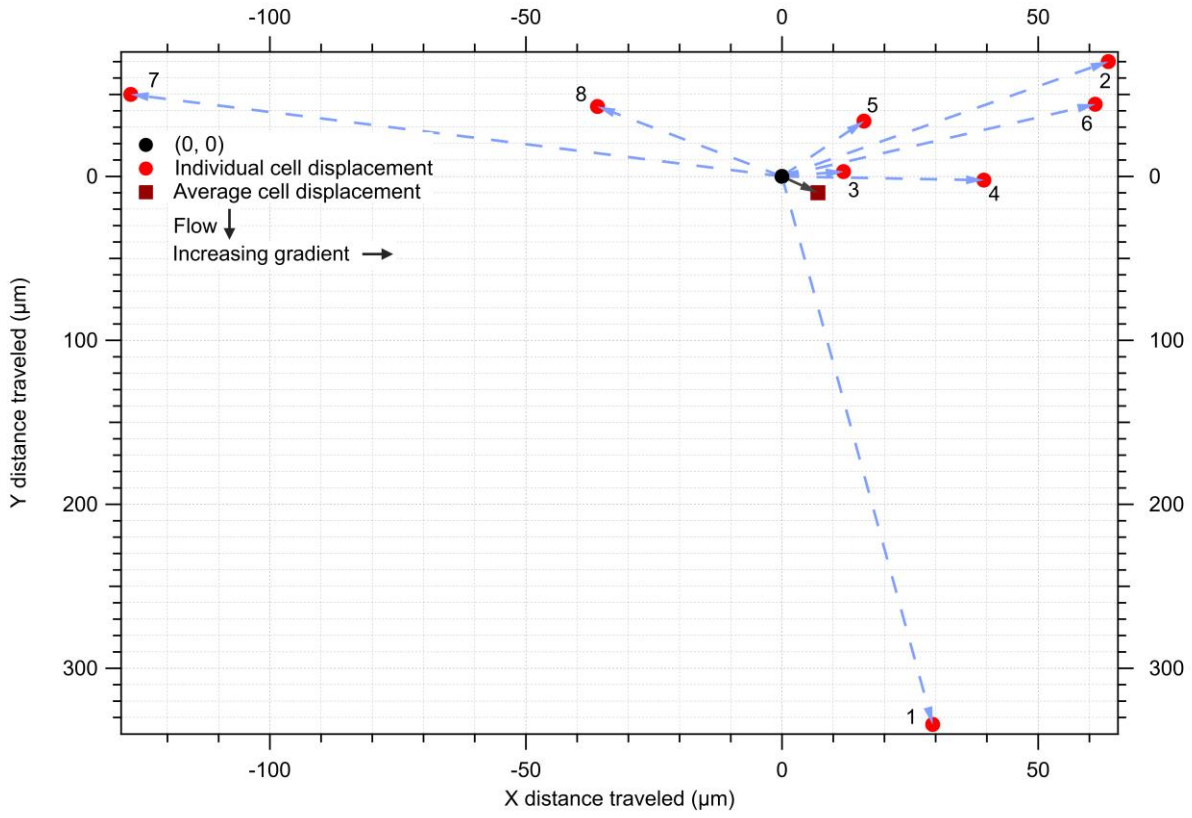

Figure 5.4. Analysis of U-87 cell movement in a 1.0 nmol/L HGF gradient. The positive x direction of the average cell displacement could signify some chemotactic GBM behavior was observed, although the value of the x component was quite small.

Even though cell 1 showed substantial displacement in the positive y direction, with the flow, the average was greatly reduced due to the number of cells with negative y displacement. A larger average x component in the positive direction was observed versus the experiment without

any chemoattractant, but the overall magnitude was small when compared to some individual cell movement and the typical diameter of a GBM cell, 10-30 μm.[102]

In an attempt to enhance the chemotactic response, HGF was combined in solution with another reported U-87 chemoattractant, TGF-α.[143] A gradient of FBS was also created by only using supplemented DMEM in the chemoattractant solution. This experimental condition was chosen based on a microfluidic chemotaxis study of U-87 spheroids.[144] Imaging alignment at 6.25 mm down towards the higher concentration side of the observation channel was repeated. The movement analysis is shown below (Figure 5.5).

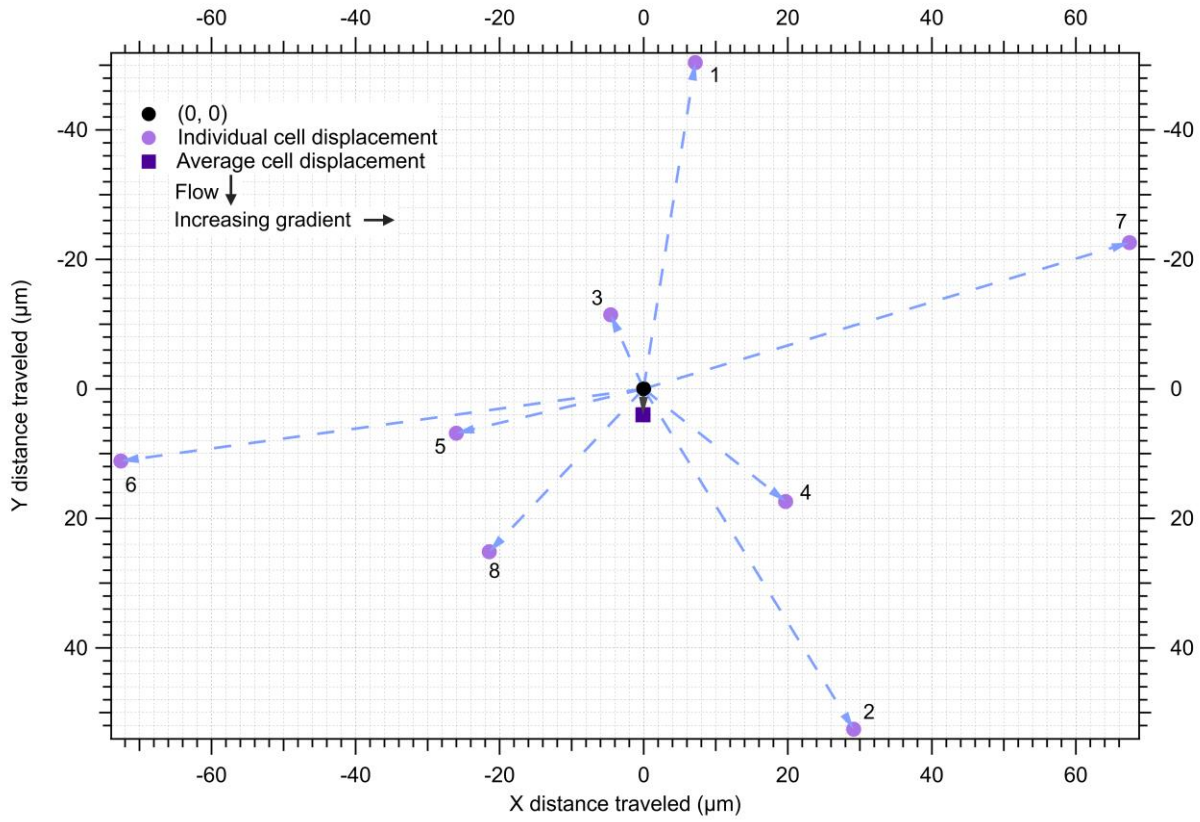

Figure 5.5. Analysis of U-87 cell movement in response to the chemoattractant gradient comprised of 0.5 nmol/L HGF, 5.0 nmol/L TGF-α, and 10% FBS-supplemented DMEM. A larger variety in the direction of cell movement was observed, resulting in a far smaller average displacement overall.

Cell movement was far more spread under these conditions, which contributed to small average cell displacement in both the x and y directions. This was more similar to the results from the first migration study without a chemoattractant solution, although the y displacement was slightly positive instead of negative. The lack of FBS in the native cell media could have prompted more cell migration in all directions as the cells surveyed for growth factors they were recently starved of. As a result of this change in cell behavior, the use of supplemented DMEM was resumed in all solutions.

For the final conditions tested in these initial migration studies, the chemoattract solution included 0.5 nmol/L HGF and 5.0 nmol/L TGF-α. In addition, the imaging location was shifted in the x direction towards the side with a lower expected concentration of chemoattractant, as shown on the left of Figure 5.1. The change in imaging alignment was implemented to see if more substantial chemotaxis was observable in a region transitioning from no chemoattractant to low levels as compared to a transition from moderate to high chemoattractant concentration. The results are reported below (Figure 5.6).

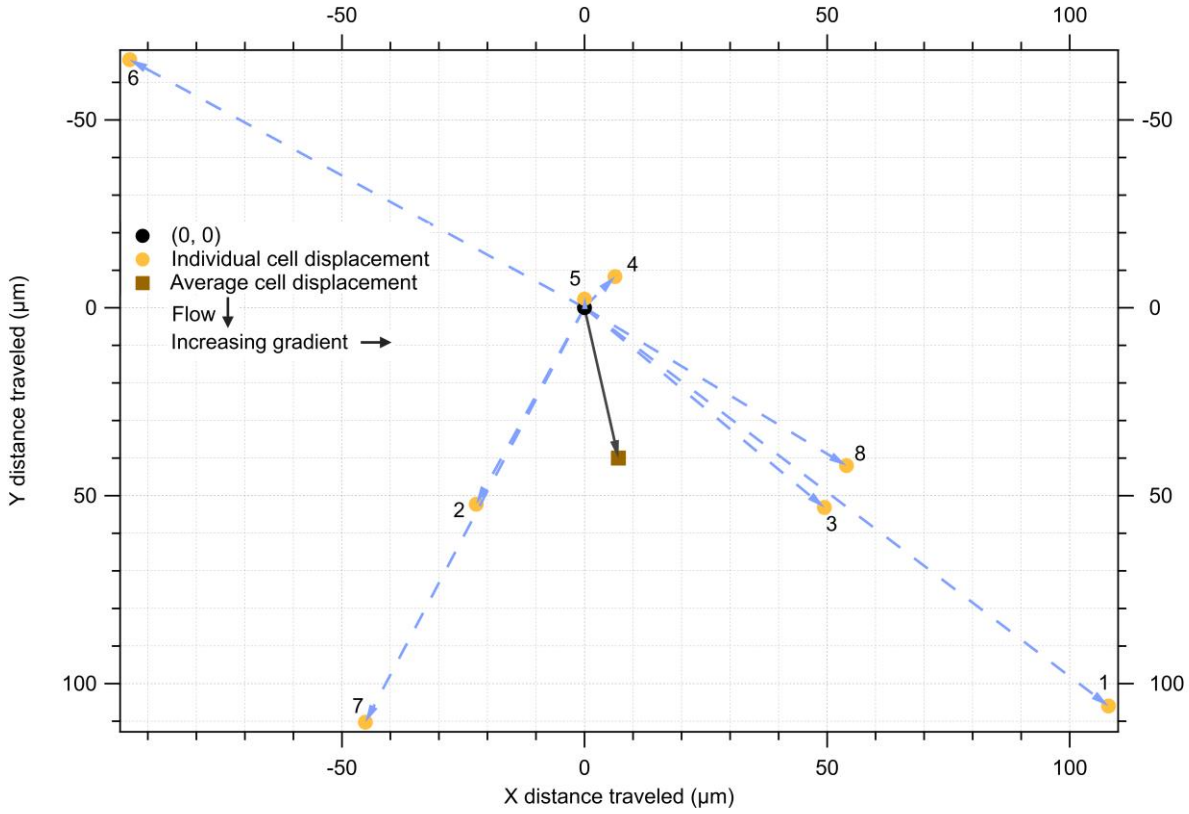

Figure 5.6. Analysis of U-87 cell movement when aligned toward the lower concentration side of a 0.5 nmol/L HGF and 5.0 nmol/L TGF-α chemoattractant gradient. More significant migration was observed in the positive y direction than in any other experiment.

A similar degree of positive average x displacement was observed for this experiment and the 1.0 nmol/L HGF gradient, a compelling indicator that a near-linear gradient profile was established across the entire width of the observation channel. This experiment resulted in the largest average y displacement with the direction of flow. It was possible that the combination of chemoattractants, without any interference from a FBS gradient, prompted this more significant y movement. The displacement values for all monitored cells, and the average displacement under all experimental conditions, are summarized in Table 5.1. To better compare the average displacements, all four results are presented in Figure 5.7.

Table 5.1. Summary of cell displacement results for all initial migration experiments.

Cell	No chemoattractant		HGF chemoattractant		HGF, TGF-α, FBS chemoattractant		HGF, TGF-α chemoattractant	
	$X_5 - X_1$ (μm)	$Y_5 - Y_1$ (μm)	$X_5 - X_1$ (μm)	$Y_5 - Y_1$ (μm)	$X_5 - X_1$ (μm)	$Y_5 - Y_1$ (μm)	$X_5 - X_1$ (μm)	$Y_5 - Y_1$ (μm)
1	130	-88	29	330	7.2	-50.	110	110
2	66	110	64	-70.	29	53	-22	52
3	30.	-250	12	-2.9	-4.6	-11	49	53
4	-210	3.2	39	2.3	20.	17	6.3	-8.3
5	-70.	21	16	-34	-26	6.8	0.0	-2.3
6	-69	-18	61	-44	-73	11	-94	-66
7	13	-103	-130	-50.	67	-23	-45	110
8	93	40.	-36	-43	-21	25	54	42
Avg ± stand dev	-2 ± 100	-40 ± 100	7 ± 60	10 ± 100	-0.1 ± 40	4 ± 30	7 ± 60	40 ± 60

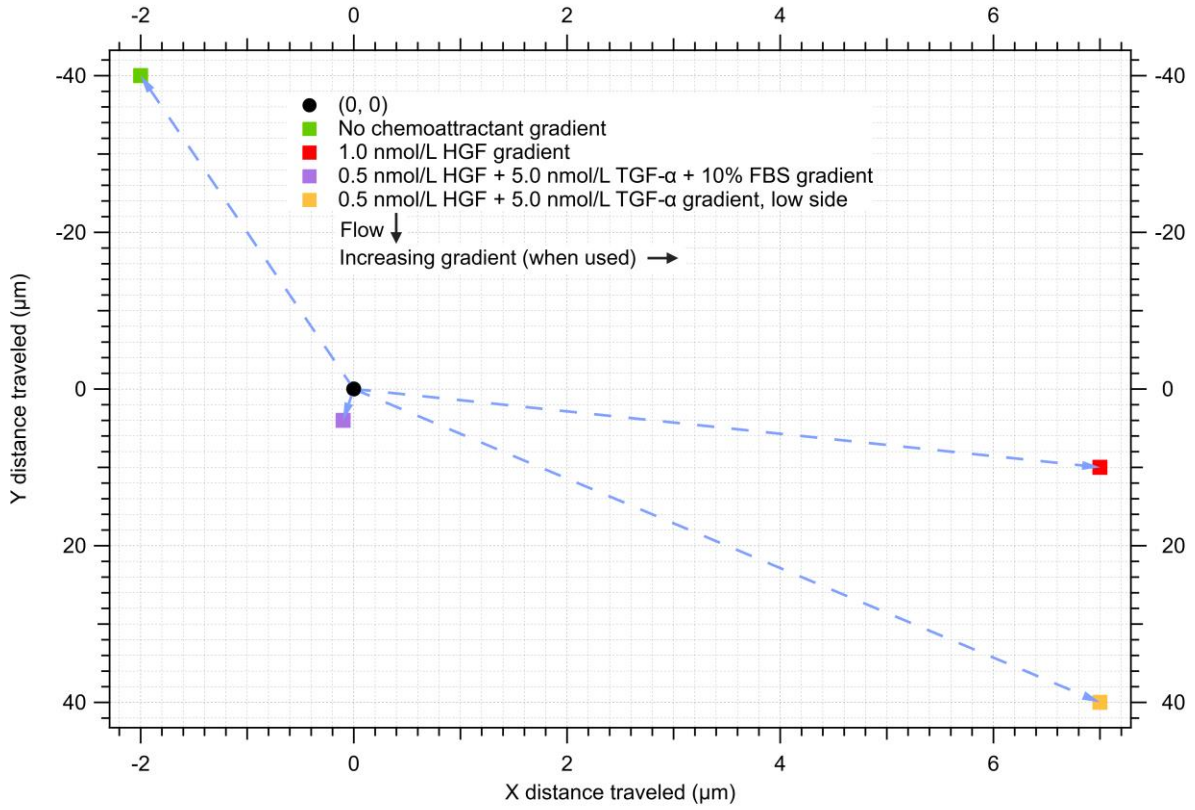

Figure 5.7. The average U-87 cell displacement for all initial experiments. The experiment without any chemoattractant gradient (green), resulted in the only negative displacement in the y direction. 1.0 nmol/L HGF (red) and the combination of 0.5 nmol/L HGF and 5.0 nmol/L TGF-α (yellow) produced comparable displacement in the positive x direction, although both were a small distance.

As previously explained, the magnitude of the positive average x displacement observed for HGF alone and the combination of HGF with TGF-α could be viewed as insignificant when the size of GBM cells, especially in the stretched morphology, is considered. However, there was a more considerable difference in average y displacement between the experiment without a chemoattractant gradient (Figure 5.7 green) and the HGF (red) and HGF with TGF-α (yellow) experiments. This variation was the strongest evidence of an observable change in cell movement from the GBM cells.

A Grubbs test, at the 95% confidence level for 8 observations, was used to identify and remove any statistical outliers from the cell displacement values of all the experimental conditions tested. Only the y displacement for cell one, 330 μm, and the x displacement for cell seven, -130 μm, under the 1.0 nmol/L HGF gradient were outliers (Table 5.1). This resulted in an adjusted average x displacement of 30 ± 30 μm and an adjusted average y displacement of -30 ± 30 μm. The larger average x displacement was stronger evidence of a chemotactic response by the U-87 cells. Additionally, the negative average y displacement was indicative of cell migration against the direction of flow. The adjusted comparison between the average displacements is shown below (Figure 5.8).

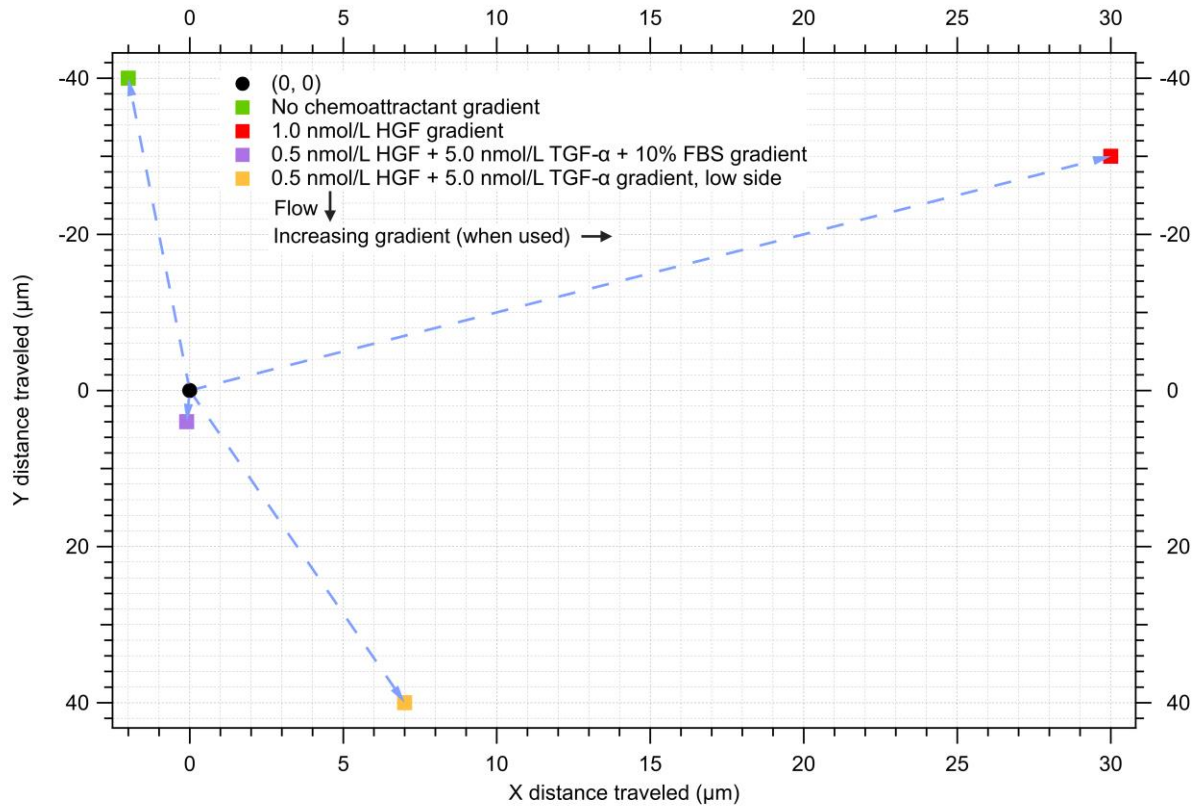

Figure 5.8. The average U-87 cell displacement with the adjusted x and y displacement for the 1.0 nmol/L HGF (red) experiment based on outlier removal via the Grubbs test. The value of this new average x displacement was far closer to the size of a GBM cell and could be indicative of a more prominent chemotactic response when a higher concentration of chemoattractant is used in these devices.

Although the analysis detailed above provided a method for analyzing cell movement, there was a lack of substantial, unified chemotaxis during these initial experiments. A variety of factors could have caused this result. The first potential reason was an error in gradient formation, but fluorescein gradient experiments, as outlined in Chapter 4, were repeated and confirmed a comparable gradient profile at the imaging location under the experimental conditions.

The next likely factor was the concentration of chemoattractants used during initial tests. The starting concentrations for both HGF and TGF-α were determined based on a reported U-87

chemotaxis study, which used a Boyden chamber to assess migration.[143] As explained in Chapter 1, there are known limitations for these experiments, especially the chance of measuring chemokinesis instead of chemotaxis. It was also possible that chemoattractant concentrations successfully implemented in Boyden chamber studies would be inappropriate for microfluidic studies given the many differences in experimental setup. More time optimizing the chemoattractant concentrations has a good chance of producing the desired chemotactic response in these devices. The adjusted average displacement results for the 1.0 nmol/L HGF gradient, after removal of outliers via the Grubbs test, showed a stronger migration response in the direction of increasing concentration, suggesting that higher concentrations of chemoattractants could induce more substantial chemotaxis of the U-87 cells.

A different source of error could have been the analysis method itself. Due to the significant size of the image files, fully automated tracking of every cell was not possible using ImageJ alone. Only 8 cells from each experiment were selected for analysis based on the cell morphology before flow was resumed. Though this made manual cell tracking and marking easier, it is possible this was too substantial of a simplification of the overall cellular response. A tracking program could be developed to both automate and expedite the movement analysis while providing a more complete examination of cell movement by including more cells.

Finally, the advanced passage of the U-87 cells, above 200, used in the initial tests could be the issue. As cells are cultured, changes in behavior can be observed. One example of this was the atypical, clumped growth of C6 cells described in Chapter 2. Repeat experiments using U-87 cells at a lower passage could result in more substantial GBM chemotaxis within these devices.

5.4 Conclusions

Initial experiments to study GBM migration were completed using three known U-87 chemoattractants and compared to cell movement when exposed to flow alone. A manual method for monitoring 8 cell positions, using (x, y) coordinates, provided a simplified representation of the average cell displacement under the various experimental conditions.

The results from this analysis showed minimal overall cell movement in the direction of increasing concentration for the HGF and TGF-α chemoattractant solution. By excluding FBS from the standard cell media, and instead utilizing it as part of the chemoattractant gradient, tracked GBM migration was more similar to the movement observed when no chemoattractant was present. The most compelling sign of observable U-87 chemotaxis was the more substantial displacement in the direction of increasing chemoattractant concentration when statistical outliers were removed from the 1.0 nmol/L HGF experimental results. More work could be done to produce a clearer chemotactic response, such as additional optimization of chemoattractant concentrations, an improved method for automated tracking of more cells, and repetition of these experiments using U-87 cells with a lower passage number. All these considerations aside, this early research demonstrated that the developed microfluidic device can be used to monitor cell migration in response to different, controllable chemical gradients.

Chapter 6 - Future directions

The research project described above included two main goals: 1) the development of a low-cost and simple-to-use microfluidic device for studying cell migration and 2) the study GBM migration to better understand the enhanced mobility of this brain cancer. Significant progress towards the fabrication of this microfluidic device and the validation of its key functions were explored in detail in Chapters 2, 3, and 4. Initial GBM migration studies reported in Chapter 5 showed some potential indications that a small chemotactic response was observed, and further optimization of chemoattractant concentrations and an improved cell tracking program could generate more significant results.

To expand upon this research, additional chemoattractants, such as fibroblast growth factor 1 (FGF-1), CC motif chemokine ligand 5 (CCL5), and CC motif chemokine ligand 18 (CCL18), could be explored based on U-87 migration studies reported in the literature.[29, 143, 145, 146] Experiments assessing the speed of GBM migration in response to these different chemoattractants would provide further information about the proliferation of GBM cells in response to specific cell-secreted signals.

As discussed in Chapter 1, the presence of HA, and subsequent binding to the CD44 glycoprotein, plays a critical role in the mobility of GBM.[25] Incorporating dissolved HA into the chemoattractant solution as a component of the gradient would be a quick and simple way to assess how varying concentrations of HA impact GBM migration. For a more advanced method, a hydrogel surface, comprised of a tunable concentration of HA, could be integrated into the device. This would also better represent the gel-like consistency of the space between cells within the brain.[20] Micropatterning of a methacrylated HA precursor solution would be crosslinked via exposure to UV light.[147, 148] Additionally, a small molecule inhibitor, such as 4-

methylumbelliferone, could be utilized to inhibit HA production from the cells themselves, allowing for more control over the amount of HA within the device during experiments.[149] The impacts on GBM migration as a result of differing environmental HA concentrations could reveal further insights on GBM mobility.

Finally, incorporating a mixture of cell lines within the device would better mimic the GBM tumor environment. Microglia and astrocytes complete important functions in the maintenance of a healthy brain, but both can also be manipulated by GBM to encourage pro-tumor conditions.[15] By including human microglia and astrocytes, conditions which elicit isolated GBM migration could be determined. Furthermore, the crosstalk between these cell types could be analyzed by collecting the waste throughout experiments to identify, and potentially quantify, the biomarkers exchanged within the tumor environment. It is the goal of this work to not only highlight an affordable and approachable microfluidic device for cellular studies, but to use this device to gain knowledge regarding the mobility of GBM in the hopes of improving therapeutics for this deadly brain cancer.

References

(1) Thakkar, J. P.; Dolecek, T. A.; Horbinski, C.; Ostrom, Q. T.; Lightner, D. D.; Barnholtz-Sloan, J. S.; Villano, J. L. Epidemiologic and molecular prognostic review of glioblastoma. *Cancer Epidemiol Biomarkers Prev* **2014**, *23* (10), 1985-1996. DOI: 10.1158/1055-9965.EPI-14-0275.

(2) Ostrom, Q. T.; Bauchet, L.; Davis, F. G.; Deltour, I.; Fisher, J. L.; Langer, C. E.; Pekmezci, M.; Schwartzbaum, J. A.; Turner, M. C.; Walsh, K. M.; et al. The epidemiology of glioma in adults: a "state of the science" review. *Neuro Oncol* **2014**, *16* (7), 896-913. DOI: 10.1093/neuonc/nou087.

(3) Alexander, B. M. C., Timothy F. Adult Glioblastoma. *J Clinical Oncology* **2017**, *35*. DOI: 10.1200/JCO.2017.

(4) Guan, X.; Hasan, M. N.; Maniar, S.; Jia, W.; Sun, D. Reactive Astrocytes in Glioblastoma Multiforme. *Mol Neurobiol* **2018**, *55* (8), 6927-6938. DOI: 10.1007/s12035-018-0880-8.

(5) Logun, M.; Zhao, W.; Mao, L.; Karumbaiah, L. Microfluidics in Malignant Glioma Research and Precision Medicine. *Adv Biosyst* **2018**, *2* (5). DOI: 10.1002/adbi.201700221.

(6) Vital-Lopez, F. G.; Armaou, A.; Hutnik, M.; Maranas, C. D. Modeling the effect of chemotaxis on glioblastoma tumor progression. *AIChE Journal* **2011**, *57* (3), 778-792. DOI: 10.1002/aic.12296.

(7) Louis, D. N.; Perry, A.; Reifenberger, G.; von Deimling, A.; Figarella-Branger, D.; Cavenee, W. K.; Ohgaki, H.; Wiestler, O. D.; Kleihues, P.; Ellison, D. W. The 2016 World Health Organization Classification of Tumors of the Central Nervous System: a summary. *Acta Neuropathol* **2016**, *131* (6), 803-820. DOI: 10.1007/s00401-016-1545-1.

(8) Graeber, M. B.; Scheithauer, B. W.; Kreutzberg, G. W. Microglia in brain tumors. *Glia* **2002**, *40* (2), 252-259. DOI: 10.1002/glia.10147.

(9) Watters, J. J.; Schartner, J. M.; Badie, B. Microglia function in brain tumors. *J Neurosci Res* **2005**, *81* (3), 447-455. DOI: 10.1002/jnr.20485.

(10) Morisse, M. C.; Jouannet, S.; Dominguez-Villar, M.; Sanson, M.; Idbaih, A. Interactions between tumor-associated macrophages and tumor cells in glioblastoma: unraveling promising targeted therapies. *Expert Rev Neurother* **2018**, *18* (9), 729-737. DOI: 10.1080/14737175.2018.1510321.

(11) Arcuri, C. F., Bernard; Bianchi, Roberta; Mecca, Carmen; Tubaro, Claudia; Beccari, Tommaso; Franciolini, Fabio; Giambanco, Ileana; Donato, Rosario. Microglia-glioma cross-talk: a two way approach to new strategies against glioma. *Frontiers in Bioscience* **2017**, *22*, 268-309.

(12) Aloisi, F. Immune function of microglia. *Glia* **2001**, *36* (2), 165-179. DOI: 10.1002/glia.1106.

(13) Roesch, S.; Rapp, C.; Dettling, S.; Herold-Mende, C. When Immune Cells Turn Bad-Tumor-Associated Microglia/Macrophages in Glioma. *Int J Mol Sci* **2018**, *19* (2). DOI: 10.3390/ijms19020436.

(14) Dong, Y.; Benveniste, E. N. Immune function of astrocytes. *Glia* **2001**, *36* (2), 180-190. DOI: 10.1002/glia.1107.

(15) Matias, D.; Balca-Silva, J.; da Graca, G. C.; Wanjiru, C. M.; Macharia, L. W.; Nascimento, C. P.; Roque, N. R.; Coelho-Aguiar, J. M.; Pereira, C. M.; Dos Santos, M. F.; et al. Microglia/Astrocytes-Glioblastoma Crosstalk: Crucial Molecular Mechanisms and Microenvironmental Factors. *Front Cell Neurosci* **2018**, *12*, 235. DOI: 10.3389/fncel.2018.00235.

(16) Park, J. B. K., Hee-Jin; Lee, Seung-Hoon. Role of hyaluronan in glioma invasion. *Cell Adhesion & Migration* **2008**, *2* (3), 202-207.

(17) Ananthanarayanan, B.; Kim, Y.; Kumar, S. Elucidating the mechanobiology of malignant brain tumors using a brain matrix-mimetic hyaluronic acid hydrogel platform. *Biomaterials* **2011**, *32* (31), 7913-7923. DOI: 10.1016/j.biomaterials.2011.07.005.

(18) Somaweera, H.; Ibraguimov, A.; Pappas, D. A review of chemical gradient systems for cell analysis. *Anal Chim Acta* **2016**, *907*, 7-17. DOI: 10.1016/j.aca.2015.12.008.

(19) Denisin, A. K.; Pruitt, B. L. Tuning the Range of Polyacrylamide Gel Stiffness for Mechanobiology Applications. *ACS Appl Mater Interfaces* **2016**, *8* (34), 21893-21902. DOI: 10.1021/acsami.5b09344.

(20) Cuddapah, V. A.; Robel, S.; Watkins, S.; Sontheimer, H. A neurocentric perspective on glioma invasion. *Nat Rev Neurosci* **2014**, *15* (7), 455-465. DOI: 10.1038/nrn3765 From NLM Medline.

(21) Watkins, S.; Sontheimer, H. Hydrodynamic Cellular Volume Changes Enable Glioma Cell Invasion. *The Journal of Neuroscience* **2011**, *31* (47), 17250-17259. DOI: 10.1523/jneurosci.3938-11.2011.

(22) Sen, S.; Dong, M.; Kumar, S. Isoform-specific contributions of alpha-actinin to glioma cell mechanobiology. *PLoS One* **2009**, *4* (12), e8427. DOI: 10.1371/journal.pone.0008427 From NLM Medline.

(23) Farin, A.; Suzuki, S. O.; Weiker, M.; Goldman, J. E.; Bruce, J. N.; Canoll, P. Transplanted glioma cells migrate and proliferate on host brain vasculature: A dynamic analysis. *Glia* **2006**, *53* (8), 799-808. DOI: 10.1002/glia.20334.

(24) Bourguignon, L. Y. Hyaluronan-mediated CD44 activation of RhoGTPase signaling and cytoskeleton function promotes tumor progression. *Semin Cancer Biol* **2008**, *18* (4), 251-259. DOI: 10.1016/j.semcancer.2008.03.007.

(25) Mooney, K. L.; Choy, W.; Sidhu, S.; Pelargos, P.; Bui, T. T.; Voth, B.; Barnette, N.; Yang, I. The role of CD44 in glioblastoma multiforme. *J Clin Neurosci* **2016**, *34*, 1-5. DOI: 10.1016/j.jocn.2016.05.012.

(26) Dzwonek, J.; Wilczynski, G. M. CD44: molecular interactions, signaling and functions in the nervous system. *Front Cell Neurosci* **2015**, *9*, 175. DOI: 10.3389/fncel.2015.00175.

(27) Wang, C.; Wang, Z.; Chen, C.; Fu, X.; Wang, J.; Fei, X.; Yan, X.; Xu, R. A low MW inhibitor of CD44 dimerization for the treatment of glioblastoma. *Br J Pharmacol* **2020**, *177* (13), 3009-3023. DOI: 10.1111/bph.15030.

(28) Xu, Y.; Stamenkovic, I.; Yu, Q. CD44 attenuates activation of the hippo signaling pathway and is a prime therapeutic target for glioblastoma. *Cancer Res* **2010**, *70* (6), 2455-2464. DOI: 10.1158/0008-5472.CAN-09-2505.

(29) Zhao, L.; Wang, Y.; Xue, Y.; Lv, W.; Zhang, Y.; He, S. Critical roles of chemokine receptor CCR5 in regulating glioblastoma proliferation and invasion. *Acta Biochim Biophys Sin (Shanghai)* **2015**, *47* (11), 890-898. DOI: 10.1093/abbs/gmv095.

(30) Angeli, E.; Nguyen, T. T.; Janin, A.; Bousquet, G. How to Make Anticancer Drugs Cross the Blood-Brain Barrier to Treat Brain Metastases. *Int J Mol Sci* **2019**, *21* (1). DOI: 10.3390/ijms21010022.

(31) Barbarisi, M.; Iaffaioli, R. V.; Armenia, E.; Schiavo, L.; De Sena, G.; Tafuto, S.; Barbarisi, A.; Quagliariello, V. Novel nanohydrogel of hyaluronic acid loaded with quercetin alone and in combination with temozolomide as new therapeutic tool, CD44 targeted based, of glioblastoma multiforme. *J Cell Physiol* **2018**, *233* (10), 6550-6564. DOI: 10.1002/jcp.26238.

(32) Haumann, R.; Videira, J. C.; Kaspers, G. J. L.; van Vuurden, D. G.; Hulleman, E. Overview of Current Drug Delivery Methods Across the Blood-Brain Barrier for the Treatment of Primary Brain Tumors. *CNS Drugs* **2020**, *34* (11), 1121-1131. DOI: 10.1007/s40263-020-00766-w.

(33) Townsley, C.; Pond, G. R.; Peloza, B.; Kok, J.; Naidoo, K.; Dale, D.; Herbert, C.; Holowaty, E.; Straus, S.; Siu, L. L. Analysis of treatment practices for elderly cancer patients in Ontario, Canada. *J Clin Oncol* **2005**, *23* (16), 3802-3810. DOI: 10.1200/JCO.2005.06.742.

(34) Balducci, L. C., Giuseppe; Cesari, Matteo; Gambassi, Giovanni. . Assessment and treatment of elderly patients with cancer. *Surgical Oncology* **2010**, *19* (3), 117-123.

(35) Horwitz, R.; Webb, D. Cell migration. *Curr Biol* **2003**, *13* (19), R756-759. DOI: 10.1016/j.cub.2003.09.014.

(36) Trepat, X.; Chen, Z.; Jacobson, K. Cell migration. *Compr Physiol* **2012**, *2* (4), 2369-2392. DOI: 10.1002/cphy.c110012.

(37) Vicente-Manzanares, M. H., Alan Rick. Cell Migration: An Overview. In *Cell Migration Developmental Methods and Protocols*, 2 ed.; Wells, C. M. P., Maddy Ed.; Vol. 769; Humana Press, 2011; pp 1-24.

(38) SenGupta, S.; Parent, C. A.; Bear, J. E. The principles of directed cell migration. *Nat Rev Mol Cell Biol* **2021**, *22* (8), 529-547. DOI: 10.1038/s41580-021-00366-6.

(39) Luster, A. D. Chemotaxis: role in immune response. *e LS* **2001**.

(40) Walker, C.; Mojares, E.; Del Rio Hernandez, A. Role of Extracellular Matrix in Development and Cancer Progression. *Int J Mol Sci* **2018**, *19* (10). DOI: 10.3390/ijms19103028.

(41) Levine, H.; Rappel, W. J. The physics of eukaryotic chemotaxis. *Phys Today* **2013**, *66* (2). DOI: 10.1063/PT.3.1884.

(42) Manes, S.; Gomez-Mouton, C.; Lacalle, R. A.; Jimenez-Baranda, S.; Mira, E.; Martinez, A. C. Mastering time and space: immune cell polarization and chemotaxis. *Semin Immunol* **2005**, *17* (1), 77-86. DOI: 10.1016/j.smim.2004.09.005.

(43) Jeon, N. L.; Dertinger, S. K. W.; Chiu, D. T.; Choi, I. S.; Stroock, A. D.; Whitesides, G. M. Generation of Solution and Surface Gradients Using Microfluidic Systems. *Langmuir* **2000**, *16* (22), 8311-8316. DOI: 10.1021/la000600b.

(44) Bagorda, A.; Parent, C. A. Eukaryotic chemotaxis at a glance. *J Cell Sci* **2008**, *121* (Pt 16), 2621-2624. DOI: 10.1242/jcs.018077.

(45) Kim, B. J.; Wu, M. Microfluidics for mammalian cell chemotaxis. *Ann Biomed Eng* **2012**, *40* (6), 1316-1327. DOI: 10.1007/s10439-011-0489-9.

(46) Zhang, C.; Jang, S.; Amadi, O. C.; Shimizu, K.; Lee, R. T.; Mitchell, R. N. A sensitive chemotaxis assay using a novel microfluidic device. *Biomed Res Int* **2013**, *2013*, 373569. DOI: 10.1155/2013/373569.

(47) Chaubey, S. R., A.J.; Wells, C.M. Using the Dunn Chemotaxis Chamber to Analyze Primary Cell Migration in Real Time. In *Cell Migration Developmental Methods and Protocols*, 2 ed.; Wells, C. M. P., Maddy Ed.; Vol. 769; Humana Press, 2011; pp 41-51.

(48) Wu, H. J.; Liu, Y. J.; Li, H. Q.; Chen, C.; Dou, Y.; Lou, H. F.; Ho, M. S.; Li, X. M.; Gao, Z.; Duan, S. Analysis of microglial migration by a micropipette assay. *Nat Protoc* **2014**, *9* (2), 491-500. DOI: 10.1038/nprot.2014.015.

(49) Whitesides, G. M. The origins and the future of microfluidics. *Nature* **2006**, *442* (7101), 368-373. DOI: 10.1038/nature05058.

(50) Ongaro, A. E.; Ndlovu, Z.; Sollier, E.; Otieno, C.; Ondoa, P.; Street, A.; Kersaudy-Kerhoas, M. Engineering a sustainable future for point-of-care diagnostics and single-use microfluidic devices. *Lab Chip* **2022**. DOI: 10.1039/d2lc00380e.

(51) Terry, S. C. J., J. H.; Angell, J. B. A gas chromatographic air analyzer fabricated on a silicon wafer. *IEEE Transactions on Electron Devices* **1979**, *26*, 1880-1886.

(52) Stone, H. A. K., S. Microfluidics: basic issues, applications, and challenges. *AIChE Journal* **2001**, *47* (6), 1250-1254.

(53) Ren, K. Z., Jianhua; Wu, Hongkai. Materials for Micrfluidic Chip Fabrication. *Accounts of Chemical Research* **2012**, *46*, 2396-2406.

(54) Weibel, D. B.; Whitesides, G. M. Applications of microfluidics in chemical biology. *Curr Opin Chem Biol* **2006**, *10* (6), 584-591. DOI: 10.1016/j.cbpa.2006.10.016.

(55) Sackmann, E. K.; Fulton, A. L.; Beebe, D. J. The present and future role of microfluidics in biomedical research. *Nature* **2014**, *507* (7491), 181-189. DOI: 10.1038/nature13118.

(56) Wang, X.; Liu, Z.; Pang, Y. Concentration gradient generation methods based on microfluidic systems. *RSC Advances* **2017**, *7* (48), 29966-29984. DOI: 10.1039/c7ra04494a.

(57) Breslauer, D. N.; Lee, P. J.; Lee, L. P. Microfluidics-based systems biology. *Mol Biosyst* **2006**, *2* (2), 97-112. DOI: 10.1039/b515632g.

(58) Sibbitts, J.; Sellens, K. A.; Jia, S.; Klasner, S. A.; Culbertson, C. T. Cellular Analysis Using Microfluidics. *Anal Chem* **2018**, *90* (1), 65-85. DOI: 10.1021/acs.analchem.7b04519.

(59) Battat, S.; Weitz, D. A.; Whitesides, G. M. An outlook on microfluidics: the promise and the challenge. *Lab Chip* **2022**. DOI: 10.1039/d1lc00731a.

(60) del Barrio, J.; Sánchez-Somolinos, C. Light to Shape the Future: From Photolithography to 4D Printing. *Advanced Optical Materials* **2019**, *7* (16). DOI: 10.1002/adom.201900598.

(61) Kim, P. K., Keon Woo; Park, Min Cheol; Lee, Sung Hoon; Kim, Sun Min; Suh, Kahp Yang. Soft Lithography for Microfluidics: a Review. *Biochip Journal* **2008**, *2*, 1-11.

(62) Company, T. D. C. *SYLGARD™ 184 Silicone Elastomer Kit Technical Data Sheet*. The Dow Chemical Company, 2017. https://www.dow.com/en-us/document-viewer.html?docPath=/content/dam/dcc/documents/en-us/productdatasheet/11/11-31/11-3184-sylgard-184-elastomer.pdf (accessed August 20, 2021).

(63) Geng, Y.; Ling, S.; Huang, J.; Xu, J. Multiphase Microfluidics: Fundamentals, Fabrication, and Functions. *Small* **2020**, *16* (6), e1906357. DOI: 10.1002/smll.201906357.

(64) Becker, H. L., L. E. Polymer microfluidic devices. *Talanta* **2002**, *56* (2), 267-287.

(65) Focke, M.; Kosse, D.; Muller, C.; Reinecke, H.; Zengerle, R.; von Stetten, F. Lab-on-a-Foil: microfluidics on thin and flexible films. *Lab Chip* **2010**, *10* (11), 1365-1386. DOI: 10.1039/c001195a.

(66) Bhattacharjee, N.; Urrios, A.; Kang, S.; Folch, A. The upcoming 3D-printing revolution in microfluidics. *Lab Chip* **2016**, *16* (10), 1720-1742. DOI: 10.1039/c6lc00163g.

(67) Carney, C. M.; Muszynski, J. L.; Strotman, L. N.; Lewis, S. R.; O'Connell, R. L.; Beebe, D. J.; Theberge, A. B.; Jorgensen, J. S. Cellular microenvironment dictates androgen production by murine fetal Leydig cells in primary culture. *Biol Reprod* **2014**, *91* (4), 85. DOI: 10.1095/biolreprod.114.118570.

(68) Kosoff, D.; Yu, J.; Suresh, V.; Beebe, D. J.; Lang, J. M. Surface topography and hydrophilicity regulate macrophage phenotype in milled microfluidic systems. *Lab Chip* **2018**, *18* (19), 3011-3017. DOI: 10.1039/c8lc00431e.

(69) Guckenberger, D. J.; de Groot, T. E.; Wan, A. M.; Beebe, D. J.; Young, E. W. Micromilling: a method for ultra-rapid prototyping of plastic microfluidic devices. *Lab Chip* **2015**, *15* (11), 2364-2378. DOI: 10.1039/c5lc00234f.

(70) Gong, M. M.; Sinton, D. Turning the Page: Advancing Paper-Based Microfluidics for Broad Diagnostic Application. *Chem Rev* **2017**, *117* (12), 8447-8480. DOI: 10.1021/acs.chemrev.7b00024.

(71) Mark, D.; Haeberle, S.; Roth, G.; von Stetten, F.; Zengerle, R. Microfluidic lab-on-a-chip platforms: requirements, characteristics and applications. *Chem Soc Rev* **2010**, *39* (3), 1153-1182. DOI: 10.1039/b820557b.

(72) Martinez, A. W.; Phillips, S. T.; Butte, M. J.; Whitesides, G. M. Patterned Paper as a Platform for Inexpensive, Low-Volume, Portable Bioassays. *Angewandte Chemie* **2007**, *119* (8), 1340-1342. DOI: 10.1002/ange.200603817.

(73) Lam, T.; Devadhasan, J. P.; Howse, R.; Kim, J. A Chemically Patterned Microfluidic Paper-based Analytical Device (C-microPAD) for Point-of-Care Diagnostics. *Sci Rep* **2017**, *7* (1), 1188. DOI: 10.1038/s41598-017-01343-w.

(74) Nishat, S.; Jafry, A. T.; Martinez, A. W.; Awan, F. R. Paper-based microfluidics: Simplified fabrication and assay methods. *Sensors and Actuators B: Chemical* **2021**, *336*. DOI: 10.1016/j.snb.2021.129681.

(75) Akyazi, T.; Basabe-Desmonts, L.; Benito-Lopez, F. Review on microfluidic paper-based analytical devices towards commercialisation. *Anal Chim Acta* **2018**, *1001*, 1-17. DOI: 10.1016/j.aca.2017.11.010.

(76) Carrell, C.; Kava, A.; Nguyen, M.; Menger, R.; Munshi, Z.; Call, Z.; Nussbaum, M.; Henry, C. Beyond the lateral flow assay: A review of paper-based microfluidics. *Microelectronic Engineering* **2019**, *206*, 45-54. DOI: 10.1016/j.mee.2018.12.002.

(77) Cramer, S. M.; Larson, T. S.; Lockett, M. R. Tissue Papers: Leveraging Paper-Based Microfluidics for the Next Generation of 3D Tissue Models. *Anal Chem* **2019**, *91* (17), 10916-10926. DOI: 10.1021/acs.analchem.9b02102.

(78) Ho, C. M.; Ng, S. H.; Li, K. H.; Yoon, Y. J. 3D printed microfluidics for biological applications. *Lab Chip* **2015**, *15* (18), 3627-3637. DOI: 10.1039/c5lc00685f.

(79) Gross, B.; Lockwood, S. Y.; Spence, D. M. Recent Advances in Analytical Chemistry by 3D Printing. *Anal Chem* **2017**, *89* (1), 57-70. DOI: 10.1021/acs.analchem.6b04344.

(80) Wang, L.; Pumera, M. Recent advances of 3D printing in analytical chemistry: Focus on microfluidic, separation, and extraction devices. *TrAC Trends in Analytical Chemistry* **2021**, *135*. DOI: 10.1016/j.trac.2020.116151.

(81) Lücking, T. H.; Sambale, F.; Schnaars, B.; Bulnes-Abundis, D.; Beutel, S.; Scheper, T. 3D-printed individual labware in biosciences by rapid prototyping: In vitro biocompatibility and applications for eukaryotic cell cultures. *Engineering in Life Sciences* **2015**, *15* (1), 57-64. DOI: 10.1002/elsc.201400094.

(82) Piironen, K.; Haapala, M.; Talman, V.; Jarvinen, P.; Sikanen, T. Cell adhesion and proliferation on common 3D printing materials used in stereolithography of microfluidic devices. *Lab Chip* **2020**. DOI: 10.1039/d0lc00114g.

(83) Au, A. K.; Bhattacharjee, N.; Horowitz, L. F.; Chang, T. C.; Folch, A. 3D-printed microfluidic automation. *Lab Chip* **2015**, *15* (8), 1934-1941. DOI: 10.1039/c5lc00126a.

(84) Urrios, A.; Parra-Cabrera, C.; Bhattacharjee, N.; Gonzalez-Suarez, A. M.; Rigat-Brugarolas, L. G.; Nallapatti, U.; Samitier, J.; DeForest, C. A.; Posas, F.; Garcia-Cordero, J. L.; et al. 3D-printing of transparent bio-microfluidic devices in PEG-DA. *Lab Chip* **2016**, *16* (12), 2287-2294. DOI: 10.1039/c6lc00153j.

(85) Gross, B. C.; Anderson, K. B.; Meisel, J. E.; McNitt, M. I.; Spence, D. M. Polymer Coatings in 3D-Printed Fluidic Device Channels for Improved Cellular Adherence Prior to Electrical Lysis. *Anal Chem* **2015**, *87* (12), 6335-6341. DOI: 10.1021/acs.analchem.5b01202.

(86) Anderson, K. B.; Lockwood, S. Y.; Martin, R. S.; Spence, D. M. A 3D printed fluidic device that enables integrated features. *Anal Chem* **2013**, *85* (12), 5622-5626. DOI: 10.1021/ac4009594.

(87) Chiado, A.; Palmara, G.; Chiappone, A.; Tanzanu, C.; Pirri, C. F.; Roppolo, I.; Frascella, F. A modular 3D printed lab-on-a-chip for early cancer detection. *Lab Chip* **2020**. DOI: 10.1039/c9lc01108k.

(88) Salonitis, K. Stereolithography. In *Comprehensive Materials Processing*, 2014; pp 19-67.

(89) Steyrer, B.; Neubauer, P.; Liska, R.; Stampfl, J. Visible Light Photoinitiator for 3D-Printing of Tough Methacrylate Resins. *Materials (Basel)* **2017**, *10* (12). DOI: 10.3390/ma10121445.

(90) Gong, H.; Beauchamp, M.; Perry, S.; Woolley, A. T.; Nordin, G. P. Optical Approach to Resin Formulation for 3D Printed Microfluidics. *RSC Adv* **2015**, *5* (129), 106621-106632. DOI: 10.1039/C5RA23855B.

(91) Chatani, S.; Kloxin, C. J.; Bowman, C. N. The power of light in polymer science: photochemical processes to manipulate polymer formation, structure, and properties. *Polym. Chem.* **2014**, *5* (7), 2187-2201. DOI: 10.1039/c3py01334k.

(92) Musgrove, H. B.; Catterton, M. A.; Pompano, R. R. Applied tutorial for the design and fabrication of biomicrofluidic devices by resin 3D printing. *Anal Chim Acta* **2022**, *1209*, 339842. DOI: 10.1016/j.aca.2022.339842.

(93) de Almeida Monteiro Melo Ferraz, M.; Nagashima, J. B.; Venzac, B.; Le Gac, S.; Songsasen, N. 3D printed mold leachates in PDMS microfluidic devices. *Sci Rep* **2020**, *10* (1), 994. DOI: 10.1038/s41598-020-57816-y.

(94) Macdonald, N. P.; Zhu, F.; Hall, C. J.; Reboud, J.; Crosier, P. S.; Patton, E. E.; Wlodkowic, D.; Cooper, J. M. Assessment of biocompatibility of 3D printed photopolymers using zebrafish embryo toxicity assays. *Lab Chip* **2016**, *16* (2), 291-297. DOI: 10.1039/c5lc01374g.

(95) Moreno-Rivas, O.; Hernández-Velázquez, D.; Piazza, V.; Marquez, S. Rapid prototyping of microfluidic devices by SL 3D printing and their biocompatibility study for cell culturing. *Materials Today: Proceedings* **2019**, *13*, 436-445. DOI: 10.1016/j.matpr.2019.03.189.

(96) Piruska, A.; Nikcevic, I.; Lee, S. H.; Ahn, C.; Heineman, W. R.; Limbach, P. A.; Seliskar, C. J. The autofluorescence of plastic materials and chips measured under laser irradiation. *Lab Chip* **2005**, *5* (12), 1348-1354. DOI: 10.1039/b508288a.

(97) Park, H. K.; Shin, M.; Kim, B.; Park, J. W.; Lee, H. A visible light-curable yet visible wavelength-transparent resin for stereolithography 3D printing. *NPG Asia Materials* **2018**, *10* (4), 82-89. DOI: 10.1038/s41427-018-0021-x.

(98) Cai, D.; Neyer, A. Cost-effective and reliable sealing method for PDMS (PolyDiMethylSiloxane)-based microfluidic devices with various substrates. *Microfluidics and Nanofluidics* **2010**, *9* (4-5), 855-864. DOI: 10.1007/s10404-010-0596-1.

(99) Carrell, C. S.; McCord, C. P.; Wydallis, R. M.; Henry, C. S. Sealing 3D-printed parts to poly(dimethylsiloxane) for simple fabrication of Microfluidic devices. *Anal Chim Acta* **2020**, *1124*, 78-84. DOI: 10.1016/j.aca.2020.05.014.

(100) Wasay, A.; Sameoto, D. Gecko gaskets for self-sealing and high-strength reversible bonding of microfluidics. *Lab Chip* **2015**, *15* (13), 2749-2753. DOI: 10.1039/c5lc00342c.

(101) Gong, H.; Bickham, B. P.; Woolley, A. T.; Nordin, G. P. Custom 3D printer and resin for 18 mum x 20 mum microfluidic flow channels. *Lab Chip* **2017**, *17* (17), 2899-2909. DOI: 10.1039/c7lc00644f.

(102) Oraiopoulou, M. E.; Tzamali, E.; Tzedakis, G.; Vakis, A.; Papamatheakis, J.; Sakkalis, V. In Vitro/In Silico Study on the Role of Doubling Time Heterogeneity among Primary Glioblastoma Cell Lines. *Biomed Res Int* **2017**, *2017*, 8569328. DOI: 10.1155/2017/8569328 From NLM Medline.

(103) Gong, H.; Woolley, A. T.; Nordin, G. P. 3D printed high density, reversible, chip-to-chip microfluidic interconnects. *Lab Chip* **2018**, *18* (4), 639-647. DOI: 10.1039/c7lc01113j.

(104) Products, N. *Norland Optical Adhesive 86H*. https://www.norlandprod.com/adhesives/NOA86H.html (accessed September 2, 2020).

(105) Technologies, M. M. M. *3M Microfluidic Diagnostic Tape 9795R Single-Sided Clear Delayed Tack Adhesive Tape*. 3M^{TM}, 2002. https://www.3m.com/3M/en_US/p/d/v000176401/ (accessed May 5, 2021).

(106) Specialties, M. M. *Technical Information Sheet Product Number 9964* 3M^{TM}, 2005. https://www.3m.com/3M/en_US/p/d/v000256803/ (accessed May 5, 2021).

(107) Specialties, M. M. *Technical Information Sheet Product Number 9793R*. 3M^{TM}, 2010. https://www.3m.com/3M/en_US/p/d/v000176400/ (accessed May 5, 2021).

(108) Razavi Bazaz, S.; Rouhi, O.; Raoufi, M. A.; Ejeian, F.; Asadnia, M.; Jin, D.; Ebrahimi Warkiani, M. 3D Printing of Inertial Microfluidic Devices. *Sci Rep* **2020**, *10* (1), 5929. DOI: 10.1038/s41598-020-62569-9.

(109) Oyama, Y.; Osaki, T.; Kamiya, K.; Sawai, M.; Sakai, M.; Takeuchi, S. A sensitive point-of-care testing chip utilizing superabsorbent polymer for the early diagnosis of infectious disease. *Sensors and Actuators B: Chemical* **2017**, *240*, 881-886. DOI: 10.1016/j.snb.2016.09.046.

(110) Schulz, M.; Ruediger, J.; Landmann, E.; Bakheit, M.; Frischmann, S.; Rassler, D.; Homann, A. R.; von Stetten, F.; Zengerle, R.; Paust, N. High Dynamic Range Digital Assay Enabled by Dual-Volume Centrifugal Step Emulsification. *Anal Chem* **2021**, *93* (5), 2854-2860. DOI: 10.1021/acs.analchem.0c04182.

(111) Arcot, L.; Kandaswamy, S.; Modali, A.; Gorthi, S. S.; Rai Dastidar, T. Developing microscopy based microfluidic SLS assay for on-chip hemoglobin estimation. *AIP Advances* **2021**, *11* (2). DOI: 10.1063/5.0036446.

(112) Ko, J.; Ahn, J.; Kim, S.; Lee, Y.; Lee, J.; Park, D.; Jeon, N. L. Tumor spheroid-on-a-chip: a standardized microfluidic culture platform for investigating tumor angiogenesis. *Lab Chip* **2019**, *19* (17), 2822-2833. DOI: 10.1039/c9lc00140a.

(113) Baman, N. K.; Schneider, G. B.; Terry, T. L.; Zaharias, R.; Salem, A. K. Spatial control over cell attachment by partial solvent entrapment of poly lysine in microfluidic channels. *Int J Nanomedicine* **2006**, *1* (2), 213-217. DOI: 10.2147/nano.2006.1.2.213 From NLM Medline.

(114) Tian, W. M. H., S.P.; Ma, J.; Zhang, C.L.; Xu, Q.Y.; Lee, I.S.; Li, H.D.; Spector, M.; Cui, F.Z. Hyaluronic Acid-Poly-D-Lysine-Based Three-Dimensional Hydrogel for Traumatic Brain Injury. *Tissue Engineering* **2005**, *11* (3-4), 513-525. DOI: 10.1089/ten.2005.11.513.

(115) Knopf-Marques, H.; Pravda, M.; Wolfova, L.; Velebny, V.; Schaaf, P.; Vrana, N. E.; Lavalle, P. Hyaluronic Acid and Its Derivatives in Coating and Delivery Systems: Applications in Tissue Engineering, Regenerative Medicine and Immunomodulation. *Adv Healthc Mater* **2016**, *5* (22), 2841-2855. DOI: 10.1002/adhm.201600316.

(116) Samanipour, R.; Tahmooressi, H.; Rezaei Nejad, H.; Hirano, M.; Shin, S. R.; Hoorfar, M. A review on 3D printing functional brain model. *Biomicrofluidics* **2022**, *16* (1), 011501. DOI: 10.1063/5.0074631.

(117) Simulescu, V.; Kalina, M.; Mondek, J.; Pekar, M. Long-term degradation study of hyaluronic acid in aqueous solutions without protection against microorganisms. *Carbohydr Polym* **2016**, *137*, 664-668. DOI: 10.1016/j.carbpol.2015.10.101.

(118) Sigma-Aldrich. *Poly-D-lysine Hydrobromide Product Information Sheet*. https://www.sigmaaldrich.com/US/en/product/sigma/p6407 (accessed March 14, 2022).

(119) Gautam, R.; Singh, R. D.; Sharma, V. P.; Siddhartha, R.; Chand, P.; Kumar, R. Biocompatibility of polymethylmethacrylate resins used in dentistry. *J Biomed Mater Res B Appl Biomater* **2012**, *100* (5), 1444-1450. DOI: 10.1002/jbm.b.32673.

(120) Biotium. *NucSpot Nuclear Stains Product Informamtion*. 2023. https://biotium.com/product/nucspot-nuclear-stains/ (accessed July 19, 2024).

(121) Seghir, R.; Arscott, S. Extended PDMS stiffness range for flexible systems. *Sensors and Actuators A: Physical* **2015**, *230*, 33-39. DOI: 10.1016/j.sna.2015.04.011.

(122) Park, J. Y.; Ahn, D.; Choi, Y. Y.; Hwang, C. M.; Takayama, S.; Lee, S. H.; Lee, S.-H. Surface chemistry modification of PDMS elastomers with boiling water improves cellular adhesion. *Sensors and Actuators B: Chemical* **2012**, *173*, 765-771. DOI: 10.1016/j.snb.2012.06.096.

(123) Dertinger, S. K. C., D. T.; Jeon, N. L.; Whitesides, G. M. Generation of Gradients Having Complex Shapes Using Microfluidic Networks. *Anal Chem* **2001**, *73*, 1240-1246.

(124) Li, C. W.; Chen, R.; Yang, M. Generation of linear and non-linear concentration gradients along microfluidic channel by microtunnel controlled stepwise addition of sample solution. *Lab Chip* **2007**, *7* (10), 1371-1373. DOI: 10.1039/b705525k.

(125) Lee, K.; Kim, C.; Ahn, B.; Panchapakesan, R.; Full, A. R.; Nordee, L.; Kang, J. Y.; Oh, K. W. Generalized serial dilution module for monotonic and arbitrary microfluidic gradient generators. *Lab Chip* **2009**, *9* (5), 709-717. DOI: 10.1039/b813582g.

(126) Gao, Y.; Sun, J.; Lin, W. H.; Webb, D.; Li, D. A compact microfluidic gradient generator using passive pumping. *Microfluid Nanofluidics* **2012**, *12* (6), 887-895. DOI: 10.1007/s10404-011-0908-0.

(127) Lochovsky, C.; Yasotharan, S.; Gunther, A. Bubbles no more: in-plane trapping and removal of bubbles in microfluidic devices. *Lab Chip* **2012**, *12* (3), 595-601. DOI: 10.1039/c1lc20817a.

(128) Karlsson, J. M.; Gazin, M.; Laakso, S.; Haraldsson, T.; Malhotra-Kumar, S.; Maki, M.; Goossens, H.; van der Wijngaart, W. Active liquid degassing in microfluidic systems. *Lab Chip* **2013**, *13* (22), 4366-4373. DOI: 10.1039/c3lc50778e.

(129) Pereiro, I.; Fomitcheva Khartchenko, A.; Petrini, L.; Kaigala, G. V. Nip the bubble in the bud: a guide to avoid gas nucleation in microfluidics. *Lab Chip* **2019**, *19* (14), 2296-2314. DOI: 10.1039/c9lc00211a.

(130) Inc., A. *Alconox Technical Bulletin*. 2022. https://www.alconox.com/sds-sheets/ (accessed June 13, 2022).

(131) Bodas, D.; Khan-Malek, C. Formation of more stable hydrophilic surfaces of PDMS by plasma and chemical treatments. *Microelectronic Engineering* **2006**, *83* (4-9), 1277-1279. DOI: 10.1016/j.mee.2006.01.195.

(132) Kim, H. T.; Jeong, O. C. PDMS surface modification using atmospheric pressure plasma. *Microelectronic Engineering* **2011**, *88* (8), 2281-2285. DOI: 10.1016/j.mee.2011.02.084.

(133) Kim, L.; Vahey, M. D.; Lee, H. Y.; Voldman, J. Microfluidic arrays for logarithmically perfused embryonic stem cell culture. *Lab Chip* **2006**, *6* (3), 394-406. DOI: 10.1039/b511718f.

(134) Anderson, E. J.; Knothe Tate, M. L. Open access to novel dual flow chamber technology for in vitro cell mechanotransduction, toxicity and pharamacokinetic studies. *Biomed Eng Online* **2007**, *6*, 46. DOI: 10.1186/1475-925X-6-46 From NLM Medline.

(135) Shemesh, J.; Jalilian, I.; Shi, A.; Heng Yeoh, G.; Knothe Tate, M. L.; Ebrahimi Warkiani, M. Flow-induced stress on adherent cells in microfluidic devices. *Lab Chip* **2015**, *15* (21), 4114-4127. DOI: 10.1039/c5lc00633c From NLM Medline.

(136) Guillou, L.; Dahl, J. B.; Lin, J. G.; Barakat, A. I.; Husson, J.; Muller, S. J.; Kumar, S. Measuring Cell Viscoelastic Properties Using a Microfluidic Extensional Flow Device. *Biophys J* **2016**, *111* (9), 2039-2050. DOI: 10.1016/j.bpj.2016.09.034 From NLM Medline.

(137) Hardy, B. S.; Uechi, K.; Zhen, J.; Pirouz Kavehpour, H. The deformation of flexible PDMS microchannels under a pressure driven flow. *Lab Chip* **2009**, *9* (7), 935-938. DOI: 10.1039/b813061b From NLM Medline.

(138) Poon, C. Measuring the density and viscosity of culture media for optimized computational fluid dynamics analysis of *in vitro* devices. *Journal of the Mechanical Behavior of Biomedical Materials* **2022**, *126*. DOI: 10.1101/2020.08.25.266221.

(139) Whitesides, G. M. O., E.; Takayama, S.; Jiang, X.; Ingber, D. E. Soft Lithography in Biology and Biochemistry. *Annu Rev Biomed Eng* **2001**, *3*, 335-373.

(140) Siddharthan, V.; Kim, Y. V.; Liu, S.; Kim, K. S. Human astrocytes/astrocyte-conditioned medium and shear stress enhance the barrier properties of human brain microvascular endothelial cells. *Brain Res* **2007**, *1147*, 39-50. DOI: 10.1016/j.brainres.2007.02.029.

(141) Qazi, H.; Shi, Z. D.; Tarbell, J. M. Fluid shear stress regulates the invasive potential of glioma cells via modulation of migratory activity and matrix metalloproteinase expression. *PLoS One* **2011**, *6* (5), e20348. DOI: 10.1371/journal.pone.0020348 From NLM Medline.

(142) Li, W.; Mao, S.; Khan, M.; Zhang, Q.; Huang, Q.; Feng, S.; Lin, J. M. Responses of Cellular Adhesion Strength and Stiffness to Fluid Shear Stress during Tumor Cell Rolling Motion. *ACS Sens* **2019**, *4* (6), 1710-1715. DOI: 10.1021/acssensors.9b00678 From NLM Medline.

(143) Brockmann, M. A.; Ulbricht, U.; Gruner, K.; Fillbrandt, R.; Westphal, M.; Lamszus, K. Glioblastoma and cerebral microvascular endothelial cell migration in response to tumor-associated growth factors. *Neurosurgery* **2003**, *52* (6), 1391-1399; discussion 1399. DOI: 10.1227/01.neu.0000064806.87785.ab.

(144) Rao, C. V.; Ayuso, J. M.; Basheer, H. A.; Monge, R.; Sánchez-Álvarez, P.; Doblaré, M.; Shnyder, S. D.; Vinader, V.; Afarinkia, K.; Fernández, L. J.; et al. Study of the Chemotactic Response of Multicellular Spheroids in a Microfluidic Device. *Plos One* **2015**, *10* (10). DOI: 10.1371/journal.pone.0139515.

(145) Hashimoto, N.; Kitai, R.; Fujita, S.; Yamauchi, T.; Isozaki, M.; Kikuta, K. I. Single-Cell Analysis of Unidirectional Migration of Glioblastoma Cells Using a Fiber-Based Scaffold. *ACS Appl Bio Mater* **2023**, *6* (2), 765-773. DOI: 10.1021/acsabm.2c00958 From NLM Medline.

(146) Grochans, S.; Korbecki, J.; Siminska, D.; Zwierello, W.; Rzeszotek, S.; Kolasa, A.; Kojder, K.; Tarnowski, M.; Chlubek, D.; Baranowska-Bosiacka, I. CCL18 Expression Is Higher in a Glioblastoma Multiforme Tumor than in the Peritumoral Area and Causes the Migration of Tumor Cells Sensitized by Hypoxia. *Int J Mol Sci* **2022**, *23* (15). DOI: 10.3390/ijms23158536 From NLM Medline.

(147) Burdick, J. A.; Prestwich, G. D. Hyaluronic acid hydrogels for biomedical applications. *Adv Mater* **2011**, *23* (12), H41-56. DOI: 10.1002/adma.201003963.

(148) Tenje, M.; Cantoni, F.; Porras Hernández, A. M.; Searle, S. S.; Johansson, S.; Barbe, L.; Antfolk, M.; Pohlit, H. A practical guide to microfabrication and patterning of hydrogels for biomimetic cell culture scaffolds. *Organs-on-a-Chip* **2020**, *2*. DOI: 10.1016/j.ooc.2020.100003.

(149) Morohashi, H.; Kon, A.; Nakai, M.; Yamaguchi, M.; Kakizaki, I.; Yoshihara, S.; Sasaki, M.; Takagaki, K. Study of hyaluronan synthase inhibitor, 4-methylumbelliferone derivatives on human pancreatic cancer cell (KP1-NL). *Biochem Biophys Res Commun* **2006**, *345* (4), 1454-1459. DOI: 10.1016/j.bbrc.2006.05.037.

Appendix A - 3D printing protocols

Leveling and zeroing the build plate protocol

Adapted by Abigail Kreznor from Mars 4 Series 3D Printer User Manual on elegoo.com

Tools:

- Hex key
- Leveling paper
- If attaching glass slide: fugitive glue, heat gun, treated glass slide

Important notes:

- If releveling printer without replacing resin vat film, by careful to avoid touching or damaging plastic film
- If releveling and zeroing to account for addition of glass slide, follow steps 1-5 then follow specialized steps to avoid damaging the printer

For resin 3D printers:

1. Remove resin vat from printer
2. Use hex key to loosen all screws on build plate
3. Place leveling paper on tempered glass
4. Select "Tool" → "Manual" → "Home" to move z-axis to zero
5. After build plate stops, ensure four corners are evenly aligned, gently hold the build plate in place, and tighten the front followed by the side build plate screws with the hex key (***stop here*** if attaching glass slide and continue to specialized steps)
6. Use the manual "Up" and "Down" arrows to raise or lower the build plate by 0.10 mm steps until the leveling paper can be pulled out from under the build plate with slight resistance
7. Set the current z-axis position as the new "Home" location by selecting "Set Z=0" → "Confirm"
8. Manually return the build plate to the fully raised position
9. Return the resin vat to the printer

When attaching glass slide:

6. Use the manual "Up" arrow to raise the build plate until there is enough space to account for fugitive glue and glass slide
7. Remove the build plate from the printer and carefully attach the glass slide using a heat gun to activate the adhesive
8. Let the build plate return to room temperature

9. Use the manual “Down” arrow to ***carefully*** lower the build plate until the glass slide barely touches the leveling paper
10. Use the manual “Up” and “Down” arrows to raise or lower the build plate by 0.10 mm steps until the leveling paper can be pulled out from under the build plate with slight resistance
11. Set the current z-axis position as the new “Home” location by selecting “Set Z=0” → “Confirm”
12. Manually return the build plate to the fully raised position
13. Return the resin vat to the printer

General resin 3D printing protocol

Adapted by Abigail Kreznor from Elegoo User Guides at elegoo.com, intended for Mars 3 Pro 4K or Mars 4 DLP printers

Reagents, consumables, tools, and software:

- Selected resin type
- IPA
- Resin 3D printer
- AutoCAD
- Fusion 360
- Chitubox basic slicer
- Compressed air
- IPA rinse setup
- Ultrasonic bath
- Post-print cure setup
- Kimwipes
- Mallet
- Metal scraper
- IPA spray bottle

Design preparation:

1. Use a computer drawing software, like AutoCAD, to create a 2-dimensional design
2. Transform the drawing to a 3-dimensional object using a software like Fusion 360
   Note: Including a chamfered edge to the base of the print will make removal from the build plate easier
3. Export the 3D object as an appropriate file type for the selected slicing software (.stl for Chitubox)
4. Select the correct resin 3D printer in the Chitubox slicer, and load in the 3D object file
5. Orient the design appropriately on the digital build plate

Note: For microfluidic designs, printing flat on the build plate has provided the best success and eliminates unsupported regions

6. Set the appropriate print settings for the design
   Note: Table A.1 below shows settings for different resins and printers used in this work
7. Select the slice button, confirm the projected layers match the design, and save the sliced file onto a USB drive

Table A.1. Optimized print settings for the different resins used throughout this work fabricating microfluidic designs.

Printer	Resin	Layer height (mm)	Bottom layers	Bottom exposure time (s)	Normal exposure time (s)	Rest before lift (s)	Rest after lift (s)	Rest after retract (s)
Elegoo Mars 4 DLP	Elegoo 8K Standard in Space Grey	0.05	5	35	5	5	1	1
Elegoo Mars 3 Pro 4K	Elegoo Standard in Black	0.10	4	35	8	5	2	2
	Elegoo ABS-like Translucent	0.025	4	35	4.5	5	2	2
Elegoo Mars 2 Pro Mono	Elegoo ABS-like Translucent	0.025	4	45	2.25	10	2	2
Anycubic Photon S	Elegoo ABS-like Translucent	0.025	4	40	3	10	N/A	N/A
	Anycubic Basic Black	0.020	5	50	2.5	15	N/A	N/A
	Anycubic Basic Red	0.020	4	40	3	10	N/A	N/A
	Anycubic Basic Green	0.025	3	40	4	N/A	N/A	N/A

Resin printing:

8. Connect the USB drive to the printer
9. Turn the printer on
10. Complete the leveling or zeroing procedure if needed (see detailed Leveling and zeroing the build plate protocol)
11. Ensure enough resin is in the vat and that it is well mixed
12. Replace the UV cover over the printer
13. Select the "Print" option from the home screen, and choose the design to the printed
14. Ensure the first layer is completed and the build plate is repositioned for the second layer ***before*** stepping away until the print is finished

Post-print processing:

15. Let the print rest until there is no more substantial resin dripping
16. Loosen the upper knob to remove the build plate from the printer
17. Wipe excess uncured resin from the build plate with IPA-soaked kimwipe
    Note: All trash with uncured resin ***must be collected and cured before*** disposal
18. Use the metal scraper and mallet to carefully remove the print from the build plate
19. Transfer the print into the IPA rinse setup for a first round of uncured resin removal
20. Place the rinsed print into a secondary container with fresh IPA, float in ultrasonic bath, and sonicate for 5 min
21. Dry IPA from print with compressed air
22. Position print in curing setup and expose to light until no longer tacky to the touch
    Note: For microfluidic designs, typical post-print cure between 5 and 15 min

Other important printer maintenance:

23. Fully clean resin from build plate using IPA-soaked kimwipe(s), dry, and replace in resin printer
24. ***Regularly*** check underneath the resin vat to ensure no punctures or leaks
25. Replace the resin vat film as needed
26. Perform vat cleaning after failed prints by initiating full vat exposure (See printer User Manual for details)

Appendix B - Tissue culture protocols

C6 glioma culture protocol

Adapted by Abigail Kreznor and Jay Sibbitts from subculture method on ATCC.org

Reagents:

- 5 mL Trypsin-EDTA (0.25%) phenol red (frozen aliquot)
- 30 mL F-12K media supplemented with
    - 15% v/v heat inactivated Horse serum
    - 2.5% v/v FBS
    - 5% v/v Penicillin streptomycin (1x)

Important notes:

- 30 mL media is enough for trypsin neutralization and two new flasks (1:2 and 1:3)
- Culture C6 cells laying flat
- Split when cell layer reaches 80% confluency
- Be sure to mix solutions by pipetting before use
- Do not hit or shake flask during trypsinization to avoid cell clumping
- Do not let liquid in flasks touch inside flask neck
- Total volume 15 mL within T75 flask
- Rinse aspirator jar tubing with concentrated bleach then deionized water when done

For T75 flasks:

1. Follow the standard setup protocol for tissue culture
2. Turn water bath on to 37 ℃ and place 5 mL conical tube of trypsin in water bath
3. After trypsin has thawed, take tube from water bath, clean with 70% EtOH, and bring into biosafety cabinet
4. Remove previous flask from incubator and bring into biosafety cabinet
5. Discard spent culture media
6. Briefly rinse cell layer with 2 mL trypsin, use gentle rocking to cover cell layer
7. Discard 2 mL trypsin
8. Add remaining 3 mL trypsin to flask, ensure the entire cell layer is covered
9. Let the trypsin sit until the cell layer is detached (5-15 min at room temperature)
10. While cells sit in the trypsin, label 2 new T75 flasks, deliver the determined volume of fresh media needed for desired split ratios (10 mL for 1:2, 11.7 mL for 1:3)
11. Neutralize the trypsin by adding 7 mL of fresh media, mix using gentle pipetting
12. Deliver the determined volume of cell suspension to the new flasks (5 mL for 1:2, 3.3 mL for 1:3) and carefully mix using gentle rocking
13. Transfer new flasks to incubator

14. Follow standard cleanup and shutdown protocol for tissue culture

U-87 MG glioma culture protocol

Adapted by Abigail Kreznor and Jay Sibbitts from subculture method on ATCC.org

Reagents:

- 5 mL Trypsin-EDTA (0.25%) phenol red (frozen aliquot)
- 32 mL DMEM (high glucose) media supplemented with
    - 10% v/v FBS
    - 5% v/v Penicillin streptomycin (1x)

Important notes:

- 30 mL media is enough for trypsin neutralization and two new flasks (1:3 and 1:5)
- Culture U-87 cells laying flat
- Split when cell layer reaches 80% confluency
- Be sure to mix solutions by pipetting before use
- Do not hit or shake flask during trypsinization to avoid cell clumping
- Do not let liquid in flasks touch inside flask neck
- Total volume 15 mL within T75 flask
- Rinse aspirator jar tubing with concentrated bleach then deionized water when done

For T75 flasks:

1. Follow the standard setup protocol for tissue culture
2. Turn water bath on to 37 ℃ and place 5 mL conical tube of trypsin in water bath
3. After trypsin has thawed, take tube from water bath, clean with 70% EtOH, and bring into biosafety cabinet
4. Remove previous flask from incubator and bring into biosafety cabinet
5. Discard spent culture media
6. Briefly rinse cell layer with 2 mL trypsin, use gentle rocking to cover cell layer
7. Discard 2 mL trypsin
8. Add remaining 3 mL trypsin to flask, ensure the entire cell layer is covered
9. Let the trypsin sit until the cell layer is detached (5-15 min at room temperature)
10. While cells sit in the trypsin, label 2 new T75 flasks, deliver the determined volume of fresh media needed for desired split ratios (11.7 mL for 1:3, 13 mL for 1:5)
11. Neutralize the trypsin by adding 7 mL of fresh media, mix using gentle pipetting
12. Deliver the determined volume of cell suspension to the new flasks (3.3 mL for 1:3, 2 mL for 1:5) and carefully mix using gentle rocking
13. Transfer new flasks to incubator
14. Follow standard cleanup and shutdown protocol for tissue culture

CMFDA staining protocol

Adapted by Abigail Kreznor from Invitrogen CellTracker fluorescent probes product information sheet

Reagents:

- 1 mg CMFDA
- 215.1 µL DMSO
- 2998.5 µL serum-free DMEM
- 5 mL Trypsin-EDTA (0.25%) phenol red (frozen aliquot)
- 7 mL DMEM media supplemented with
    - 10% v/v FBS
    - 5% v/v Penicillin streptomycin (1x)

Preparation of 5 µM CMFDA working solution:

1. Follow the standard setup protocol for tissue culture
2. Warm dye vial to room temperature
3. Dissolve 1 mg of CMFDA with 215.1 µL of DMSO directly in dye vial to make 10 mM stock solution
4. Transfer 2998.5 µL of sterile, serum-free DMEM into a 5 mL conical tube
5. Pipet 1.5 µL of 10mM CMFDA stock solution into 5 mL conical tube to make 5 µM CMFDA working solution
6. Repeat until desired number of 3 mL aliquots are prepared
7. 5 µM CMFDA working solution aliquots should be frozen until use

Staining U-87 cells cultured in T75 flasks:

8. Follow the standard setup protocol for tissue culture
9. Turn water bath on to 37 ℃ and place 5 mL conical tubes of trypsin and 5 µM CMFDA staining solution in water bath
10. After both solutions have thawed, take CMFDA from water bath, clean with 70% EtOH, and bring into biosafety cabinet
11. Remove desired flask from incubator and bring into biosafety cabinet
12. Discard spent culture media
13. Add 3 mL of CMFDA solution to flask, ensure the entire cell layer is covered
14. Return the flask to the incubator for 30 min
15. Take trypsin from water bath, clean with 70% EtOH, and bring into biosafety cabinet
16. Remove stained flask from incubator and bring into biosafety cabinet
17. Discard CMFDA staining solution
18. Briefly rinse cell layer with 2 mL trypsin, use gentle rocking to cover cell layer
19. Discard 2 mL trypsin
20. Add remaining 3 mL trypsin to flask, ensure the entire cell layer is covered

21. Let the trypsin sit until the cell layer is detached (5-15 min at room temperature)
22. Neutralize the trypsin by adding 7 mL of fresh media, mix using gentle pipetting
23. Transfer 10 mL CMFDA-stained cell suspension to a 15 mL conical tube to be used for experiments

PI staining protocol

Adapted by Abigail Kreznor from Invitrogen propidium iodide nucleic acid stain product information, MP Biomedicals technical information, and Affymetrix staining protocol sheets

Reagents:

- PI (solid)
- DI water
- Serum-free DMEM media (not supplemented)

Important notes:

- When using Annexin V CF350, PI, and CMFDA simultaneously, the Annexin V CF350 and binding buffer staining solution should be replaced with media before an addition of PI stain to avoid overwhelming overlap of PI when using the B-2A filter set for CMFDA imaging
- PI kills cells over time, analysis must be completed within 4 hr of exposure to stain

Preparation of PI stock and working solutions:

1. Dissolve solid PI in DI water at 1 mg/mL concentration
   Note: this solution is stable stored at 4 °C, desiccated, and protected from light, up to 6 months
2. Further dilute 100 µL of the 1 mg/mL PI stock solution in 900 µL of serum-free DMEM to make 1 mL of 100 µg/mL PI working solution
   Note: this solution does not have a documented length of stability and should be used within a week

Staining U-87 cells:

3. Turn on the heating block to 37 °C
4. Pipet the desired volume of 100 µg/mL PI working solution into a sterile amber vial and warm in the heating block
5. Prepare cells as desired (seeded in well plate or microfluidic device)
6. After selected length of time, expose cells to desired volume of PI working solution
   Note: the 100 µg/mL PI working solution should be diluted to a final concentration between 20-30 µg/mL for cell staining
7. Incubate cells with stain for at least 5 min

Annexin V CF350 conjugate staining protocol

Adapted by Abigail Kreznor from Biotium Annexin V Conjugate and Annexin V Binding Buffer product information sheets

Reagents:

- 5X Annexin V Binding Buffer
- Ultrapure water
- 50 µg/mL Annexin V CF350 stock solution
- DMEM media supplemented with
    - 10% v/v FBS
    - 5% v/v Penicillin streptomycin (1x)

Important notes:

- Although the standard protocols for Annexin V Conjugate staining recommend multiple rinses with PBS and 1X binding buffer before and after stain incubation, these steps have been eliminated to make its use on cells within a microfluidic device simpler
- When using Annexin V CF350, PI, and CMFDA simultaneously, the Annexin V CF350 and binding buffer staining solution should be replaced with media before an addition of PI stain to avoid overwhelming overlap of PI when using the B-2A filter set for CMFDA imaging
- The total volume of 1X binding buffer and 1.5 µg/mL Annexin V CF350 staining solution needed for each experiment will vary based on the experimental design and, therefore, not specified here

Preparation of 1X Annexin V binding buffer and CF350 staining solution:

1. Dilute the 5X binding buffer to 1X using ultrapure water
2. Dilute the 50 µg/mL Annexin V CF350 stock solution to 1.5 µg/mL using 1X binding buffer
   Note: these dilutions should be completed before use, not premade and stored

Staining U-87 cells:

3. Ensure the Annexin V CF350 staining solution is at room temperature
4. Prepare cells as desired (seeded in well plate or microfluidic device)
5. Expose cells to an appropriate volume of 1.5 µg/mL Annexin V CF350 staining solution
6. Incubate the cells in staining solution for 15 min at room temperature ***in the dark***
7. Remove staining solution from cells and replace with fresh DMEM media

NucSpot® 568/580 staining protocol

Adapted by Abigail Kreznor from Biotium NucSpot Nuclear Stains product information sheet

Reagents:

- NucSpot 568/580 1000X in DMSO
- DMEM media supplemented with
    - 10% v/v FBS
    - 5% v/v Penicillin streptomycin (1x)

Important notes:

- The total volume of NucSpot staining solution needed for each experiment will vary based on the experimental design and, therefore, not specified here
- Follow standard setup and shutdown protocols for tissue culture and work in the BSC

Preparation of 10X NucSpot staining solution:

1. Pipet the required volume of complete DMEM into an amber Eppendorf tube
2. Add the required volume of 1000X NucSpot to the amber tube, pipet gently to mix
3. Store at 37 °C until ready for use

NucSpot staining of U-87 cells:

4. Prepare cells as desired in T75 flask
5. Add required volume of 10X NucSpot staining solution to cell suspension, gently mix via pipet
6. Incubate cells with NucSpot for 15 min in the **dark**
7. Prepare cell suspension for experiment as desired
   Note: for continuous viability monitoring, the required concentration of NucSpot must be maintained in all media throughout experiment duration

CMFDA + NucSpot® 568/580 staining protocol

Adapted by Abigail Kreznor from Invitrogen CellTracker fluorescent probes and Biotium NucSpot Nuclear Stains product information sheets

Reagents:

- 3 mL 5 µM CMFDA in serum-free DMEM (frozen aliquot)
- 5 mL Trypsin-EDTA (0.25%) phenol red (frozen aliquot)
- 11 mL DMEM media supplemented with
    - 10% v/v FBS
    - 5% v/v Penicillin streptomycin (1x)
- NucSpot 568/580 1000X in DMSO

Important notes:

- This protocol is designed to prepare a dual-stained U-87 cell suspension for manual injection into gradient-producing microfluidic devices, and all volumes were optimized for this specific application
- Follow standard setup and shutdown protocols for tissue culture and work in the BSC

CMFDA staining of U-87 cells:

1. Turn water bath on to 37 °C and place 5 mL conical tubes of trypsin and 5 µM CMFDA staining solution in water bath
2. After both solutions have thawed, take CMFDA from water bath, clean with 70% EtOH, and bring into biosafety cabinet
3. Remove desired flask from incubator and bring into biosafety cabinet
4. Discard spent culture media
5. Add 3 mL of CMFDA solution to flask, ensure the entire cell layer is covered
6. Return the flask to the incubator for at least 30 min
7. Take trypsin from water bath, clean with 70% EtOH, and bring into biosafety cabinet
8. Remove stained flask from incubator and bring into biosafety cabinet
9. Discard CMFDA staining solution
10. Briefly rinse cell layer with 2 mL trypsin, use gentle rocking to cover cell layer
11. Discard 2 mL trypsin
12. Add remaining 3 mL trypsin to flask, ensure the entire cell layer is covered
13. Let the trypsin sit until the cell layer is detached (5-15 min at room temperature)
14. Neutralize the trypsin by adding 6 mL of fresh media, mix using gentle pipetting
15. Transfer 9 mL CMFDA-stained cell suspension to a 15 mL conical tube
16. Remove 50 µL of CMFDA-stained cell suspension for hemocytometer analysis to determine starting cell density and viability
    Note: Keep CMFDA-stained cell suspension in water bath during hemocytometer work

Preparation of 10X NucSpot solution:
(recommended to be completed during CMFDA incubation)

17. Pipet 346.5 µL of complete DMEM into a 1.5 mL amber Eppendorf tube
18. Pipet 3.5 µL of 1000X NucSpot 568/580 into the same amber tube, gently mix via pipet
19. Store 10X NucSpot solution in the heating block at 37 °C until needed

Preparation of 0.25X NucSpot solution:
(recommended to be completed during trypsinization)

20. Pipet 3.9 mL of complete DMEM into a 15 mL conical tube
21. Pipet 100 µL of 10X NucSpot solution into the same tube, mix gently via pipet
22. Keep this solution at 37 °C until needed

U-87 resuspension:

23. Centrifuge CMFDA-stained cell suspension at 1200 rpm for 5 min
24. Carefully remove supernatant and discard
25. Add desired volume of 0.25X NucSpot in complete DMEM to tube, gently resuspend
    Note: It is **very** important to ensure cell suspension is homogenous without cell clumps
26. Transfer dual-stained cell suspension into 5 mL Eppendorf tube
27. Carefully fill a sterile syringe with 2.5-3 mL dual-stained cell suspension
28. Keep the syringe at 37 °C until needed for manual cell injection into device
    Note: After successful cell seeding via manual injection, device must incubate in **darkness** for 15 min before collecting any images

Appendix C - Other procedures

PDMS device fabrication from resin molds protocol

Adapted by Abigail Kreznor from previous Culbertson Group PDMS protocols

Tools:

- Precision balance
- Disposable cup
- Stirrer
- Vacuum desiccator
- Plexiglass frame
- Scotch Magic tape
- Double-sided tape
- Oven
- Laminar flow hood
- Scalpel and/ or single edge razor blade
- Blunted 23-gauge needle
- Petri dish

Reagents:

- Dow Sylgard 184 PDMS elastomer base and curing agent kit

Important notes:

- Laboratory temperature and humidity have significant impact on the success of casting PDMS devices from resin molds
- A ratio of 5:1 elastomer base to curing agent was used for this research

Device fabrication:

1. Ensure the oven is preheated to 50 °C
2. Zero disposable cup on balance
3. Pour desired mass of elastomer base into cup
4. Re-zero balance
5. Pour desired mass of curing agent into cup
6. Thoroughly stir the two parts together
7. Place in the vacuum desiccator until all bubbles are removed
8. Use an air blow gun and Scotch Magic tape to clean off the resin mold and store in a laminar flow hood
9. Use double-sided tape to secure resin mold and/ or plexiglass frame in place

10. Carefully pour PDMS into frame over the mold, avoiding bubbles
11. Transfer the PDMS into the oven and bake until fully cured
    Note: for this work, PDMS was baked for 5.5 hr
12. Remove the cured PDMS from the oven and cool to room temperature in a laminar flow hood
13. Use a scalpel and/ or a razor blade to remove the frame from the cured PDMS
14. Carefully peel up the PDMS slab from the resin mold and place channel-side up
15. Trim off any excess PDMS from the edges of the device
16. Use the 23-gauge needle to punch out reservoirs
17. Store the prepared device in a labeled petri dish, channel-side up, until use

Profilometer protocol

This was completed using the XP-2 Stylus Profiler from AMBiOS Technology.

Important notes:

- Best program performance comes from measuring from elevated to low-lying regions
- Be careful to avoid crashing the stylus tip into any samples
- Confirm the correct units are noted for each scan measurement

How to use the profilometer:

1. Turn on the profiler using the switch on the back
2. Open the "Shortcut to XP2" program
3. Select "Yes" after prompted to home the system, and wait until completed
4. Select "Setup" to adjust the scan settings for the sample
5. Place the calibration Step Height Reference on the center of the stage
6. Raise the stylus selecting "Z+" to ensure it is higher than the Step Height Reference
7. Select the "Center" load position to move the stage
8. Use "X+" "X-" "Y+" and "Y-" to position the stage
9. Use "Z-" to carefully lower the stylus tip towards the sample
10. Select "Engage" to automatically lower the stylus to the sample
11. Select "Scan" to begin the scan of your sample, and confirm by selecting "Yes" when prompted if ready to scan
12. After the scan is done, and the data window appears, place both red cursors on the edges of a flat section of the scan and select to "Level Data"
13. To calibrate, place one red cursor on the upper flat region and the other on the lower region
14. Right click and select to "Size Cursor" and drag each to cover the majority of each flat region
15. Selection "Calibration" and "Yes" when prompted if the cursors are placed correctly

16. Enter the measured calibrated height of the feature, select “Ok,” and close the data window
17. Replace the Step Height Reference with the next sample
18. Repeat the same process, without the calibration steps, to scan the next sample
19. When the data window appears and the leveling process is completed, place the red cursors, the resulting difference in X and Y positions will display on the right
20. If needed, individual scan data can be saved by exporting as a text file
21. After all scans are completed, remove all samples from the stage, raise the stylus tip up, and return the stage to the starting position
22. Close the program and turn off the profiler

Fluorescence imaging protocol

This was completed using the Nikon Eclipse TE2000-U inverted microscope, the B-2A, G-2A, and UV-2E/C filter cubes, the X-Cite 120 Fluorescence Illumination System, and the Sony Alpha a6400 camera with the remote operation computer software.

Important notes:

- When using Annexin V CF350, PI, and CMFDA simultaneously, the Annexin V CF350 and binding buffer staining solution should be replaced with media before an addition of PI stain to avoid overwhelming overlap of PI when using the B-2A filter set for CMFDA imaging

Preparation for fluorescent imaging:

1. Power on the inverted microscope, X-Cite system, Sony Alpha a6400 camera, and remote camera software
2. Confirm the X-Cite source has warmed up before collecting images (bulb icon changes from flashing to constant)
3. Turn on the medium grid with diagonals digital crosshair gridlines on remote camera window
4. Select desired file location to save pictures
5. Align appropriate filter set for selected fluorescent dye
6. Ensure the Alpha a6400 camera is on the manual setting
7. Place stained sample on microscope
8. Turn off overhead lights

Imaging procedure for 24-well plates:

9. Using the 2X objective, align the upper left edge of the eyepiece image with the outer perimeter of the selected well (as shown in Figure C.1)
10. Switch to desired magnification, adjusting focus as needed by observing remote camera software on computer window

11. Collect brightfield image
    a. Dia-illumination on
    b. Set ISO auto
    c. Set shutter 1/30 – 1/600
12. Confirm appropriate image quality, adjust settings as needed
13. Collect fluorescent image(s)
    a. Dia-illumination off
    b. Set ISO 600-4000
    c. Set shutter 0.5-4 s
14. Confirm appropriate image quality, adjust settings as needed
15. For a second imaging location, use the 2X objective, align the lower right edge of the eyepiece image with the outer perimeter of the selected well (as shown in Figure C.1)
16. Repeat steps 9-15 to collect more images in other wells, switching to other filter sets as required

Imaging procedure for 96-well plates and tape pseudo-well plates:

9. Using the 4X objective, align the upper left edge of the eyepiece image with the outer perimeter of the selected well (as shown in Figure C.1)
10. Switch to desired magnification, adjusting focus as needed by observing remote camera software on computer window
11. Collect brightfield image
    a. Dia-illumination on
    b. Set ISO auto
    c. Set shutter 1/30 – 1/600
12. Confirm appropriate image quality, adjust settings as needed
13. Collect fluorescent image(s)
    a. Dia-illumination off
    b. Set ISO 600-4000
    c. Set shutter 0.5-4 s
14. Confirm appropriate image quality, adjust settings as needed
15. For a second imaging location, use the 4X objective, align the lower right edge of the eyepiece image with the outer perimeter of the selected well (as shown in Figure C.1)
16. Repeat steps 9-15 to collect more images in other wells, switching to other filter sets as required

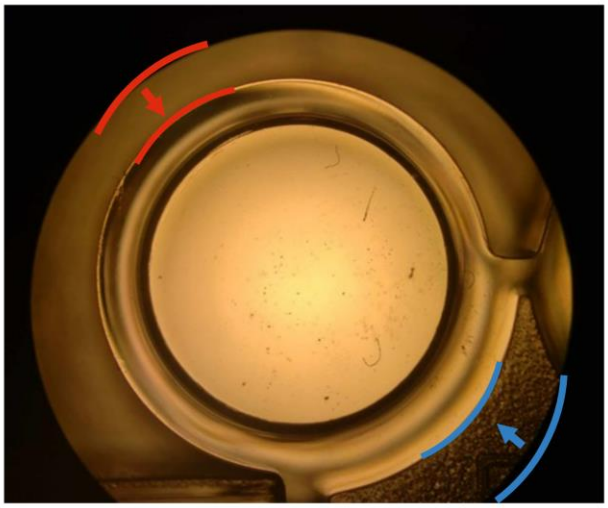

Figure C.1. The edge of the eyepiece view was aligned with the outer perimeter of the selected well in two separate locations for imaging.

Imaging procedure for microfluidic devices:

9. Using the desired objective, gridlines, and distance markers, align the device for imaging, focusing using the remote camera software window
10. Collect brightfield image
    a. Dia-illumination on
    b. Set ISO auto
    c. Set shutter 1/30 – 1/600
11. Confirm appropriate image quality, adjust settings as needed
12. Collect fluorescent image(s)
    a. Dia-illumination off
    b. Set ISO as needed
    c. Set shutter as needed
13. Confirm appropriate image quality, adjust settings as needed
14. Repeat steps 9-13 to collect more images at other locations, switching to other filter sets as required

Cell viability analysis protocol

This analysis was completed using ImageJ.

Important notes:

- Brightfield images at each location are used to provide alignment info for fluorescent images

Adjusting image qualities:

1. Open all experimental images in ImageJ
2. Convert the images to a stack
3. Adjust the brightness/ contrast for the stack based on the image requiring the most adjusting
4. Convert the stack back to individual images
5. Save edited image files with new names

Assessing cell populations:

6. Count all cells manually by adding markers to each
7. Distinguish dead cells, using Trypan blue, PI, or NucSpot staining, from live cells and count manually
8. Distinguish dying cells, using Annexin V staining, from live and dead cells and count manually

Fluorescent intensity analysis protocol

This analysis was completed using ImageJ and Igor Pro.

Important notes:

- Brightfield images at each location are used to provide alignment info for fluorescent images
- Images without any fluorescence and with complete fluorescence at each location are used for background subtraction and illumination correction
- Data was smoothed using binomial, moving average box, and Savitzky-Golay 2^{nd} and 4^{th} order with similar results for each method

Adjusting image qualities:

1. Open all experimental images in ImageJ
2. Convert the images to a stack
3. Adjust the brightness/ contrast for the stack based on the image requiring the most adjusting
4. Convert the stack back to individual images
5. Save edited image files with new names

Extracting fluorescent intensity values:

6. Open all experimental images in ImageJ
7. Convert all images to a stack
8. Convert the stack image type to 8-bit
9. Use the distance markers on the brightfield image to select a rectangular region of interest for analysis

10. Analyze the plot profile and save the data for each image in the stack at the same region of interest

Fluorescent intensity data workup:

11. Load all plot profile data as waves into Igor Pro
12. Perform a background correction by subtracting the no fluorescence data from all waves at that imaging location, create a new wave for each background-corrected data set
13. Determine where to trim the data using the full fluorescence and brightfield images, create a new trimmed wave
14. Make a correction wave to account for difference in illumination/ emission collection using full fluorescence image

Equation C.1. Correction for fluorescent intensity across observation channel.

$$Y_{corr} = \left[{(Y_{max} - Y_i)}/{Y_{max}}\right] + 1$$

Y_{max} = maximum intensity (Y) value of full fluorescence data

Y_i = full fluorescence wave

15. Multiply each data set at that image location by the correction wave, create a new corrected wave
16. Normalize the data for easier comparison, create a new normalized wave

Equation C.2. Normalization for fluorescent intensity across observation channel.

$$Y_{norm} = \left[{(Y_i - Y_{min})}/{(Y_{max} - Y_{min})}\right]$$

Y_i = corrected wave

Y_{min} = minimum intensity (Y) value for corrected wave

Y_{max} = maximum intensity (Y) value for corrected wave

17. Smooth the data with a moving average box, 10 points, create a new smoothed wave
18. Repeat steps 12-18 for all imaging locations

Cell tracking analysis protocol

This analysis was completed using Microsoft Pain, ImageJ, and Igor Pro.

Adjusting image qualities:

1. Open all experimental CMFDA images in ImageJ
2. Convert the images to a stack
3. Adjust the brightness/ contrast for the stack based on the image requiring the most adjusting
4. Convert the stack back to individual images
5. Save edited image files with new names
6. Convert edited images back to a stack
7. Convert the stack image type into 8-bit grey value

8. Save all edited images as files with new names

Marking cells for tracking:

9. Open the scaled, black and white version of the CMFDA image in Microsoft Paint
10. Add a new layer to the image
11. Use the brush tool to put a 50-pixel red dot at the center or each cell selected for tracking
12. Save both the marked cell image and the isolated layer with dots as new image files
13. Repeat this process for all images placing new dots on the selected cells as they move at each timepoint

Extracting (x, y) coordinates for tracked cells:

14. Open all isolated dot cell tracking images in ImageJ
15. Convert the images to a stack
16. Convert the stack image type into 8-bit grey value
17. Invert black and white in the images
    Note: the dots should now be white, and the background should be black
18. Adjust the brightness/ contrast for the stack so the dots are bright white spots
19. Transform the stack by rotating all images 90° to the left
20. Set the image scale, apply this setting globally to all images in stack
    Note: for images collected at 10X magnification using this setup, 1 μm = 3.5 pixels
21. Adjust the threshold until the dots are isolated from the dark background
22. Use Analyze Particles and the Centroid measurement to determine the central (x, y) coordinates of each dot, corresponding to the location of each tracked cell
23. Save the coordinates in a spreadsheet
24. Repeat this process for each image at all required timepoints
    Note: ensure that the coordinates for each cell are consistent between images since the order listed may change as cells move

Determining and plotting cell displacement:

25. Use the (x, y) coordinates to determine cell displacement for each cell, average the displacement for each experimental condition, and save data in the spreadsheet

Equation C.3. Calculation for x displacement.

$$x_{displacement} = x_{end} - x_{start}$$

Equation C.4. Calculation for y displacement.

$$y_{displacement} = y_{end} - y_{start}$$

26. Load the spreadsheet values in Igor Pro
27. Plot the displacement for each tracked cell and the average displacement as markers on a graph
28. Repeat the graphing process for each experiment

LabSmith uProcess sequences

This was completed using uProcess version 2.066.

Important notes:

- To prep the LabSmith equipment and tubing for an experiment, the syringe pumps are dispensed completely to 0.0 µL, but this is changed to 23.0 µL during experiments to ensure any small bubbles remain in the syringe pump
- High flowrates, 900 µL/min, are used for device filling, but this is lowered significantly during experiments
- Sequences without a specific end step must be stopped manually
- 4-port valves must be set to High Speed, 3-port valves must be set to Standard operation

Continuous filling sequence (03-28-24_ContFillPDMS_SplitValves):

```
*Valves_4VM02     =     4VM                    //initializing all valves
*Syringe1    =    SPS   80 ul                  //initializing all syringe pumps
*Syringe2    =    SPS   80 ul
*Syringe3    =    SPS   80 ul
*Syringe4    =    SPS   80 ul

1_allVA:                                       //name of step 1
     Valves_4VM02:     SetValves(1, 0, 1, 0)   //set Valves 1 and 3 to position A
     WaitDone()                                //wait until step is complete
     Valves_4VM02:     SetValves(0, 1, 0, 1)   //set Valves 2 and 4 to position A
     WaitDone()                                //wait until step is complete

2_FillS1S4:                                    //name of step 2
     Syringe1:    SetFlowRate( 900.000 ul/min) //flowrate for Syringe 1 filling
     Syringe1:    MoveTo( 100.000 ul)          //set fill volume for Syringe 1
     Syringe4:    SetFlowRate( 900.000 ul/min) //flowrate for Syringe 4 filling
     Syringe4:    MoveTo( 100.000 ul)          //set fill volume for Syringe 4
     WaitDone()                                //wait until step is complete

3_V2V4B:                                       //name of step 3
     Valves_4VM02:     SetValves(0, 3, 0, 3)   //set Valves 2 and 4 to position B
     WaitDone()                                //wait until step is complete

4_FillS2S3_EmptyS1S4:                          //name of step 4
     Syringe2:    SetFlowRate( 900.000 ul/min) //flowrate for Syringe 2 filling
     Syringe2:    MoveTo( 100.000 ul)          //set fill volume for Syringe 2
     Syringe3:    SetFlowRate( 900.000 ul/min) //flowrate for Syringe 3 filling
```

```
        Syringe3:       MoveTo( 100.000 ul)             //set fill volume for Syringe 2
        Syringe1:       SetFlowRate( 900.000 ul/min)    //flowrate for Syringe 1 dispensing
        Syringe1:       MoveTo( 0.000 ul)               //set delivery volume for Syringe 1
        Syringe4:       SetFlowRate( 900.000 ul/min)    //flowrate for Syringe 4 dispensing
        Syringe4:       MoveTo( 0.000 ul)               //set delivery volume for Syringe 4
        WaitDone()                                      // wait until step is complete

5_V2V4A:                                                //name of step 5
        Valves_4VM02:   SetValves(0, 1, 0, 1)           //set Valves 2 and 4 for position B
        WaitDone()                                      // wait until step is complete

6_FillS1S4_EmptyS2S3:                                   //name of step 6
        Syringe1:       SetFlowRate( 900.000 ul/min)    //flowrate for Syringe 1 filling
        Syringe1:       MoveTo( 100.000 ul)             //set fill volume for Syringe 1
        Syringe4:       SetFlowRate( 900.000 ul/min)    //flowrate for Syringe 4 filling
        Syringe4:       MoveTo( 100.000 ul)             //set fill volume for Syringe 4
        Syringe2:       SetFlowRate( 900.000 ul/min)    //flowrate for Syringe 2 dispensing
        Syringe2:       MoveTo( 0.000 ul)               //set dispense volume for Syringe 2
        Syringe3:       SetFlowRate( 900.000 ul/min)    //flowrate for Syringe 3 dispensing
        Syringe3:       MoveTo( 0.000 ul)               //set dispense volume for Syringe 3
        WaitDone()                                      // wait until step is complete
        Goto 3_V2V4B                                    //loop to step 3
```

Reynolds number and shear stress annotated spreadsheet

An annotated version of the spreadsheet used to calculate Reynolds number and shear stress based on established experimental parameters.

	A	B	C	Annotations
1	**Variable symbol**	**Variable names and units**	**Values**	
2	a or h	channel height (m)	0.0002	user-entered dimensions of observation channel
3	b or w	channel width (m)	0.0043	
4	l	channel length (m)	0.009	
5	D_H	hydraulic diameter (m)	0.00038222	=((2*C2*C3)/(C2+C3))
6	μ	dynamic viscosity (kg/(m·s))	0.00093	from Christine Poon[138]
7	ρ	density (kg/m^3)	1009	
8	ν	kinematic viscosity (m^2/s)	9.21705E-07	=(C6/C7)
9	A	cross sectional area (m^2)	0.00000086	=(C2*C3)
10	Q (high)	HIGH flowrate (m^3/s)	9.33E-08	2800 μL/min at BOTH inlets (set by LabSmith equipment)
11	Q (low)	LOW flowrate (m^3/s)	3.33E-11	1.0 μL/min at BOTH inlets (set by LabSmith equipment)
12	Re (high)	HIGH Reynolds # (unitless)	44.98910394	=((C10*C5)/(C8*C9))
13	Re (low)	LOW Reynolds # (unitless)	0.016057204	=((C11*C5)/(C8*C9))
14	τ (high)	HIGH shear stress (dyne/cm^2)	0.302682558	=((6*C6*C10)/((C2^2)*C3))*10^5/100^3
15	τ (low)	LOW shear stress (dyne/cm^2)	0.000108031	=((6*C6*C11)/((C2^2)*C3))*10^5/100^3